# Aspects of Low Reynolds Number Microswimming Using Singularity Methods

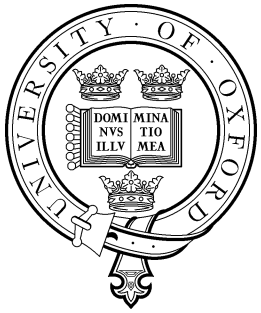


Mark Curtis
St Catherine's College
University of Oxford

A thesis submitted for the degree of
*Doctor of Philosophy*

Trinity 2013

This thesis is dedicated to my son, Mateo, born a few weeks after my viva.

# Acknowledgements

The thesis would not have been possible without the guidance and support of my supervisor, Dr. Eamonn Gaffney, whose approachability, dedication to frequent meetings and passion for the subject matter have made working with him a genuine pleasure.

I would like to thank my experimental collaborators at The University of Birmingham and the Centre for Human Reproductive Science, Dr. David Smith, Dr. Jackson Kirkman-Brown and Dr. Thomas Connolly, for their experimental contributions to the work on hyperactivated, sperm motility in Chapter 3.

At The University of Oxford, I would like to acknowledge my colleagues who offered both mathematical and general advice throughout the early stages of my graduate degree. These include Dr. Hermes Gadêlha and Dr. Henry Shum, both previously in the Centre for Mathematical Biology (CMB), and Dr. Heike Gramberg, previously in the Oxford Centre for Industrial and Applied Mathematics (OCIAM).

I must also acknowledge my research centre for providing a productive and social working environment, the Oxford Centre for Collaborative and Applied Mathematics (OCCAM), and my funding, award No. KUK-C1-013-04, made possible by the King Abdullah University of Science and Technology (KAUST), Saudi Arabia. In additional, my thanks are extended to The Complutense University of Madrid for providing me with an office for a month while writing up the thesis over the Christmas period in 2012.

Finally, I would like to thank my wife, Nadia, for her ongoing support and my family and friends for making my graduate life so enjoyable!

# Abstract

Three different models, relating to the study of microswimmers immersed in a low Reynolds number fluid, are presented. The underlying, mathematical concepts employed in each are developed using singularity methods of Stokes flow.

The first topic concerns the motility of an artificial, three-sphere microswimmer with prescribed, non-reciprocal, internal forces. The swimmer progresses through a low Reynolds number, nonlinear, viscoelastic medium. The model developed illustrates that the presence of the viscoelastic rheology, when compared to a Newtonian environment, increases both the net displacement and swimming efficiency of the microswimmer.

The second area concerns biological microswimming, modelling a sperm cell with a hyperactive waveform (vigorous, asymmetric beating), bound to the epithelial walls of the female, reproductive tract. Using resistive-force theory, the model concludes that, for certain regions in parameter space, hyperactivated sperm cells can induce mechanical forces that pull the cell away from the wall binding. This appears to occur via the regulation of the beat amplitude, wavenumber and beat asymmetry.

The next topic presents a novel generalisation of slender-body theory that is capable of calculating the approximate flow field around a long, thin, slender body with circular cross sections that vary arbitrarily in radius along a curvilinear centre-line. New, permissible, slender-body shapes include a tapered flagellum and those with ribbed, wave-like structures.

Finally, the detailed analytics of the generalised, slender-body theory are exploited to develop a numerical implementation capable of simulating a wider range of slender-body geometries compared to previous studies in

the field.

# Contents

# List of Figures

# Chapter 1

# Introduction

The introduction begins by developing the theme summarised in the thesis title, with descriptions of a '**low Reynolds number**' environment, a '**microswimmer**', and how '**singularity methods**' can be used to model numerous aspects of low Reynolds number microswimming, as illustrated in this thesis. The background information for the specific models explored are subsequently detailed, along with their respective motivations for investigation and the background fluid mechanics. A literature review follows, documenting published work surrounding the application of singularity methods to microswimming models. The introduction concludes with a chapter-by-chapter description of the thesis structure and a statement of originality, especially highlighting any work conducted by collaborating experimentalists.

## 1.1 The Background

As an overview, the thesis applies and develops mathematical theories underlying viscous fluid mechanics to a variety of scenarios modelling the dynamics of swimming bodies immersed in the fluid. The subsequent studies employ singularity methods to model the generated flow fields, forces and net velocities around both artificial and biological microswimmers immersed in a low Reynolds number fluid. The bodies studied typically have geometric dimensions on the order of micrometres and are thus termed '**microswimmers**'. These include artificial constructions, for example made from moving spheres connected by extending rods [62, 70], or relate to biological microorganisms, such as swimming bacteria and spermatozoa [64].

The microswimmers modelled are immersed in either a viscous or viscoelastic fluid. While exact definitions of the fluid mechanics are given in Section 1.3, the fluid envi-

ronments modelled are always assumed to be incompressible with constant viscosities. They possess the property that the inertial effects, associated with the acceleration of the fluid, are negligible when compared to the effects due to viscosity. The latter characteristic is best defined using a dimensionless parameter called the Reynolds number (see Section 1.3.1.1), expressing the ratio of the inertial to viscous forces. Thus, if viscous forces dominate, the fluid is referred to as a '**low Reynolds number**' medium.

In Section 1.3, linear, governing equations describing the low Reynolds number fluids (the Stokes equations) are presented. These equations possess a Green's function, named the Stokeslet, which physically represents the flow field around a point-force acting in one direction within the fluid domain. The magnitude of the Stokeslet solution in its far field is inversely proportional to the distance away from the point-force; thus, the influence of the point-force on the fluid decays as one moves further into the 'far-field'. However, if one were to inspect the flow field approaching the point-force, the 'near-field', fluid velocities tend to infinity and hence the Stokeslet is said to be singular at the point-force location; it is often referred to as a fundamental, singular solution of Stokes flow. Other singular solutions to the Stokes equations exist, for example the potential dipole describing a point-source acting in all directions; see Section 1.3.1.6. Together, combinations or distributions of these singular solutions, each with prescribed strengths, can be used to deduce velocity fields around moving, rigid bodies lying within the fluid. Techniques for determining the flow field and forces using these singular solutions are referred to as '**singularity methods**' [79].

## 1.2 Models and Motivations

There are countless aspects of low Reynolds number microswimming that have been, and have yet to be, studied. In this thesis, particular attention is given to three, different topics within low Reynolds number microswimming. Each requires the direct implementation, or use of theories derived from, singularity methods in Stokes flow. Brief backgrounds are provided for each of the three topics, accompanied respectively by motivations outlining the significance of their investigation.

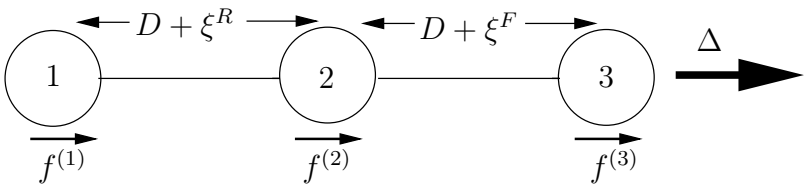


Figure 1.1: An artificial microswimmer made up of three spheres, colinearly connected by thin rods of mean length $D$ that oscillate out of phase via rod displacements, $\xi^R(t)$ for the rear rod and $\xi^F(t)$ for the front rod; this induces a net motion per beat cycle, $\Delta$. Each sphere has velocity $\mathbf{U}^{(k)}$ for $k \in \{1, 2, 3\}$, where the force acting on each sphere is similarly denoted $\mathbf{f}^{(k)}$.

### 1.2.1 The Three-Sphere Microswimmer in a Viscoelastic Fluid

The first topic analytically explores the effects, if any, of considering nonlinear, viscoelastic rheology in the context of a low Reynolds number fluid environment. In particular, the net displacement and efficiency of the three-sphere microswimmer immersed in such a fluid are investigated.

The three-sphere model, or Najafi–Golestanian swimmer [70], is a simple, idealised model for swimming locomotion consisting of three, colinearly linked spheres connected by two, thin rods; see figure 1.1. These rods oscillate out of phase to induce a net motion in the swimmer. By prescribing the internal forces acting on the three spheres, for example due to internal motors that oscillate the rods, the swimming dynamics are determined analytically in both a standard, Newtonian fluid and a low Reynolds number, nonlinear, viscoelastic fluid, the latter constituting novel work. The effects of viscoelasticity on the net displacement and efficiency of the swimmer are subsequently highlighted.

Modelling the motion and flow fields produced by artificial microswimmers in a low Reynolds number, viscoelastic medium is of considerable importance in developing our understanding of complex, biological processes. Such processes include the movement of bacteria to study infection, the beating of cilia inducing mucosal flows [67, 84] and sperm motility for reproduction [40]. Microorganisms such as these have to overcome the challenges of low Reynolds number environments that are dominated by viscous-drag forces and viscoelastic rheology, for example in cervical or lung mucus [93]. Furthermore, microswimmer models can also contribute to understanding the effects of surfaces and cellular interactions between swimmers within low Reynolds

number, viscoelastic environments [105].

Alongside the biological motivations for simple swimmer models, studying locomotion at a low Reynolds number has implications in the design and construction of artificial, micro-robotic swimmers, so as to optimise the net displacement given the surrounding fluid environment. Engineering artificial swimmers has applications to medical fields such as drug delivery within the body, for example [11]. The mathematical analysis also provides the groundwork for subsequent, controlled, experimental testing [62].

Important numerical motivations exist for deriving analytical expressions from simple swimmer models. They provide useful validation checks for numerical codes capable of simulating more complex swimming motions and fluid rheologies. The analytical expressions also allow for straightforward parameter investigations, given appropriate parameter regimes, greatly reducing the computational time if one were to solve the full problem numerically.

### 1.2.2 Hyperactivated, Tethered-Sperm Motility

The second topic models the forces exerted by the beating flagellum (tail) of a sperm cell that has become tethered (caught) on the walls of the female reproductive tract. Sperm cells are examples of biological microswimmers immersed in low Reynolds number, physiological fluids, where their motility is dependent on the beat patterns propagating down their flagella.

Flagella are ubiquitous and slender organelles responsible for inducing cell propagation and fluid mixing in numerous, biological settings; these include reproduction and filter feeding [64]. The flagellum axoneme (inner core) consists of nine microtubule doublets (pairs of microtubules) running down the flagellum, surrounding a central pair of single microtubules [34]; see figure 1.2. This '9 + 2' canonical axoneme drives flagellar motility via the contraction of dynein, molecular motors linking the doublets together [102]. In the context of mammalian reproduction, flagellated motility is critical for the transport of sperm [50], which must traverse immunologically hostile, and biophysically diverse, microenvironments on the journey to the egg.

The beat patterns of mammalian, sperm flagella observed under the microscope can be categorised into two different types; see figure 1.2. The first is **symmetric** beating,

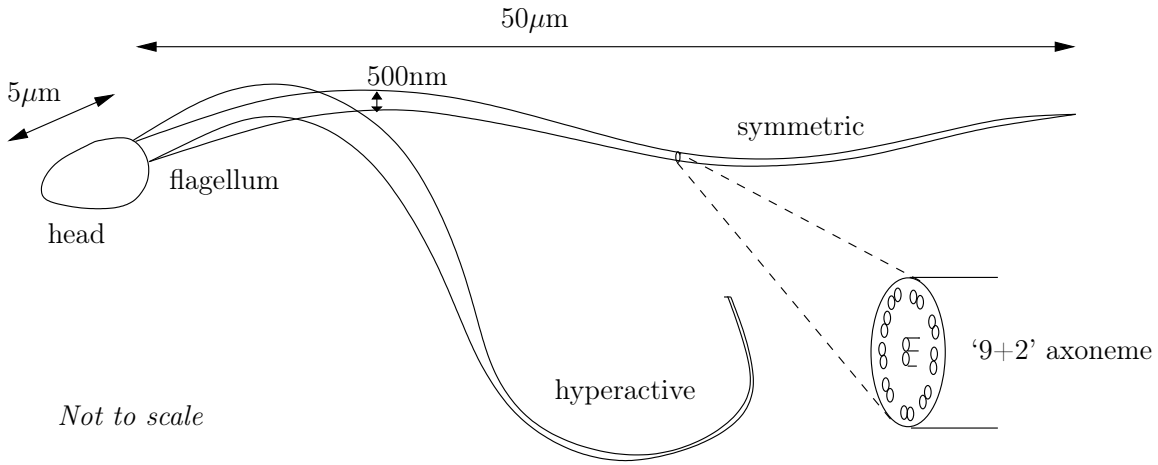


Figure 1.2: An illustration of the symmetric beat propagating along the sperm flagellum, where the typical dimensions are given for a mammalian sperm [28] and the '9+2' axoneme is highlighted in a cross section of the flagellum [34]; note that the figure is not to scale. A hyperactive beat is also shown, characterised by a larger amplitude and lower wavenumber.

involving symmetric, low-amplitude waves propagating down the flagellum with a net, linear propulsion of the sperm cell. The second, **hyperactive**, waveform is classified by vigorous, asymmetric waves of higher amplitude, lower wavenumber and lower frequency propagating down the flagellum. Hyperactive beating results in highly curved trajectories of the sperm cells in watery media, though this is less clear in very viscoelastic solutions [90]. It is also part of the capacitation process, whereby a sperm prepares for the prospective penetration of the zona pellucida (the extracellular coating surrounding the plasma membrane of the egg [17]) and subsequent, egg fusion [99].

The exact mechanism for the induction of the waveform asymmetry upon hyperactivation is not known, though demembranated, flagellar studies do indicate that regulation occurs in the axoneme, and calcium-calmodulin (calcium-modulated proteins) complexes have been at least partially implicated [19, 47, 74]. In contrast to understanding the complex, regulatory dynamics underlying the hyperactive waveform, its kinematical characterisation is relatively straightforward, especially for rodent studies where the sickle-shaped (falciform) sperm head highlights a natural, body-fixed, reference frame for observations. In particular, Ohmuro and Ishijima's work on golden-hamster sperm [72] suggests that the hyperactive-flagellum wavenumber is reduced by 4/7th when compared to symmetric beating, while the frequency is reduced by around a factor of 0.25–0.35. They also show that the waveform amplitude increases by three or four times for hyperactive beating, relative to symmetric waveforms.

These altered kinematics of the beat pattern associated with hyperactivation are, in golden hamsters [88], observed to facilitate the successful penetration of the zona pellucida and are hypothesised to enable sperm to surmount rheological, and geometrical, impediments within the female reproductive tract [92]. Hyperactivation is also observed to initiate as sperm escape from ciliary and epithelial (wall) bindings, or tethers, formed within regions of the female oviducts. This leads to the conjecture in the literature that hyperactivation is mechanically important for sperm escape. The mechanical implications of hyperactive, flagellar waveforms are, however, underexplored.

It is the latter of these biological observations which motivates the model for a hyperactive, tethered sperm cell. The question as to whether or not it is mechanically feasible for a sperm cell to generate forces that pull away from the point of tethering (binding site) is addressed; this is in contrast to the intuitive notion that a sperm cell is always pushed by its flagellum.

### 1.2.3 Slender-Body Theory with Generalisations to Different Body Shapes

The third topic focuses on the development of a theory to describe the Stokes fluid flow around a long, thin, slender body with circular cross sections that can vary arbitrarily in radius along a curvilinear centre-line. These slender bodies are motivated by, but not restricted to, microswimmer geometries.

Determining the fluid flow around slender bodies with circular cross sections in a low Reynolds number environment has been well-studied, as documented in the upcoming literature review in Section 1.4. These slender-body theories (SBTs) are based on asymptotic methods exploiting a small, slenderness ratio, $\varepsilon$. This is the ratio between the maximum, cross-sectional radius of the body divided by the total (or half) length of the body centre-line. Notable theories include those describing the flow around tubular bodies with cylindrical geometries distorted along a curvilinear centre-line [27, 57] and slender bodies based on prolate-spheroidal geometries [53].

SBTs which can incorporate a body with circular cross sections that vary in radius along a curvilinear centre-line include Batchelor's logarithmically accurate SBT [9]

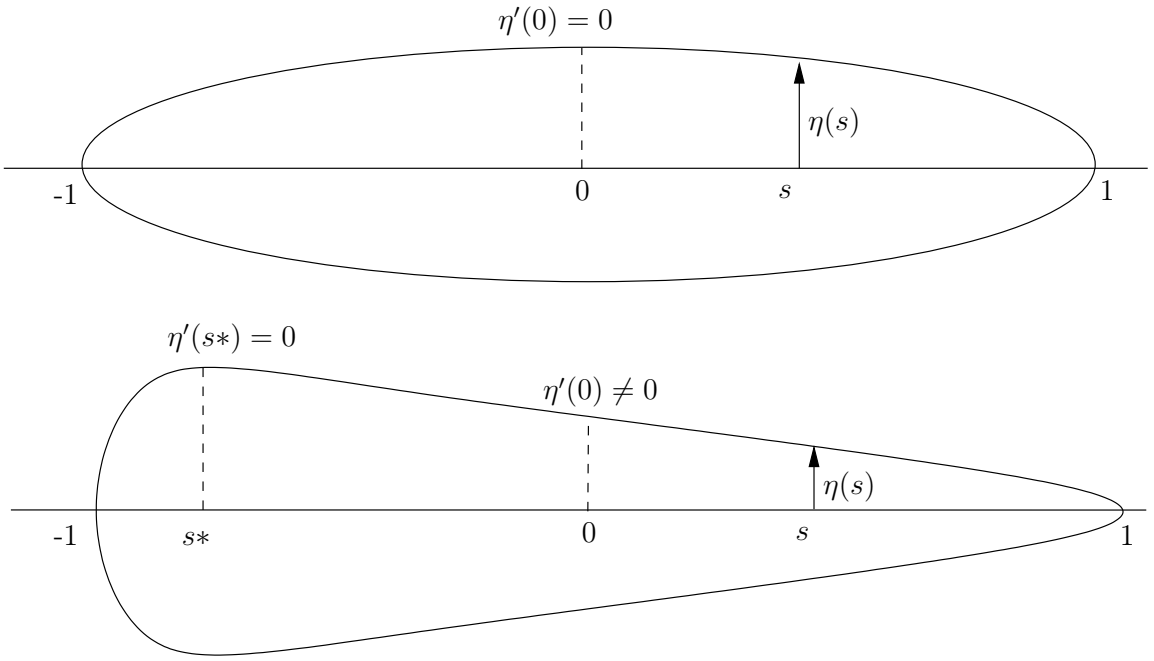


Figure 1.3: Two slender bodies are shown with different geometries: the first shape has a maximum at $s = 0$, thus is permissible in Johnson's SBT [53], however the second shape has a zero derivative at $-1 < s* < 0$ and is thus not permissible; it is this latter shape which motivates the development of a SBT that can incorporate varying, cross-sectional radii.

and Johnson's improved, algebraically accurate SBT [53], the latter using singularity methods. In particular, Johnson represents the flow field around the body in terms of an integral of weighted, singular solutions, distributed along the slender-body centre-line. However, his work on varying cross sections requires the slender body to be split into a central region and two end regions, with different weightings of the singularities in each region. More restrictively, the range of permissible, cross-sectional radius functions that vary with arc-length, $\eta(s)$ say, had to satisfy the condition that $d\eta/ds = 0$ at, and only at, the centre of the body; see figure 1.3.

For a straight centre-line, permissible shapes in Johnson's formalism have circular cross sections that grow from a radius of zero at one end, increasing monotonically to the centre of the body, at which there must be a maximum turning point before decreasing monotonically back to zero at the other end. The theory does not encompass, for example, tapering shapes (where the turning point is not at the centre) or wave-like / ribbed shapes (where more than one turning point exists).

Thus, there is a motivation for developing a theory which can include a wider variety

of permissible shapes with arbitrary radius functions. These shapes are central to many biological contexts, such as tapering, mammalian, sperm flagella or the ridges seen in the flagellated protozoa *Astasia Longa* [81]. The developed theory can also apply to the modelling of artificial, shape-changing microswimmers based on smoothed, dumbbell designs. Currently, these shapes require a more computationally expensive, and numerically involved, method such as boundary elements [76]. Hence, a numerical motivation also exists in developing a simple-to-implement SBT, capable of incorporating these cross-sectional variations.

## 1.3 Background Fluid Mechanics

This section covers the background fluid mechanics required to develop the upcoming mathematical models of low Reynolds number microswimming in Chapters 2 to 5. Upon introducing the Stokes equations, two important singularities are identified: the Stokeslet and the potential dipole. These are discussed in the context of translating spheres and prolate spheroids, highlighting the effectiveness of singularity methods in calculating flow fields and drag forces around the respective bodies; the results for spheres in particular are recalled in Chapter 2 to model the three-sphere swimmer.

Resistive-force theory (RFT) is subsequently introduced, being central to Chapter 3 on the flagellar mechanics of sperm cells. RFT expressions describing the approximate forces exerted by a slender filament in a Stokes fluid are discussed. The section concludes with the introduction of regularised singularities, the building blocks of the SBT developed in Chapters 4 and 5.

### 1.3.1 Stokes' Equations

#### 1.3.1.1 Non-dimensionalising the Navier–Stokes Equations

In order to study the motion of solid bodies in a viscous-fluid environment, the nonlinear, governing equations of incompressible, viscous-fluid dynamics are presented, the Navier–Stokes equations. These are given by

$$\nabla \cdot \mathbf{u} = 0, \tag{1.1}$$

$$\rho\left(\frac{\partial \mathbf{u}}{\partial t} + \mathbf{u} \cdot \nabla \mathbf{u}\right) = \nabla \cdot \boldsymbol{\sigma} + \rho \mathbf{g}, \tag{1.2}$$

where $\mathbf{u}(\mathbf{x}, t)$ is the fluid velocity at a field point $\mathbf{x}$, located in the fluid domain, measured at time $t$. The parameters $\rho$ and $\mathbf{g}$ are, respectively, the fluid density and gravity vector acting vertically downwards and are assumed to be constant. The variable $\boldsymbol{\sigma}(\mathbf{x}, t)$ denotes the stress tensor, given by

$$\boldsymbol{\sigma}(\mathbf{x}, t) := -p(\mathbf{x}, t)\mathbf{I} + \boldsymbol{\tau}(\mathbf{x}, t), \tag{1.3}$$

where $\mathbf{I}$ is the identity operator, $p(\mathbf{x}, t)$ is the pressure due to the surrounding fluid and $\boldsymbol{\tau}(\mathbf{x}, t)$ is the deviatoric-stress tensor. For an incompressible, Newtonian fluid,

$$\boldsymbol{\tau} = \mu \left[ (\nabla \mathbf{u})^T + \nabla \mathbf{u} \right], \tag{1.4}$$

where $\mu$ is the constant, dynamic viscosity of the fluid. When investigating non-Newtonian, viscoelastic fluid in Chapter 2, however, the constitutive relation in (1.4) is modified; see Section 2.2.2.

Physically, the Navier–Stokes equations, (1.1)–(1.2), represent the conservation of mass and conservation of momentum respectively [71]. Equation (1.2) in particular states that the rate of change of momentum, per unit volume, on the left-hand side is equal to the sum of the forces, per unit volume, on the right-hand side.

To non-dimensionalise these governing equations, a velocity scale $U$ is introduced, representing a typical speed of interest in the problem. For example, when modelling the motion of mammalian sperm cells through a static, background fluid, the velocity scale can be taken to be the typical, flagellum wave-speed, $U \approx 4 \times 10^{-4}$m/s [85] (using a beat frequency of 10Hz and wavelength of 40$\mu$m). Given that the flow field in the surrounding, ambient fluid is driven by the velocities of moving boundaries, such as the beating flagellum, this choice of $U$ ensures the flow field generated is $O(1)$. In each chapter, the physical motivations of the typical scales used to non-dimensionalise variables are clearly explained.

Along with a velocity scale $U$, a length scale $L$ is also chosen, representing a typical length of interest in the problem. Again, for the example of mammalian sperm cells, this could be the typical flagellum length, $L \approx 50\mu$m, the head length of around $5\mu$m, the cross-sectional, head diameter of $3\mu$m or the flagellum radius of 200 nm, [28]; in each case, the largest possible value of the typical length scale is chosen for non-dimensionalisation.

Scales associated with the properties of the fluid, unaffected by the geometry of the swimmer or the fluid domain, include the constant, dynamic viscosity, $\mu$, and constant, fluid density, $\rho$. Completing the sperm-cell example, the viscosities of interest range from $10^{-3}$ Pa s (1 cP) in water to 1 Pa s (1000 cP) in a laboratory, viscous medium such as a dilute, methylcellulose solution at 37°C. The densities can vary from $10^3$ kg/m$^3$ in water to greater values in the female reproductive tract.

The variables in (1.1)–(1.2) are thus non-dimensionalised by introducing $\mathbf{u} = U\hat{\mathbf{u}}$, $\mathbf{x} = L\hat{\mathbf{x}}$ and $t = L/U\hat{t}$, where the latter is the convective time scale of the typical length over the typical velocity scale and all hatted variables are dimensionless. The deviatoric-stress tensor in (1.4) is hence non-dimensionalised by $\boldsymbol{\tau} = (\mu U/L)\hat{\boldsymbol{\tau}}$. For dimensional consistency in equation (1.3), $p$ and $\boldsymbol{\sigma}$ are also non-dimensionalised with $\mu U/L$. Upon substituting equations (1.3) and (1.4) into (1.1) and (1.2) [71, 79],

$$\hat{\nabla} \cdot \hat{\mathbf{u}} = 0, \tag{1.5}$$

$$Re\left(\frac{\partial \hat{\mathbf{u}}}{\partial \hat{t}} + \hat{\mathbf{u}} \cdot \hat{\nabla}\hat{\mathbf{u}}\right) = -\hat{\nabla}\hat{p} + \hat{\nabla}^2\hat{\mathbf{u}} + B\hat{\mathbf{g}}, \tag{1.6}$$

where $Re := UL\rho/\mu$ is the dimensionless Reynolds number expressing the magnitude of inertial to viscous forces, $B := \rho L^2 g/\mu U$ is another dimensionless constant related to the gravity term and $\hat{\mathbf{g}}$ is the unit, downward, vertical direction in which gravity acts.

For all the models presented in this thesis, the Reynolds number, $Re$, is assumed to be very small, enough to neglect the dimensionless, nonlinear, inertial terms on the left-hand side of the conservation-of-momentum equation, (1.6). By neglecting $Re$, the right-hand side of (1.6) effectively states that the sum of all the forces must equal zero; see Section 1.3.1.3.

The assumption of a negligible Reynolds number is justified, or imposed, throughout the topics covered in this thesis. For the work in Chapter 2 on the three-sphere microswimmer, a negligible Reynolds number is imposed, resulting in conditions that must be satisfied by the design of the swimmer and the choice of fluid properties. Moreover, in the non-dimensionalisation of Section 2.2.3, the time scale is taken to be $1/\omega$ where $\omega$ is the beat frequency of the prescribed, periodic forces of the swimmer. This gives rise to a Reynolds number based on the frequency, $\omega$, denoted the frequency Reynolds number, $Re_\omega := \rho\omega a^2/\mu$, where $a$ is the radius of the spheres;

thus, a negligible frequency Reynolds number is imposed. In Chapter 3 on sperm motility, the sperm geometry and fluid properties are biological, predetermined parameters, thus cannot be adjusted. Instead, the Reynolds number assumption is simply validated by these existing parameters (listed as examples for the previous non-dimensionalisation), giving values of $Re$ between $5 \times 10^{-5}$ to $2 \times 10^{-2}$, confirming its negligibility. The work in Chapters 4 and 5 on slender bodies follow similar arguments, depending respectively on whether the body is artificially constructed or modelled on existing, physical phenomena.

The gravity term in equation (1.6) can be absorbed into the gradient of the pressure, $\hat{\nabla}\hat{p}$, using a dimensionless modified pressure [8], $\hat{\bar{p}} = \hat{p} + B\hat{z}$, where $\hat{z}$ is the dimensionless vertical direction. This removes the $B\hat{\mathbf{g}}$ term from equation (1.6), though an additional $-B\hat{z}\mathbf{I}$ term now appears in the stress tensor in equation (1.3).

Upon re-dimensionalisation and neglecting the Reynolds number, the linear, Stokes equations remain [71, 89],

$$\nabla \cdot \mathbf{u} = 0, \tag{1.7}$$

$$\mathbf{0} = -\nabla \bar{p} + \mu \nabla^2 \mathbf{u} = \nabla \cdot \boldsymbol{\sigma}, \tag{1.8}$$

where $\bar{p} = p + \rho g z$.

Due to the absence of the inertial terms on the left-hand side of (1.8), the Stokes equations are quasi-steady; for a particular point in time, $t = t*$, the velocity flow field, $\mathbf{u}$, and pressure field, $p$, are steady-state solutions of the Stokes equations for a given boundary condition, evaluated at $t = t*$. Hence, variables with a time-dependency may be treated as though the time argument, $t$, were behaving as a parameter. Thus the $t$-dependence may not be explicitly written in subsequent, variable arguments (except for cases of clarity or emphasis) but is always assumed.

The standard boundary condition on solid bodies or domain boundaries in a viscous environment is the no-slip condition, whereby the fluid velocity, $\mathbf{u}$, exactly matches the velocity of the moving body (or boundary). For static bodies or domain walls, this implies $\mathbf{u} = \mathbf{0}$ on these surfaces. The no-slip condition is referred to throughout the thesis.

#### 1.3.1.2 Stokes Flow Uniqueness

The velocity field, $\mathbf{u}$, and pressure field, $p$, satisfying the Stokes equations in (1.7) and (1.8) are unique, except that the pressure is determined up to a constant, though this has no dynamical effect; this can be demonstrated via a proof by contradiction as follows. Initially, one assumes that there are two, distinct velocity and pressure fields, $(\mathbf{u}_1, p_1)$ and $(\mathbf{u}_2, p_2)$, that both satisfy the Stokes equations with the same, given boundary conditions on a closed surface, $D$. Variables representing their difference, $\mathbf{U}$ and $P$, are given by

$$\begin{aligned} \mathbf{U} &:= \mathbf{u}_1 - \mathbf{u}_2, \\ P &:= p_1 - p_2, \end{aligned} \tag{1.9}$$

satisfying

$$\nabla \cdot \mathbf{U} = 0, \tag{1.10}$$

$$\mathbf{0} = -\nabla P + \mu \nabla^2 \mathbf{U}, \tag{1.11}$$

with

$$\mathbf{U} = \mathbf{0} \qquad \text{on } D. \tag{1.12}$$

Upon taking the scalar product of equation (1.11) with $\mathbf{U}$ and integrating over the volume, $V$, enclosed by $D$,

$$\mathbf{0} = -\iiint_V \mathbf{U} \cdot \nabla P \, \mathrm{d}V + \mu \iiint_V \mathbf{U} \cdot \nabla^2 \mathbf{U} \, \mathrm{d}V. \tag{1.13}$$

Using equation (1.10) along with the divergence theorem and the boundary condition in (1.12), the first term integrates to zero, leaving

$$\mathbf{0} = \mu \iiint_V \mathbf{U} \cdot \nabla^2 \mathbf{U} \, \mathrm{d}V. \tag{1.14}$$

A second use of equation (1.10), the divergence theorem and the boundary condition in (1.12) gives, in standard index notation (summation over $i$ and $j$ assumed),

$$0 = \iiint_V \left( \frac{\partial U_i}{\partial x_j} \right)^2 \mathrm{d}V. \tag{1.15}$$

This implies $\partial U_i / \partial x_j = 0$ for all $i$ and $j$, thus $\mathbf{U}$ is a constant vector. In fact, from the boundary condition, (1.12), this constant must be identically equal to zero. Hence, from (1.9), there do not exist two, distinct, velocity solutions which satisfy the Stokes equations with the same boundary conditions. Thus, from equation (1.11), $\nabla P = \mathbf{0}$ and hence the pressure difference is at most a constant.

#### 1.3.1.3 Forces and Torques

The surface force, $\mathbf{f}(\mathbf{X})$, at a field point $\mathbf{X}$, lying on a closed surface, $D$, enclosing a volume of fluid $V$ within the fluid domain is defined in terms of the stress tensor from (1.3) as

$$\mathbf{f}(\mathbf{X}) = \boldsymbol{\sigma}(\mathbf{X})\mathbf{n}(\mathbf{X}). \tag{1.16}$$

Here, $\mathbf{n}(\mathbf{X})$ is the unit normal to $D$ at $\mathbf{X}$, pointing away from the enclosed volume of fluid, $V$; note that $\mathbf{X}$ is capitalised to emphasise that its location is restricted to lie on the surface, $D$, and not elsewhere in the fluid domain. The total force, $\mathbf{F}$, exerted on the entire, closed surface, $D$, is thus

$$\mathbf{F} := \iint_D \boldsymbol{\sigma}(\mathbf{X})\mathbf{n}(\mathbf{X})\,\mathrm{d}S(\mathbf{X}). \tag{1.17}$$

The total torque exerted on $D$ with respect to the origin, a fixed point in an inertial frame of reference, is denoted $\mathbf{L}$ and given by

$$\mathbf{L} := \iint_D \mathbf{X} \times \boldsymbol{\sigma}(\mathbf{X})\mathbf{n}(\mathbf{X})\,\mathrm{d}S(\mathbf{X}). \tag{1.18}$$

Applying the divergence theorem to (1.17) and (1.18) and using the Stokes equations, (1.7) and (1.8), the total force and torque exerted on a closed surface within the fluid domain both integrate to zero [79],

$$\mathbf{F} = \mathbf{L} = \mathbf{0}. \tag{1.19}$$

An assumption has been made in that the velocity field is assumed to be regular throughout the domain, so as not to attain singular, infinite values which could affect the application of the divergence theorem.

Using Newton's second law, the equation of motion of a body of mass $M_b$, surface $S_b$, volume $V_b$ and velocity $\mathbf{v}$ immersed in a Stokes fluid takes the form

$$M_b \frac{\mathrm{d}\mathbf{v}}{\mathrm{d}t} = \iint_{S_b} (-p\mathbf{I} + \boldsymbol{\tau})\mathbf{n}\,dS + (-M_b g + \rho g V_b)\mathbf{e}_z, \tag{1.20}$$

where the terms on the right-hand side represent the surface forces due to the surrounding fluid, the force due to gravity and the buoyancy force; here, $\mathbf{e}_z$ is the unit vector in the vertical direction. Note that the modified pressure, $\bar{p}$, from equation (1.8) has been written back in terms of the original variables, $\bar{p} = p + \rho g z$, with the divergence theorem applied to the gravity term. Alongside the low Reynolds number

assumption, a further simplification is used, whereby the microswimmers of Chapter 2 and slender bodies in Chapters 4 and 5 are assumed to be neutrally buoyant. In the case of swimming sperm in Chapter 3, experiments conducted by Winet, Bernstein and Head [104] highlight that swimming sperm cells are unaffected by gravity and can therefore also be assumed to be neutrally buoyant; dead cells eventually sediment but on much longer time scales than the ones of interest. This assumption of neutral buoyancy throughout the thesis implies a cancelling of the last two terms in equation (1.20), while the inertialess regime of a Stokes fluid ensures the surface integral is negligible. Hence, the inertia of the body on the left-hand side is also negligible, thus the net force, and torque, on a neutrally buoyant body in a Stokes fluid is zero.

In Chapter 2, this property is exploited for the three-sphere microswimmer, a composite body comprising three spheres and two dynamically negligible, connecting rods, implying that the sum of the forces on the spheres must equal zero. In Chapter 3, this property is also used for a sperm cell caught on the walls of the female reproductive tract, stating that the force exerted by the flagellum on the fluid is exactly balanced by the force exerted on the tethering point, given they must sum to zero.

#### 1.3.1.4 Reversibility

Note that $-\mathbf{u}$, $-\mathbf{p}$ and $-t$ are also solutions of the linear Stokes equations, (1.7) and (1.8). Thus, as observed by Purcell [80], a swimmer in a Stokes fluid exhibiting entirely reciprocal motion, in which swimming strokes are identical when viewed both forward and backward in time, will generate forces and torques that cancel each other out; the result is no net swimming motion. Sperm cells break this reciprocal motion by sending travelling waves down the flagellum, from the head (proximal end) to the tip of the tail (distal end); these strokes viewed forward in time are not identical when viewed in reverse.

However, in a fluid environment where the deviatoric-stress tensor is not governed by the constitutive law for a Newtonian fluid in equation (1.4), such as the viscoelastic model in Chapter 2, the reversibility property need not apply. Consider, for example, a constitutive relation of the form

$$\boldsymbol{\tau} + \lambda \frac{\partial \boldsymbol{\tau}}{\partial t} = \mu \left[ (\nabla \mathbf{u})^T + \nabla \mathbf{u} \right], \tag{1.21}$$

for some constant, $\lambda$ (this particular example is for a linear Maxwell fluid, where $\lambda$ represents the relaxation time of the fluid). In this case, $-\mathbf{u}$, $-\boldsymbol{\tau}$ and $-t$ do not satisfy equation (1.21) due to the linear time derivative. Similarly, adding nonlinear terms (of an even order) involving $\mathbf{u}$ and / or $\boldsymbol{\tau}$ in place of the time derivative could also prohibit the reversed solution satisfying the constitutive relation. The significance of the irreversibility of non-Newtonian rheologies is discussed in the upcoming literature review (Section 1.4) with regards to simple swimmer models.

#### 1.3.1.5 The Infinite-Space Stokeslet

The Green's function for the Stokes equations, (1.7) and (1.8), in an infinite, fluid domain is now considered. The Green's function is derived by equating the right-hand side of (1.8) to the three-dimensional, Dirac delta function at a position $\mathbf{y}$, say, denoted $\delta^3(\mathbf{x}-\mathbf{y})$, multiplied by a vector $8\pi\mu\boldsymbol{\alpha}$; the factor $8\pi\mu$ has been added to simplify later calculations. Thus,

$$\nabla \cdot \mathbf{u}(\mathbf{x}) = 0, \tag{1.22}$$

$$8\pi\mu\delta^3(\mathbf{x}-\mathbf{y})\boldsymbol{\alpha} = -\nabla p(\mathbf{x}) + \mu\nabla^2\mathbf{u}(\mathbf{x}), \tag{1.23}$$

These equations can be interpreted physically as the Stokes flow induced by a point-force located at $\mathbf{y}$ of strength $8\pi\mu|\boldsymbol{\alpha}|$, acting in the unit direction $-\boldsymbol{\alpha}/|\boldsymbol{\alpha}|$, where the minus sign arises due to forces usually being written on the right-hand side of (1.23).

Upon noting the linearity of equations (1.22) and (1.23), the fluid velocity, $\mathbf{u}$, and pressure, $p$, are rewritten in terms of $3\times 3$ and $3\times 1$ tensors, $\mathbf{S}$ and $\mathbf{P}$ respectively, so that

$$\mathbf{u}(\mathbf{x}) = \mathbf{S}(\mathbf{x},\mathbf{y})\boldsymbol{\alpha}, \tag{1.24}$$

$$p(\mathbf{x}) = \mu\mathbf{P}(\mathbf{x},\mathbf{y})\cdot\boldsymbol{\alpha}, \tag{1.25}$$

where $\mathbf{S}$ and $\mathbf{P}$ are Green's functions to be found. Substituting (1.24) and (1.25) into equations (1.22) and (1.23) gives, using standard index notation,

$$\frac{\partial S_{ij}}{\partial x_i} = 0, \tag{1.26}$$

$$8\pi\mu\delta_{ij}\delta^3(\mathbf{x}-\mathbf{y}) = -\frac{\partial P_j}{\partial x_i} + \mu\nabla^2 S_{ij}, \tag{1.27}$$

for $i,j\in\{1,2,3\}$ and the field point $\mathbf{x}=(x_1,x_2,x_3)^T$ written in standard, Cartesian components. Without loss of generality, the delta function is taken to be at the origin,

so that $\mathbf{y} = \mathbf{0}$. Using the three-dimensional Fourier transform, defined by

$$\mathcal{F}[f(\mathbf{x})] = \tilde{f}(\mathbf{k}) := \iiint_{\mathcal{R}^3} f(\mathbf{x}) e^{i\mathbf{k}\cdot\mathbf{x}} \, \mathrm{d}^3\mathbf{x}, \tag{1.28}$$

where $\mathbf{k} = (k_1, k_2, k_3)^T$ are the Fourier variables and $k^2 := k_1^2 + k_2^2 + k_3^2$, equations (1.26) and (1.27) transform to give

$$-ik_i\tilde{S}_{ij} = 0, \tag{1.29}$$

$$8\pi\mu\delta_{ij} = ik_i\tilde{P}_j - \mu k^2\tilde{S}_{ij}, \tag{1.30}$$

using the fact that

$$\mathcal{F}\left[\frac{\partial f}{\partial x_i}\right] = -ik_i\mathcal{F}[f]. \tag{1.31}$$

Contracting equation (1.30) with $k_i$, where summation over the $i$ index is assumed, gives

$$8\pi\mu k_j = ik^2\tilde{P}_j - \mu k_i k^2\tilde{S}_{ij}, \tag{1.32}$$

which, using equation (1.29) to eliminate $\tilde{S}_{ij}$, allows $\tilde{P}_j$ to be written

$$\tilde{P}_j = -\frac{8\pi\mu i k_j}{k^2}. \tag{1.33}$$

By substituting (1.33) back into equation (1.30),

$$\tilde{S}_{ij} = 8\pi\left(\frac{\delta_{ij}}{k^2} + \frac{k_i k_j}{k^4}.\right) \tag{1.34}$$

Before inverting (1.33) and (1.34), note the relation

$$\nabla^4\left(\frac{r}{2}\right) = \nabla^2\left(\frac{1}{r}\right) = -4\pi\delta(r), \tag{1.35}$$

where $r = |\mathbf{x}|$ is the radial distance of the field point, $\mathbf{x}$, from the point-force at the origin and in three-dimensional analysis, for a radial function, $\phi(r)$,

$$\nabla^2\phi(r) = \frac{1}{r}\frac{\mathrm{d}^2}{\mathrm{d}r^2}\left(r\phi(r)\right). \tag{1.36}$$

The second of the two relations in (1.35) is verified by integrating the Laplacian over the region $r > \epsilon$ where $\epsilon \to 0$, using the divergence theorem to evaluate the integral around the surface $r = \epsilon$. Fourier transforming (1.35) gives

$$\frac{1}{k^2} = \mathcal{F}\left(\frac{1}{4\pi r}\right), \qquad \frac{1}{k^4} = -\mathcal{F}\left(\frac{r}{8\pi}\right). \tag{1.37}$$

Thus, from (1.33) using (1.37), the tensor $\mathbf{P}$ associated with pressure is given by

$$\begin{aligned} P_j &= 8\pi\mu\mathcal{F}^{-1}\left(-\frac{ik_j}{k^2}\right), \\ &= 8\pi\mu\frac{\partial}{\partial x_j}\left(\frac{1}{4\pi r}\right), \\ &= \frac{2x_j}{r^3}, \end{aligned} \tag{1.38}$$

while, from (1.34) using (1.37), the tensor $\mathbf{S}$ associated with fluid velocity is

$$\begin{aligned} S_{ij} &= 8\pi\left(\delta_{ij}\mathcal{F}^{-1}\left[\frac{1}{k^2}\right] + \mathcal{F}^{-1}\left[\frac{k_i k_j}{k^4}\right]\right), \\ &= 8\pi\left(\delta_{ij}\left[\frac{1}{4\pi r}\right] - \frac{\partial^2}{\partial x_i x_j}\mathcal{F}^{-1}\left[\frac{1}{k^4}\right]\right), \\ &= \left(\frac{\delta_{ij}}{r} + \frac{x_i x_j}{r^3}\right). \end{aligned} \tag{1.39}$$

Equation (1.39), the Green's function for the velocity field, is referred to as the infinite-space Stokeslet, decaying like $O(1/r)$ where $r$ is radial the distance of the field point, $\mathbf{x}$, from the location of the singularity. The Stokeslet has an associated Stokeslet pressure, given by equation (1.38). A Stokeslet defined at a point $\mathbf{y}$ which is not necessarily at the origin, satisfies

$$S_{ij}(\mathbf{x},\mathbf{y}) := \frac{\delta_{ij}}{|\mathbf{x}-\mathbf{y}|} + \frac{(\mathbf{x}-\mathbf{y})_i(\mathbf{x}-\mathbf{y})_j}{|\mathbf{x}-\mathbf{y}|^3}, \tag{1.40}$$

where $(\mathbf{x}-\mathbf{y})_i$ is the $i$th component of the vector $(\mathbf{x}-\mathbf{y})$. Note that the $(\mathbf{x}-\mathbf{y})_i(\mathbf{x}-\mathbf{y})_j$ term is often written in vector notation using the dyadic product: $(\mathbf{x}-\mathbf{y})\otimes(\mathbf{x}-\mathbf{y})$.

Inserting the Stokeslet (1.40) and Stokeslet pressure (1.38) into the expressions for velocity (1.24) and pressure (1.25) respectively, gives

$$\mathbf{u}(\mathbf{x}) = \frac{\boldsymbol{\alpha}}{|\mathbf{x}-\mathbf{y}|} + \boldsymbol{\alpha}\cdot(\mathbf{x}-\mathbf{y})\frac{(\mathbf{x}-\mathbf{y})}{|\mathbf{x}-\mathbf{y}|^3}, \tag{1.41}$$

$$p(\mathbf{x}) = \frac{2\mu(\mathbf{x}-\mathbf{y})\cdot\boldsymbol{\alpha}}{|\mathbf{x}-\mathbf{y}|^3}. \tag{1.42}$$

These velocity and pressure fields satisfy the usual Stokes equations, (1.7) and (1.8), for a field point, $\mathbf{x}$, measuring a point in the fluid domain that is not at the location of the singularity itself, $\mathbf{y}$.

The weighting of the Stokeslet, $8\pi\mu\boldsymbol{\alpha}$ from (1.23), represents minus of the strength of the point force located at $\mathbf{y}$, as discussed following equation (1.23). It can be related

to the total force exerted on any surface that encloses the Stokeslet. To examine this total force, a $3 \times 3 \times 3$ stress tensor for the Stokeslet is introduced, $\mathbf{T}(\mathbf{x}, \mathbf{y})$, by letting

$$\boldsymbol{\sigma}(\mathbf{x}) = \mu \mathbf{T}(\mathbf{x}, \mathbf{y}) \boldsymbol{\alpha}, \tag{1.43}$$

where $\mathbf{T}$ has components $T_{ijk}$, such that

$$\sigma_{ik}(\mathbf{x}) = \mu T_{ijk}(\mathbf{x}, \mathbf{y}) \alpha_j. \tag{1.44}$$

By substituting equations (1.41) and (1.42) into the definition of the Newtonian stress tensor (1.3), one obtains from (1.44) that

$$T_{ijk}(\mathbf{x}, \mathbf{y}) = -\frac{6(\mathbf{x}-\mathbf{y})_i (\mathbf{x}-\mathbf{y})_j (\mathbf{x}-\mathbf{y})_k}{|\mathbf{x}-\mathbf{y}|^5}. \tag{1.45}$$

The total force is given by

$$\mathbf{F} = \iint_D \boldsymbol{\sigma}(\mathbf{X}) \mathbf{n}(\mathbf{X}) \, \mathrm{d}S(\mathbf{X}), \tag{1.46}$$

where $\mathbf{X}$ denotes a field point on the closed surface, D, surrounding the singularity. Upon substituting (1.44) and (1.45) into (1.46), the surface $D$ is analytically deformed to a spherical surface surrounding the singularity, allowing the integral to be evaluated via the divergence theorem. This gives

$$\mathbf{F} = -8\pi\mu\boldsymbol{\alpha}, \tag{1.47}$$

independent of the sphere radius. Thus, the strength of the point-force in equation (1.23), $-8\pi\mu\boldsymbol{\alpha}$, is equal to the total force exerted on any surface enclosing the Stokeslet.

#### 1.3.1.6 The Stokeslet Doublet and The Potential Dipole

Consider again the velocity and pressure fields relating to a point-force in an infinite, Stokes flow, (1.41) and (1.42) respectively. Any spatial derivatives with respect to $\mathbf{y}$ of the singularities in (1.41) and (1.42) will also generate solutions that satisfy the Stokes equations, (1.7) and (1.8), as the spatial $\mathbf{y}$ derivatives commute with the spatial $\mathbf{x}$ derivatives. Differentiating the Stokeslet, (1.40), and the associated Stokeslet pressure with respect to $\mathbf{y}$ introduces new singularities called the Stokeslet doublet, $\mathbf{S}^D(\mathbf{x}, \mathbf{y})$, and associated doublet pressure $\mathbf{P}^D(\mathbf{x}, \mathbf{y})$ [16, 79],

$$S^D_{ijk} = \frac{\partial S_{ij}}{\partial y_k}, \qquad P^D_{jk} = \frac{\partial P_j}{\partial y_k}. \tag{1.48}$$

Hence $u_i = S^D_{ijk} b_{jk}$ and $p_i = \mu P^D_{jk} b_{jk}$ would satisfy the Stokes equations for $\mathbf{x} \neq \mathbf{y}$, where $b_{jk}$ is a constant. By taking the derivative of these singularities with respect to $\mathbf{y}$ a second time, the Stokeslet quadrupole and associated quadruple pressure are obtained,

$$S^Q_{ijkl} = \frac{\partial^2 S_{ij}}{\partial y_l \partial y_k}, \qquad P^Q_{jkl} = \frac{\partial P_j}{\partial y_l \partial y_k}, \tag{1.49}$$

and hence $u_i = S^Q_{ijkl} c_{jkl}$ and $p_i = \mu P^Q_{jkl} c_{jkl}$ would satisfy the Stokes equations, where $c_{jkl}$ is a constant. These singularities are not required for the work in this thesis but their properties and applications have been widely studied [16, 22, 79]. It is worth highlighting, however, the special case of setting $l = k$ in (1.49), giving the Laplacian of the Stokeslet with respect to $\mathbf{y}$,

$$\frac{\partial^2 S_{ij}}{\partial y_l^2} = \nabla^2_{\mathbf{y}} S_{ij} = -2\left(-\frac{\delta_{ij}}{|\mathbf{x}-\mathbf{y}|^3} + \frac{3(\mathbf{x}-\mathbf{y})_i(\mathbf{x}-\mathbf{y})_j}{|\mathbf{x}-\mathbf{y}|^5}\right), \tag{1.50}$$

with associated pressure

$$\nabla^2_{\mathbf{y}} P_j = 0, \tag{1.51}$$

for $\mathbf{x} \neq \mathbf{y}$. Equation (1.50) motivates the definition of the potential-dipole singularity, $\mathbf{D}(\mathbf{x}, \mathbf{y})$ located at $\mathbf{y}$, as

$$D_{ij}(\mathbf{x}, \mathbf{y}) := -\frac{\delta_{ij}}{|\mathbf{x}-\mathbf{y}|^3} + \frac{3(\mathbf{x}-\mathbf{y})_i(\mathbf{x}-\mathbf{y})_j}{|\mathbf{x}-\mathbf{y}|^5}, \tag{1.52}$$

with an associated, constant, potential-dipole pressure which, without loss of generality can be taken to equal zero. Thus solutions of the Stokes equations are

$$\mathbf{u}(\mathbf{x}) = \mathbf{D}(\mathbf{x}, \mathbf{y})\boldsymbol{\beta}, \tag{1.53}$$

$$p(\mathbf{x}) \equiv 0, \tag{1.54}$$

where $\boldsymbol{\beta}$ is a constant vector.

While the potential dipole is related to the Laplacian of the Stokeslet, it can also be obtained by considering a unit point source at $\mathbf{y}$ in an irrotational, Stokes flow with constant pressure. At a field point, $\mathbf{x}$, irrotationality allows the fluid velocity to be written as $\mathbf{u}(\mathbf{x}) = \nabla\Phi(\mathbf{x})$ for some potential function $\Phi(\mathbf{x})$ satisfying

$$\nabla^2 \Phi = \delta^3(\mathbf{x}-\mathbf{y}). \tag{1.55}$$

Using equation (1.35), $\Phi(\mathbf{x})$ is deduced and hence the velocity for a point source is given by

$$\mathbf{u}(\mathbf{x}) = \frac{1}{4\pi}\frac{(\mathbf{x}-\mathbf{y})}{|\mathbf{x}-\mathbf{y}|^3}. \tag{1.56}$$

Differentiating the above point-source singularity with respect to $\mathbf{y}$ yields the dipole of the potential source, commonly referred to as the potential dipole.

The total force exerted on a surface, $D$, enclosing the potential dipole can be evaluated in a similar way to the Stokeslet analysis. With the flow field and pressure field given by equations (1.52–1.54) respectively, a potential-dipolar stress tensor, $\mathbf{R}(\mathbf{x},\mathbf{y})$, is introduced such that

$$\boldsymbol{\sigma}(\mathbf{x}) = \mu\mathbf{R}(\mathbf{x},\mathbf{y})\boldsymbol{\beta}, \tag{1.57}$$

where the $\mathbf{R}$ has components $R_{ijk}$, satisfying

$$\sigma_{ik}(\mathbf{x}) = \frac{1}{4\pi}R_{ijk}(\mathbf{x},\mathbf{y})\beta_j. \tag{1.58}$$

Substituting equations (1.52), (1.53) and (1.54) into the definition of the Newtonian stress tensor, (1.3), one obtains from (1.58) that

$$\begin{aligned} R_{ijk} = 6\left(\frac{\delta_{ij}(\mathbf{x}-\mathbf{y})_k + \delta_{ik}(\mathbf{x}-\mathbf{y})_j + \delta_{jk}(\mathbf{x}-\mathbf{y})_i}{|\mathbf{x}-\mathbf{y}|^5}\right) \\ - 30\frac{(\mathbf{x}-\mathbf{y})_i(\mathbf{x}-\mathbf{y})_j(\mathbf{x}-\mathbf{y})_k}{|\mathbf{x}-\mathbf{y}|^7}. \end{aligned} \tag{1.59}$$

The total force exerted on a surface, $D$, enclosing the potential dipole is again given by

$$\mathbf{F} = \iint_D \boldsymbol{\sigma}(\mathbf{X})\mathbf{n}(\mathbf{X})\,\mathrm{d}S, \tag{1.60}$$

where $\mathbf{X}$ denotes a field point on the closed surface, $D$, surrounding the potential dipole. Upon substituting (1.58) and (1.59) into (1.60), the surface $D$ is analytically deformed to a spherical surface surrounding the singularity, allowing the integral to be evaluated via the divergence theorem. This gives

$$\mathbf{F} = \mathbf{0}, \tag{1.61}$$

demonstrating that the potential dipole does not exert a net force on any surrounding surfaces. Furthermore, it can be shown that only the presence of a Stokeslet results in a net force exerted on a closed surface surrounding any Stokes flow singularities [79].

### 1.3.2 Translating Spheres and Prolate Spheroids in a Stokes Flow

#### 1.3.2.1 Translating Spheres

Consider a translating sphere of radius $a$, moving with a translational velocity, $\mathbf{U}$, in a Stokes fluid. One can derive the flow field directly by writing the Stokes equations, (1.7) and (1.8), in spherical-polar coordinates, introducing a stream function and satisfying the no-slip boundary condition on the sphere surface [71]. A second approach is to pose an initial, singularity *ansatz* for the flow field based on properties of the singular solutions discussed in this section [79]. When contracted with strengths (weights) of suitable dimensions, these singular solutions are all solutions of the Stokes equations, (1.7) and (1.8), thus an *ansatz* for the flow field consisting of any linear combination of these singularities will itself satisfy the Stokes equations. The no-slip boundary condition can then be enforced, determining a relationship between the weightings of the singularities. Furthermore, a velocity solution found via a singularity representation satisfying the boundary conditions must be the unique solution; see Section 1.3.1.2.

Using this approach, no direct analysis on the equations themselves are needed. A singularity representation can often be quicker to implement than using PDE methods and allow for certain properties, such as the total surface force or torque, to be deduced easily.

Using this singularity-representation approach, the flow field around the translating sphere is postulated as the combination of a Stokeslet and a potential dipole, so that

$$\mathbf{u}(\mathbf{x}) = \mathbf{S}(\mathbf{x}, \mathbf{y})\boldsymbol{\alpha} + \mathbf{D}(\mathbf{x}, \mathbf{y})\boldsymbol{\beta}, \tag{1.62}$$

where $\mathbf{y}$ is the centre of the sphere at time $t$, though time dependence is not written explicitly; see Section 1.3.1.1. The no-slip boundary condition states that

$$\mathbf{u}(\mathbf{X}) = \mathbf{U}, \tag{1.63}$$

where $\mathbf{X}$ is a position vector on the surface of the sphere, of the form

$$\mathbf{X} = \mathbf{y} + a\mathbf{e}_r, \tag{1.64}$$

where $\mathbf{e}_r$ is the unit, radial vector from the centre of the sphere outwards to a point on the surface; see figure 1.4. The boundary condition should hold for all points on the

surface of the sphere and hence be independent of the radial direction $\mathbf{e}_r$. Enforcing this condition in (1.62) and using the singularity definitions from (1.40) and (1.52), implies

$$\boldsymbol{\alpha} = \frac{3a\mathbf{U}}{4}, \qquad \boldsymbol{\beta} = -\frac{a^3\mathbf{U}}{4}. \tag{1.65}$$

The surface force over the sphere is readily calculated from equations (1.47) and (1.61), the former giving the total force exerted on any surface enclosing a Stokeslet and the latter recalling that the potential dipole does not contribute to the surface force. Thus,

$$\mathbf{F} = -8\pi\mu\boldsymbol{\alpha} + \mathbf{0} = -6\pi\mu a\mathbf{U}, \tag{1.66}$$

which is the famous Stokes drag on a sphere [89]. Knowing the properties of the singularities allowed the force to be written down immediately; this avoids calculating a surface integral of the stress tensor in the form of (1.17), where the stress tensor itself, (1.3), requires the velocity, (1.62), and pressure, the latter of which is calculated from Stokes equations, (1.7) and (1.8).

Admittedly, the solution for the Stokes flow around a translating sphere is well-known to be a weighted Stokeslet and weighted potential dipole, thus starting with a singularity *ansatz* of a Stokeslet and potential dipole with *a priori* unknown weightings appears forced. However, the singularity representation for a sphere can be used as a building block to determine flows around more complex geometries, for which a number of singularities might have to be posed as an initial *ansatz* for the velocity flow field. The form of the singularity representation postulated is usually based on a

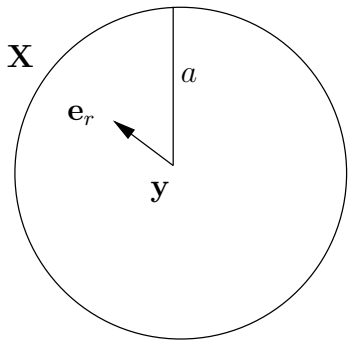


Figure 1.4: A sphere of radius $a$ is shown, with a radial vector, $\mathbf{e}_r$, point outward from the centre of the sphere, $\mathbf{y}$. The no-slip boundary condition must be enforced at all points on the surface, $\mathbf{X}$.

familiarity with the singular solutions themselves, along with intuition based on their respective properties [16, 79].

#### 1.3.2.2 Translating Prolate Spheroids

As with the translating sphere in a Stokes flow, the translating, prolate spheroid can be solved via a direct, but lengthy analysis on the Stokes equations using separable solutions and ellipsoidal harmonics [103]. A singularity representation, however, proves to be far more concise. Motivated by the singularity representation of the flow field around a translating, solid sphere, Chwang and Wu [22] pose a singularity representation of the flow field around a translating, prolate spheroid by distributing Stokeslets and potential dipoles along the centre-line of the body, between the two foci. The prolate-spheroidal surface is given in Cartesian coordinates as

$$\frac{x^2}{L^2} + \frac{y^2}{a^2} + \frac{z^2}{a^2} = 1, \quad L > a, \tag{1.67}$$

where the centre-line is given by the $x$-axis for $x \in [-L, L]$ and the transverse, cross section to the centre-line is circular, with radius $a$, lying in the $(y, z)$ plane. The eccentricity, $e$, of the prolate spheroid is, by definition,

$$e = \sqrt{1 - \left(\frac{a}{L}\right)^2}, \tag{1.68}$$

with foci at $\pm Le$ on the $x$-axis, lying within the interval $(-L, L)$; see figure 1.5. Chwang and Wu postulate the following *ansatz* for the flow field:

$$\mathbf{u}(\mathbf{x}) = \int_{-Le}^{Le} \mathbf{S}(\mathbf{x}, x'\mathbf{e}_x)\boldsymbol{\alpha} + \{(Le)^2 - x'^2\}\mathbf{D}(\mathbf{x}, x'\mathbf{e}_x)\boldsymbol{\beta}\, \mathrm{d}x', \tag{1.69}$$

where $x'$ is the integration variable along the $x$-axis, $\mathbf{e}_x$ is the unit vector along the positive $x$-axis, $\boldsymbol{\alpha}$ is the *a priori* unknown strength of the Stokeslet distribution and $\boldsymbol{\beta}$ is the *a priori* unknown strength of the potential-dipole distribution. The parabolic factor of $\{(Le)^2 - x'^2\}$ in front of the potential dipole is motivated by Chwang and Wu's previous work, [21].

For a translating, prolate spheroid with translational velocity $\mathbf{U}$, the no-slip boundary condition is

$$\mathbf{u}(\mathbf{X}) = \mathbf{U}, \tag{1.70}$$

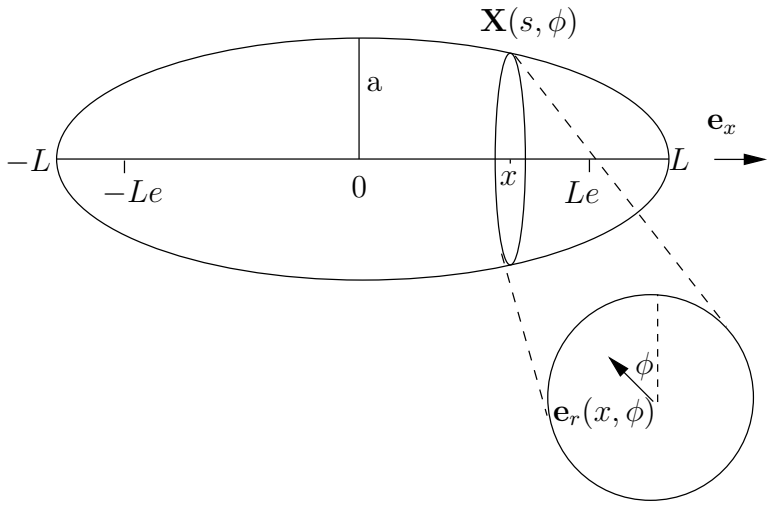


Figure 1.5: The prolate spheroid aligned with the $x$-axis, with semi-major axis $L$ and semi-minor axis $a$. The foci are at $\pm Le$, for eccentricity $e$. The cross section shows the radial vector, $\mathbf{e}_r$, cross-sectional angle, $\phi$ and a point on the surface, $\mathbf{X}$, at which the no-slip boundary condition must be satisfied.

where $\mathbf{X}$ is on the body surface. Thus,

$$\mathbf{X} = x\mathbf{e}_x + a^2(1 - x^2/L^2)\mathbf{e}_r, \tag{1.71}$$

where $\mathbf{e}_r$ is the cross-sectional, radial, unit vector such that

$$\mathbf{e}_r = \cos\phi\mathbf{e}_y + \sin\phi\mathbf{e}_z, \tag{1.72}$$

for unit vectors $\mathbf{e}_y$ and $\mathbf{e}_z$ in the positive $y$ and $z$ directions; $\phi$ here is the cross-sectional angle $\mathbf{e}_r$ makes to the vertical $y$ axis. The boundary condition, (1.70), must hold for all values of $\phi$ in (1.71), hence the integral must be independent of $\mathbf{e}_r$, giving

$$\boldsymbol{\beta} = -\frac{(1-e^2)}{2e^2}\boldsymbol{\alpha}. \tag{1.73}$$

Thus (1.69), when evaluated on the surface of the prolate ellipsoid, becomes an integral equation for $\boldsymbol{\alpha}$ given by

$$\mathbf{U} = \int_{-Le}^{Le} \left[\mathbf{S}(\mathbf{X}, x'\mathbf{e}_x) - \frac{(1-e^2)}{2e^2}\{(Le)^2 - x'^2\}\mathbf{D}(\mathbf{X}, x'\mathbf{e}_x)\right]\boldsymbol{\alpha}\,\mathrm{d}x'. \tag{1.74}$$

By direct integration of the kernel, using the definitions (1.40) and (1.52) of the Stokeslet and potential dipole respectively, $\boldsymbol{\alpha}$ is determined as

$$\alpha_x = \frac{U_x e^2}{-2e + (1+e^2)\log\left(\frac{1+e}{1-e}\right)}, \quad \alpha_y = \frac{2U_y e^2}{2e + (3e^2-1)\log\left(\frac{1+e}{1-e}\right)}. \tag{1.75}$$

Here, the subscript $x$, $y$ and $z$ indicate the component of the vector in the respective, Cartesian directions, and $\alpha_z$ take the same form as $\alpha_y$, with $U_z$ replacing $U_y$.

### 1.3.3 Resistive-Force Theory (RFT)

Attention is now given to a body taking the form of a long, thin, slender filament, such as a sperm flagellum [34], immersed in a low Reynolds number environment. As documented in the literature review (later in Section 1.4), in 1955, Gray and Hancock introduced resistive-force theory (RFT) [42] to model such a situation. They concluded that, for a thin filament with a curvilinear centre-line, $\boldsymbol{\xi}(s,t)$, where $s$ is the arc-length along the centre-line, the force per-unit-length exerted by the flagellum to balance viscous drag, $\mathbf{f}(s,t)$, is given by

$$\mathbf{f}(s,t) \approx C_T V_t(s,t)\mathbf{e}_t(s,t) + C_N V_n(s,t)\mathbf{e}_n(s,t) + C_B V_b(s,t)\mathbf{e}_b(s,t). \tag{1.76}$$

Here, $\boldsymbol{e_t}(s,t)$, $\boldsymbol{e_n}(s,t)$ and $\boldsymbol{e_b}(s,t)$ are the tangential, normal and binormal unit vectors respectively of the centre-line at $s$; see figure 1.6. The constants $C_T$, $C_N$ and $C_B$ are termed the tangential, normal and binormal, resistance coefficients respectively.

The resistance coefficients depend on the constant, fluid viscosity, $\mu$, and the geometry of the slender body. For the slender-body theory (SBT) developed in Chapter 4, these coefficients are derived exactly in Section 4.3.3, taking the same form as those derived from Johnson's SBT [53]. They are directly proportional to $\mu$ and inversely proportional to $\log(1/\varepsilon)$, where $\varepsilon$ is the slenderness ratio defined, in this case, as the maximum, cross-sectional radius of the slender body divided by the half-length of its centre-line. The coefficients are given by

$$C_T := \frac{2\pi\mu}{\log\left(\frac{2}{\varepsilon}\right) - \frac{1}{2}}, \tag{1.77}$$

$$C_N := \frac{4\pi\mu}{\log\left(\frac{2}{\varepsilon}\right) + \frac{1}{2}}, \tag{1.78}$$

$$C_B := \frac{4\pi\mu}{\log\left(\frac{2}{\varepsilon}\right) + \frac{1}{2}}. \tag{1.79}$$

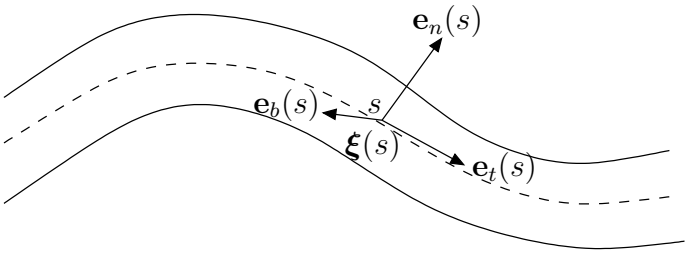


Figure 1.6: The tangential, normal and binormal unit vectors of a slender filament at a point $s$ along the arc-length of the centre-line, given respectively by $\mathbf{e}_t(s)$, $\mathbf{e}_n(s)$ and $\mathbf{e}_b(s)$, where time dependence is implicit.

The exact form of the coefficients, however, depend on the assumptions used in the SBT from which they are derived. For example, Lighthill [64] uses a simplified SBT based on cylindrical elements, introducing an intermediate distance, $q$, to separate the near field and far field approximations of the fluid velocity around the body. The coefficients derived from this theory take the similar form,

$$C_T := \frac{2\pi\mu}{\log\left(\frac{2q}{a}\right) - \frac{1}{2}}, \tag{1.80}$$

$$C_N := \frac{4\pi\mu}{\log\left(\frac{2q}{a}\right) + \frac{1}{2}}, \tag{1.81}$$

$$C_B := \frac{4\pi\mu}{\log\left(\frac{2q}{a}\right) + \frac{1}{2}}. \tag{1.82}$$

however the *ad hoc* parameter $q$ remains in the expressions. For a filament of constant, cross-sectional radius exhibiting a beat pattern with a wavelength of $\lambda$, say, this intermediate distance, $q$, is found to minimise errors if it satisfies

$$q = 0.09 \times \lambda. \tag{1.83}$$

It has been shown that Lighthill's coefficients, (1.82), perform very well in comparison with full SBT models [54] and are subsequently used in Chapter 3.

Both models highlight the anisotropy between forces generated due to tangential motions of the slender body, at a point $s$, compared to motion in the normal, or binormal, directions. As mentioned in the upcoming literature review (Section 1.4) this anisotropy was first characterised by Hancock [43] in 1953 (and subsequently used in Gray and Hancock's RFT [42]), who stated the normal coefficient is approximately twice as large as the tangential coefficient. For the coefficients in (1.79), with those of Lighthill (1.82) following the same idea, a more accurate ratio of the normal to the tangential coefficient, denoted $\gamma$, is given by

$$\gamma = 2\left(\frac{2\log\left(\frac{2}{\varepsilon}\right) - 1}{2\log\left(\frac{2}{\varepsilon}\right) + 1}\right), \tag{1.84}$$

which, for $\varepsilon = 0.01$, say, gives $\gamma = 1.65$. However, (1.84) shows that, in the limit of an infinitely thin flagellum, $\gamma \to 2$.

### 1.3.4 Regularised Singularities

In Section 1.3.1.5, a point-force acting in the fluid domain at a position $\mathbf{y}$ was considered, given by equations (1.22) and (1.23); these equations are re-written here, in the form:

$$\nabla \cdot \mathbf{u}(\mathbf{x}) = 0, \tag{1.85}$$

$$\mathbf{0} = -\nabla p(\mathbf{x}) + \mu \nabla^2 \mathbf{u}(\mathbf{x}) + \mathbf{F}\delta^3(\mathbf{x} - \mathbf{y}), \tag{1.86}$$

where, from (1.47), the force exerted on a surface surrounding the Stokeslet is given by $\mathbf{F} = -8\pi\mu\boldsymbol{\alpha}$. The resulting flow field, $\mathbf{u}(\mathbf{x})$, is given in terms of the Stokeslet singularity, (1.40).

In 2001, Cortez [23] recognised the difficulties in numerically implementing code based on singular solutions. This motivated the consideration of a distributed force, often referred to as a "blob" force, as opposed to a point-force, in which the three-dimensional, Dirac delta from (1.86) is effectively smoothed, or "regularised", using a blob function, $\phi(|\mathbf{x}-\mathbf{y}|)$, depending on a regularisation parameter, $\delta$. The blob function must satisfy

$$\iiint_{R^3} \phi(r)\, \mathrm{d}V(\mathbf{r}) = 1, \tag{1.87}$$

where $\mathbf{r} = \mathbf{x} - \mathbf{y}$ and $r = |\mathbf{r}|$.

The analogous, regularised, Stokeslet solution can be derived analytically (without Fourier transforming) from the equations:

$$\nabla \cdot \mathbf{u}(\mathbf{x}) = 0, \tag{1.88}$$

$$\mathbf{0} = -\nabla p(\mathbf{x}) + \mu \nabla^2 \mathbf{u}(\mathbf{x}) + \mathbf{F}\phi(r). \tag{1.89}$$

Upon defining radial functions, $G(r)$ and $B(r)$, through their Laplacians, such that

$$\nabla^2 G(r) = \phi(r), \qquad \nabla^2 B(r) = G(r), \tag{1.90}$$

the divergence of (1.89), using (1.88), gives that

$$\begin{aligned} 0 &= -\nabla^2 p(\mathbf{x}) + (\mathbf{F} \cdot \nabla)\phi(r), \\ &= -\nabla^2 p(\mathbf{x}) + (\mathbf{F} \cdot \nabla)\nabla^2 G(r). \end{aligned} \tag{1.91}$$

A solution for the regularised pressure is thus

$$p(\mathbf{x}) = (\mathbf{F}\cdot\nabla)G(r). \tag{1.92}$$

Inserting the regularised pressure back into (1.89) gives an equation for $\mathbf{u}(\mathbf{x})$,

$$\mathbf{0} = -\nabla[(\mathbf{F}\cdot\nabla)G(r)] + \mu\nabla^2\mathbf{u} + \mathbf{F}\nabla^2 G(r). \tag{1.93}$$

which, upon noting (1.90), results in a solution for the regularised velocity given by

$$\mu\mathbf{u} = (\mathbf{F}\cdot\nabla)\nabla B(r) - \mathbf{F}G(r). \tag{1.94}$$

Thus, upon prescribing a blob function, $\phi(r)$, $G(r)$ and $B(r)$ are deduced using (1.90), which determine the form of the "regularised" Stokeslet in (1.94).

Further still, a regularised, potential dipole can also be calculated in terms of $G(r)$ and $\phi(r)$. Recall that a singular, potential dipole is related to the singular Stokeslet, in that it is proportional to the Laplacian, in $\mathbf{y}$, of the Stokeslet solution, as illustrated in (1.50). Hence, by taking the Laplacian in $\mathbf{y}$ of the *regularised* Stokeslet, (1.94), one obtains

$$\nabla^2_{\mathbf{y}}\mathbf{u} = -(\mathbf{F}\cdot\nabla)\nabla G(r) + \mathbf{F}\phi(r). \tag{1.95}$$

The right-hand side of (1.95) gives rise to the regularised, potential dipole.

In order to simplify the expressions for both flow fields, two different blob functions are prescribed, $\phi_1(r)$ for the regularised Stokeslet in (1.94), and $\phi_2(r)$ for the regularised, potential dipole in (1.95) [2, 23]. These are given by

$$\phi_1(r) = \frac{15\delta^4}{8\pi(r^2+\delta^2)^{7/2}}, \qquad \phi_2(r) = \frac{3\delta^2}{4\pi(r^2+\delta^2)^{5/2}}, \tag{1.96}$$

where the pre-factors are necessary to satisfy (1.87); these functions are shown in figure 1.7 for $\delta = 1$. Noting that

$$\begin{aligned}(\mathbf{F}\cdot\nabla)\nabla B(r) &= (\mathbf{F}\cdot\nabla)\left[B'(r)\frac{\mathbf{r}}{r}\right], \\ &= \mathbf{F}\frac{B'(r)}{r} + (\mathbf{F}\cdot\mathbf{r})\frac{\mathbf{r}}{r}\left[\frac{B''(r)}{r} + \frac{B'(r)}{r^2}\right],\end{aligned} \tag{1.97}$$

with an analogous expression for $G(r)$, the regularised Stokelet is calculated to be

$$\mathbf{S}^{\delta}(\mathbf{x},\mathbf{y}) := \frac{(|\mathbf{x}-\mathbf{y}|^2+2\delta^2)\mathbf{I}}{(\,|\mathbf{x}-\mathbf{y}|^2+\delta^2\,)^{3/2}} + \frac{(\mathbf{x}-\mathbf{y})\otimes(\mathbf{x}-\mathbf{y})}{(\,|\mathbf{x}-\mathbf{y}|^2+\delta^2\,)^{3/2}}, \tag{1.98}$$

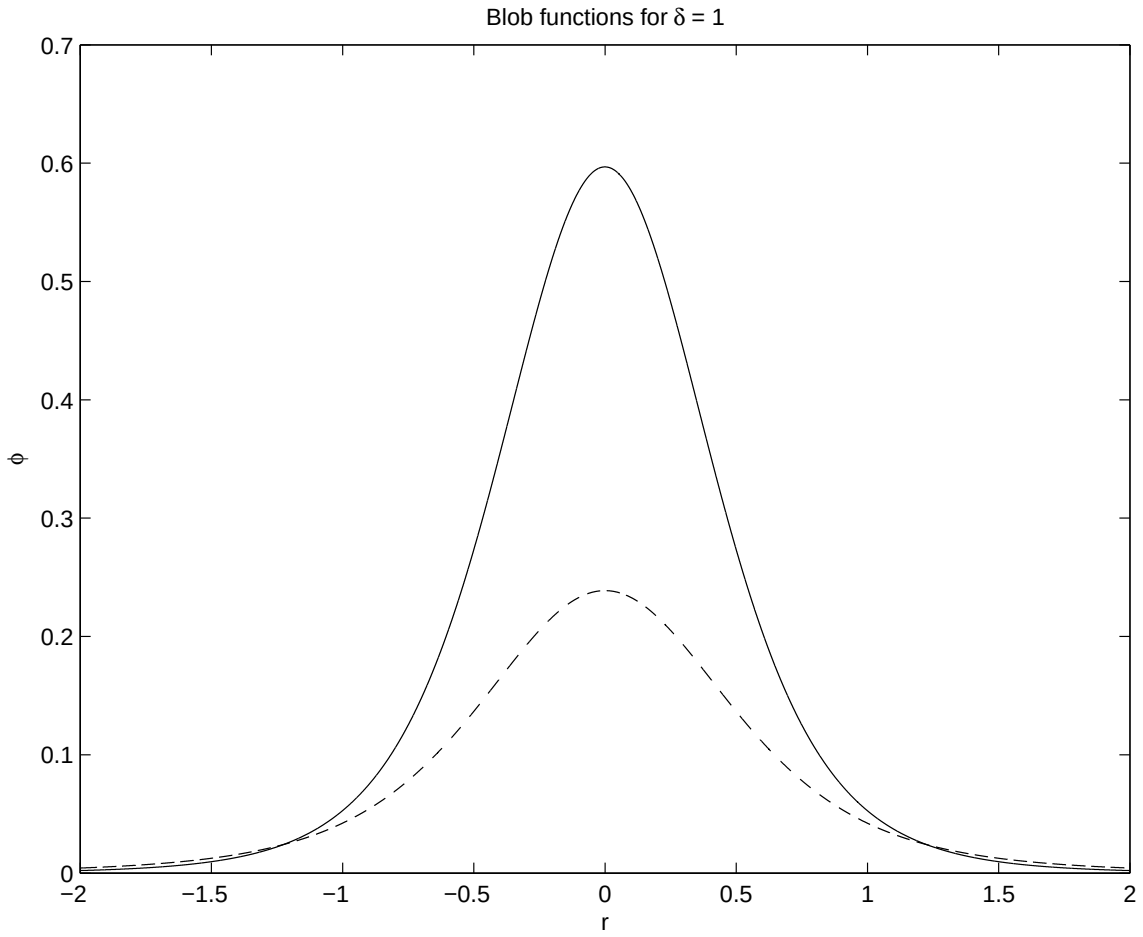


Figure 1.7: The two blob functions, $\phi_1(r)$ (continuous line) and $\phi_2(r)$ (dashed line) from (1.96), used to generate the regularised Stokeslet and regularised, potential dipole respectively. The regularisation parameter, $\delta$ is unity for this plot.

while the regularised, potential dipole is given by

$$\mathbf{D}^{\delta}(\mathbf{x},\mathbf{y}) := -\frac{(|\mathbf{x}-\mathbf{y}|^2 - 2\delta^2)\mathbf{I}}{(\,|\mathbf{x}-\mathbf{y}|^2+\delta^2\,)^{5/2}} + \frac{3(\mathbf{x}-\mathbf{y})\otimes(\mathbf{x}-\mathbf{y})}{(\,|\mathbf{x}-\mathbf{y}|^2+\delta^2\,)^{5/2}}. \tag{1.99}$$

Note that factors of $8\pi\mu$ have not been included in the definitions, (1.98) and (1.99), for consistency with the notation in Chapter 4, in which the regularised singularities are used extensively.

Although the development of regularised singularities originated from previous computational errors in numerical simulations due to singular (or near-singular) points, their motivation of use in Chapter 4 is purely analytical. In order to determine the flow past slender bodies with arbitrary, circular cross sections, line integrals of singularities can be distributed along the body centre-line (such as for the flow past a

prolate spheroid in Section 1.3.2.2). As the cross-sectional radius of the body varies, the force distribution along the centre-line must vary accordingly. By considering the theory of regularised singularities, the regularised force in equation (1.89) depends on the constant regularisation parameter, $\delta$, used to regularise the blob function, $\phi(r)$ from (1.96). If $\delta$ were chosen to vary along the arc-length of the centre-line, in accordance with the variations of the cross-sectional radius, a distribution of regularised singularities could be used to generate the required force distribution for the slender body; this is the motivation behind the theory developed in Chapter 4.

## 1.4 Literature Review

### 1.4.1 Overview

Before presenting the models related to the three topics of investigation, a review of existing and relevant literature is established, broadening the current background and adding a sense of perspective to the studies.

The first paper to explore the propulsion of an organism immersed in a low Reynolds number, viscous fluid using a driving force to compensate the viscous drag was Taylor's analysis of the swimming of organisms in 1951 [94]. By exploiting the fact that the sum of all forces in a Stokes fluid is zero (see Section 1.3.1.3), Taylor was able to model swimming sheets with propagating, small-amplitude, travelling waves. In 1952, Taylor extended the work into three dimensions, with the first representation of a spermatozoon flagellum being a flexible, cylindrical tail exhibiting small-amplitude, planar beating [95].

Subsequently, more detailed studies of the Stokes flow around slender bodies, such as flagella, emerged. In addition, other simple swimmer models were being designed with the requirement that they break the scallop theorem (see Section 1.3.1.4) in order to generate a net displacement. Thus, the remainder of the literature review splits accordingly into two sections: the first considers the development of so-called slender-body theory, while the second section considers simple swimmer models and the breakdown of the scallop theorem.

### 1.4.2 Slender-Body Theories

In 1953, Hancock [43] explored singularity representations of the flow field around a flagellum. The singularities used were those arising in the velocity field of the steady, Stokes flow past a sphere, namely the Stokeslet and potential dipole singularities (see Section 1.3.2.1). Hancock demonstrated how an integral of weighted Stokeslets and potential dipoles, distributed along a beating, flagellum centre-line, can be used to calculate the surrounding, velocity field; this became the groundwork for slender-body theory (SBT). Using cylindrical, flagellum elements, Hancock was able to show that translating motion of a cylindrical element in a direction radially outwards from the flagellum centre-line (the 'normal' direction), is twice as effective at producing a net propagation than translating motion in a direction tangential to the centre-line. The study prescribed sinusoidal beat patterns down the centre-lines of the flagella and calculated the singularity strengths needed to satisfy the no-slip boundary condition associated with viscous fluids.

Shortly after, in 1955, Gray and Hancock [42] together developed resistive-force theory (RFT) while studying sea-urchin spermatozoa. RFT states that, for each flagellum element, the resistive, viscous-drag forces acting on that element in the tangential, normal and binormal directions to the flagellum centre-line are directly proportional to the centre-line velocities in these respective directions. The constants of proportionality, called resistance coefficients, differ between the tangential case and the normal and binormal cases. In their theory, the latter two are twice as large as the tangential, resistance coefficient, highlighting the anisotropy noted by Hancock. It later transpired that RFT is the leading-order approximation to SBT in the asymptotically small, slenderness ratio, $\varepsilon$, where $\varepsilon$ is the maximum cross-sectional radius over the total centre-line length [53, 64]. From SBT, one can calculate explicitly the expressions for the resistance coefficients used in RFT, though the definitions vary slightly depending on the approximations made in SBT; see Section 1.3.3. In general, however, these resistance coefficients are directly proportional to $\mu$, the dynamic viscosity of the fluid, and inversely proportional to $\log(1/\varepsilon)$.

In 1971, Blake [14] used Fourier transforms to deduce the image system for a Stokeslet singularity placed a distance $z = h$ above a planar wall at $z = 0$, and in 1974 calculated the resistance coefficients adjusted to include wall effects [15]. It was assumed that the flagellum, cross-sectional radius, $a$, and centre-line length, $L$, satisfied $a \ll h \ll L$

where $h$ is the height of a point on the flagellum above the boundary. A further assumption was that the flagellar motion was in a plane parallel to that of the wall. Soon after, in 1975, Blake released another paper on RFT near a surface with Katz and Paveri-Fontana [55], highlighting that the amplitude of the flagellar motion needs to be small for the approximations to hold.

The implementation of RFT to model slender filaments in a Stokes fluid is notably more straightforward, but less accurate than the full SBT based on integrals of singularities. Nonetheless, both have been, and still are, used extensively in subsequent studies of flagellar motion [29, 83, 85]. In 1976, the first, numerical simulation of SBT was described by Liron and Mochon [67], in which the system of equations for flow past a slender body were discretised. The force was assumed to be constant on each segment of the discretised flagellum and an iterative procedure was applied, calculating the force distribution along the body and the net, swimming velocity. In 1979, Higdon [46] considered a model for a microswimmer with both a spherical head and flagellum. The force distribution along the flagellum was calculated from SBT, along with the translational, and angular, velocities of the head. Results were compared with those of RFT, the latter inevitably losing accuracy as the head-size increased.

Alongside the numerical work on SBT, there were significant, analytical advances using asymptotic methods, exploiting the slenderness ratio, $\varepsilon$. Examples of such work include Cox [27] in 1970, who considered a locally cylindrical, slender body with a general, curvilinear centre-line that was not necessarily sinusoidal. Cox calculated an inner solution, describing the flow field at a field point in the fluid domain located near to the slender-body surface; the inner solution was deduced using separable solutions of the Stokes' equations in cylindrical coordinates. This introduced logarithmic terms, motivating expansions in the parameter $(\log \varepsilon)^{-1}$ in order to subsequently match the inner solution sensibly to the outer solution. The outer solution itself, for a field point in the fluid far from the body surface, was viewed as a line distribution of weighted, point-force singularities. The outer solution thus introduced integrals of Stokeslets along the centre-line of the cylindrical body, with limits of integration between the end-points of the body. The distribution of the strengths of the Stokeslets was determined via the inspection of the inner solution when written in terms of outer variables. The resulting flow field, and pressure field, are given as asymptotic expansions in $(\log \varepsilon)^{-1}$. A similar approach was conducted by Batchelor [9] in 1970, who considered slender bodies with arbitrary cross-sectional radii, again with locally

cylindrical geometry.

In 1976, Lighthill [64] considered the same cylindrical, slender body and represented the fluid velocity as an integral of Stokeslets and potential dipoles distributed along the centre-line; both singularity distributions had *a priori* unknown weightings. By introducing an intermediate distance, $q$, Lighthill defines both a far field and near field, depending on a field point in the fluid domain being further, or closer, than the distance $q$. Lighthill then constructs an integral expression, based on various assumptions, relating the surface velocity to the force distribution along the centre-line. However, the parameter $q$ remained *ad hoc*, while eliminating it resulted in two non-local integrals and some local terms.

Keller and Rubinow [57], also in 1976, considered again the cylindrical, slender bodies with curvilinear centre-lines, writing down the inner solution as the flow field past an infinite cylinder. They also included the additional effects of twisting and dilating, although these effects are not discussed in this thesis. The outer solution was written down as the integral of a line of Stokeslets, the strengths of which were *a priori* unknown. This outer solution was subsequently matched to the inner solution (the reverse matching of Cox [27]), resulting in an integral equation for the Stokeslet strengths. The integral equation is then solved iteratively, again introducing logarithmic expansions.

These methods, however, suffered from inaccuracies at the end-points, where surface velocities were predicted to be infinite due to the use of cylindrical geometries and integrals that ranged from one end to the other. Tuck [100] had noted the analytical difficulties of cylindrical coordinates back in 1964, when proposing the use of prolate, spheroidal coordinates, $(x, y) = (L\cos\xi\cosh\eta, L\sin\xi\sinh\eta)$. These reduced the inaccuracies at the end-points and allowing the slender-body shape to have blunt ends. However, the theory was only presented with regards to axial flow past a slender body, without a curvilinear centre-line. Tillet [98], in 1970, also minimised inaccuracies at the ends of a slender body when investigating axially symmetric, slender bodies with straight centre-lines in uniform, axial and transverse streams. Tillet again uses weighted, integral distributions of singularities, where the singularity strengths were to be determined. The limits of integration along the centre-line, however, did not include the problematic end-points, but instead ranged over a subset of the straight

centre-line. The bodies, centre-lines and body orientations, however, were still restricted.

In 1980, Johnson [53] resolved these issues by offering an improved, slender-body theory with increased asymptotic accuracy (algebraic instead of logarithmic), reduced end-errors and no assumptions of cylindrical coordinates or geometries. His theory considers motion in all directions of a curvilinear, slender body with prolate-spheroid caps at the ends of the body. The flow field around the slender body is motivated by Chwang and Wu's [22] solution for the Stokes' flow around prolate spheroids in 1974, so that the leading-order velocity is represented by an integral of Stokeslet and potential dipole singularities. The range of integration along the centre-line, however, is between two effective foci, not the end-points of the body. Thus, both the recommendations from Tuck [100] and Tillet [98] were incorporated and, as long as the end regions of the body were prolate spheroidal caps, the end-errors were controlled. The analysis splits the slender body into a central region and two end regions, where the weighting of the potential dipole changes between the regions. As mentioned in Section 1.2.3, cross-sectional, radius functions that varied with arc-length, $\eta(s)$, can be prescribed in the central region, but must satisfy the condition that $d\eta/ds = 0$ at, and only at, the centre of the body.

Johnson compared his formalism of SBT to RFT and found agreement for headless, beating flagella, even for finite, beat amplitudes that were not small, so long as his resistance coefficients were adjusted by adding *ad hoc* correction factors; with a large head, however, these adjustments could not be made. Brokaw and Johnson [54] also demonstrated that the resistance coefficients of Lighthill [64] did not need this correction factor; thus, Lighthill's coefficients are subsequently used in the RFT model in Chapter 3 on hyperactive, sperm motility.

More recently, boundary-integral methods (BIMs), whereby singularities are placed around the boundaries of bodies immersed in a Stokes fluid, became popular as they could incorporate more general, boundary geometries. A study of rigid, rotating, helical flagella using BIMs was conducted by Phan-Thien, Tran-Cong and Ramia in 1987 [76] and generalised to the vicinity of planar surfaces by Shum, Gaffney and Smith [82]. The ideas behind SBT can be derived from the analysis of BIMs [65], illustrating how singularities can be distributed along the centre-line of the slender body as opposed to the body surface. Hybrid models have also been used in which a

sperm head is modelled via BIM and the flagellum is modelled by SBT [85]. A direct, numerical simulation using just BIMs on both the head and around the surface of the flagellum has not yet been presented in the literature for flagellated, eukaryotic cells (cells with a nucleus).

Motivated by the numerical instabilities that arise when simulating singularity-based models, in 2001, Cortez [23] introduced the construct of a regularised singularity. These were derived by effectively smoothing the point-force via a local, spherically symmetric function. Regularised singularities have been used, for example, to investigate various biological, motility scenarios [2, 24, 25, 26, 75, 87]. The SBT of Lighthill [64], Cox [27] and Keller and Rubinow [57] have all been re-derived in terms of regularised singularities and tested numerically on slender bodies without ends, such as tori [26], however Johnson's improved SBT [53] has not; Chapter 4 builds on the SBT of Johnson incorporating the regularised singularities of Cortez [25] in order to greatly expand the range of permissible, slender, body shapes.

### 1.4.3 Simple Swimmer Models and The Scallop Theorem

Alongside slender bodies immersed in viscous fluids, the study of artificial microswimmers has experienced an explosion of interest, with many being modelled using singularity methods. In 1977, Purcell [80], noted that a swimmer in a low Reynolds number environment cannot generate a net motion by exhibiting swimming strokes with completely reciprocal motion. This motion is such that the reverse stroke is simply the forward stroke reversed in time. One example of reciprocal motion, highlighted by Purcell, was that of a scallop flapping. There are many swimmer models that break this time-reversibility condition in order to swim effectively; see Section 1.3.1.4. These include squirming spheres [63] in which the sphere exhibits small oscillations of shape, 'push-me-pull-you' models [6] based on connected, spherical bladders changing their volumes and models using connected, moving arms [10]. Microswimmers comprised of combinations of spheres and rods, such as the three-sphere model [70] introduced by Najafi and Golestanian in 2004, have been the subject of extensive work [4, 41, 70, 78]. The three-sphere swimmers have also been subject to explicit, empirical testing using optical traps in a highly viscous, Newtonian fluid [62]. Further, analytical extensions include the development of a model for the interactions of two of these swimmers in 2007 by Pooley, Alexander and Yeomans [78].

While various other geometries of microswimmers were explored, the effects of different swimming environments were of interest, from a low Reynolds number, viscous, Newtonian fluid to shear-thinning fluid [69] and viscoelastic rheologies [38, 59, 96]. The designs of the swimmers outlined above were motivated by the requirement that they must break the scallop theorem in order to obtain a net displacement in one swimming cycle when immersed in a Newtonian fluid [80]. However, in a fluid medium with a non-Newtonian rheology, the scallop theorem need not hold, as shown in Section 1.3.1.4. This irreversibility has been illustrated explicitly for a nonlinear, viscoelastic fluid via two mixing-unmixing simulations [97], the first based on rotating, cylindrical pegs and the second using peristaltic waves down elastic walls. Upon mixing an initial configuration of fluid, an exact unmixing process highlights that the fluid particles do not return to their original positions, contrary to the predictions of reversibility. Simple swimmer models have been developed which exploit this irreversibility of the non-Newtonian fluid medium to obtain a net displacement, despite exhibiting reciprocal swimming strokes. Examples include a two-link, scalloping swimmer in a viscoelastic fluid [101] whereby relaxation stresses induce asymmetric stresses on the swimmer body, and a squirming sphere [60] for which the boundary velocity has a fore-aft asymmetry, thus differing under reversal.

Microswimming results for the net displacement in nonlinear rheologies have been varied. One of the first, viscoelastic, motility studies in 1998, by Fulford and Katz [38], considered filament swimmers with heads and finite flagella exhibiting low-amplitude, sinusoidal, beat patterns in a linear, viscoelastic fluid. A generalisation of RFT was used to relate forces directly to body velocities. The resulting predictions were faster swimming speeds in the linear, viscoelastic fluid given the same viscosity and energy expenditure [*ibid*]; improvements for swimming in rheological media have also been illustrated by models of swimming sheets with large undulations in nonlinear, viscoelastic fluid [96].

In contrast, Lauga [59] in 2007, when considering an infinite, undulating sheet in a viscoelastic, polymeric fluid, concluded that the net displacement of the swimmer is decreased. In 2009, Lauga [60] developed analytical formulae to calculate the net, swimming displacement for a simple, shape-changing swimmer in a low Reynolds number, nonlinear, viscoelastic environment with a high Deborah number (the ratio of the viscoelastic-relaxation time scale to the swimming stroke time scale). Other studies modelled with RFT, accounting for prescribed forces of infinite, filament swimmers

as opposed to prescribed, swimming motions, also suggest viscoelasticity decreases the swimming speed [36, 37]. Viscoelasticity has not, however, been investigated in the context of a three-sphere swimmer, hence motivating the study in Chapter 2.

## 1.5 Thesis Structure

The background fluid mechanics, the associated singular solutions and the methods used to construct flow fields around immersed bodies were covered in Section 1.3, "Background Fluid Mechanics". This section presents the Stokes equations governing the flow of a background, low Reynolds number, Newtonian fluid, including derivations of the relevant, singular solutions satisfying these equations. Flow fields and drag forces around translating spheres and prolate spheroids are discussed, the latter using integrals of singularity distributions along the spheroid centre-line. Resistive-force theory (RFT) for slender filaments is presented, directly relating the velocity of the body centre-line to the forces generated by the body due to viscous drag. The section concludes with an introduction to regularised singularities of Stokes flow.

Chapter 2 builds upon the background material relating to spheres in order to calculate the net displacement of the three-sphere microswimmer immersed in a low Reynolds number, nonlinear, viscoelastic fluid. The nonlinear, constitutive laws governing the fluid environment are presented. An initial motility study for the Newtonian case, including sphere-interaction terms, is conducted and compared to an existing model that neglects interaction terms, [78]. Viscoelasticity is subsequently included, followed by a multi-parameter, asymptotic analysis, obtaining expressions for the displacement of the microswimmer in one, swimming cycle. Results in both media are presented and a discussion follows, highlighting the subtleties between prescribing the rod displacements (the *kinematic* problem) and the internal forces (the *mobility* problem) of the swimmer.

Chapter 3 implements the relatively straightforward RFT in the complex modelling scenario of assessing the forces exerted by a sperm cell with a beating flagellum, tethered to on the wall of the female reproductive tract. Focusing on the biological context and modelling procedure, an explanation of the relevant physiology is presented, followed by a justification for the use of RFT over the more accurate SBT.

Expressions for the pushing and pulling forces exerted by the sperm cell on the tethering point are derived via RFT. Two different boundary conditions, related to the nature of the binding at the tethering point, are discussed. Motivated by experimental data, representations of the flagella waveforms are constructed, both symmetric and hyperactive, and inserted into the model. A parameter study that varies beat-amplitude, frequency, wavenumber and asymmetry is conducted. Conclusions are presented along with discussions of the biological relevance of the findings and any model limitations.

Chapter 4 develops a SBT that incorporates bodies with circular, cross-sectional radii, capable of varying in size along the centre-line. The SBT of Johnson [53] is first introduced, motivating an ansatz for the flow field around a slender body using regularised singularities. By enforcing the ansatz to satisfy the no-slip boundary condition around the surface of the body, the leading-order velocity around the generalised shape is deduced. The new theory is summarised, followed by a discussion in relation to the slender-body shapes that are now permissible.

Chapter 5 concerns the numerical validation, and implementation, of the theory in Chapter 4. The chapter begins with the discretisation of the integral equation arising in the theory due to the no-slip boundary condition. The numerical solution of this integral equation is calculated and inserted back into the model, determining the flow field at any point in the fluid domain. The model is tested using various slender-body shapes, including both tapered and wave-like bodies with curvilinear centre-lines given by either linear, quadratic or cubic curves. Errors are determined between the calculated, fluid velocity for a point on the body surface and the known, surface velocity of the slender body itself. These errors are investigated both along the centre-line and around a circular, cross section. Conclusions are drawn, highlighting the simple, numerical implementation of the theory compared to existing theories, and the requirement that errors are asymptotically small everywhere on the body surface.

Chapter 6 summarises the main findings of Chapters 2 through to 5, while also suggesting potential, future work to advance the models and theories in the thesis.

## 1.6 Statement of Originality

The background fluid mechanics introduced in Section 1.3, regarding the Stokes equations and singularity methods, is well-known and available in the literature.

The three-sphere swimmer results in Chapter 2 regarding the net displacement of the swimmer when immersed in a linear, Newtonian fluid are available in the literature and referenced in the literature review, Section 1.4. The higher-order analytics in the Newtonian case are novel and consist of original work by the thesis author, as does the rest of the chapter. The addition of viscoelastic rheology to the surrounding, fluid environment, the non-dimensionalisation identifying two, small parameters and the associated, asymptotic analysis, comprise original work by the thesis author. It has been accepted as a journal manuscript by APS Physics Review E.

The work on hyperactive, sperm motility in Chapter 3 has been published, [29]. While the RFT used is well known in the literature and referenced in the literature review, Section 1.4, the application of low Reynolds number fluid dynamics and mechanics to the biological context of tethered sperm cells undergoing hyperactivation is novel. The experimental imaging was solely the work of Thomas Connolly and J. Kirkman-Brown, both from The University of Birmingham, U.K., and the Centre for Human Reproductive Science, Birmingham, U.K.; see acknowledgment. This imaging was subsequently used by the thesis author to compare theoretical modelling with observation.

While Chapter 4 initially revisits the slender-body theory of Johnson, [53], the development of the subsequent model using regularised singularities to incorporate varying, cross-sectional radii along the body is original work. The numerical implementation and error analysis in Chapter 5 relates to the theory developed in Chapter 4, thus this chapter content is also original work by the thesis author.

# Chapter 2

# The Three-Sphere Microswimmer in a Viscoelastic Fluid

## 2.1 Chapter Introduction

The first aspect of low Reynolds number microswimming to be modelled is that of the three-sphere swimmer in a viscoelastic environment, with the motivations for studying these microswimmers outlined in Section 1.2.1. While extensive work has been performed for the swimmer in a Newtonian fluid, [4, 41, 70, 78] (see literature review, Section 1.4), the effects of viscoelasticity have not yet been explored.

The chapter begins with a description of the swimmer model and governing, fluid equations, followed by a non-dimensionalisation, highlighting the two small parameters arising. Asymptotic analysis for the swimmer in a Newtonian fluid is presented, using a more rigorous, asymptotic derivation than existing models [4, 41, 70, 78] by including sphere-interaction terms in the flow field. Time-averaged results for the net displacement of the swimmer over one beat cycle in terms of the rod oscillations, however, are consistent with the existing work [*ibid*].

Using the calculated force-velocity relationship associated with the spheres in the model when immersed in a Newtonian fluid, the net displacement of the swimmer per beat cycle is also deduced in terms of the prescribed, internal forces, for example due to motors within the spheres themselves.

The full viscoelastic model follows, again deriving asymptotically the net displacement in terms of the rod oscillations. At leading order, the expression is identical to that of the Newtonian fluid. However, rewriting the rod displacements in terms of

internal forces via the calculated, force-velocity relationship for a viscoelastic fluid, results in an expression for the net displacement which depends on the dimensionless, viscoelastic, fluid parameters. This expression highlights the differences between the two fluids.

The efficiency of the swimmer is discussed and an example is presented of a three-sphere swimmer with sinusoidal, internal forces prescribed. Discussions of the results follow.

## 2.2 Model Formulation

### 2.2.1 The Three-Sphere Microswimmer

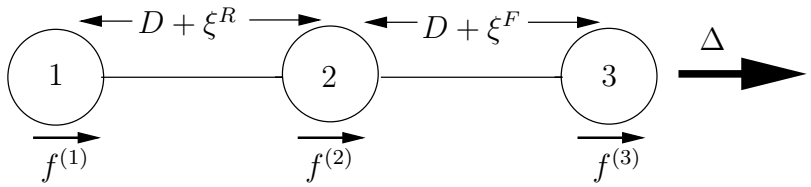


Figure 2.1: The Najafi-Golestanian three-sphere swimmer. Three, colinear, identical, neutrally buoyant spheres are connected by rods of mean length $D$ with periodic, but, in general, non-reciprocal oscillations given by $\xi^R(t)$ and $\xi^F(t)$. The force acting on each sphere, due to internal motors for example, is denoted $\mathbf{f}^{(\alpha)}(t)$, where $\alpha \in \{1, 2, 3\}$, and the net displacement over one beat cycle is denoted $\Delta$ for the Newtonian problem and $\Delta_v$ for the viscoelastic analogue.

The three-sphere swimmer [70] consists of three, colinear, identical, neutrally buoyant spheres, each of radius $a$, connected by thin, dynamically negligible rods with oscillating lengths $D + \xi^R(t)$ between spheres 1 and 2 (the rear) and $D + \xi^F(t)$ between spheres 2 and 3 (the front); see figure 2.2.1. The axis of motion of the swimmer is taken to be the $z$-axis with unit vector $\mathbf{e}_z$, along which the rods lie. Variables relating to each sphere are denoted with Greek superscripts, i.e. $\mathbf{x}^{(\alpha)}$ is the position of sphere $\alpha$, where $\alpha \in \{1, 2, 3\}$, in order to avoid any later confusion with subscript $i$ and $j$ denoting vector components.

The force acting on each sphere is denoted $\mathbf{f}^{(\alpha)}(t)$, where $\alpha \in \{1, 2, 3\}$; these are the equal and opposite forces arising, for example, due to motor devices located inside, and acting on, the spheres themselves. In order to compare both the swimming

progress and efficiency of the swimmer in a viscoelastic fluid to that in a Newtonian fluid, periodic forces on spheres 1 and 3 are prescribed, denoted $\mathbf{f}^{(1)}(t)$ and $\mathbf{f}^{(3)}(t)$ respectively. These prescribed forces have a beat frequency, $\omega$, and phase difference, $\phi$, present between them to break the time reversibility of the stroke, so as not to induce reciprocal motion; see Section 1.3.1.4. Note that the force on sphere 2, $\mathbf{f}^{(2)}(t)$, is automatically determined via an important consequence of the negligible body inertia and inertialess regime, in that the sum of all the forces on the spheres is zero; see Section 1.3.1.3. Thus,

$$\sum_{\alpha=1}^{3} \mathbf{f}^{(\alpha)} = \mathbf{0}. \tag{2.1}$$

The sphere separations vary about their mean length, $D$, via the rod displacements, $\xi^R(t)$ and $\xi^F(t)$, which are induced by, and calculated from, the prescribed, periodic forces, $\mathbf{f}^{(1)}(t)$ and $\mathbf{f}^{(3)}(t)$. Note that this differs from existing work, in which the rod displacements are prescribed directly [4, 41, 70, 78]. Prescribing the rod displacements in order to calculate the net, swimmer displacement is straightforward in a Newtonian environment and denoted the *kinematic* problem. However, in a viscoelastic fluid, the relationship is not as intuitive [36] and hence the internal forces are prescribed throughout the chapter, termed the *mobility* problem.

Upon neglecting any initial, transient behaviour of the swimmer by assuming it has settled into periodic motion, the rod displacements are themselves periodic, with beat frequency $\omega$, inherited from the internal, periodic forces. Sphere $\alpha$, where $\alpha \in \{1, 2, 3\}$, is centred at $\mathbf{x}^{(\alpha)}(t)$ with velocity $\mathbf{U}^{(\alpha)}(t)$. Thus,

$$\mathbf{U}^{(2)} - \mathbf{U}^{(1)} = \dot{\xi}^R \mathbf{e}_z, \tag{2.2}$$

$$\mathbf{U}^{(3)} - \mathbf{U}^{(2)} = \dot{\xi}^F \mathbf{e}_z, \tag{2.3}$$

$$|\mathbf{x}^{(2)} - \mathbf{x}^{(1)}| = D + \xi^R, \tag{2.4}$$

$$|\mathbf{x}^{(3)} - \mathbf{x}^{(2)}| = D + \xi^F, \tag{2.5}$$

where the superscript dot denotes differentiation with respect to time and, without loss of generality, the spheres move along the $z$-axis.

The procedure for determining the net displacement of the swimmer in one beat stroke, denoted $\Delta$ in a Newtonian fluid and $\Delta_v$ in a viscoelastic fluid, is as follows. The centre of sphere 2 is chosen as a reference point of the swimmer, without loss of

generality, so that $\Delta$ (or $\Delta_v$) is the integral of $\mathbf{U}^{(2)}$ in time, over one swimming-stroke period, hence $\mathbf{U}^{(2)}$ must be determined. Given the forces are prescribed, as discussed above, a relationship between the force on each sphere, $\mathbf{f}^{(\alpha)}(t)$ for $\alpha \in \{1,2,3\}$, and the velocities of each sphere, $\mathbf{U}^{(\beta)}$ for $\beta \in \{1,2,3\}$, is required; this force-velocity relationship is derived asymptotically using the governing, fluid equations, requiring the flow field around the microswimmer to be calculated, in particular on the surface of the spheres. The force-velocity relationship, the form of which differs between the Newtonian and viscoelastic media, can be inverted to obtain the required expression for $\mathbf{U}^{(2)}$.

### 2.2.2 Viscoelastic (Oldroyd-B) Equations

To derive the force-velocity relationship for the spheres in the viscoelastic case, the viscoelastic-fluid framework must first be established. The fluid is taken to have a constant density, $\rho$, and a constant, dynamic viscosity, $\mu$. The fluid velocity is denoted $\mathbf{u}(\mathbf{x},t)$ with modified pressure (assuming a neutrally buoyant swimmer [8], discussed in Section 1.3.1.1), $p(\mathbf{x},t)$, where quantities are measured at a field point, $\mathbf{x}$, in the fluid domain at time $t$. Prior to assuming a low Reynolds number environment, the fluid dynamics are governed by the principles of the Navier–Stokes equations, (1.1) and (1.2), though the deviatoric-stress tensor, $\boldsymbol{\tau}(\mathbf{x},t)$, follows an Oldroyd-B, constitutive relation [73]. The governing equations are thus

$$\begin{aligned} \nabla \cdot \mathbf{u} &= 0, \\ -\nabla p + \nabla \cdot \boldsymbol{\sigma} &= \rho \left( \frac{\partial \mathbf{u}}{\partial t} + (\mathbf{u} \cdot \nabla)\mathbf{u} \right), \end{aligned} \tag{2.6}$$

recalling equation (1.3) for the stress tensor,

$$\boldsymbol{\sigma}(\mathbf{x},t) := -p(\mathbf{x},t)\mathbf{I} + \boldsymbol{\tau}(\mathbf{x},t). \tag{2.7}$$

The deviatoric-stress tensor is given by the constitutive relation

$$\begin{aligned} &\boldsymbol{\tau} + \lambda \left[ \frac{\partial \boldsymbol{\tau}}{\partial t} + \mathbf{u} \cdot \nabla \boldsymbol{\tau} - \kappa_1 \left( [\nabla \mathbf{u}]^T \cdot \boldsymbol{\tau} + \boldsymbol{\tau} \cdot [\nabla \mathbf{u}] \right) \right] \\ &= \mu \boldsymbol{\mathcal{E}} + \mu\gamma \left[ \frac{\partial \boldsymbol{\mathcal{E}}}{\partial t} + \mathbf{u} \cdot \nabla \boldsymbol{\mathcal{E}} - \kappa_2 \left( [\nabla \mathbf{u}]^T \cdot \boldsymbol{\mathcal{E}} + \boldsymbol{\mathcal{E}} \cdot [\nabla \mathbf{u}] \right) \right], \end{aligned} \tag{2.8}$$

where $\lambda$ and $\gamma$ are relaxation times, and the rate-of-strain tensor is given by

$$\boldsymbol{\mathcal{E}} := (\nabla \mathbf{u})^T + \nabla \mathbf{u}. \tag{2.9}$$

Note that the constitutive relation in equation (2.8) is non-reciprocal, in that it is not satisfied by $-\boldsymbol{\tau}$, $-\boldsymbol{\mathcal{E}}$ and $-t$ due to the time derivatives and the nonlinear terms. The constitutive relation for the Newtonian fluid, (1.4), is reobtained by setting the relaxation times $\lambda$ and $\gamma$ to zero, so that $\boldsymbol{\tau} = \mu\boldsymbol{\mathcal{E}}$; this relation is reciprocal, as discussed in Section (1.3.1.4).

For an Oldroyd-B fluid in particular, $\kappa_1 = \kappa_2 = 1$ so that the spatial derivatives in the constitutive law, (2.8), are said to be upper convected. For a representation of a polymeric, Oldroyd-B fluid comprised of a polymer in a solvent, the constant $\gamma = \lambda\mu_s/(\mu_s + \mu_p)$ is termed the retardation time, where $\mu_s$ and $\mu_p$ are the respective viscosities of the solvent and polymer, [12, 33]. This framework also includes the parameters $\gamma = 0$ and $\kappa_1 = \kappa_2 = 1$, which is an upper-convected, Maxwell fluid, used to describe a polymer melt [51]. The constitutive law in (2.8) immediately generalises to other parameters in the constitutive relation, for example $\gamma = 0$, and $\kappa_1 = \kappa_2 = -1$, a lower-convected, Maxwell fluid [12, 13], $\gamma = 0$, and $\kappa_1 = \kappa_2 = 0$, a Jaumann model [77] and a polymeric, Boger fluid [51].

The fluid mechanics are coupled to the kinetics of the three-sphere swimmer via no-slip boundary conditions, imposed on all sphere surfaces, stating

$$\mathbf{u} = \mathbf{U}^{(\alpha)}(t) \quad \text{on} \quad |\mathbf{x} - \mathbf{x}^{(\alpha)}| = a, \quad \alpha \in \{1,2,3\}. \tag{2.10}$$

The force acting on sphere $\alpha$ due to the viscous drag and the interactions of the other spheres is calculated by integrating the radial component of the stress tensor, (2.7), over the sphere surface, $|\mathbf{x}| = a$. Pozrikidis [79] simplifies the calculation by considering the flow past a sphere where the velocity at infinity decays at least as fast as $1/r$, a condition satisfied here given the flow fields are generated by spheres, the solution for which behaves as $O(1/r)$ in the far-field; see Section 1.3.2.1. Pozrikidis states that the force acting on the sphere due to the surrounding fluid is given by

$$\mathbf{f}^{(\alpha)} = \frac{3\mu}{2a} \int_{|\mathbf{x}|=a} \mathbf{u}^{(\alpha)background} \, \mathrm{d}S. \tag{2.11}$$

The term $\mathbf{u}^{(\alpha)background}$ denotes the flow due to the motions and interactions of the other spheres with themselves, neglecting the disturbance flow due to the presence of sphere $\alpha$ itself. This does, however, include the background flow, $-\mathbf{U}^{(\alpha)}$, arising from fixing the coordinate frame in sphere $\alpha$. Upon solving the governing equations, the calculated flow field, $\mathbf{u}(\mathbf{x}, t)$, around the three-sphere microswimmer will

depend on the sphere velocities, $\mathbf{U}^{(\beta)}$ where $\beta \in \{1, 2, 3\}$. Equation (2.11) will then be used to derive the force-velocity relationship for the spheres in the Newtonian case, although it is not immediately applicable to the viscoelastic case. However, the subsequent asymptotic analysis splits the viscoelastic case into a Newtonian problem transformed by a temporal operator, and a forced Stokes problem. The latter is shown not to contribute to the force, while equation (2.11) is shown to be valid for the transformed Newtonian problem.

### 2.2.3 Non-dimensionalisation and Simplifications

The three-sphere model incorporates three length scales: the sphere radius, $a$, the mean length of the rod, $D$, and the amplitude of the rod displacements, $b$, where $|\xi^R(t)| \leq b$ and $|\xi^F(t)| \leq b$. All length scales are non-dimensionalised by $a$, while time is non-dimensionalised by $1/\omega$, where $\omega$ is the frequency of the periodic, internal forces, $\mathbf{f}^{(1)}(t)$ and $\mathbf{f}^{(3)}(t)$, and the induced, rod displacements, $\xi^R(t)$ and $\xi^F(t)$. Motivated by the pragmatic constraint that the swimmer mechanism, such as internal motor devices, must sit within the spheres themselves, one might envisage that $b < a$. It is hence assumed that $\epsilon := b/a \ll 1$, so that the amplitude of the swimmer oscillations is much smaller than the radius of the spheres. In addition, the mean distance of separation between the spheres due to the rods, $D$, is assumed to be much greater than the radii of the spheres, $a$, so that $\delta := a/D \ll 1$; see figure 2.2. In summary:

$$b \ll a \ll D, \qquad \epsilon := b/a \ll 1, \qquad \delta := a/D \ll 1. \tag{2.12}$$

By non-dimensionalising lengths with $a$, $\xi^R(t)$ and $\xi^F(t)$ in dimensionless variables are $O(\epsilon)$, thus

$$\mathbf{x} = a\hat{\mathbf{x}}, \quad \nabla = \hat{\nabla}/a, \quad t = \hat{t}/\omega, \quad \xi^\beta(t) = \epsilon a \hat{\xi}^\beta(\hat{t}), \tag{2.13}$$

where $\beta \in \{R, F\}$ and hatted variables are both dimensionless and $O(1)$. Note that, dimensionally, the velocity field outside a sphere for the parameter regime of interest is algebraic in $1/r$ based on the solution for the Stokes flow around a translating sphere in Section 1.3.2.1. Thus, near the sphere surface, the scaling $\nabla = \hat{\nabla}/a$ ensures $\hat{\nabla}\hat{\mathbf{u}} \sim O(1)$, which can be confirmed *a posteriori*.

Equations (2.2) and (2.3) suggest that the scale of the sphere velocities, $U$, induced by the rod oscillations is given by $U = b\omega = \epsilon a\omega$. The velocity field generated in the

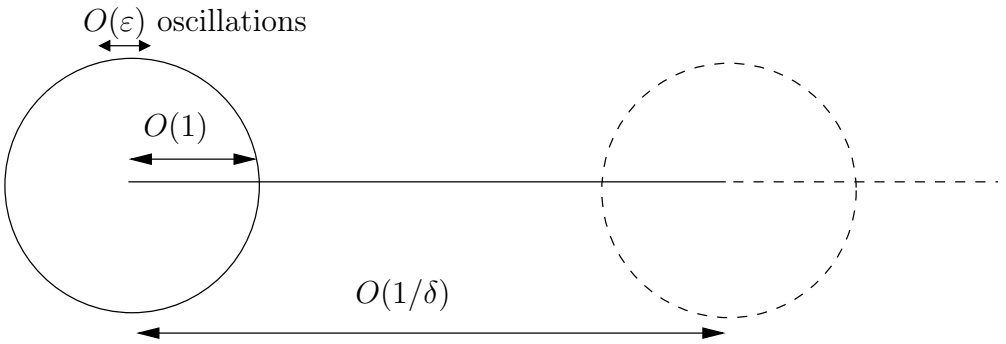


Figure 2.2: The two, asymptotically small parameters are identified as $\epsilon$, denoting the magnitude of the oscillations of the spheres due to the rod displacements, and $\delta$, where $1/\delta$ denotes the mean length of the sphere separations due to the rods.

surrounding fluid is driven by this oscillatory motion, thus inheriting the same scale, giving

$$\mathbf{U}^{(\alpha)} = \epsilon a\omega\hat{\mathbf{U}}^{(\alpha)}, \quad \frac{\mathrm{d}\mathbf{x}^{(\alpha)}}{\mathrm{d}\hat{t}} = \epsilon\hat{\mathbf{U}}^{(\alpha)}, \quad \mathbf{u} = \epsilon a\omega\hat{\mathbf{u}}, \tag{2.14}$$

where, again, hatted variables are dimensionless and $O(1)$. Dropping the hat notation and working in dimensionless variables henceforth, equations (2.2)–(2.5) from the swimmer geometry become

$$\begin{aligned}
\mathbf{U}^{(2)} - \mathbf{U}^{(1)} &= \dot{\xi}^R\mathbf{e}_z, \\
\mathbf{U}^{(3)} - \mathbf{U}^{(2)} &= \dot{\xi}^F\mathbf{e}_z, \\
|\mathbf{x}^{(2)} - \mathbf{x}^{(1)}| &= 1/\delta + \epsilon\xi^R, \\
|\mathbf{x}^{(3)} - \mathbf{x}^{(2)}| &= 1/\delta + \epsilon\xi^F.
\end{aligned} \tag{2.15}$$

Motivated by the observation that the deviatoric-stress tensor in a Newtonian fluid is proportional to the gradient of the velocity, (2.9), $\boldsymbol{\tau}$, $p$ and hence $\boldsymbol{\sigma}$ from (2.7) are non-dimensionalised by $\mu\epsilon\omega$ to ensure they are $O(1)$. The force on sphere $\alpha$, $\mathbf{f}^{(\alpha)}$, is related to the surface integral of $\boldsymbol{\sigma}$ via (1.17) and is consequently non-dimensionalised with $\mu\epsilon\omega a^2$.

All length scales are assumed to be sufficiently small to neglect the advective, Reynolds number, $Re$. By assigning an appropriate sphere radius and oscillation frequency such that $\omega a^2 \ll \mu/\rho$, the frequency Reynolds number, $Re_\omega := \rho\omega a^2/\mu$, can also be taken to be negligible, thus allowing the concepts of Section 1.3, associated with Stokes flow, to be used. In the upcoming, asymptotic analysis, an *a posteriori* check implies that one requires $Re \sim Re_\omega \sim O(\delta^3)$ or less. A regime is considered in which the Deborah

numbers, $\Lambda := \omega\lambda$ and $\Gamma := \omega\gamma$ [59], are $O(1)$, implying that the relaxation time and retardation time of the fluid are comparable to the time scale of the swimmer oscillations. In particular, the order-one Deborah number regime has already been observed numerically to give rise to a peak in swimming efficiency of free-swimming sheets [96] and thus is of clear interest in understanding swimmer-rheological interactions.

The governing, fluid equations, (2.6)–(2.8), are rewritten in a frame centred in sphere $\alpha$, so that the origin is at $\mathbf{x}^{(\alpha)}(t)$; variables in this non-inertial frame are denoted by a superscript $\alpha$. The new spatial coordinates, $\mathbf{x}'$ say, with associated gradient $\nabla_{x'}$, satisfy, dimensionlessly,

$$\mathbf{x}' = \mathbf{x} - \mathbf{x}^{(\alpha)}(t), \quad \nabla_{x'} = \nabla, \quad \frac{\partial}{\partial t|_x} = \frac{\partial}{\partial t|_{x'}} - \epsilon \mathbf{U}^{(\alpha)}(t) \cdot \nabla_{x'|_t}. \tag{2.16}$$

Throughout the rest of the chapter, it is assumed that the frame is always centred in sphere $\alpha$, thus for ease of presentation, coordinates $\mathbf{x}'$ will be written simply as $\mathbf{x}$.

Upon non-dimensionalising, neglecting inertial terms and setting, for example, $\kappa_1 = \kappa_2 = 1$ (though other $O(1)$ values are acceptable), the governing equations become:

$$\begin{aligned}
\nabla \cdot \mathbf{u}^{(\alpha)} &= 0, \\
-\nabla p^{(\alpha)} + \nabla \cdot \boldsymbol{\tau}^{(\alpha)} &= \mathbf{0}, \\
\left(1 + \Lambda \frac{\partial}{\partial t}\right) \boldsymbol{\tau}^{(\alpha)} &= \left(1 + \Gamma \frac{\partial}{\partial t}\right) \boldsymbol{\mathcal{E}}^{(\alpha)} \\
&\quad - \epsilon \Big[ \mathbf{u}^{(\alpha)} \cdot \nabla [\Lambda \boldsymbol{\tau}^{(\alpha)} - \Gamma \boldsymbol{\mathcal{E}}^{(\alpha)}] \\
&\quad - \{ (\nabla \mathbf{u}^{(\alpha)})^T \cdot [\Lambda \boldsymbol{\tau}^{(\alpha)} - \Gamma \boldsymbol{\mathcal{E}}^{(\alpha)}] \\
&\quad + [\Lambda \boldsymbol{\tau}^{(\alpha)} - \Gamma \boldsymbol{\mathcal{E}}^{(\alpha)}] \cdot \nabla \mathbf{u}^{(\alpha)} \} \\
&\quad - \mathbf{U}^{(\alpha)} \cdot \nabla [\Lambda \boldsymbol{\tau}^{(\alpha)} - \Gamma \boldsymbol{\mathcal{E}}^{(\alpha)}] \Big], \\
\boldsymbol{\mathcal{E}}^{(\alpha)} &:= \left(\nabla \mathbf{u}^{(\alpha)}\right)^T + \nabla \mathbf{u}^{(\alpha)}.
\end{aligned} \tag{2.17}$$

The no-slip boundary conditions on the spheres are given by

$$\mathbf{u}^{(\alpha)} = \mathbf{U}^{(\beta)} - \mathbf{U}^{(\alpha)} \text{ on } |\mathbf{x} - \mathbf{x}^{(\beta)}| = 1, \qquad \beta \in \{1,2,3\}, \tag{2.18}$$

where $\mathbf{x}^{(\beta)} = \mathbf{0}$ for $\beta = \alpha$, recalling the frame is centred in sphere $\alpha$.

The dimensionless force on sphere $\alpha$ from (2.11) derived by Pozrikidis [79], non-dimensionalised by $\epsilon\omega\mu a^2$, is given by

$$\mathbf{f}^{(\alpha)} = \frac{3}{2} \int_{|\mathbf{x}|=1} \mathbf{u}^{(\alpha) background} \, \mathrm{d}S. \tag{2.19}$$

## 2.3 The Newtonian Fluid Case

### 2.3.1 The Newtonian Flow Field

Before considering the full, viscoelastic model given by equations (2.15)–(2.19), an initial insight can be gained by considering the Newtonian problem [4, 32, 41, 70, 78], whereby the three-sphere swimmer is immersed in a viscous, Newtonian fluid with no viscoelastic properties. The results obtained are subsequently required when examining the viscoelastic case.

Expressions are reproduced for the net displacement after one beat cycle in a Newtonian fluid, $\Delta$, in agreement with existing results [4]. However, higher-order terms of the sphere interactions are consistently accounted for in order to obtain the force on the spheres in a Newtonian fluid; deducing a net motion over a beat cycle *necessitates* the consideration of these higher-order corrections, though they *a posteriori* do not contribute. Also, as with existing approaches [*ibid*], the potential-dipolar terms arising in the flow field are neglected, although careful treatment is given to this assumption, with $\delta \ll \epsilon$ emerging as a necessary condition.

Using the same notation as before in a coordinate frame centred in sphere $\alpha$, setting $\Lambda$ and $\Gamma$ to zero in (2.17), the Newtonian, governing equations are

$$\begin{aligned} -\nabla p^{(\alpha)} + \nabla \cdot \boldsymbol{\tau}^{(\alpha)} &= \mathbf{0}, \\ \nabla \cdot \mathbf{u}^{(\alpha)} &= 0, \\ \boldsymbol{\tau}^{(\alpha)} = \boldsymbol{\mathcal{E}}^{(\alpha)} &:= (\nabla \mathbf{u}^{(\alpha)})^T + \nabla \mathbf{u}^{(\alpha)}, \end{aligned} \tag{2.20}$$

with

$$\begin{aligned} \mathbf{U}^{(2)} - \mathbf{U}^{(1)} &= \dot{\xi}^R \mathbf{e}_z, \\ \mathbf{U}^{(3)} - \mathbf{U}^{(2)} &= \dot{\xi}^F \mathbf{e}_z, \\ \frac{1}{|\mathbf{x}^{(2)} - \mathbf{x}^{(1)}|} &= \delta(1 + \delta\epsilon\xi^R)^{-1}, \\ \frac{1}{|\mathbf{x}^{(3)} - \mathbf{x}^{(2)}|} &= \delta(1 + \delta\epsilon\xi^F)^{-1}, \end{aligned} \tag{2.21}$$

and boundary conditions,

$$\mathbf{u}^{(\alpha)} = \mathbf{U}^{(\beta)} - \mathbf{U}^{(\alpha)} \text{ on } |\mathbf{x} - \mathbf{x}^{(\beta)}| = 1, \qquad \beta \in \{1,2,3\}. \tag{2.22}$$

The fluid environment is inertialess, given the Reynolds number, $Re$, has been assumed to be negligible. This ensures there are no inertial terms in the governing equations, (2.20), allowing time-dependent variables to be treated as quasi-steady in the Newtonian case; see Section 1.3.1.1. With the subsequent viscoelastic case, there is the potential for initial, transient behaviour, though only solutions where this transient behaviour, arising from initial conditions in time, has decayed and the swimmer has settled into periodic beating are considered. Hence, in both fluid cases, the variables in the boundary conditions such as $\mathbf{U}^{(\alpha)}(t)$, can be considered with time, $t$, simply behaving as a parameter.

Recall the Newtonian flow field due to a single, translating sphere of unit radius, with sphere velocity $\mathbf{U}$ and centre $\mathbf{y}$ in an infinite domain, is represented via a linear combination of a Stokeslet, $\mathbf{S}(\mathbf{x}, \mathbf{y})$, and potential dipole, $\mathbf{D}(\mathbf{x}, \mathbf{y})$; see Section (1.3.2.1). Dimensionlessly,

$$\mathbf{u}(\mathbf{x}) = \mathbf{G}(\mathbf{x}, \mathbf{y})\mathbf{U}, \tag{2.23}$$

where

$$\mathbf{G}(\mathbf{x}, \mathbf{y}) := \frac{3}{4}\mathbf{S}(\mathbf{x}, \mathbf{y}) - \frac{1}{4}\mathbf{D}(\mathbf{x}, \mathbf{y}), \tag{2.24}$$

from equation (1.62) and

$$\mathbf{G}(\mathbf{x}, \mathbf{y}) = \mathbf{I} \quad \text{on} \quad |\mathbf{x} - \mathbf{y}| = 1. \tag{2.25}$$

The known solution for one, translating sphere in an infinite domain motivates an *ansatz*, $\mathbf{u}_A^{(\alpha)}(\mathbf{x})$, for the velocity flow field, centred in sphere $\alpha$, as

$$\mathbf{u}_A^{(\alpha)}(\mathbf{x}) = -\mathbf{U}^{(\alpha)} + \sum_{k=1}^{3} \mathbf{G}(\mathbf{x}, \mathbf{x}^{(k)})\mathbf{U}^{(k)}. \tag{2.26}$$

However, the flow field in (2.26) does not satisfy the boundary conditions, (2.22), as interaction terms between the spheres are not included, given (2.26) assumes each sphere is in an infinite domain, unaffected by other spheres. This flow-field approximation, (2.26), is used in existing work [4], which assumes that the spheres are sufficiently separated to drop the higher-order terms in (2.24) from the potential dipole. However, by neglecting potential-dipolar terms, any interaction terms of a lower, asymptotic order then the potential-dipolar terms should be retained; thus (2.26) needs improvement.

In order to account for the interaction terms, reflection methods for singularities with spherical boundaries can be implemented [58]. However, to simplify the calculations and make analytical progress, an asymptotic approach is taken, exploiting the small, geometric parameters, $\epsilon$ and $\delta$.

Applying the boundary conditions, (2.22), to the *ansatz* of the flow field, (2.26), gives

$$\mathbf{u}_A^{(\alpha)}(\mathbf{x}^{(\beta)} + \mathbf{e}_r^{(\beta)}) = \mathbf{U}^{(\beta)} - \mathbf{U}^{(\alpha)} + \sum_{\gamma=1,\, \gamma\neq\beta}^{3} \mathbf{G}(\mathbf{x}^{(\beta)} + \mathbf{e}_r^{(\beta)}, \mathbf{x}^{(\gamma)})\mathbf{U}^{(\gamma)}, \tag{2.27}$$

where $\mathbf{x}$ has been taken to lie on the surface of sphere $\beta$, denoted by

$$\mathbf{x} = \mathbf{x}^{(\beta)} + \mathbf{e}_r^{(\beta)}. \tag{2.28}$$

In (2.28), the $\mathbf{e}_r^{(\beta)}$ term is the unit, radial vector from the centre of sphere $\beta$ to its surface. The tensor $\mathbf{G}(\mathbf{x}, \mathbf{y})$ is defined in terms of Stokeslets and potential dipoles from (2.24), both of which rely on the differences in the arguments, $\mathbf{x} - \mathbf{y}$. Thus, noting $|\mathbf{x}^{(\beta)} - \mathbf{x}^{(\gamma)}| \sim O(1/\delta)$ for $\beta \neq \gamma$ is large compared to the unit, radial vector $\mathbf{e}_r$, one can expand the singularity terms in (2.27) as

$$\mathbf{G}(\mathbf{x}^{(\beta)} + \mathbf{e}_r^{(\beta)}, \mathbf{x}^{(\gamma)}) = \mathbf{G}(\mathbf{x}^{(\beta)}, \mathbf{x}^{(\gamma)}) + (\mathbf{e}_r^{(\beta)} \cdot \nabla)\mathbf{G}(\mathbf{x}^{(\beta)}, \mathbf{x}^{(\gamma)}) + ... \tag{2.29}$$

Explicitly, defining the short-hand notation $\mathbf{G}^{(\beta,\gamma)} := \mathbf{G}(\mathbf{x}^{(\beta)}, \mathbf{x}^{(\gamma)})$,

$$\begin{aligned}
\mathbf{G}^{(2,1)} &= \frac{3}{4}\mathbf{S}(\mathbf{x}^{(2)}, \mathbf{x}^{(1)}) - \frac{1}{4}\mathbf{D}(\mathbf{x}^{(2)}, \mathbf{x}^{(1)}), \\
&= \frac{3}{4}\left(\frac{\mathbf{I} + \mathbf{e}_z \otimes \mathbf{e}_z}{|\mathbf{x}^{(2)} - \mathbf{x}^{(1)}|}\right) - \frac{1}{4}\left(\frac{-\mathbf{I} + \mathbf{e}_z \otimes \mathbf{e}_z}{|\mathbf{x}^{(2)} - \mathbf{x}^{(1)}|^3}\right), \\
&\sim \frac{3}{4}(\mathbf{I} + \mathbf{e}_z \otimes \mathbf{e}_z)(\delta - \delta^2\epsilon\xi^R) + O(\delta^3),
\end{aligned} \tag{2.30}$$

where potential-dipolar contributions are $O(\delta^3)$. No further Stokeslet expansion terms are required in (2.30), given the next term is $O(\delta^3\epsilon^2)$ and thus smaller than the potential-dipole contributions. Similarly,

$$\mathbf{G}^{(3,2)} \sim \frac{3}{4}(\mathbf{I} + \mathbf{e}_z \otimes \mathbf{e}_z)(\delta - \delta^2\epsilon\xi^F) + O(\delta^3), \tag{2.31}$$

and

$$\mathbf{G}^{(3,1)} \sim \frac{3}{8}(\mathbf{I} + \mathbf{e}_z \otimes \mathbf{e}_z)\left(\delta - \frac{\delta^2\epsilon[\xi^R + \xi^F]}{2}\right) + O(\delta^3). \tag{2.32}$$

To proceed, the $O(\delta^3)$ terms (and hence the potential dipole) are neglected, given that, *a posteriori*, this level of accuracy is not required for the conclusions in this

chapter. The $O(\delta^2\epsilon)$ terms in (2.30)–(2.32), however, are required. In order to satisfy both conditions, one must impose $\epsilon \gg \delta$; physically, this requires the ratio of a sphere radius to the separation of the spheres be much less than the ratio of the amplitude of rod oscillations to the sphere radius, $a$, which is a design requirement of the swimmer.

Expansions (2.30)–(2.32) highlight how terms of the form $\mathbf{G}^{(\beta,\gamma)}$ for $\beta \neq \gamma$ are comprised of constant, $O(\delta)$ terms, denoted $\delta\boldsymbol{K}^{(\beta,\gamma)}$, and quasi-steady, $O(\delta^2\epsilon)$ terms (given $\xi^R(t)$ and $\xi^F(t)$ are time-dependent), denoted $\delta^2\epsilon\mathbf{H}^{(\beta,\gamma)}$. Also, by neglecting $O(\delta^3)$, the expressions $(\mathbf{e}_r^{(\beta)} \cdot \nabla)\mathbf{G}(\mathbf{x}^{(\beta)}, \mathbf{x}^{(\gamma)})$ from expansion (2.29) only consist of $O(\delta^2)$ terms with no time-dependence, denoted $\delta^2\boldsymbol{\Gamma}^{(\beta,\gamma;\mathbf{e}_r^\beta)}$, where the superscript $\mathbf{e}_r^\beta$ refers to the linear, spatial dependence on $\mathbf{e}_r^{(\beta)}$ from (2.28). Higher-order derivatives in equation (2.29) are $O(\delta^3)$ and hence negligible. Formally,

$$\boldsymbol{K}^{(\beta,\gamma)} := \lim_{\delta\to 0} \frac{\mathbf{G}^{(\beta,\gamma)}}{\delta}, \tag{2.33}$$

$$\mathbf{H}^{(\beta,\gamma)} := \lim_{\delta,\epsilon\to 0} \left( \frac{\mathbf{G}^{(\beta,\gamma)} - \boldsymbol{K}^{(\beta,\gamma)}}{\delta^2\epsilon} \right), \tag{2.34}$$

$$\boldsymbol{\Gamma}^{(\beta,\gamma;\mathbf{e}_r^\beta)} := \lim_{\delta\to 0} \frac{(\mathbf{e}_r^{(\beta)} \cdot \nabla)\mathbf{G}^{(\beta,\gamma)}}{\delta^2}. \tag{2.35}$$

Inserting the expansion from (2.29) back into equation (2.27), the initial postulation for the flow field, $\mathbf{u}_A^{(\alpha)}(\mathbf{x})$, thus satisfies the boundary condition, on sphere $\beta$,

$$\begin{aligned} \mathbf{u}_A^{(\alpha)}(\mathbf{x}^{(\beta)} + \mathbf{e}_r^{(\beta)}) \sim\ & \mathbf{U}^{(\beta)} - \mathbf{U}^{(\alpha)} \\ & + \sum_{\gamma\neq\beta} (\delta\mathbf{K}^{(\beta,\gamma)} + \delta^2\epsilon\mathbf{H}^{(\beta,\gamma)} \\ & + \delta^2\boldsymbol{\Gamma}^{(\beta,\gamma;\mathbf{e}_r^\beta)})\mathbf{U}^{(\gamma)} + O(\delta^3), \end{aligned} \tag{2.36}$$

where $\gamma \neq \beta$, $\gamma \in \{1,2,3\}$. From (2.30)–(2.32),

$$\begin{aligned} &\mathbf{K}^{(1,2)} = \mathbf{K}^{(2,1)} = \mathbf{K}^{(2,3)} = \mathbf{K}^{(3,2)} = \frac{3\mathbf{J}}{4}, \qquad \mathbf{K}^{(1,3)} = \mathbf{K}^{(3,1)} = \frac{3\mathbf{J}}{8}, \\ &\mathbf{H}^{(1,2)} = \mathbf{H}^{(2,1)} = -\frac{3\xi^R\mathbf{J}}{4}, \qquad \mathbf{H}^{(2,3)} = \mathbf{H}^{(3,2)} = -\frac{3\xi^F\mathbf{J}}{4}, \\ &\mathbf{H}^{(1,3)} = \mathbf{H}^{(3,1)} = -\frac{3(\xi^R + \xi^F)\mathbf{J}}{16}, \end{aligned} \tag{2.37}$$

where $\mathbf{J} := (\mathbf{I} + \mathbf{e}_z \otimes \mathbf{e}_z)$. The $\boldsymbol{\Gamma}$ terms are not written out explicitly as they will not be required in the following analysis.

The approximate flow field, $\mathbf{u}_A^{(\alpha)}(\mathbf{x})$, based upon infinitely separated spheres, does not satisfy the exact boundary conditions in (2.22), but instead contains additional $O(\delta)$ terms, illustrated by equation (2.36). In order to correct these boundary conditions so that $\mathbf{u}_A^{(\alpha)}(\mathbf{x})$ is to within $O(\delta^3)$ accuracy, correction variables are introduced, $\delta\mathbf{u}_B^{(\alpha)}(\mathbf{x})$ and $\delta^2\hat{\mathbf{u}}^{(\alpha)}(\mathbf{x})$, with corresponding pressures of the form

$$\begin{aligned}\mathbf{u}^{(\alpha)}(\mathbf{x}) &= \mathbf{u}_A^{(\alpha)}(\mathbf{x}) + \delta\mathbf{u}_B^{(\alpha)}(\mathbf{x}) + \delta^2\hat{\mathbf{u}}^{(\alpha)}(\mathbf{x}),\\ p(\mathbf{x}) &= p_A(\mathbf{x}) + \delta p_B(\mathbf{x}) + \delta^2\hat{p}(\mathbf{x}).\end{aligned} \tag{2.38}$$

The correction variable $\delta\mathbf{u}_B^{(\alpha)}(\mathbf{x})$ satisfies

$$-\nabla p_B^{(\alpha)} + \nabla^2\mathbf{u}_B^{(\alpha)} = \mathbf{0}, \tag{2.39}$$

$$\nabla\cdot\mathbf{u}_B^{(\alpha)} = 0, \tag{2.40}$$

with spatially constant boundary conditions

$$\mathbf{u}_B^{(\alpha)}(\mathbf{x}^{(\beta)} + \mathbf{e}_r^{(\beta)}) = -\sum_{\gamma\neq\beta}(\mathbf{K}^{(\beta,\gamma)} + \delta\epsilon\mathbf{H}^{(\beta,\gamma)})\mathbf{U}^{(\gamma)}, \tag{2.41}$$

while the correction variable $\delta^2\hat{\mathbf{u}}^{(\alpha)}(\mathbf{x})$ satisfies

$$\begin{aligned}-\nabla\hat{p}^{(\alpha)} + \nabla^2\hat{\mathbf{u}}^{(\alpha)} &= \mathbf{0},\\ \nabla\cdot\hat{\mathbf{u}}^{(\alpha)} &= 0,\end{aligned} \tag{2.42}$$

with spatially varying boundary conditions

$$\hat{\mathbf{u}}^{(\alpha)}(\mathbf{x}^{(\beta)} + \mathbf{e}_r^{(\beta)}) = -\sum_{\gamma\neq\beta}\mathbf{\Gamma}^{(\beta,\gamma;\mathbf{e}_r^{\beta})}\mathbf{U}^{(\gamma)}, \tag{2.43}$$

for $\beta = 1, 2$ and 3. Note that these variables can still contain higher-order $\delta$ and $\epsilon$ terms, as indicated in the boundary condition of the $\delta\mathbf{u}_B^{(\alpha)}(\mathbf{x})$ problem, (2.41).

The $\mathbf{u}_B^{(\alpha)}(\mathbf{x})$ problem in (2.40) with spatially constant boundary conditions, (2.41), is of the same form as the original, Newtonian problem in (2.20) with constant, boundary conditions given by (2.22). Thus, a similar, approximate solution, $\mathbf{u}_{BA}^{(\alpha)}$, to the $\mathbf{u}_B^{(\alpha)}(\mathbf{x})$ problem, based again on infinite-domain Stokeslets and potential dipoles, is

$$\mathbf{u}_{BA}^{(\alpha)}(\mathbf{x}) = \sum_{\gamma=1}^{3}\mathbf{G}(\mathbf{x},\mathbf{x}^{(\gamma)})\left[-\sum_{\nu\neq\gamma}(\mathbf{K}^{(\gamma,\nu)} + \delta\epsilon\mathbf{H}^{(\gamma,\nu)})\mathbf{U}^{(\nu)}\right], \tag{2.44}$$

where $\nu$ ranges from 1 to 3. Again, this does not exactly satisfy the $\mathbf{u}_B^{(\alpha)}(\mathbf{x})$ boundary conditions in (2.41), so a further correction term, $\mathbf{u}_C^{(\alpha)}$, is sought,

$$\mathbf{u}_B^{(\alpha)}(\mathbf{x}) = \mathbf{u}_{BA}^{(\alpha)}(\mathbf{x}) + \delta \mathbf{u}_C^{(\alpha)}(\mathbf{x}). \tag{2.45}$$

Equations for $\mathbf{u}_C^{(\alpha)}(\mathbf{x})$ similarly motivate the next *ansatz*, $\mathbf{u}_{CA}^{(\alpha)}(\mathbf{x})$, where $\mathbf{u}_C^{(\alpha)} = \mathbf{u}_{CA}^{(\alpha)} + O(\delta)$, given by

$$\mathbf{u}_{CA}^{(\alpha)}(\mathbf{x}) = \sum_{\gamma=1}^{3} \mathbf{G}(\mathbf{x}, \mathbf{x}^{(\gamma)}) \left[ \sum_{\nu \neq \gamma} \mathbf{K}^{(\gamma,\nu)} \left\{ \sum_{\chi \neq \nu} \mathbf{K}^{(\nu,\chi)} \mathbf{U}^{(\chi)} \right\} \right], \tag{2.46}$$

where $\chi$ ranges from 1 to 3. Piecing the solution so far together gives the Newtonian flow field, up to $O(\delta^3)$ corrections, as

$$\begin{aligned} \mathbf{u}^{(\alpha)}(\mathbf{x}) = -\mathbf{U}^{(\alpha)} + \sum_{\gamma=1}^{3} \mathbf{G}(\mathbf{x}, \mathbf{x}^{(\gamma)}) \Bigg[ \mathbf{U}^{(\gamma)} - \sum_{\nu \neq \gamma} \Bigg\{ & (\delta \mathbf{K}^{(\gamma,\nu)} + \delta^2 \epsilon \mathbf{H}^{(\gamma,\nu)}) \mathbf{U}^{(\nu)} \\ & + \delta^2 \mathbf{K}^{(\gamma,\nu)} \left( \sum_{\chi \neq \nu} \mathbf{K}^{(\nu,\chi)} \mathbf{U}^{(\chi)} \right) \Bigg\} \Bigg] + \delta^2 \hat{\mathbf{u}}^{(\alpha)} + O(\delta^3). \end{aligned} \tag{2.47}$$

It will be shown that calculating $\hat{\mathbf{u}}^{(\alpha)}(\mathbf{x})$ explicitly will not be required, though its evaluation can be reduced to the problem of a sphere in an inertialess, shear flow, which possesses a well-known solution [58, 79]. The asymptotic expression for the flow field around the microswimmer in a Newtonian fluid, (2.47), can now be used to deduce the force acting on a sphere; this force-velocity relationship is needed in order to find the velocity of sphere 2 (and hence net displacement) in terms of the prescribed forces.

### 2.3.2 Newtonian Force Calculations

Recall from equation (2.19), that the dimensionless force acting on sphere $\alpha$, due to the viscous drag and the interactions of the other spheres, depends on a background flow, $\mathbf{u}^{(\alpha)background}$. This is flow due to the motions and interactions of the other spheres with themselves, neglecting the disturbance flow due to the presence of sphere $\alpha$ itself. It also includes the flow arising from fixing the coordinate frame in sphere $\alpha$, namely $-\mathbf{U}^{(\alpha)}$. The surface integral in (2.19) highlights that this background flow need only be evaluated on the surface of sphere $\alpha$, where $\mathbf{x} = \mathbf{x}^{(\alpha)} + \mathbf{e}_r^{(\alpha)}$.

From (2.47), the background flow on the surface of sphere $\alpha$ itself is

$$\begin{aligned}\mathbf{u}^{(\alpha)background}(\mathbf{x}^{(\alpha)}+\mathbf{e}_r^{(\alpha)}) = -\mathbf{U}^{(\alpha)} + \sum_{\gamma\neq\alpha}\mathbf{G}(\mathbf{x}^{(\alpha)}+\mathbf{e}_r^{(\alpha)},\mathbf{x}^{(\gamma)})\Big[\mathbf{U}^{(\gamma)} \\ -(\delta\mathbf{K}^{(\gamma,\sigma)}+\delta^2\epsilon\mathbf{H}^{(\gamma,\sigma)})\mathbf{U}^{(\sigma)}+\delta^2\mathbf{K}^{(\gamma,\sigma)}\mathbf{K}^{(\sigma,\gamma)}\mathbf{U}^{(\gamma)}\Big] \\ +\delta^2\hat{\mathbf{u}}^{(\alpha)background}(\mathbf{x}^{(\alpha)}+\mathbf{e}_r^{(\alpha)})+O(\delta^3),\end{aligned} \tag{2.48}$$

where, for each $\gamma \in \{1,2,3\}$, $\sigma$ labels the remaining sphere such that $\sigma \neq \gamma$ and $\sigma \neq \alpha$. The $\hat{\mathbf{u}}^{(\alpha)background}$ term on the boundary of sphere $\alpha$ is deducible from the $\hat{\mathbf{u}}^{(\alpha)}(\mathbf{x})$ boundary condition in (2.43). However, as the background flow requires no disturbance flows due to the presence of sphere $\alpha$ itself,

$$\hat{\mathbf{u}}^{(\alpha)background}(\mathbf{x}^{(\alpha)}+\mathbf{e}_r^{(\alpha)}) \sim \mathbf{0}+O(\delta^3). \tag{2.49}$$

The tensor $\mathbf{G}(\mathbf{x}^{(\alpha)}+\mathbf{e}_r^{(\alpha)},\mathbf{x}^{(k)})$ in (2.48) is expanded, using the ideas of equation (2.29), giving

$$\begin{aligned}\mathbf{u}^{(\alpha)background}(\mathbf{x}^{(\alpha)}+\mathbf{e}_r^{(\alpha)}) = -\mathbf{U}^{(\alpha)} + \sum_{\gamma\neq\alpha}\Big[\delta\mathbf{K}^{(\alpha,\gamma)}\left(\mathbf{U}^{(\gamma)}-\delta\mathbf{K}^{(\gamma,\sigma)}\mathbf{U}^{(\sigma)}\right) \\ +\delta^2\epsilon\mathbf{H}^{(\alpha,\gamma)}\mathbf{U}^{(k)}\Big] \\ +\delta^2\sum_{\gamma\neq\alpha}\mathbf{\Gamma}^{(\alpha,\gamma;\mathbf{e}_r^{\alpha})}\mathbf{U}^{(\gamma)}+O(\delta^3).\end{aligned} \tag{2.50}$$

The $\mathbf{\Gamma}^{(\alpha,\gamma;\mathbf{e}_r^{\alpha})}$ term integrates to zero around the surface of sphere $\alpha$ by radial symmetry, thus the force on sphere $\alpha$, neglecting $O(\delta^3)$ and using (2.19), is

$$\mathbf{f}^{(\alpha)} = -6\pi\mathbf{U}^{(\alpha)} + 6\pi\sum_{\gamma\neq\alpha}\left[\delta\mathbf{K}^{(\alpha,\gamma)}\left(\mathbf{U}^{(\gamma)}-\delta\mathbf{K}^{(\gamma,\sigma)}\mathbf{U}^{(\sigma)}\right)+\delta^2\epsilon\mathbf{H}^{(\alpha,\gamma)}\mathbf{U}^{(\gamma)}\right]. \tag{2.51}$$

Equation (2.51) is the force-velocity relationship for a Newtonian fluid, relating the force on sphere $\alpha$ to the sphere velocities. It is subsequently used to determine the net displacement over one beat cycle via the calculation of $\mathbf{U}^{(2)}$. Whilst existing work [4] takes the leading-order force-velocity relationship, namely Stokes drag in which $\mathbf{f}^{(\alpha)} = -6\pi\mathbf{U}^{(\alpha)}$ [89], the $O(\delta)$, $O(\delta^2)$ and $O(\varepsilon\delta^2)$ interaction terms are neglected. These terms are all larger in magnitude than the neglected $O(\delta^3)$, potential-dipolar contributions in (2.30)–(2.32). The analogue of the force-velocity relationship, (2.51), for a viscoelastic fluid is derived in Section 2.4.5.

### 2.3.3 Net Swimmer Displacement in Newtonian Fluid

By inserting the Newtonian force-velocity relationship, (2.51), into the force balance from (2.1), namely

$$\sum_{\gamma=1}^{3} \mathbf{f}^{(\gamma)} = \mathbf{0}, \tag{2.52}$$

and rewriting $\mathbf{U}^{(1)}$ and $\mathbf{U}^{(3)}$ in terms of $\mathbf{U}^{(2)}$ via

$$\begin{aligned} \mathbf{U}^{(1)} &= \mathbf{U}^{(2)} - \dot{\xi}^R \mathbf{e}_z, \\ \mathbf{U}^{(3)} &= \mathbf{U}^{(2)} + \dot{\xi}^F \mathbf{e}_z, \end{aligned} \tag{2.53}$$

an equation for $\mathbf{U}^{(2)}$ is obtained. As $\mathbf{U}^{(2)} = U^{(2)}\mathbf{e}_z$, this equation is scalar and of the form,

$$QU^{(2)} = B, \tag{2.54}$$

where, after some algebra,

$$Q = 3\left(1 - \frac{5\delta}{2} + 3\delta^2 + \frac{5\delta^2\epsilon}{4}(\xi^R + \xi^F)\right), \tag{2.55}$$

$$\begin{aligned} B = &\left(1 - \frac{9\delta}{4} + \frac{27\delta^2}{8}\right)(\dot{\xi^R} - \dot{\xi^F}) \\ &+ \frac{3\delta^2\epsilon}{8}\left(\xi^F\dot{\xi^R} - \xi^R\dot{\xi^F} + 5[\xi^R\dot{\xi^R} - \xi^F\dot{\xi^F}]\right). \end{aligned} \tag{2.56}$$

Motivated by (2.56), perturbation expansions of the following form are used:

$$\begin{aligned} U^{(2)} &= U^{(2)}_{0,0} + \delta U^{(2)}_{1,0} + \delta^2 U^{(2)}_{2,0} + \delta^2\epsilon U^{(2)}_{2,1} + O(\delta^3), \\ \xi^{R,F} &= \xi^{R,F}_{0,0} + \delta\xi^{R,F}_{1,0} + \delta^2\xi^{R,F}_{2,0} + \delta^2\epsilon\xi^{R,F}_{2,1} + O(\delta^3), \end{aligned} \tag{2.57}$$

where terms involving $\epsilon$ have been separated for emphasis, given they are the only terms that end up contributing to the final expression of net displacement; see equations (2.62) and (2.73). The procedure can, however, be done without this separation.

At each order,

$$
\begin{aligned}
O(1): \quad & 3U^{(2)}_{0,0} = \dot{\xi^R}_{0,0} - \dot{\xi^F}_{0,0}, \\
O(\delta): \quad & 3U^{(2)}_{1,0} - \frac{15}{2}U^{(2)}_{0,0} = \dot{\xi^R}_{1,0} - \dot{\xi^F}_{1,0} - \frac{9}{4}(\dot{\xi^R}_{0,0} - \dot{\xi^F}_{0,0}), \\
O(\delta^2): \quad & 3U^{(2)}_{2,0} - \frac{15}{2}U^{(2)}_{1,0} + 9U^{(2)}_{0,0} = \dot{\xi^R}_{2,0} - \dot{\xi^F}_{2,0} - \frac{9}{4}(\dot{\xi^R}_{1,0} - \dot{\xi^F}_{1,0}) + \\
& \qquad \frac{27}{8}(\dot{\xi^R}_{0,0} - \dot{\xi^F}_{0,0}), \\
O(\delta^2\epsilon): \quad & 3U^{(2)}_{2,1} + \frac{15}{4}(\xi^R_{0,0} + \xi^F_{0,0})U^{(2)}_{0,0} = \dot{\xi^R}_{2,1} - \dot{\xi^F}_{2,1} + \left( \left[ \frac{3\xi^F_{0,0}}{8} + \frac{15\xi^R_{0,0}}{8} \right] \dot{\xi^R}_{0,0} \right. \\
& \qquad \left. - \left[ \frac{15\xi^F_{0,0}}{8} + \frac{3\xi^R_{0,0}}{8} \right] \dot{\xi^F}_{0,0} \right), \qquad (2.58)
\end{aligned}
$$

and thus

$$
\begin{aligned}
U^{(2)}_{0,0} &= \frac{1}{3}(\dot{\xi^R}_{0,0} - \dot{\xi^F}_{0,0}), \\
U^{(2)}_{1,0} &= \frac{1}{3}(\dot{\xi^R}_{1,0} - \dot{\xi^F}_{1,0}) + \frac{1}{12}(\dot{\xi^R}_{0,0} - \dot{\xi^F}_{0,0}), \\
U^{(2)}_{2,0} &= \frac{1}{3}(\dot{\xi^R}_{2,0} - \dot{\xi^F}_{2,0}) + \frac{1}{12}(\dot{\xi^R}_{1,0} - \dot{\xi^F}_{1,0}) + \frac{1}{3}(\dot{\xi^R}_{0,0} - \dot{\xi^F}_{0,0}), \\
U^{(2)}_{2,1} &= \frac{1}{3}(\dot{\xi^R}_{2,1} - \dot{\xi^F}_{2,1}) + \frac{5}{24}(\xi^R_{0,0}\dot{\xi^R}_{0,0} - \xi^F_{0,0}\dot{\xi^F}_{0,0}) + \frac{7}{24}(\xi^R_{0,0}\dot{\xi^F}_{0,0} - \xi^F_{0,0}\dot{\xi^R}_{0,0}). \qquad (2.59)
\end{aligned}
$$

Hence, with $O(\delta^3)$ corrections, it is valid to write

$$
\begin{aligned}
U^{(2)} \sim \frac{1}{3}(\dot{\xi^R} - \dot{\xi^F}) \left\{ 1 + \frac{\delta}{4} + \delta^2 \right\} + \delta^2\epsilon \left[ \frac{5}{24}(\xi^R\dot{\xi^R} - \xi^F\dot{\xi^F}) \right. \\
\left. + \frac{7}{24}(\xi^R\dot{\xi^F} - \xi^F\dot{\xi^R}) \right] + O(\delta^3). \qquad (2.60)
\end{aligned}
$$

This is in agreement with existing work [4, 32], if one were to expand in $a/D$ in their notation and set $\epsilon = 1$ in the above; note that Earl *et al.* [32] present corrected displacement expressions to the original work by Najafi and Golestanian [70]. Thus, the inclusion of the interaction terms between the spheres in this chapter, while asymptotically necessary, *a posteriori* does not affect the net velocity of the microswimmer.

The net displacement of the swimmer over one beat cycle in a Newtonian fluid, $\Delta$, is given by

$$
\Delta = \int_0^{2\pi} U^{(2)} \, \mathrm{d}t, \qquad (2.61)
$$

where $2\pi$ is the dimensionless period of the beat. The rod displacements, $\xi^R(t)$ and $\xi^F(t)$, are $2\pi$-periodic, induced by the prescribed, internal forces. All linear terms larger than $O(\delta^2\epsilon)$ in (2.60) integrate to zero in (2.61) when calculating $\Delta$. This leaves

$$\Delta \sim \frac{7\delta^2\epsilon}{24}\int_0^{2\pi}(\xi^R\dot{\xi^F} - \xi^F\dot{\xi^R})\,\mathrm{d}t + O(\delta^3), \tag{2.62}$$

thus justifying the need to retain $O(\delta^2\epsilon)$ terms. Re-dimensionalising equation (2.62), assuming dimensional variables, gives

$$\Delta = \frac{7a}{24D^2}\int_0^{2\pi/\omega}(\xi^R\dot{\xi^F} - \xi^F\dot{\xi^R})\,\mathrm{d}t. \tag{2.63}$$

For an intuitive understanding of equation (2.62), in a reference frame centred in sphere $\alpha$, the surface force acting on sphere $\alpha$, $\mathbf{f}^{(\alpha)}$, must be due to any contributions of a background flow on the surface of sphere $\alpha$. This background flow includes the term $-\mathbf{U}^{(\alpha)}(t)$ due to the reference frame, along with all the flows produced by the interactions of the other spheres with themselves, i.e. spheres $\gamma \in \{1,2,3\}$ where $\gamma \neq \alpha$. Approximating the other spheres as a combination of a Stokeslet and potential dipole, $\mathbf{G}(\mathbf{x},\mathbf{y})$, the total background flow on the surface of sphere $\alpha$ is hence

$$\begin{aligned}
&\mathbf{u}^{(\alpha)background}(\mathbf{x}^{(\alpha)}(t) + \mathbf{e}_r^{(\alpha)}) \\
&\approx -\mathbf{U}^{(\alpha)}(t) + \sum_{\gamma\neq\alpha}\mathbf{G}(\mathbf{x}^{(\alpha)}(t) + \mathbf{e}_r^{(\alpha)}, \mathbf{x}^{(\gamma)}(t))\mathbf{U}^{(\gamma)}(t), \\
&\approx -\mathbf{U}^{(\alpha)}(t) + \sum_{\gamma\neq\alpha}\mathbf{S}(\mathbf{x}^{(\alpha)}(t), \mathbf{x}^{(\gamma)}(t))\mathbf{U}^{(\gamma)}(t),
\end{aligned} \tag{2.64}$$

where the Stokeslet, $\mathbf{S}(\mathbf{x},\mathbf{y})$, approximates $\mathbf{G}(\mathbf{x},\mathbf{y})$, given the potential-dipolar contributions are of higher order. Using equation (2.15),

$$\begin{aligned}
\mathbf{S}(\mathbf{x}^{(\alpha)}(t),&\mathbf{x}^{(\gamma)}(t)) \sim O\left(\frac{1}{|\mathbf{x}^{(\gamma)} - \mathbf{x}^{(\alpha)}|}\right), \\
&\sim \delta A_1 + \delta^2 A_2 + \delta^2\epsilon B[\xi^R(t), \xi^F(t)],
\end{aligned} \tag{2.65}$$

for constants $A_1$ and $A_2$ and a function, $B[\xi^R, \xi^F]$, linear in $\xi^R(t)$ and $\xi^F(t)$. *A posteriori* motivated by (2.65), the neglected dipoles in (2.64) were $O(\delta^3)$, while any terms which were not linear in $\mathbf{e}_r^{(\alpha)}$ from the Taylor series are also $O(\delta^3)$. Thus, integrating (2.64) around sphere $\alpha$, as is necessary to find $\mathbf{f}^{(\alpha)}$, just adds a constant so that $\mathbf{f}^{(\alpha)} \propto \mathbf{u}^{(\alpha)background}(\mathbf{x}^{(\alpha)}(t))$ to $O(\delta^3)$ corrections. Knowing the sum of all forces is zero and that $\mathbf{U}^{(\gamma)}(t)$ relates to $\mathbf{U}^{(\alpha)}(t)$ via $\dot{\xi}^R(t)$ and $\dot{\xi}^F(t)$ from the swimmer geometry, an expression for $\mathbf{U}^{(\alpha)}(t)$ is obtainable from (2.64). Moreover, this expression

for $\mathbf{U}^{(\alpha)}(t)$ can be written asymptotically in the same form as the expanded Stokeslet from (2.65), albeit with terms multiplied by linear combinations of $\dot{\xi}^R(t)$ and $\dot{\xi}^F(t)$. Time-averaging over one beat cycle gives non-zero contributions at $O(\epsilon\delta^2)$, as these terms depend nonlinearly on $B(\xi^R, \xi^F)$ multiplied by $\xi(t)$ and $\dot{\xi}(t)$.

Further, the resulting quadratic combination takes the form:

$$B_1\dot{\xi}^R(t)\xi^R(t)+B_2\dot{\xi}^F(t)\xi^F(t) + B_3\dot{\xi}^F(t)\xi^R(t) + B_4\dot{\xi}^R(t)\xi^F(t). \tag{2.66}$$

Clearly the first two terms integrate to zero when time averaged over a period, and, by the anti-symmetry of the map $(\xi^R, \xi^F) \to (\xi^F, \xi^R)$ implying $\Delta \to -\Delta$, we must have that $B_4 = -B_3$. This is in agreement with equation (2.62) and gives its form to within a constant factor.

The net displacement, $\Delta$, is currently written in terms of the rod oscillations, $\xi^R(t)$ and $\xi^F(t)$. Existing work [4] proceeds to prescribe the rod oscillations as periodic functions in time, thus calculating the net displacement via (2.62). However, the model in the current context considers a swimmer with prescribed forces (termed the *mobility* problem), not prescribed rod displacements (termed the *kinematic* problem), as discussed in Section 2.1. Prescribed forces especially highlight the influence of viscoelasticity on swimming progress and efficiency for a swimmer [36]. Thus, to write equation (2.62) in terms of the forces on sphere 1 and 3, $\mathbf{f}^{(1)} = f^{(1)}\mathbf{e}_z$ and $\mathbf{f}^{(3)} = f^{(3)}\mathbf{e}_z$, $\mathbf{f}^{(2)}$ being deduced from (2.52), a further relationship between $(f^{(1)}, f^{(3)})$ and $(\dot{\xi}^R, \dot{\xi}^F)$ is required. Given (2.60) relates $U^{(2)}(t)$ to $\dot{\xi}^R(t)$ and $\dot{\xi}^F(t)$, this is inserted into (2.53) to find $U^{(1)}(t)$ and $U^{(3)}(t)$ also in terms of $\dot{\xi}^R(t)$ and $\dot{\xi}^F(t)$. These expressions can then be inserted into (2.51) to obtain

$$\begin{pmatrix} f^{(1)} \\ f^{(3)} \end{pmatrix} = \pi\mathbf{M}\begin{pmatrix} \dot{\xi}^R \\ \dot{\xi}^F \end{pmatrix}, \tag{2.67}$$

where

$$\begin{aligned}\mathbf{M} = &\begin{pmatrix} 4 & 2 \\ -2 & -4 \end{pmatrix} + \delta\begin{pmatrix} 4 & \frac{1}{2} \\ -\frac{1}{2} & -4 \end{pmatrix} + \delta^2\begin{pmatrix} -\frac{61}{8} & -\frac{47}{8} \\ \frac{47}{8} & \frac{61}{8} \end{pmatrix} \\ &+ \delta^2\epsilon\begin{pmatrix} \xi^F - 5\xi^R & -\frac{\xi^F+\xi^R}{4} \\ \frac{\xi^F+\xi^R}{4} & 5\xi^F - \xi^R \end{pmatrix} + O(\delta^3).\end{aligned} \tag{2.68}$$

The inverse, $\mathbf{N} := \mathbf{M}^{-1}$, when written in the same form,

$$\mathbf{N} = \mathbf{N}_{0,0} + \delta\mathbf{N}_{1,0} + \delta^2\mathbf{N}_{2,0} + \delta^2\epsilon\mathbf{N}_{2,1} + O(\delta^3), \tag{2.69}$$

and using $\mathbf{NM} = \mathbf{I}$ for all $\delta$ and $\epsilon$, gives

$$\begin{aligned}
\mathbf{N}_{0,0} &= \mathbf{M}_{0,0}^{-1}, \\
\mathbf{N}_{1,0} &= -\mathbf{M}_{0,0}^{-1}\mathbf{M}_{1,0}\mathbf{M}_{0,0}^{-1}, \\
\mathbf{N}_{2,0} &= \mathbf{M}_{0,0}^{-1}\mathbf{M}_{1,0}\mathbf{M}_{0,0}^{-1}\mathbf{M}_{1,0}\mathbf{M}_{0,0}^{-1} - \mathbf{M}_{0,0}^{-1}\mathbf{M}_{2,0}\mathbf{M}_{0,0}^{-1}, \\
\mathbf{N}_{2,1} &= -\mathbf{M}_{0,0}^{-1}\mathbf{M}_{2,1}\mathbf{M}_{0,0}^{-1}.
\end{aligned} \tag{2.70}$$

Thus, asymptotically,

$$\begin{pmatrix} \dot{\xi^R} \\ \dot{\xi^F} \end{pmatrix} = \frac{1}{\pi}\mathbf{N}\begin{pmatrix} f^{(1)} \\ f^{(3)} \end{pmatrix}, \tag{2.71}$$

where

$$\begin{aligned}
\mathbf{N} = &\begin{pmatrix} \frac{1}{3} & \frac{1}{6} \\ -\frac{1}{6} & -\frac{1}{3} \end{pmatrix} + \delta\begin{pmatrix} -\frac{4}{9} & -\frac{1}{72} \\ \frac{1}{72} & \frac{4}{9} \end{pmatrix} + \delta^2\begin{pmatrix} \frac{311}{216} & \frac{71}{432} \\ -\frac{71}{432} & -\frac{311}{216} \end{pmatrix} \\
&+ \delta^2\epsilon\begin{pmatrix} \frac{5\xi^R-\xi^F}{9} & \frac{\xi^F+\xi^R}{144} \\ -\frac{(\xi^F+\xi^R)}{144} & \frac{\xi^R-5\xi^F}{9} \end{pmatrix} + O(\delta^3).
\end{aligned} \tag{2.72}$$

Note how the inverse is a constant matrix up to, and including, $O(\delta^2)$; the $\xi^F(t)$ and $\xi^R(t)$ terms do not appear in the inverse matrix until $O(\delta^2\epsilon)$. Upon using (2.71) and (2.72) to rewrite $\mathbf{U}^{(2)}$ from (2.60) in terms of forces, (2.61) becomes, assuming dimensionless $2\pi$-periodic forcing,

$$\Delta \sim \frac{29\delta^2\epsilon}{432\pi^2}\int_0^{2\pi}(g^{(3)}\dot{g}^{(1)} - g^{(1)}\dot{g}^{(3)})\,\mathrm{d}t + O(\delta^3). \tag{2.73}$$

Here, $\dot{g}^{(\alpha)} := f^{(\alpha)}$ so that

$$g^{(\alpha)}(t) = \int^t \dot{g}^{(\alpha)}(\bar{t})\,\mathrm{d}\bar{t}, \tag{2.74}$$

allowing the net displacement over one beat cycle to be written solely in terms of the prescribed forces on the spheres.

In order to investigate the effects of nonlinear, viscoelastic rheology on the net, swimmer displacement when compared to that of a Newtonian environment, the viscoelastic analogue to equation (2.73) is needed. While the Newtonian calculations exploit the asymptotically small parameter $\delta$ up to $O(\delta^3)$ corrections, the viscoelastic equations are first expanded asymptotically using the small parameter $\epsilon$, then examined in terms of $\delta$, again neglecting $O(\delta^3)$ contributions.

## 2.4 The Viscoelastic Fluid Case

### 2.4.1 The Force-Velocity Relationship at Leading-Order

The work is now extended to investigate the full, dimensionless, viscoelastic model from Section 2.2.3, in a frame fixed in sphere $\alpha$. The equations are rewritten here for convenience:

$$\begin{aligned}
\nabla \cdot \mathbf{u}^{(\alpha)} &= 0, \\
-\nabla p^{(\alpha)} + \nabla \cdot \boldsymbol{\tau}^{(\alpha)} &= \mathbf{0}, \\
\left(1 + \Lambda \frac{\partial}{\partial t}\right) \boldsymbol{\tau}^{(\alpha)} &= \left(1 + \Gamma \frac{\partial}{\partial t}\right) \boldsymbol{\mathcal{E}}^{(\alpha)} \\
&\quad - \epsilon \Big[ \mathbf{u}^{(\alpha)} \cdot \nabla [\Lambda \boldsymbol{\tau}^{(\alpha)} - \Gamma \boldsymbol{\mathcal{E}}^{(\alpha)}] \\
&\quad - \{ (\nabla \mathbf{u}^{(\alpha)})^T \cdot [\Lambda \boldsymbol{\tau}^{(\alpha)} - \Gamma \boldsymbol{\mathcal{E}}^{(\alpha)}] \\
&\quad + [\Lambda \boldsymbol{\tau}^{(\alpha)} - \Gamma \boldsymbol{\mathcal{E}}^{(\alpha)}] \cdot \nabla \mathbf{u}^{(\alpha)} \} \\
&\quad - \mathbf{U}^{(\alpha)} \cdot \nabla [\Lambda \boldsymbol{\tau}^{(\alpha)} - \Gamma \boldsymbol{\mathcal{E}}^{(\alpha)}] \Big], \\
\boldsymbol{\mathcal{E}}^{(\alpha)} &:= \left(\nabla \mathbf{u}^{(\alpha)}\right)^T + \nabla \mathbf{u}^{(\alpha)},
\end{aligned} \tag{2.75}$$

with

$$\begin{aligned}
\mathbf{U}^{(2)} - \mathbf{U}^{(1)} &= \dot{\xi}^R \mathbf{e}_z, \\
\mathbf{U}^{(3)} - \mathbf{U}^{(2)} &= \dot{\xi}^F \mathbf{e}_z, \\
\frac{1}{|\mathbf{x}^{(2)} - \mathbf{x}^{(1)}|} &= \delta (1 + \delta \epsilon \xi^R)^{-1}, \\
\frac{1}{|\mathbf{x}^{(3)} - \mathbf{x}^{(2)}|} &= \delta (1 + \delta \epsilon \xi^F)^{-1},
\end{aligned} \tag{2.76}$$

and boundary conditions

$$\mathbf{u}^{(\alpha)} = \mathbf{U}^{(\beta)} - \mathbf{U}^{(\alpha)} \text{ on } |\mathbf{x} - \mathbf{x}^{(\beta)}| = 1, \qquad \beta \in \{1,2,3\}, \tag{2.77}$$

where $\mathbf{x}^{(\beta)} = \mathbf{0}$ when $\beta = \alpha$. The obvious difference between these equations, when compared with those of the Newtonian problem, is the nonlinear, constitutive, Oldroyd-B law used to describe the deviatoric-stress tensor. In particular, recalling the dimensionless, Deborah numbers, $\Lambda$ and $\Gamma$, are assumed to be $O(1)$, the partial time derivatives in (2.75) are $O(1)$, while the nonlinear terms are $O(\epsilon)$.

All dimensionless variables are expanded in powers of $\epsilon$, such that a variable $\mathbf{q}^{(\alpha)}$, say, has the expansion

$$\mathbf{q}^{(\alpha)} \sim \mathbf{q}_0^{(\alpha)} + \epsilon \mathbf{q}_1^{(\alpha)} + O(\epsilon^2), \tag{2.78}$$

where $\mathbf{q}_0^{(\alpha)}$ and $\mathbf{q}_1^{(\alpha)}$ can depend on $\delta$. As the Newtonian calculations are needed in the analysis here, the $\delta$-dependence of each $\epsilon$-expanded variable is up to $O(\delta^2)$, neglecting $O(\delta^3)$ following the discussion after equation (2.32).

The leading-order problem in $\epsilon$ is given by

$$\begin{aligned}
\nabla \cdot \mathbf{u}_0^{(\alpha)} &= 0, \\
-\nabla p_0^{(\alpha)} + \nabla \cdot \boldsymbol{\tau}_0^{(\alpha)} &= \mathbf{0}, \\
\mathcal{L}[\boldsymbol{\tau}_0^{(\alpha)}] &= \boldsymbol{\mathcal{E}}_0^{(\alpha)} \\
\boldsymbol{\mathcal{E}}_0^{(\alpha)} &= (\nabla \mathbf{u}_0^{(\alpha)})^T + \nabla \mathbf{u}_0^{(\alpha)}, \\
\mathbf{U}_0^{(2)} - \mathbf{U}_0^{(1)} &= \dot{\xi}_0^R \mathbf{e}_z, \\
\mathbf{U}_0^{(3)} - \mathbf{U}_0^{(2)} &= \dot{\xi}_0^F \mathbf{e}_z, \\
\left( \frac{1}{|\mathbf{x}^{(2)} - \mathbf{x}^{(1)}|} \right)_0 &= \delta, \\
\left( \frac{1}{|\mathbf{x}^{(3)} - \mathbf{x}^{(2)}|} \right)_0 &= \delta, \\
\mathbf{u}_0^{(\alpha)} = \mathbf{U}_0^{(\beta)} - \mathbf{U}_0^{(\alpha)} \text{ on } |\mathbf{x} - \mathbf{x}^{(\beta)}| &= 1, \qquad \beta \in \{1,2,3\},
\end{aligned} \tag{2.79}$$

where the temporal operator $\mathcal{L}$ is defined as

$$\mathcal{L} := \left(1 + \Gamma \frac{\partial}{\partial t}\right)^{-1} \left(1 + \Lambda \frac{\partial}{\partial t}\right). \tag{2.80}$$

Care is required to uniquely define the inverse operator for the definition (2.80), as it is contingent on the initial conditions. This can be highlighted by inverting $(1 + \Lambda\partial/\partial t)f(t) = g(t)$ for arbitrary, time-dependent functions $f(t)$ and $g(t)$, introducing a non-unique term involving $f(t*)$, where $t*$ is the initial time of reference. Only solutions where transient behaviour, arising from initial conditions in time, has decayed and the swimmer has settled into periodic beating are considered; this ensures uniqueness of the operator, thus the solutions are perfectly periodic. Other than the temporal operator, $\mathcal{L}$, acting on the deviatoric-stress tensor, the viscoelastic equations at leading order are essentially those of the Newtonian fluid. This is highlighted by introducing the change of variables:

$$\mathbf{w}_0^{(\alpha)} := \mathbf{u}_0^{(\alpha)}, \quad q_0^{(\alpha)} := \mathcal{L}[p_0^{(\alpha)}], \quad \boldsymbol{\tau}_{w_0}^{(\alpha)} = \left(\nabla \mathbf{w}_0^{(\alpha)}\right)^T + \nabla \mathbf{w}_0^{(\alpha)} := \mathcal{L}[\boldsymbol{\tau}_0^{(\alpha)}]. \tag{2.81}$$

This casts the leading-order problem, (2.79), exactly into the previously calculated, Newtonian case. Hence $\mathbf{w}_0^{(\alpha)}$ is the Newtonian, flow-field solution given by equation

(2.47), albeit with $\epsilon = 0$ and the sphere velocities, $\mathbf{U}^{(\gamma)}$, taken at leading order, so that

$$\mathbf{w}_0^{(\alpha)}(\mathbf{x}) \sim -\mathbf{U}_0^{(\alpha)} + \sum_{\gamma=1}^{3} \mathbf{G}(\mathbf{x}, \mathbf{x}^{(\gamma)}) \Big[ \mathbf{U}_0^{(\gamma)} - \sum_{\nu \neq \gamma} \Big\{ \delta \mathbf{K}^{(\gamma,\nu)} \mathbf{U}_0^{(\nu)} \Big\} \Big] + \delta^2 \hat{\mathbf{u}}^{(\alpha)}|_{\epsilon=0} + O(\delta^3). \tag{2.82}$$

This $\mathbf{w}_0^{(\alpha)}$ problem has an associated force on sphere $\alpha$, denoted $\mathbf{f}_{w_0}^{(\alpha)}(t)$, given by the Newtonian force calculated earlier, (2.51), again with the added change of setting $\epsilon = 0$ and velocity $\mathbf{U}^{(\alpha)}$ taken at leading order. Thus,

$$\mathbf{f}_{w_0}^{(\alpha)} \sim -6\pi \mathbf{U}_0^{(\alpha)} + 6\pi \sum_{k \neq \alpha} \Big[ \delta \mathbf{K}^{(\alpha,k)} \Big( \mathbf{U}_0^{(k)} - \delta \mathbf{K}^{(k,\sigma)} \mathbf{U}_0^{(\sigma)} \Big) \Big] + O(\delta^3). \tag{2.83}$$

The force in (2.83), $\mathbf{f}_{w_0}^{(\alpha)}(t)$, can be used to calculate the force of the leading-order, viscoelastic problem in (2.79), denoted $\mathbf{f}_0^{(\alpha)}(t)$. They are related by writing the force as a surface integral in terms of the stress tensor, (1.17), and using the new variables in (2.81), so that

$$\begin{aligned} \mathcal{L}[\mathbf{f}_0^{(\alpha)}(t)] &= \mathcal{L} \left[ \iint_{|\mathbf{x}|=1} \Big( -p_0^{(\alpha)} \mathbf{I} + \boldsymbol{\tau}_0^{(\alpha)} \Big) \cdot \mathbf{dS} \right], \\ &= \iint_{|\mathbf{x}|=1} \Big( -\mathcal{L}[p_0^{(\alpha)}] \mathbf{I} + \mathcal{L}[\boldsymbol{\tau}_0^{(\alpha)}] \Big) \cdot \mathbf{dS}, \\ &= \iint_{|\mathbf{x}|=1} \Big( -q_0^{(\alpha)} \mathbf{I} + \boldsymbol{\tau}_{w_0}^{(\alpha)} \Big) \cdot \mathbf{dS}, \\ &= \mathbf{f}_{w_0}^{(\alpha)}(t), \end{aligned} \tag{2.84}$$

with $\mathbf{f}_{w_0}^{(\alpha)}(t)$ given by (2.83). Note that the surface integral is evaluated around a time-independent surface, given the coordinate frame is fixed about the centre of sphere $\alpha$; thus the spatial integral commutes with the temporal operator, $\mathcal{L}$.

Using (2.83) and (2.84), the force-velocity relationship at leading order in the viscoelastic problem satisfies

$$\mathcal{L}[\mathbf{f}_0^{(\alpha)}(t)] \sim -6\pi \mathbf{U}_0^{(\alpha)} + 6\pi \sum_{k \neq \alpha} \Big[ \delta \mathbf{K}^{(\alpha,k)} \Big( \mathbf{U}_0^{(k)} - \delta \mathbf{K}^{(k,\sigma)} \mathbf{U}_0^{(\sigma)} \Big) \Big] + O(\delta^3). \tag{2.85}$$

### 2.4.2 The Force-Velocity Relationship at $O(\epsilon)$

The $O(\epsilon)$ equations are given by

$$\begin{aligned}
\nabla \cdot \mathbf{u}_1^{(\alpha)} &= 0, \\
-\nabla p_1^{(\alpha)} + \nabla \cdot \boldsymbol{\tau}_1^{(\alpha)} &= \mathbf{0}, \\
\mathcal{L}[\boldsymbol{\tau}_1^{(\alpha)}] + \boldsymbol{\eta}^{(\alpha)} &= \boldsymbol{\mathcal{E}}_1^{(\alpha)}, \\
\boldsymbol{\mathcal{E}}_1^{(\alpha)} &= (\nabla \mathbf{u}_1^{(\alpha)})^T + \nabla \mathbf{u}_1^{(\alpha)}, \\
\mathbf{U}_1^{(2)} - \mathbf{U}_1^{(1)} &= \dot{\xi}_1^R \mathbf{e}_z, \\
\mathbf{U}_1^{(3)} - \mathbf{U}_1^{(2)} &= \dot{\xi}_1^F \mathbf{e}_z, \\
\left( \frac{1}{|\mathbf{x}^{(2)} - \mathbf{x}^{(1)}|} \right)_1 &= \delta^2 \xi_0^R, \\
\left( \frac{1}{|\mathbf{x}^{(3)} - \mathbf{x}^{(2)}|} \right)_1 &= -\delta^2 \xi_0^F, \\
\mathbf{u}_1^{(\alpha)} = \mathbf{U}_1^{(\beta)} - \mathbf{U}_1^{(\alpha)} \text{ on } |\mathbf{x} - \mathbf{x}^{(\beta)}| &= 1, \qquad \beta = 1,2,3,
\end{aligned} \tag{2.86}$$

where

$$\begin{aligned}
\boldsymbol{\eta}^{(\alpha)} := \left( 1 + \Gamma \frac{\partial}{\partial t} \right)^{-1} \Big\{ & \mathbf{u}_0^{(\alpha)} \cdot \nabla [\Lambda \boldsymbol{\tau}_0^{(\alpha)} - \Gamma \boldsymbol{\mathcal{E}}_0^{(\alpha)}] \\
& - \{ (\nabla \mathbf{u}_0^{(\alpha)})^T \cdot [\Lambda \boldsymbol{\tau}_0^{(\alpha)} - \Gamma \boldsymbol{\mathcal{E}}_0^{(\alpha)}] \\
& + [\Lambda \boldsymbol{\tau}_0^{(\alpha)} - \Gamma \boldsymbol{\mathcal{E}}_0^{(\alpha)}] \cdot \nabla \mathbf{u}_0^{(\alpha)} \} \\
& - \mathbf{U}_0^{(\alpha)} \cdot \nabla [\Lambda \boldsymbol{\tau}_0^{(\alpha)} - \Gamma \boldsymbol{\mathcal{E}}_0^{(\alpha)}] \Big\}.
\end{aligned} \tag{2.87}$$

Here, $\boldsymbol{\eta}^{(\alpha)}$ is a known function as, from (2.79), both $\boldsymbol{\tau}_0^{(\alpha)}$ and $\boldsymbol{\mathcal{E}}_0^{(\alpha)}$ are defined in terms of the calculated, leading-order flow field, $\mathbf{u}_0^{(\alpha)}$. This flow field is known, as $\mathbf{u}_0^{(\alpha)} =: \mathbf{w}_0^{(\alpha)}$ from (2.81), where $\mathbf{w}_0^{(\alpha)}$ is given by (2.82).

The $O(\epsilon)$ problem is subsequently split, using

$$\begin{aligned}
\mathbf{u}_1^{(\alpha)} &= \mathbf{v}_1^{(\alpha)} + \mathbf{w}_1^{(\alpha)}, \\
\mathcal{L}[p_1^{(\alpha)}] &= s_1^{(\alpha)} + q_1^{(\alpha)}, \\
\mathcal{L}[\boldsymbol{\tau}_1^{(\alpha)}] &= (\boldsymbol{\tau}_{v_1}^{(\alpha)} - \boldsymbol{\eta}^{(\alpha)}) + \boldsymbol{\tau}_{w_1}^{(\alpha)},
\end{aligned} \tag{2.88}$$

where

$$\begin{aligned}
\boldsymbol{\tau}_{v_1}^{(\alpha)} &:= (\nabla \mathbf{v}_1^{(\alpha)})^T + \nabla \mathbf{v}_1^{(\alpha)}, \\
\boldsymbol{\tau}_{w_1}^{(\alpha)} &:= (\nabla \mathbf{w}_1^{(\alpha)})^T + \nabla \mathbf{w}_1^{(\alpha)},
\end{aligned} \tag{2.89}$$

such that

$$\begin{aligned} \nabla \cdot \mathbf{v}_1^{(\alpha)} &= 0, \\ -\nabla s_1^{(\alpha)} + \nabla \cdot \boldsymbol{\tau}_{v_1}^{(\alpha)} &= \nabla \cdot \boldsymbol{\eta}^{(\alpha)}, \\ \mathbf{v}_1^{(\alpha)} &= \mathbf{0} \qquad \text{on } |\mathbf{x}| = 1, \end{aligned} \tag{2.90}$$

and

$$\begin{aligned} \nabla \cdot \mathbf{w}_1^{(\alpha)} &= 0, \\ -\nabla q_1^{(\alpha)} + \nabla \cdot \boldsymbol{\tau}_{w_1}^{(\alpha)} &= \mathbf{0}, \\ \mathbf{U}_1^{(2)} - \mathbf{U}_1^{(1)} &= \dot{\xi}_1^R \mathbf{e}_z, \\ \mathbf{U}_1^{(3)} - \mathbf{U}_1^{(2)} &= \dot{\xi}_1^F \mathbf{e}_z, \\ \left( \frac{1}{|\mathbf{x}^{(2)} - \mathbf{x}^{(1)}|} \right)_1 &= \delta^2 \xi_0^R, \\ \left( \frac{1}{|\mathbf{x}^{(3)} - \mathbf{x}^{(2)}|} \right)_1 &= -\delta^2 \xi_0^F, \\ \mathbf{w}_1^{(\alpha)} = (\mathbf{U}_1^{(\beta)} - \mathbf{v}_1^{(\alpha)}) - \mathbf{U}_1^{(\alpha)} &\text{ on } |\mathbf{x} - \mathbf{x}^{(\beta)}| = 1, \end{aligned} \tag{2.91}$$

with $\beta \in \{1, 2, 3\}$. The two problems are linked through the boundary condition of the $\mathbf{w}_1^{(\alpha)}$ problem in (2.91), requiring the solution of the $\mathbf{v}_1^{(\alpha)}$ problem from (2.90) to be known, though only on the surfaces of spheres $\beta \neq \alpha$. The $\mathbf{v}_1^{(\alpha)}$ equations themselves take the form of a forced, Stokes problem for the flow around a unit sphere centred at the origin. The forcing term, $\nabla \cdot \boldsymbol{\eta}^{(\alpha)}$, is the known function (2.87), encompassing the terms arising due to the nonlinearities in the model. It will subsequently be shown that the $\mathbf{v}_1^{(\alpha)}$ problem only contributes $O(\delta^3)$, and hence negligible, terms.

Using (2.88), the viscoelastic force at $O(\epsilon)$, $\mathbf{f}_1^{(\alpha)}(t)$, satisfies

$$\begin{aligned}
\mathcal{L}[\mathbf{f}_1^{(\alpha)}(t)] &= \mathcal{L}\left[\iint_{|\mathbf{x}|=1}\left(-p_1^{(\alpha)}\mathbf{I}+\boldsymbol{\tau}_1^{(\alpha)}\right)\cdot\mathbf{dS}\right],\\
&= \iint_{|\mathbf{x}|=1}\left(-\mathcal{L}[p_1^{(\alpha)}]\mathbf{I}+\mathcal{L}[\boldsymbol{\tau}_1^{(\alpha)}]\right)\cdot\mathbf{dS},\\
&= \iint_{|\mathbf{x}|=1}\left(-[s_1^{(\alpha)}+q_1^{(\alpha)}]\mathbf{I}+(\boldsymbol{\tau}_{v_1}^{(\alpha)}-\boldsymbol{\eta}^{(\alpha)})+\boldsymbol{\tau}_{w_1}^{(\alpha)}\right)\cdot\mathbf{dS},\\
&= \iint_{|\mathbf{x}|=1}\left(-s_1^{(\alpha)}\mathbf{I}+\boldsymbol{\tau}_{v_1}^{(\alpha)}\right)\cdot\mathbf{dS}-\iint_{|\mathbf{x}|=1}\boldsymbol{\eta}^{(\alpha)}\cdot\mathbf{dS}\\
&\qquad\qquad +\iint_{|\mathbf{x}|=1}\left(-q_1^{(\alpha)}\mathbf{I}+\boldsymbol{\tau}_{w_1}^{(\alpha)}\right)\cdot\mathbf{dS},\\
&= \iiint_{|\mathbf{x}|\le 1}\nabla\cdot\boldsymbol{\eta}^{(\alpha)}\,\mathrm{d}V-\iint_{|\mathbf{x}|=1}\boldsymbol{\eta}^{(\alpha)}\cdot\mathbf{dS}+\mathbf{f}_{w_1}^{(\alpha)}(t),\\
&= \iint_{|\mathbf{x}|=1}\boldsymbol{\eta}^{(\alpha)}\cdot\mathbf{dS}-\iint_{|\mathbf{x}|=1}\boldsymbol{\eta}^{(\alpha)}\cdot\mathbf{dS}+\mathbf{f}_{w_1}^{(\alpha)}(t),\\
&= \mathbf{f}_{w_1}^{(\alpha)}(t). \qquad (2.92)
\end{aligned}$$

where $\mathbf{f}_{w_1}^{(\alpha)}(t)$ is the force on sphere $\alpha$ in the $\mathbf{w}_1^{(\alpha)}$ problem, (2.91). Thus, having split the $O(\epsilon)$ problem into both a $\mathbf{v}_1^{(\alpha)}$ and $\mathbf{w}_1^{(\alpha)}$ part, the force at $O(\epsilon)$ is solely reliant on the force associated with the $\mathbf{w}_1^{(\alpha)}$ problem. It transpires that the same relationship is true of the $O(\epsilon^k)$ problem, for $k \ge 2$, if one were to split up the problem similarly, as discussed in the following section.

Although the $O(\epsilon)$, viscoelastic force in (2.92) has no explicit dependence on the forces generated in the $\mathbf{v}_1^{(\alpha)}$ problem, there is still an implicit link to the $\mathbf{v}_1^{(\alpha)}$ problem via the $\mathbf{w}_1^{(\alpha)}$ boundary conditions. Thus, our attention is first directed to the $\mathbf{v}_1^{(\alpha)}$ problem (2.90), where, in the Appendix it is shown that

$$\begin{aligned}
&\mathbf{v}_1^{(\alpha)} = \mathbf{0} && \text{on} \quad |\mathbf{x}| = 1, && \beta = \alpha,\\
&\mathbf{v}_1^{(\alpha)} \sim \delta^2\mathbf{A}^{(\alpha)} && \text{on} \quad |\mathbf{x}-\mathbf{x}^{(\beta)}| = 1, && \beta \neq \alpha, \qquad (2.93)
\end{aligned}$$

where $\mathbf{A}^{(\alpha)}$ is an $O(1)$, spatially constant vector. Using (2.93), the boundary condition for the $\mathbf{w}_1^{(\alpha)}$ problem is thus

$$\mathbf{w}_1^{(\alpha)} = (\mathbf{U}_1^{(\beta)}-\delta^2\mathbf{A}^{(\beta)})-\mathbf{U}_1^{(\alpha)} \text{ on } |\mathbf{x}-\mathbf{x}^{(\beta)}| = 1, \qquad (2.94)$$

where $\beta \in \{1, 2, 3\}$. The vector $\mathbf{A}^{(\alpha)}$ is the only remaining feature of the $\mathbf{v}_1^{(\alpha)}$ problem that could affect the viscoelastic force at $O(\epsilon)$ in (2.92).

Using (2.94), $\mathbf{f}_{w_1}^{(\alpha)}(t)$ can be calculated in order to complete the force-velocity relationship in (2.92). Recall that the leading-order problem, (2.79), was transformed, by the variables (2.81), into the Newtonian problem, (2.20), for which $\epsilon = 0$. The $\mathbf{w}_1^{(\alpha)}$ problem, (2.91), is similarly cast into a Newtonian form via the variables in (2.88), representing the $O(\epsilon)$ contributions in the Newtonian problem, (2.20); these are obtained if one were to expand the Newtonian problem in powers of $\epsilon$ and inspect the $O(\epsilon)$ terms.

Thus, the force on sphere $\alpha$ in the $\mathbf{w}_1^{(\alpha)}$ problem is the $O(\epsilon)$ contribution to the Newtonian force, albeit with slightly adjusted boundary conditions, (2.94), when compared to the Newtonian, boundary conditions, (2.22). Specifically, the terms $\mathbf{U}_1^{(\beta)} - \mathbf{U}_1^{(\alpha)}$ now have an added contribution of $-\delta^2 \mathbf{A}^{(\beta)}$ in (2.94). It follows that the force in the $\mathbf{w}_1^{(\alpha)}$ problem, $\mathbf{f}_{w_1}^{(\alpha)}(t)$, is thus the $O(\epsilon)$ contribution to the Newtonian force in (2.51), had that Newtonian force been calculated with these adjusted boundary conditions. This gives

$$\mathbf{f}_{w_1}^{(\alpha)}(t) \sim -6\pi \mathbf{U}_1^{(\alpha)} + 6\pi \sum_{\gamma \neq \alpha} \left[ \delta \mathbf{K}^{(\alpha,\gamma)} \left( \mathbf{U}_1^{(\gamma)} - \delta \mathbf{K}^{(\gamma,\sigma)} \mathbf{U}_1^{(\sigma)} \right) + \delta^2 \mathbf{H}_0^{(\alpha,\gamma)} \mathbf{U}_0^{(\gamma)} \right] + O(\delta^3), \tag{2.95}$$

where $\mathbf{H}_0^{(\alpha,\gamma)} := \mathbf{H}^{(\alpha,\gamma)}(\xi_0^R, \xi_0^F)$ from (2.34). Importantly, the extra contribution of $-\delta^2 \mathbf{A}^{(\beta)}$ in the boundary conditions (2.94) does not contribute, thus decoupling the $\mathbf{v}_1^{(\alpha)}$ problem completely. This is due to a factor of $\delta$ in (2.95) pre-multiplying the $-\delta^2 \mathbf{A}^{(\beta)}$ contribution, making it $O(\delta^3)$ and hence negligible. Given that the $\mathbf{v}_1^{(\alpha)}$ problem accounted for any effects due to the nonlinear terms in the constitutive law, by neglecting the potential-dipolar singularities, consistent with neglecting $O(\delta^3)$ terms, the nonlinear effects of viscoelasticity are negligible, leaving only those of linearly viscoelasticity via the temporal operator $\mathcal{L}$.

Using (2.92) and (2.95), the force-velocity relationship at $O(\epsilon)$ in the viscoelastic problem satisfies

$$\mathcal{L}[\mathbf{f}_1^{(\alpha)}(t)] \sim -6\pi \mathbf{U}_1^{(\alpha)} + 6\pi \sum_{\gamma \neq \alpha} \left[ \delta \mathbf{K}^{(\alpha,\gamma)} \left( \mathbf{U}_1^{(\gamma)} - \delta \mathbf{K}^{(\gamma,\sigma)} \mathbf{U}_1^{(\sigma)} \right) + \delta^2 \mathbf{H}_0^{(\alpha,\gamma)} \mathbf{U}_0^{(\gamma)} \right] + O(\delta^3). \tag{2.96}$$

### 2.4.3 Higher Orders in $\epsilon$

The equations for $O(\epsilon^k)$ where $k \geq 2$ are

$$\begin{aligned}
-\nabla p_k^{(\alpha)} + \nabla \cdot \boldsymbol{\tau}_k^{(\alpha)} &= \mathbf{0}, \\
\nabla \cdot \mathbf{u}_k^{(\alpha)} &= 0, \\
\mathcal{L}[\boldsymbol{\tau}_k^{(\alpha)}] &= (\nabla \mathbf{u}_k^{(\alpha)})^T + \nabla \mathbf{u}_k^{(\alpha)} - \boldsymbol{\eta}_k^{(\alpha)}, \\
\mathbf{U}_k^{(2)} - \mathbf{U}_k^{(1)} &= \dot{\xi}_k^R \mathbf{e}_z, \\
\mathbf{U}_k^{(3)} - \mathbf{U}_k^{(2)} &= \dot{\xi}_k^F \mathbf{e}_z, \\
\left( \frac{1}{|\mathbf{x}^{(2)} - \mathbf{x}^{(1)}|} \right)_k &= \delta^2 \xi_{k-1}^R, \\
\left( \frac{1}{|\mathbf{x}^{(3)} - \mathbf{x}^{(2)}|} \right)_k &= -\delta^2 \xi_{k-1}^F, \\
\mathbf{u}_k^{(\alpha)} = \mathbf{U}_k^{(\beta)} - \mathbf{U}_k^{(\alpha)} \quad &\text{on} \quad |\mathbf{x} - \mathbf{x}^{(\beta)}| = 1, \quad \beta \in \{1,2,3\},
\end{aligned} \tag{2.97}$$

where $\boldsymbol{\eta}_k^{(\alpha)}$ is

$$\begin{aligned}
\boldsymbol{\eta}_k^{(\alpha)} := \left(1 + \Gamma \frac{\partial}{\partial t}\right)^{-1} \sum_{\{m,l \,|\, m+l=k\}} \Big[ & \mathbf{u}_m^{(\alpha)} \cdot \nabla [\Lambda \boldsymbol{\tau}_l^{(\alpha)} - \Gamma \boldsymbol{\mathcal{E}}_l^{(\alpha)}] \\
& - \{ (\nabla \mathbf{u}_m^{(\alpha)})^T \cdot [\Lambda \boldsymbol{\tau}_l^{(\alpha)} - \Gamma \boldsymbol{\mathcal{E}}_l^{(\alpha)}] \\
& + [\Lambda \boldsymbol{\tau}_m^{(\alpha)} - \Gamma \boldsymbol{\mathcal{E}}_m^{(\alpha)}] \cdot \nabla \mathbf{u}_l^{(\alpha)} \} \\
& - \mathbf{U}_m^{(\alpha)} \cdot \nabla [\Lambda \boldsymbol{\tau}_l^{(\alpha)} - \Gamma \boldsymbol{\mathcal{E}}_l^{(\alpha)}] \Big] .
\end{aligned} \tag{2.98}$$

for $0 \leq m, l \leq k$.

For $k = 2$, the $O(\epsilon^2)$ velocity can be split into a $\mathbf{v}_2^{(\alpha)}$ part and a $\mathbf{w}_2^{(\alpha)}$ part, both analogous to the the system of equations in (2.90) and (2.91) respectively. The former, $\mathbf{v}_2^{(\alpha)}$ problem thus takes the form of the forced, Stokes equations, in particular forced by $\nabla \cdot \boldsymbol{\eta}_2^{(\alpha)}$, which in turn relies on the pre-calculated $\mathbf{u}_0^{(\alpha)}$ and $\mathbf{u}_1^{(\alpha)}$ terms. The largest term in $\mathbf{u}_0^{(\alpha)}$ in the far field is $O(1/r)$; see equations (2.81) and (2.82). From the $O(\epsilon)$ problem where $\mathbf{u}_1^{(\alpha)} = \mathbf{v}_1^{(\alpha)} + \mathbf{w}_1^{(\alpha)}$, it is deduced that $\mathbf{v}_1^{(\alpha)}$ is $O(1/r^2)$ (see Appendix) and $\mathbf{w}_1^{(\alpha)}$ is $O(1/r)$ from (2.47). Thus, the largest term in $\mathbf{u}_1^{(\alpha)}$ is again $O(1/r)$, implying the largest term in $\nabla \cdot \boldsymbol{\eta}_2^{(\alpha)}$ has the same dimensional form as before, rendering the $\mathbf{v}_2^{(\alpha)}$ contribution to the forces in the $\mathbf{w}_2^{(\alpha)}$ problem negligible. This can be seen by following both the analysis of the Appendix and the derivation of equation (2.95). The process repeats for each integer, $k$.

Hence, the forces at $O(\epsilon^k)$ in the viscoelastic problem satisfy

$$\mathcal{L}[\mathbf{f}_k^{(\alpha)}(t)] = \mathbf{f}_{w_k}^{(\alpha)}(t) \sim -6\pi\mathbf{U}_k^{(\alpha)} + 6\pi \sum_{\gamma\neq\alpha} \Bigg[ \delta\mathbf{K}^{(\alpha,\gamma)} \Big(\mathbf{U}_k^{(\gamma)} - \delta\mathbf{K}^{(\gamma,\sigma)}\mathbf{U}_k^{(\sigma)}\Big) + \sum_{\{m,\,l\,|\,m+l=k-1\}} \delta^2\mathbf{H}_m^{(\alpha,\gamma)}\mathbf{U}_l^{(\gamma)} \Bigg] + O(\delta^3), \quad (2.99)$$

where $\mathbf{H}_m^{(\alpha,\gamma)} := \mathbf{H}^{(\alpha,\gamma)}(\xi_m^R, \xi_m^F)$. This relationship, (2.99), is effectively the $O(\epsilon^k)$ term of the Newtonian, force-velocity relationship, (2.51), had $\mathbf{U}^{(\alpha)}$ and the arguments in $\mathbf{H}^{(\alpha,\gamma)}(\xi^R, \xi^F)$ from (2.37) been expanded in $\epsilon$.

### 2.4.4 Final, Viscoelastic, Force-Velocity Relationship

Recombining the force-velocity relationships from the leading-order equations in $\epsilon$, (2.85), the $O(\epsilon)$ equations, (2.96) and the $O(\epsilon^k)$, for $k \geq 2$, equations, (2.99), the total force, up to $O(\epsilon^k)$, is

$$\begin{aligned}\mathcal{L}[\mathbf{f}^{(\alpha)}(t)] \sim\ & -6\pi\{\mathbf{U}_0^{(\alpha)} + \epsilon\mathbf{U}_1^{(\alpha)} + \ldots + \epsilon^k\mathbf{U}_k^{(\alpha)}\} \\ & + 6\pi \sum_{\gamma\neq\alpha} \Big[\delta\mathbf{K}^{(\alpha,\gamma)} \Big(\{\mathbf{U}_0^{(\gamma)} + \epsilon\mathbf{U}_1^{(\gamma)} + \ldots + \epsilon^k\mathbf{U}_k^{(\gamma)}\} \\ & -\delta\mathbf{K}^{(\gamma,\sigma)}\{\mathbf{U}_0^{(\gamma)} + \epsilon\mathbf{U}_1^{(\gamma)} + \ldots + \epsilon^k\mathbf{U}_k^{(\gamma)}\}\Big) \\ & +\epsilon\delta^2 \sum_{p=0}^{k-1} \sum_{\{m,\,l,\,|\,m+l=p\}} \epsilon^p\mathbf{H}_m^{(\alpha,\gamma)}\mathbf{U}_l^{(\gamma)} \Big] + O(\delta^3), \end{aligned} \quad (2.100)$$

where $\mathbf{H}_m^{(\alpha,\gamma)} := \mathbf{H}^{(\alpha,\gamma)}(\xi_m^R, \xi_m^F)$. Hence, up to $O(\delta^3)$ corrections,

$$\begin{aligned}\mathcal{L}[\mathbf{f}^{(\alpha)}(t)] \approx\ & -6\pi\{\mathbf{U}^{(\alpha)} + 6\pi \sum_{m\neq\alpha} \Big[\delta\mathbf{K}^{(\alpha,m)} \Big(\mathbf{U}^{(m)} \\ & -\delta\mathbf{K}^{(m,\sigma)}\mathbf{U}^{(m)}\Big) + \epsilon\delta^2\mathbf{H}^{(\alpha,m)}\mathbf{U}^{(m)}\Big] + O(\delta^3). \end{aligned} \quad (2.101)$$

The viscoelastic, force-velocity relationship in (2.101) holds so long as $O(\delta^3)$ terms are negligible and $\delta \ll \epsilon$, as established in the Newtonian solution. This force-velocity relationship is the viscoelastic analogue to the Newtonian, force-velocity relationship, (2.51). The difference between the two relationships is the presence of the temporal operator, $\mathcal{L}$, defined by (2.80) and acting on the left-hand side of (2.101).

Equation (2.101) can now be inverted to find an expression for $\mathbf{U}^{(2)}$ in terms of the prescribed forces, thus determining the net velocity of the microswimmer in a viscoelastic environment.

It should be noted that Lauga [60] also presents a technique for calculating the average displacement of a general, shape-changing swimmer in a viscoelastic environment, though the required calculations are notably more lengthy than the simplified approach taken here (solving directly at each order). Lauga's technique is based on the reciprocal theorem [44], which states that, for two solutions satisfying the Stokes equations, $(\mathbf{u}, \boldsymbol{\sigma})$ and $(\mathbf{u}', \boldsymbol{\sigma}')$,

$$\iint_{S(t)} \mathbf{u} \cdot \boldsymbol{\sigma}' \mathbf{n} \, dS = \iint_{S(t)} \mathbf{u}' \cdot \boldsymbol{\sigma} \mathbf{n} \, dS, \tag{2.102}$$

where $S$ is the instantaneous suface of the swimmer. By assigning $(\mathbf{u}', \boldsymbol{\sigma}')$ to be the solution of the solid-body (undeforming) motion of the swimmer in a Newtonian flow field, the solution of the general swimming problem, $(\mathbf{u}, \boldsymbol{\sigma})$, can be obtained asymptotically in $\varepsilon$ by considering time-averaged variables. However, one must calculate the volume integral over the solid body of $\boldsymbol{\eta}^{(\alpha)}$ contracted with the gradient of the Newtonian flow field for solid-body motion, divided by the solid-body force; these are all lengthy expressions for the three-sphere swimmer. In addition, the calculation is based on the *kinematic* problem involving prescribed shape-changes, not the *mobility* problem of prescribed forces. Furthermore, Lauga's method [60] does not take into account a swimmer with more than one length scale, such as the three-sphere swimmer with lengths $a$, $b$ and $L$ and small parameters $\delta$ and $\varepsilon$; see Section 2.2.3.

### 2.4.5 Net Swimmer Displacement in Viscoelastic Fluid

The Stokes force balance gives, upon applying the temporal operator $\mathcal{L}$,

$$\sum_{\gamma=1}^{3} \mathcal{L}[\mathbf{f}^{(\gamma)}] = \mathbf{0}, \tag{2.103}$$

which can be written in terms of sphere velocities using (2.101). One can write $\mathbf{U}^{(1)}$ and $\mathbf{U}^{(3)}$ in terms of $\mathbf{U}^{(2)}$ via (2.53), giving the same expression for $U^{(2)}$ in terms of rod displacements, $\xi^R(t)$ and $\xi^F(t)$, as in (2.60). Thus, the equation for the net displacement of the swimmer in one beat cycle in a viscoelastic fluid, $\Delta_v$, when written

in terms of rod displacements, $\xi^R(t)$ and $\xi^F(t)$, is equal to the net displacement in a Newtonian fluid, $\Delta$, given by (2.62),

$$\Delta_v \sim \frac{7\delta^2\epsilon}{24}\int_0^{2\pi}(\xi^R\dot{\xi^F} - \xi^F\dot{\xi^R})\,\mathrm{d}t + O(\delta^3). \tag{2.104}$$

This highlights how, in viscoelastic fluid, prescribing any form of displacement such as $\xi^R(t)$ and $\xi^F(t)$ will leave the results for net swimmer displacement unchanged, at least up to and including $O(\delta^2\epsilon)$ for the three-sphere swimmer. This agrees with theory by Fu [36] in that prescribing kinematic conditions, such as the rod displacements (the *kinematic* problem), leads to viscoelastic effects being overlooked or unaccounted; hence, the model here considers a swimmer with prescribed forces (the *mobility* problem).

The rod displacement over one beat cycle in a viscoelastic fluid, $\Delta_v$, must be written in terms of the prescribed, internal forces. This is done via equation (2.101), using the same procedure to obtain (2.67) in the Newtonian case. The difference in the viscoelastic case is the addition of the temporal operator, $\mathcal{L}$, to the forces, so that (2.71) becomes

$$\begin{pmatrix}\dot{\xi}^R\\ \dot{\xi}^F\end{pmatrix} = \frac{1}{\pi}\mathbf{N}\begin{pmatrix}\mathcal{L}[f^{(1)}]\\ \mathcal{L}[f^{(3)}]\end{pmatrix}, \tag{2.105}$$

where $\mathbf{N}$ remains unchanged from (2.72). This gives

$$\Delta_v \sim \frac{29\delta^2\epsilon}{432\pi^2}\int_0^{2\pi}(g_{\mathcal{L}}^{(3)}\dot{g}_{\mathcal{L}}^{(1)} - g_{\mathcal{L}}^{(1)}\dot{g}_{\mathcal{L}}^{(3)})\,\mathrm{d}t + O(\delta^3), \tag{2.106}$$

where

$$\begin{aligned}\dot{g}_{\mathcal{L}}^{(\alpha)}(t) &:= \mathcal{L}[f^{(\alpha)}(t)],\\ &= \left(1+\Gamma\frac{\partial}{\partial t}\right)^{-1}\left(1+\Lambda\frac{\partial}{\partial t}\right)f^{(\alpha)}(t),\end{aligned} \tag{2.107}$$

and

$$g_{\mathcal{L}}^{(\alpha)}(t) = \int^t \dot{g}_{\mathcal{L}}^{(\alpha)}(\bar{t})\,\mathrm{d}\bar{t}. \tag{2.108}$$

This illustrates that viscoelasticity does indeed have an effect on the prescribed-force swimmer. Re-dimensionalising equation (2.106) gives, assuming dimensional variables,

$$\Delta = \frac{29}{432\pi^2\mu^2D^2a}\int_0^{2\pi/\omega}(g_{\mathcal{L}}^{(3)}\dot{g}_{\mathcal{L}}^{(1)} - g_{\mathcal{L}}^{(1)}\dot{g}_{\mathcal{L}}^{(3)})\,\mathrm{d}t, \tag{2.109}$$

where time scales are implicit in the force integrals.

An intuitive explanation for the net displacement in terms of internal forces is not obvious, given explicit calculation is required to obtain equation (2.92), verifying that the viscoelastic force is unaffected by the nonlinear terms from the viscoelastic constituitive relation. The validity of linear viscoelasticity, in which the $O(1)$ time-derivatives in $\mathcal{L}$ are retained but the nonlinear, spatial derivatives from the constitutive law are not, is only discovered *a posteriori*.

### 2.4.6 Efficiency

It is common, with simple-swimmer models, to investigate the efficiency of the swimmer. Using Lighthill's definition [63] of hydrodynamic efficiency, $E$, in terms of average power, $\bar{P}$, and average velocity, $\bar{\mathbf{U}}$,

$$E = 6\pi\mu\bar{\mathbf{U}}^2/\bar{P}, \tag{2.110}$$

where

$$\begin{aligned}
\bar{\mathbf{U}} &:= \frac{1}{2\pi}\int_0^{2\pi} \mathbf{U}^{(2)}(t)\,\mathrm{d}t = \frac{\Delta_v \mathbf{e}_z}{2\pi}, \\
\bar{P} &:= \frac{1}{2\pi}\int_0^{2\pi} P(t)\,\mathrm{d}t, \\
P(t) &:= \sum_{k=1}^{3} \mathbf{U}^{(k)}(t)\cdot\mathbf{f}^{(k)}(t), \\
&= -\mathbf{f}^{(1)}(t)\cdot\dot{\xi}^R(t)\mathbf{e}_z + \mathbf{f}^{(3)}(t)\cdot\dot{\xi}^F(t)\mathbf{e}_z,
\end{aligned} \tag{2.111}$$

where the power, $P(t)$, has been simplified using

$$\begin{aligned}
\mathbf{U}^{(1)} &= \mathbf{U}^{(2)} - \dot{\xi}^R\mathbf{e}_z, \\
\mathbf{U}^{(3)} &= \mathbf{U}^{(2)} + \dot{\xi}^F\mathbf{e}_z, \\
\mathbf{0} &= \mathbf{f}^{(1)} + \mathbf{f}^{(2)} + \mathbf{f}^{(3)}.
\end{aligned} \tag{2.112}$$

From equation (2.105), $\dot{\xi}^R$ and $\dot{\xi}^F$ can be written in terms of $\mathcal{L}[f^{(1)}]$ and $\mathcal{L}[f^{(3)}]$ and inserted into (2.111).

## 2.5 Results

The dimensionless, $2\pi$-periodic, internal force on sphere 1, $\mathbf{f}^{(1)}$, and sphere 3, $\mathbf{f}^{(3)}$, are now prescribed, where $\mathbf{f}^{(2)} = -\mathbf{f}^{(1)} - \mathbf{f}^{(3)}$ by the force balance in (2.1). The net displacements of the three-sphere swimmer in a Newtonian fluid, $\Delta$, or a viscoelastic fluid, $\Delta_v$, are given by equations (2.73) and (2.106) respectively. These are rewritten for convenience,

$$\Delta \sim \frac{29\delta^2\epsilon}{432\pi^2}\int_0^{2\pi}(g^{(3)}\dot{g}^{(1)} - g^{(1)}\dot{g}^{(3)})\,\mathrm{d}t + O(\delta^3), \tag{2.113}$$

$$\Delta_v \sim \frac{29\delta^2\epsilon}{432\pi^2}\int_0^{2\pi}(g_{\mathcal{L}}^{(3)}\dot{g}_{\mathcal{L}}^{(1)} - g_{\mathcal{L}}^{(1)}\dot{g}_{\mathcal{L}}^{(3)})\,\mathrm{d}t + O(\delta^3), \tag{2.114}$$

where

$$\begin{aligned}\dot{g}^{(\alpha)}(t) &:= f^{(\alpha)}(t),\\ \dot{g}_{\mathcal{L}}^{(\alpha)}(t) &:= \mathcal{L}[f^{(\alpha)}(t)],\\ &= \left(1+\Gamma\frac{\partial}{\partial t}\right)^{-1}\left(1+\Lambda\frac{\partial}{\partial t}\right)f^{(\alpha)}(t),\end{aligned} \tag{2.115}$$

and

$$\begin{aligned}g^{(\alpha)}(t) &= \int^t \dot{g}^{(\alpha)}(\bar{t})\,\mathrm{d}\bar{t},\\ g_{\mathcal{L}}^{(\alpha)}(t) &= \int^t \dot{g}_{\mathcal{L}}^{(\alpha)}(\bar{t})\,\mathrm{d}\bar{t}.\end{aligned} \tag{2.116}$$

As an example, consider the sinusoidally varying forces:

$$\begin{aligned}\mathbf{f}^{(1)} &= \sin(t)\mathbf{e}_z,\\ \mathbf{f}^{(3)} &= \sin(t-\phi)\mathbf{e}_z,\end{aligned} \tag{2.117}$$

where the phase difference, $\phi$, is included to break time reversibility so that the swimming stroke is non-reciprocal. There is the additional assumption that initial, transient behaviour has decayed so that solutions are perfectly periodic, allowing a unique inverse to be defined within the temporal-operator definition, (2.115). The displacements over one beat cycle become

$$\begin{aligned}\Delta &\sim -\frac{29\delta^2\epsilon\sin(\phi)}{216\pi} + O(\delta^3),\\ \Delta_v &\sim -\frac{29\delta^2\epsilon}{216\pi}\left(\frac{1+\Lambda^2}{1+\Gamma^2}\right)\sin(\phi) + O(\delta^3).\end{aligned} \tag{2.118}$$

The minus sign, arising from the prescription of forces in the form of (2.117), is not important when considering the magnitude of net displacement. In addition, the constant $29/216\pi \ll 1$ multiplies the factor of $\delta^2\epsilon$, making the displacements very small.

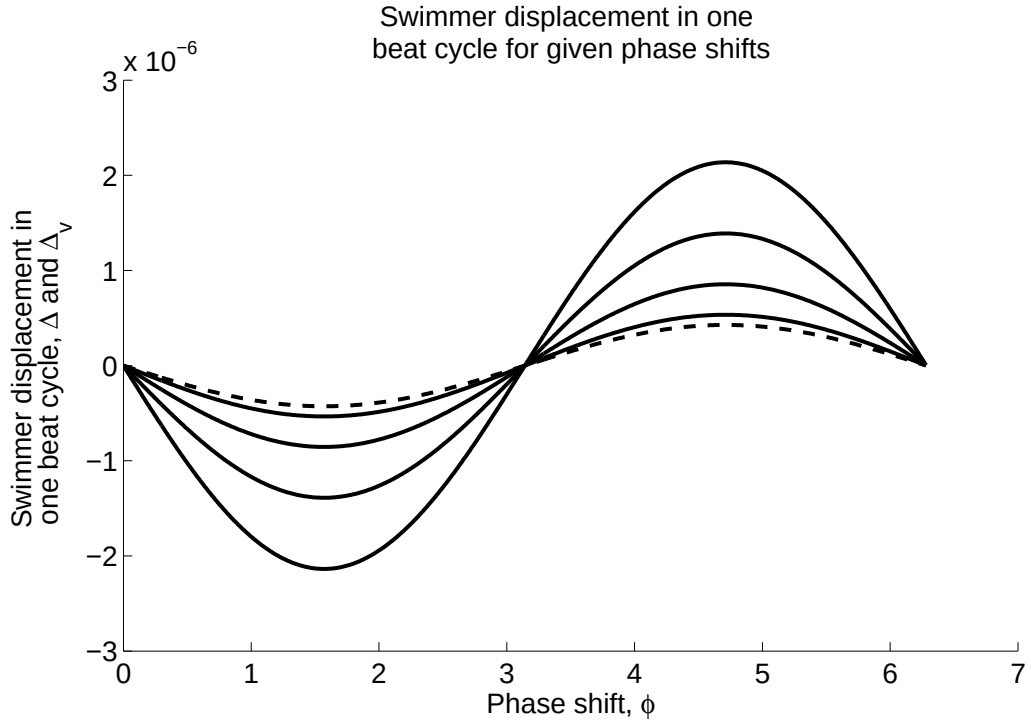


Figure 2.3: The net displacements over one beat cycle, $\Delta$ for a Newtonian fluid and $\Delta_v$ for a viscoelastic medium, are plotted as functions of rod, phase difference, $\phi$, where the internal forcing of sphere 1 is $\sin(t)$ and of sphere 3 is $\sin(t-\phi)$. Here, $\epsilon = 0.1$, $\delta = 0.01$, $\Gamma = 0$, as for an upper-convected, Maxwell fluid, and $\Lambda$ ranges from 0, the Newtonian case (given by the dashed curve), up to 2 in steps of 0.5, each step increasing the amplitude of the curve.

From the definitions of the dimensionless constants, $\Lambda := \omega\lambda$ for relaxation time $\lambda$ and $\Gamma := \omega\gamma$ for retardation time $\gamma$, where, for a polymeric fluid as discussed in Section 2.2.2, the constant $\gamma = \lambda\mu_s/(\mu_s + \mu_p)$. Hence, $\Lambda > \Gamma$ so that the net displacement of a swimmer in polymeric, viscoelastic fluid from (2.118) is greater than that in a Newtonian fluid. These results also hold if either, or both, of the Deborah numbers $\Lambda$ and $\Gamma$ are much less than one. Explicit plots of the displacement for an upper-convected, Maxwell fluid, for which $\Gamma = 0$, are illustrated in figure 2.5.

The average power in the viscoelastic case, from (2.111), using the prescribed forces in (2.117), becomes

$$\bar{P} \sim \frac{1}{432\pi}\left(\frac{1+\Lambda\Gamma}{1+\Gamma^2}\right)\left[-2(72-96\delta+311\delta^2)\right. \\ \left.+(-72+6\delta-71\delta^2)\cos\phi\right]+O(\delta^3), \tag{2.119}$$

which has a greater magnitude (given $\Lambda > \Gamma$) than the average Newtonian power (when $\Gamma = \Lambda = 0$). The hydrodynamic efficiency, (2.110), of the sinusoidal, three-sphere swimmer with prescribed forces scales with

$$\left(\frac{1+\Lambda^2}{1+\Gamma^2}\right)^2 \frac{1+\Gamma^2}{1+\Lambda\Gamma} > 1, \tag{2.120}$$

so that

$$E_{\text{viscoelastic}} > E_{\text{Newtonian}}, \tag{2.121}$$

demonstrating that the three-sphere swimmer with sinusoidal, internal forces is more efficient when immersed in a viscoelastic fluid.

## 2.6 Discussion

The distance displaced in one beat cycle of the three-sphere swimmer has been investigated in both Newtonian and viscoelastic fluid environments. The latter fluid is described by a deviatoric-stress tensor following an Oldroyd-B model, which includes an upper-convected, Maxwell model. The results also immediately generalise for other constitutive-relation parameters in equation (2.8), such as those associated with a lower-convected, Maxwell fluid.

The net displacement of the three-sphere swimmer calculated in a Newtonian fluid agrees with the results of existing models [4, 32, 41, 70, 78]. The derivation in the current context, however, followed the more rigorous approach of including the interaction flows generated between the spheres. Whilst the flow field differs, the time-averaged displacement in one swimming cycle remains asymptotically the same.

The parameter regime is such that there are two, small, dimensionless parameters, $\delta$ and $\epsilon$. The former is the ratio of the sphere sizes to their separation, so that sphere interactions are via their far fields, enabling extensive simplification. The latter is the

ratio of the sphere-oscillation amplitudes to their radii. Its small size is arguably not unreasonable for self-contained, forcing mechanisms within the spheres themselves. It also entails that the viscoelastic problem reduces to a forced, Stokes problem at each order of an asymptotic expansion, sometimes referred to as the retarded-motion expansion [59]. In addition, $\delta \ll \epsilon$ is imposed in Section 2.3.1, which also is satisfied for a sufficiently large, sphere separations. Finally, the requirement of effectively inertialess dynamics enforces sufficiently small length scales and also that $\rho\omega a^2/\mu \sim O(\delta^3)$ or less, where $\mu/\rho$ is the kinematic viscosity, $\omega$ is the frequency of the sphere oscillations and $a$ is the sphere radius. This is readily satisfied for sufficiently high, kinematic viscosity and/or sufficiently low frequency; hence the constraints are not mutually exclusive when interpreted physically.

In the far field, the centres of spheres 1 and 3 are asymptotically close to the centre of sphere 2. Thus, upon neglecting the higher-order potential dipoles, the swimmer will behave as two Stokeslet doublets, representing an asymmetric swimmer. However, if one were to average the flow field over a period in time, the periodic, singularity weightings ensure the doublets integrate to zero, implying higher orders are needed; the time-averaged swimmer would hence be symmetric (a quadrupole swimmer).

With the *kinematic* problem, where the relative, swimmer motions are unchanged in the different media, we find that viscoelasticity has no influence; however, the *mobility* problem, whereby the actuation forces are prescribed, clearly indicates substantial effects. In particular, the swimming behaviour has been compared for a given, sinusoidal, and non-reciprocal, forcing of the three-sphere swimmer within a Newtonian fluid and within a viscoelastic medium, the latter with standard, parameter constraints associated with a polymeric fluid. This leads to the prediction that within the polymeric, viscoelastic medium, the swimmer is both more efficient and moves further in one beat cycle at leading, non-trivial orders of the asymptotic expansion.

While improvements in swimming and efficiency are also observed by Teran *et. al.* [96] for the kinematic problem associated with undulating sheet swimmers at $O(1)$ Deborah numbers, the influence of viscoelasticity is very different. In particular, Teran *et. al.* reported a peak of optimal efficiency and swimming speed with a Deborah number of unity due to stresses induced by the fluid aft to the swimmer, suggesting a resonance between the undulation frequency and the fluid at optimality. In contrast, no swimmer-medium resonance is observed here, even though the

parameter regime contains $O(1)$ Deborah numbers. While Teran et. al.'s [96] study is for large-amplitude displacements, resonance phenomena are regularly observed for small-amplitude approximations with prescribed forcing, as with the simple harmonic oscillator. In turn, this suggests that the absence of resonance in this study is not solely a consequence of the small-amplitude oscillations used to facilitate an asymptotic investigation. Furthermore, Fu et. al. [37], for example, report that nonlinear, viscoelastic effects reduce swimmer speeds for an infinite, undulating cylinder. Consequently, the current study reinforces the observations of the literature that the responses of inertialess swimmers to non-Newtonian rheologies do not appear to be systematic, but vary on a case-by-case basis. In particular, this emphasises that caution must be used when extrapolating physical insight from simplified models of microswimmers in non-trivial rheologies to other systems, such as swimming cells.

In addition, our predictions are analogous to the fully linear study of Fulford and Katz [38] and would be predicted on consideration of simply linear, viscoelastic constitutive relations; here, nonlinear viscoelasticity does not alter the force balance, even though it's dynamically non-trivial. Thus, while it is commonly observed from studies of the *kinematic* problem that linear, viscoelasticity is insufficient to capture even leading-order effects in the study of microswimming [59], this is clearly not reflected here. This is despite the observation that the scalings in this paper indicate nonlinear, viscoelasticity is important, noting that higher orders in the perturbative expansion must be considered to capture the net motion of the swimmer. Thus, the fact that linear viscoelasticity is sufficient to deduce the leading-order, swimming behaviour in this study only emerges *a posteriori*; the extent to which this may generalise is unclear and merits further study if only to understand when simple, fully linear methods might be exploited in some settings for understanding inertialess swimming in rheological media.

# Chapter 3

# Hyperactivated, Tethered Sperm Motility

## 3.1 Chapter Introduction

The second aspect of low Reynolds number microswimming to be modelled concerns biological microswimmers, in particular mammalian sperm cells, which have become bound to the epithelial wall of the female, reproductive tract. Sperm exhibit two, distinct, flagellar beat patterns: symmetric and hyperactive beating; see Section 1.2.2. It is the latter, hyperactive beat which was hypothesised to contribute to the subsequent release of the sperm cell from the tether point, though there are no previous mechanical studies.

The model in this chapter, now published [29], applies resistive-force theory (RFT), outlined in Section 1.3.3, to determine the forces exerted by the flagellum on the tethering point due to both a symmetric, and hyperactive, waveform propagating down the flagellum. RFT is a leading-order approximation to SBT, which may therefore be deduced via singularity methods; see Section 4.3.3. As the flagellar waveforms are prescribed, this is a *kinematic* problem as opposed to a *mobility* problem; the latter would require further modelling assumptions about the internal mechanics of the flagellum, including the contractions and regulation of dynein motors controlling microtubule sliding (currently only hypothesised [18, 66, 74]) and the internal elastic properties [68].

The chapter begins with an extended, biological background to highlight the sperm-tethering scenario in more detail. The validity of applying RFT is subsequently discussed. Two frames of reference are established: the standard, fixed, inertial frame in

which RFT is applied, and the body-fixed frame, where the body-fixed $x$ axis is taken to be the mean axis of the symmetrically beating, flagellum centre-line. The latter frame is allowed to rotate with the tethered sperm cell in relation to the inertial frame of reference; it is also the frame of interest when calculating the pushing or pulling forces exerted by the sperm cell on the tethering point. Different boundary conditions at the tethering point itself are discussed, namely the *freely hinged* tether and the *clamped* tether. Waveforms are constructed based on experimental observations, from which the relevant forces are determined. Results are presented, including parameter studies relating to characteristics of the hyperactive beat, highlighting that hyperactive beat patterns, in certain regions of parameter space, do appear to contribute mechanically to the release of the sperm. Results are compared with experimental, imaging data obtained by T. Connolly and J. Kirkman-Brown (see statement of originality in Section 1.6) followed by a discussion of the biological relevance, together with any model limitations.

## 3.2 Biological Motivation

A specific scenario of biological interest concerns the binding of mammalian sperm to the epithelial surfaces within the oviductal isthmus, a region along the female reproductive tract. The front of the sperm head, or acrosome, fuses to cells and cilia lining the tract walls, causing the sperm to be tethered; see figure 3.1. In placental mammals exhibiting estrous cycles (differing from menstrual cycles in that the inner membrane of the uterus is reabsorbed, not shed on a regular basis) the sperm are seen to avidly bind with the tract walls in isthmic regions. Here, they are stored until ovulation, when only a few manage to escape at a time. This 'oviductal reservoir' of sperm is hypothesised to reduce the likelihood of allowing too many sperm to continue onwards, potentially resulting in more than one sperm fertlising the egg; this is called polyspermic fertilisation [91], in which there is too much DNA in the egg, inducing a failure to fertilise. Another postulated function of the oviductal reservoir is to prolong the life-span, or viability, of the sperm and to regulate the "capacitation process". Capacitation is a biochemical process in which mammalian sperm prepare for fertilisation. Observations suggest that the release of a sperm cell from its binding site is induced by changes brought about by the sperm itself, as opposed to being a result of external changes in the epithelial wall when close to ovulation (epithelial

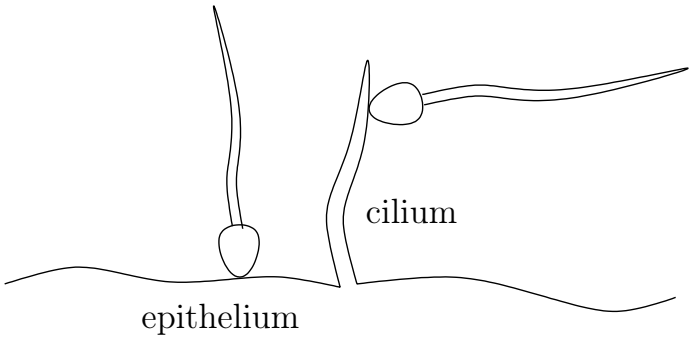


Figure 3.1: Two sperm cells tethered, respectively, to the epithelial walls of the female reproductive tract and to cilia lining the surfaces of the female-reproductive-tract epithelium.

signalling), although the latter may still be a possibility [*ibid*].

Given the flagellum appears to always push the body of a sperm cell during swimming, one may anticipate that flagellar motility will not contribute to bond breaking as it would thrust the cell further into the epithelial wall. In contrast, the escape of sperm does indeed appear to be correlated to sperm capacitation and the induction of hyperactivation along the tail [30]; see Section 1.2.2 regarding symmetric and hyperactive waveforms. This led to the hypothesis that flagellar mechanics are in fact important in sperm release. Thus, the objective in this chapter is to explore whether it is mechanically feasible for hyperactivation to assist in the epithelial escape of mammalian sperm, at least in the context of Newtonian fluid dynamics. Addressing this question requires the calculation of the forces acting on the point of tethering, exerted by the sperm cell with a prescribed, hyperactive, beat pattern.

## 3.3 Model Formulation

### 3.3.1 The Validity of Resistive-Force Theory (RFT)

In order to use background material regarding Stokes flow in Section 1.3 to calculate the forces exerted by a sperm cell in the female reproductive tract, it must first be verified that the relevant fluid dynamics are indeed governed by the Stokes equations, (1.7) and (1.8). To do so, recall that the Stokes equations rely on the dimensionless, Reynolds number being small, given by $\mathrm{Re} = UL\rho/\mu$, where $U$ is the typical velocity scale, $L$ is the flagellum length, $\rho$ is the constant, fluid density and $\mu$ is the constant,

fluid viscosity. For consistency with the upcoming, experimental results in this chapter, a relatively low viscosity medium such as water is considered, for which $\rho \approx 10^3$ kg m$^{-3}$ and $\mu \approx 10^{-3}$ Pa s [61], giving $Re \sim 10^{-3}$ for a typical mammalian sperm cell, as detailed in Section 1.3.1.1 where $U$ is the flagellum wave speed. Hence, the assumption of a low Reynolds number environment is valid.

Note that there are no additional, gravity forces included in the Stokes equations, as motivated by detailed observations of human sperm motility, illustrating that the swimming direction of human sperm relative to the gravitational field has no discernible dynamical effect [104], as would be expected for cells sufficiently close to neutral buoyancy.

As discussed in Section 1.4, there are numerous formalisms for studying flagellar mechanics. These range from RFT [42, 64] to direct numerical solutions via boundary elements [82] or immersed boundaries [31]. These methods have a spectrum of accuracy which is inversely related to the ease of implementation, as reviewed by Gaffney *et. al.* [40]. More recently, the method of regularised Stokeslets [23] has also been used to explore the motion of sperm cells, for instance in the investigation of hyperactivity coupled with calcium dynamics [75]. Here, however, RFT is used [42, 64], a classical means of modelling the connection between flagellar waveforms and the viscous drags associated with inertialess, Newtonian fluid dynamics.

This modelling framework is straightforward to implement, but is only an approximation to the relationship between the viscous drag and velocity of a slender-body element [53, 64], typically considered in the absence of nearby surfaces. Nonetheless, RFT gives reasonable agreements with observations of motile bull sperm swimming near to a surface [35]. This is due, in part, to the extreme slenderness of a flagellum and the fact that the flagellum has to be very close to a surface for the resistive-force theory relationship between viscous drag and velocity to be violated. This is explicitly verified in the context of the present study; see Section 3.5. An additional mechanism for the breakdown of RFT arises due to flows induced by the cell body, as demonstrated by Johnson [53]. For the case of a headless, beating flagellum, by adjusting his resistance coefficients using an *ad hoc* parameter, Johnson showed that SBT and RFT were in agreement, even for beat amplitudes that were not small. However, these adjustments could not be made when a large head was included into the model. Brokaw and Johnson [54] then demonstrated that Lighthill's coefficients

(see expressions in 1.82) did not need the correction factor, hence these coefficients are used throughout this chapter. Furthermore, mammalian sperm heads are sufficiently small so as not to endanger RFT in this manner [54] and the sperm head is highly constrained due to tethering point, further reducing the flow field it generates. Consequently, RFT provides a simple means of generating leading-order estimates for the forces and torques exerted by the sperm at the tethering point, further discussed in the upcoming development of the modelling framework.

### 3.3.2 The Application of RFT

Recall, from Section 1.3.3, that RFT states the force per-unit-length, exerted by the flagellum to balance viscous drag, is approximated by

$$\mathbf{f}(s,t) \approx C_T \boldsymbol{V_T}(s,t) + C_N \boldsymbol{V_N}(s,t) + C_B \boldsymbol{V_B}(s,t). \tag{3.1}$$

Here, $s$ is arc-length along the centre-line of the flagellum, $t$ is time, $\boldsymbol{V_t}(s,t)$, $\boldsymbol{V_n}(s,t)$ and $\boldsymbol{V_b}(s,t)$ are the tangential, normal and binormal, velocity vectors to the flagellum centre-line at $s$, while $C_T$, $C_N$ and $C_B$ are tangential, normal and binormal, resistance coefficients respectively. The resistance coefficients depend linearly on the fluid viscosity, although, as noted in Section 1.3.3, their exact definitions can vary slightly depending on their derivation [42, 54, 64]. In this chapter, Lighthill's coefficients from (1.82) are used [64] as they have been shown to give a good agreement to the full, slender-body theory [54],

$$C_T = 2\pi\mu/\left(\log[2q/a] - 1/2\right), \quad C_N = C_B = 4\pi\mu/\left(\log[2q/a] + 1/2\right), \tag{3.2}$$

where $\mu$ is the viscosity and $q \approx 0.09\lambda$ for a flagellar beat pattern of wavelength $\lambda$. The presence of a planar boundary [55], to leading order, replaces the parameter $q$ in (3.2) with the height of the flagellum element above the boundary, provided the height is much greater than the flagellum radius but less than the flagellum half-length. However, the subsequent results in Section 3.5 highlight that the effect of a nearby surface is typically negligible.

Unit vectors moving with the flagellum are given by $\mathbf{e}_t(s,t)$ tangential to the flagellum centre-line, $\mathbf{e}_n(s,t)$ normal to the centre-line and $\mathbf{e}_b(s,t)$ binormal to the centre-line, where $\mathbf{e}_t \times \mathbf{e}_n = \mathbf{e}_b$. Using equation (3.1), an expression for the total force exerted by

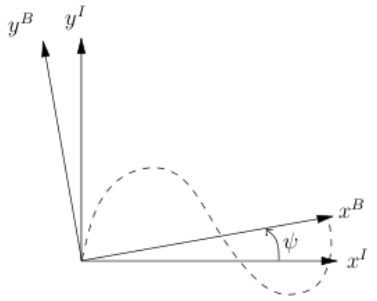


Figure 3.2: The inertial and body-fixed frames. The dashed curve represents a prescribed, flagellum waveform in the body-fixed frame.

the flagellum, $\mathbf{F}(t)$, can be obtained:

$$\begin{aligned}\mathbf{F}(t) &= \int_{\text{Flagellum}} \mathbf{f}(s',t)\ \mathrm{d}s', \\ &= \int_{\text{Flagellum}} [f_t(s',t)\mathbf{e}_t(s',t) + f_n(s',t)\mathbf{e}_n(s',t) \\ &\qquad + f_b(s',t)\mathbf{e}_b(s',t)\ ]\ \mathrm{d}s', \end{aligned} \tag{3.3}$$

where

$$f_t(s',t) := C_T\mathbf{V}(s',t)\cdot\mathbf{e}_t(s',t), \tag{3.4}$$

$$f_n(s',t) := C_N\mathbf{V}(s',t)\cdot\mathbf{e}_n(s',t), \tag{3.5}$$

$$f_n(s',t) := C_B\mathbf{V}(s',t)\cdot\mathbf{e}_b(s',t). \tag{3.6}$$

The integration is over the length of the flagellum and $\mathbf{V}(s',t)$ is the velocity of the flagellum centre-line. The total torque exerted by the flagellum, $\mathbf{L}(t)$, is determined by integrating the vector product of the centre-line position, $\boldsymbol{\xi}(s,t)$, with the force per-unit-length:

$$\mathbf{L}(t) = \int_{\text{Flagellum}} \boldsymbol{\xi}(s',t)\times\mathbf{f}(s',t)\ \mathrm{d}s'. \tag{3.7}$$

In order to model a sperm cell tethered at one point on the sperm head, a body-fixed frame is first introduced, denoted by a superscript B in figure 3.2. This is inclined at a tethering angle $\psi(t)$ from the inertial frame, indicated by the superscript I. To address the question as to whether the flagellum pushes the sperm further into the point of tethering, or pulls it away, the force in the body-fixed frame, exerted by the flagellum on the fluid, must be calculated. In particular, it is the force in the body-fixed $x$ direction, $F_x^B(t)$, which characterises the pushing or pulling behaviour of the sperm. It should be noted that $F_x^B(t)$ is the force the flagellum exerts on the

fluid, not the force the flagellum exerts on the tethering point. However, recalling that all forces in a Stokes fluid are balanced from Section 1.3.1.3, these forces exactly balance each other, giving the force on the tethering point as $-F_x^B(t)$.

A two-dimensional, planar waveform, $y(x,t)$, representing the flagellum centre-line is prescribed in the body-fixed frame along the body-fixed $x$ axis. The centre-line velocity, subject to the constraint of constant, total flagellum arc-length is thus determined. Equations (3.3) and (3.7) are then used to calculate the forces and torques in the inertial frame induced by different waveforms. The forces can subsequently be written in terms of the body-fixed frame in order to deduce $-F_x^B(t)$, as discussed above.

The notation $x$ and $y$ will denote the coordinates of the body-fixed frame, whilst $x^I$ and $y^I$ are the coordinates of the inertial frame. Thus,

$$\begin{pmatrix} x^I \\ y^I \\ 0 \end{pmatrix} = \mathbf{Q}(t) \begin{pmatrix} x \\ y \\ 0 \end{pmatrix}, \tag{3.8}$$

where

$$\mathbf{Q}(t) := \begin{pmatrix} \cos\psi(t) & -\sin\psi(t) & 0 \\ \sin\psi(t) & \cos\psi(t) & 0 \\ 0 & 0 & 0 \end{pmatrix}. \tag{3.9}$$

The centre-line is given by

$$\boldsymbol{\xi}(x,t) = \mathbf{Q}(t) \begin{pmatrix} x \\ y(x,t) \\ 0 \end{pmatrix}, \tag{3.10}$$

with unit vectors

$$\mathbf{e}_t(x,t) = \mathbf{Q}(t) \begin{pmatrix} 1 \\ \frac{\partial y}{\partial x}(x,t) \\ 0 \end{pmatrix} \frac{1}{\sqrt{1 + \left(\frac{\partial y}{\partial x}(x,t)\right)^2}}, \tag{3.11}$$

$$\mathbf{e}_n(x,t) = \mathbf{Q}(t) \begin{pmatrix} -\frac{\partial y}{\partial x}(x,t) \\ 1 \\ 0 \end{pmatrix} \frac{1}{\sqrt{1 + \left(\frac{\partial y}{\partial x}(x,t)\right)^2}}. \tag{3.12}$$

The binormal, unit vector, $\mathbf{e}_b(x,t)$, is identically zero, without loss of generality, due to the prescribed waveform, $y(x,t)$, being planar.

The required force in the body-fixed frame, $\mathbf{F}^B(t)$, can be written in terms of the force in the inertial frame, $\mathbf{F}(t)$, with the latter given by RFT in (3.3); the two coordinate frames are related by the time-dependent, rotational matrix $\mathbf{Q}(t)$ in (3.8). Noting that the integral in (3.3) is along the arc-length of the centre-line with constant limits, $\mathbf{Q}(t)$ satisfies

$$\begin{aligned}\mathbf{F}^B(t) &= \mathbf{Q}^{-1}(t)\mathbf{F}(t),\\ &= \int_{\text{Flagellum}} \mathbf{Q}^{-1}(t)\left[f_t(s',t)\mathbf{e}_t(s',t) + f_n(s',t)\mathbf{e}_n(s',t)\right]\,\mathrm{d}s',\end{aligned} \tag{3.13}$$

for the planar case being considered. The centre-line is prescribed as $y(x,t)$, thus a change of variables from arc-length to the body-fixed $x$ coordinate is required. The arc-length, $s(x,t)$, is given by the standard relation

$$s(x,t) = \int_0^x \sqrt{1 + \left(\frac{\partial y}{\partial \bar{x}}(\bar{x},t)\right)^2}\,\mathrm{d}\bar{x}, \tag{3.14}$$

thus, retaining the same notation to avoid confusion,

$$\mathbf{F}^B(t) = \int_{\text{Flagellum}_x} \mathbf{Q}^{-1}(t)\left[f_t(x',t)\mathbf{e}_t(x',t) + f_n(x',t)\mathbf{e}_n(x',t)\right]\,\sqrt{1 + \left(\frac{\partial y}{\partial x'}\right)^2}\,\mathrm{d}x'. \tag{3.15}$$

In (3.15),

$$f_t(x',t) := C_T\mathbf{V}(x',t)\cdot\mathbf{e}_t(x',t), \tag{3.16}$$

$$f_n(x',t) := C_N\mathbf{V}(x',t)\cdot\mathbf{e}_n(x',t). \tag{3.17}$$

the integration range in (3.15) covers all of the flagellum, thus the upper $x$ limit of the integral is varied to preserve the total, flagellar arc-length; a precise definition of these limits is given later, in dimensionless form, by equation (3.33). Inserting the definitions of the unit vectors in terms of $x$, (3.11) and (3.12), into (3.15) gives

$$\mathbf{F}^B(t) = \int_{\text{Flagellum}_x} \left[\begin{pmatrix} 1 \\ \frac{\partial y}{\partial x'}(x',t) \\ 0 \end{pmatrix} f_t(x',t) + \begin{pmatrix} -\frac{\partial y}{\partial x'}(x',t) \\ 1 \\ 0 \end{pmatrix} f_n(x',t)\right]\,\mathrm{d}x'. \tag{3.18}$$

Care must be taken when deducing the velocity. The centre-line is given by (3.10), thus the derivative with respect to time, whilst keeping arc-length $s$ constant, is

$$\begin{aligned}\mathbf{V}(x,t) &= \frac{\partial \boldsymbol{\xi}}{\partial s}\frac{\partial s}{\partial t} + \frac{\partial \boldsymbol{\xi}}{\partial t},\\ &= \mathbf{e}_t(x,t)\frac{\partial s}{\partial t} + \frac{\partial \mathbf{Q}}{\partial \psi}\frac{\mathrm{d}\psi}{\mathrm{d}t}\begin{pmatrix} x \\ y(x,t) \\ 0 \end{pmatrix} + \mathbf{Q}(t)\begin{pmatrix} 0 \\ \frac{\partial y}{\partial t} \\ 0 \end{pmatrix}.\end{aligned} \tag{3.19}$$

In the first term, the derivative with respect to arc-length of the centre-line is the tangent vector. In the second term, the centre-line from (3.10) was inserted and differentiated, introducing $\partial\mathbf{Q}/\partial\psi$ with matrix elements $\partial Q_{ij}/\partial\psi$ from $Q_{ij}$. The time derivative of the arc-length, from (3.14) is

$$\frac{\partial s}{\partial t} = \int_0^x \frac{\frac{\partial y}{\partial \bar{x}}\frac{\partial^2 y}{\partial t \partial \bar{x}}}{\sqrt{1+\left(\frac{\partial y}{\partial \bar{x}}\right)^2}}\,\mathrm{d}\bar{x}. \tag{3.20}$$

Inserting (3.19) and (3.20) into (3.16) and (3.17) gives, using the unit-vector definitions (3.11) and (3.12) and dropping arguments for brevity,

$$f_t(x,t) = C_T\left[\int_0^x \frac{\frac{\partial y}{\partial \bar{x}}\frac{\partial^2 y}{\partial t \partial \bar{x}}}{\sqrt{1+\left(\frac{\partial y}{\partial \bar{x}}\right)^2}}\,\mathrm{d}\bar{x} + \frac{\frac{\mathrm{d}\psi}{\mathrm{d}t}\left(-y + x\frac{\partial y}{\partial x}\right) + \frac{\partial y}{\partial x}\frac{\partial y}{\partial t}}{\sqrt{1+\left(\frac{\partial y}{\partial x}\right)^2}}\right], \tag{3.21}$$

$$f_n(x,t) = C_N\left[\frac{\frac{\mathrm{d}\psi}{\mathrm{d}t}\left(x + y\frac{\partial y}{\partial x}\right) + \frac{\partial y}{\partial t}}{\sqrt{1+\left(\frac{\partial y}{\partial x}\right)^2}}\right]. \tag{3.22}$$

These are now inserted back into (3.18). In particular, the force in the body-fixed $x$ direction, $F_x^B(t)$, is the first component of (3.18), namely

$$\begin{aligned} F_x^B(t) = \int_{\mathrm{Flagellum}_x} & C_T\left[\int_0^{x'} \frac{\frac{\partial y}{\partial \bar{x}}\frac{\partial^2 y}{\partial t \partial \bar{x}}}{\sqrt{1+\left(\frac{\partial y}{\partial \bar{x}}\right)^2}}\,\mathrm{d}\bar{x} + \frac{\frac{\mathrm{d}\psi}{\mathrm{d}t}\left(-y + x'\frac{\partial y}{\partial x'}\right) + \frac{\partial y}{\partial x'}\frac{\partial y}{\partial t}}{\sqrt{1+\left(\frac{\partial y}{\partial x'}\right)^2}}\right] \\ & - C_N\frac{\partial y}{\partial x'}\left[\frac{\frac{\mathrm{d}\psi}{\mathrm{d}t}\left(x' + y\frac{\partial y}{\partial x'}\right) + \frac{\partial y}{\partial t}}{\sqrt{1+\left(\frac{\partial y}{\partial x'}\right)^2}}\right]\mathrm{d}x'. \end{aligned} \tag{3.23}$$

Thus, by prescribing a waveform $y(x,t)$, equation (3.23) determines the pushing or pulling force exerted by the flagellum on the fluid in the body-fixed $x$ direction. However, the rate of change of the tethering angle, $d\psi/dt$, has yet to be determined, requiring specified boundary conditions to do so.

### 3.3.3 Boundary Conditions at the Tethering Point

At the point of tethering, the two different boundary conditions to be explored are, firstly, where the sperm is freely hinged and subsequently where the sperm is clamped. There are many feasible binding scenarios and hence these two cases are considered in detail as they reflect the most extreme situations for the nature of the binding at the front of the sperm head to the reproductive-tract surface. For example, the freely

hinged case could represent the binding to cilia protruding from the tract walls, while the clamped case could model a sperm wedged into a wall crypt [91].

An evolution equation for $\psi(t)$ in the **freely hinged** sperm case is derived by invoking zero torque about the tethering point, using equation (3.7). As the waveforms are planar, the torque only has a component in the binormal direction, thus this is set to zero. From the torque equation, (3.7), written in terms of $x$ and set equal to zero,

$$0 = \int_{\text{Flagellum}_x} \boldsymbol{\xi}(x',t) \times \left[ f_t(x',t)\mathbf{e}_t(x',t) + f_n(x',t)\mathbf{e}_n(x',t) \right] \sqrt{1 + \left(\frac{\partial y}{\partial x'}\right)^2}\, \mathrm{d}x'. \tag{3.24}$$

The centre-line, $\boldsymbol{\xi}(x',t)$, is given by (3.10), the force components by (3.21) and (3.22), and the unit vectors by (3.11) and (3.12). Inserting these into (3.24) and simplifying gives

$$\begin{aligned} \mathbf{0} = \int_{\text{Flagellum}_x} & C_T \left[ \frac{\frac{\mathrm{d}\psi}{\mathrm{d}t}\left(x'\frac{\partial y}{\partial x'} - y\right)^2 + \frac{\partial y}{\partial x'}\frac{\partial y}{\partial t}\left(x'\frac{\partial y}{\partial x'} - y\right)}{\sqrt{1+\left(\frac{\partial y}{\partial x'}\right)^2}} \right] \\ & + C_T \left( x'\frac{\partial y}{\partial x'} - y \right) \int_0^{x'} \frac{\frac{\partial y}{\partial \bar{x}}\frac{\partial^2 y}{\partial t \partial \bar{x}}}{\sqrt{1+\left(\frac{\partial y}{\partial \bar{x}}\right)^2}}\, \mathrm{d}\bar{x} \\ & + C_N \left[ \frac{\frac{\mathrm{d}\psi}{\mathrm{d}t}\left(y\frac{\partial y}{\partial x'} + x'\right)^2 + \frac{\partial y}{\partial t}\left(y\frac{\partial y}{\partial x'} + x'\right)}{\sqrt{1+\left(\frac{\partial y}{\partial x'}\right)^2}} \right] \mathrm{d}x'. \end{aligned} \tag{3.25}$$

The $\mathrm{d}\psi/\mathrm{d}t$ term can be taken outside the integrals, despite the time-varying limits accounting for the conservation of flagellum arc-length as $\mathrm{d}\psi/\mathrm{d}t$ is independent of arc-length. Rearranging gives

$$\frac{\mathrm{d}\psi}{\mathrm{d}t} = \frac{-\int_{\text{Flagellum}_x} \left[ \frac{C_T\left(x'\frac{\partial y}{\partial x'} - y\right)^2 + C_N\left(y\frac{\partial y}{\partial x'} + x'\right)^2}{\sqrt{1+\left(\frac{\partial y}{\partial x'}\right)^2}} + C_T\left(x'\frac{\partial y}{\partial x'} - y\right)\left( \int_0^{x'} \frac{\frac{\partial y}{\partial \bar{x}}\frac{\partial^2 y}{\partial t \partial \bar{x}}}{\sqrt{1+\left(\frac{\partial y}{\partial \bar{x}}\right)^2}}\, \mathrm{d}\bar{x} \right) \right] \mathrm{d}x'}{\int_{\text{Flagellum}_x} \left[ \frac{C_T\frac{\partial y}{\partial x'}\frac{\partial y}{\partial t}\left(x'\frac{\partial y}{\partial x'} - y\right) + C_N\frac{\partial y}{\partial t}\left(y\frac{\partial y}{\partial x'} + x'\right)}{\sqrt{1+\left(\frac{\partial y}{\partial x'}\right)^2}} \right] \mathrm{d}x'}. \tag{3.26}$$

The model does not include a sperm head due to its small size and constrained motion, as mentioned in Section (3.3). Thus, the origin of the body-fixed frame axes corresponds to the flagellum-head junction, denoted by $J$. The zero-torque condition for deriving the evolution equation for $\psi(t)$ in this freely hinged case has been enforced via the torque about $J$, i.e. $\mathbf{L}_J(t)$. However, including a head implies

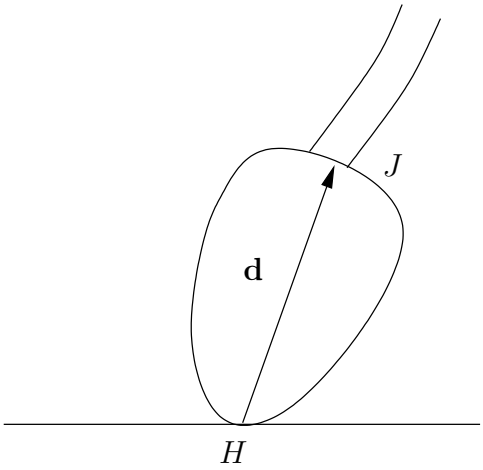


Figure 3.3: The sperm head tethered to the female reproductive tract. The tether is at $H$, the head-flagellum junction is at $J$ and the vector between them is denoted $\mathbf{d}$.

one should enforce zero torque about the tethering point at the front of the head; denote this point by $H$, with the corresponding torque about $H$ given by $\mathbf{L}_H(t)$; see figure 3.3. With $\mathbf{d}$ being the vector from $H$ to $J$, i.e. the major axis of the head,

$$\mathbf{L}_H(t) = \mathbf{L}_J(t) + \mathbf{d} \times \mathbf{F}(t). \tag{3.27}$$

By considering the sizes of the terms, $\mathbf{L}_H(t) \sim O(\tilde{F}L)$ where $L$ is the flagellum length scale and $\tilde{F}$ is the force scale. Similarly, $\mathbf{d} \times \mathbf{F}(t) \sim O(\tilde{F}d)$ where $d$ is the typical head length. Hence, in order to justify deriving equation (3.26) which enforces zero torque about $J$, not $H$, one requires $d/L \ll 1$. This is valid given typical, parameter values for mammalian sperm, for example $d \approx 5\mu$m and $L \approx 50\mu$m for human sperm and $d \approx 15\mu$m and $L \approx 180\mu$m for golden-hamster sperm, [28].

In the **clamped** scenario, the flagellum is not allowed to rotate about the tethering point and hence the evolution equation is simply

$$\frac{\mathrm{d}\psi}{\mathrm{d}t} = 0, \tag{3.28}$$

for all time $t$, giving $\psi = \psi_0$ for an initial angle $\psi_0$.

### 3.3.4 Constructing Waveforms

In order to investigate the effects of a hyperactive waveform on the pushing or pulling forces generated, both a symmetric (non-hyperactivated) and hyperactive waveform

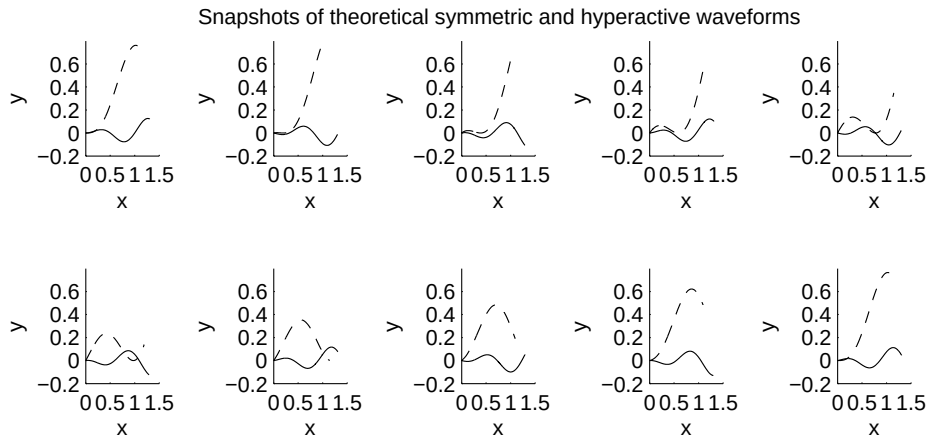


Figure 3.4: Snapshots of the theoretical symmetric and hyperactivated waveforms, represented by continuous and dashed curves respectively. The dimensionless time-steps increment by two time units for each plot across the first row, from left to right, and then analogously for the second row, over the dimensionless period of a hyperactive wave with the relative frequency of $\Omega = 0.35$, motivated by golden-hamster sperm data [72]. These flagellar, beat patterns are presented with respect to dimensionless, horizontal and vertical axes and given dimensionlessly in (3.30); see Section 3.3.5 for the non-dimensionalisation.

are theoretically constructed using sinusoidal, travelling waves. These are bounded in a linear envelope to ensure the tethered end does not oscillate, so that

$$\begin{aligned} y^s(x,t) &= Ax\sin(kx-\omega t) && \text{symmetric,} \\ y^h(x,t) &= \Delta Ax\,(1-\cos(Kkx-\Omega\omega t)) && \text{hyperactive (asymmetric),} \\ y^{hs}(x,t) &= -\Delta Ax\cos(Kkx-\Omega\omega t) && \text{hyperactive (symmetric).} \end{aligned} \tag{3.29}$$

Notice that two hyperactive waveforms are introduced, one with asymmetry as expected [72] and one without, in order to compare the effects of asymmetry in the subsequent parameter studies. Here $x$ and $y$ are the body-fixed frame coordinates, and $k$ and $\omega$ are the symmetric-beat wavenumber and frequency respectively. The constant $A$ is the ratio of a typical beat amplitude, $D$, over the symmetric-beat wavelength, $\lambda$, so that at $x = \lambda$, $y \sim A\lambda = D$. Furthermore, $\Delta$, $K$ and $\Omega$ are all positive and represent the relative changes in amplitude, wavenumber and frequency respectively, upon hyperactivation when compared to the symmetric case. In golden-hamster sperm, for example, these take the values $\Delta = 4$, $K = 4/7$ and $\Omega = 0.35$ [72].

The asymmetry in the hyperactive waveform given by (3.29) stems from the translation of a sinusoidal wave in the positive $y$ direction, yielding a larger amplitude on one side of the body-fixed $x$ axis, as illustrated in figure 3.4. This is consistent

Table 3.1: Parameter estimates for sperm cell and flagellum dimensions, together with typical, beat-pattern variables, swimming speeds, viscosities and Reynolds numbers.

| Parameter | Symbol | Golden Hamster | Human |
|---|---|---|---|
| Flagellum length | $L$ | 180 $\mu$m [28] | 50 $\mu$m [28] |
| Flagellum radius | $a$ | 370 nm [7] | 200 nm [7] |
| Head major axis | $d$ | 15 $\mu$m [28] | 5 $\mu$m [28] |
| Head minor axis | - | 3 $\mu$m [28] | 3 $\mu$m [28] |
| Swimming speed | $V$ | $10^{-4}$ m/s [72] | $7 \times 10^{-5}$ m/s [86] |
| Reynolds number (for water [61]) | $Re$ | $2 \times 10^{-2}$ | $4 \times 10^{-3}$ |
| Resistance coefficient ratio | $\gamma = C_N/C_T$ | 1.6 | 1.5 |
| No. of wavelengths down symmetric flagellum | $\Lambda$ | 1.3 [72] | 1.3 [86] |
| Symmetric-beat wavelength | $\lambda = 2\pi/k = L/\Lambda$ | 140 $\mu$m | 40 $\mu$m |
| Symmetric-beat frequency | $\omega$ | 10 Hz [72] | 10 Hz [86] |
| Symmetric-beat amplitude / wavelength | $A$ | 0.1 [72] | 0.1 [86] |

with observations of larger principle and smaller reverse waves [102]. The radius of curvature of these waveforms must be larger than the cross-sectional radius of the flagellum, and the flagellum itself must not approach self-intersection, both of which are required for a reasonable agreement of RFT with the full, slender-body theory [53, 54]. Given the centre-line curvature scales as $D/L^2$ where $D$ is the amplitude of the flagellum waveform and $L$ is the flagellum arc-length, the scale of the radius of curvature is $L^2/D$. This must be much larger than $a$, the cross-sectional radius, giving a limitation on the amplitude as $D \ll L^2/a$. Noting that $D = A\lambda$ from above and $L \approx \Lambda\lambda$, where $\Lambda$ is defined to be the number of wavelengths down a typical, symmetric beat, the constraint becomes $A \ll \Lambda L/a$ for $A$ in (3.29). This is readily satisfied for slender, biological flagella, noting that $\Lambda \sim O(1)$ from table 3.1 and $a/L \ll 1$ is the slenderness ratio, assumed to be asymptotically small when deriving RFT from SBT; see Section 4.3.3.

As an aside, note that the theory can be developed in terms of bend angle, $\theta$, and arc-length, $s$, where forces and torques are integrated along the arc-length. However, deducing waveforms in these coordinates can be analytically cumbersome and does not offer further insight.

### 3.3.5 Parameter Estimates and Non-dimensionalisation

For the typical magnitudes of the dimensions for a sperm cell, we appeal to mammalian studies [28], in particular hamster [7, 72] and human sperm [7, 86], giving the parameter estimates and scales shown in table 3.1.

In addition, a non-dimensionalisation with respect to symmetric, beating parameters is applied, thus the lengths $(x, y)$ are non-dimensionalised by the wavelength, $\lambda$, of a typical, symmetric beat pattern, which differs between hamster and human sperm; see table 3.1. Further, note that $k = 2\pi/\lambda$ where $k$ is the symmetric-beat wavenumber, and time is scaled with $1/\omega$, where $\omega$ is the symmetric-beat frequency. The dimensionless waveforms from (3.29) are given by

$$\begin{aligned}
\hat{y}^s(\hat{x},\hat{t}) &= A\hat{x}\sin(2\pi\hat{x}-\hat{t}) && \text{symmetric,}\\
\hat{y}^h(\hat{x},\hat{t}) &= A\Delta\hat{x}\left(1-\cos\left(2K\pi\hat{x}-\Omega\hat{t}\right)\right) && \text{hyperactive (asymmetric),}\\
y^{hs}(\hat{x},\hat{t}) &= -A\Delta\hat{x}\cos\left(2K\pi\hat{x}-\Omega\hat{t}\right) && \text{hyperactive (symmetric).}
\end{aligned} \tag{3.30}$$

where hats indicate dimensionless variables and $A$ is the ratio of the symmetric beat amplitude to the wavelength.

Note that the dimensionless quantities $A$ and $\Lambda$ in table 3.1 are essentially the same for golden hamster and human sperm, as is the ratio of the resistance coefficients, $\gamma$, henceforth taken to be the average of the human and hamster values (after incorporating any relative-wavenumber changes upon hyperactivation). This ensures that the qualitative conclusions drawn from the dimensionless model are valid for either species. Further, upon non-dimensionalising, the parameters of interest are identified as those representing the changes from symmetric to hyperactive behaviour, namely the relative amplitude, $\Delta$, relative wavenumber, $K$, and relative frequency, $\Omega$.

The force and torque scalings emerge as $\tilde{F} = \lambda^2 C_T \omega$ and $\tilde{L} = \lambda^3 C_T \omega$ respectively, with the dimensionless analogues of equations (3.31) and (3.32) given by

$$\begin{aligned}
\hat{F}^B_{\hat{x}}(\hat{t}) = \int_{\text{Flagellum}_{\hat{x}}} &\left[\int_0^{\hat{x}'} \frac{\frac{\partial\hat{y}}{\partial\hat{\tilde{x}}}\frac{\partial^2\hat{y}}{\partial\hat{t}\partial\hat{\tilde{x}}}}{\sqrt{1+\left(\frac{\partial\hat{y}}{\partial\hat{\tilde{x}}}\right)^2}}\,\mathrm{d}\hat{\tilde{x}} + \frac{\frac{\mathrm{d}\psi}{\mathrm{d}\hat{t}}\left(-\hat{y}+\hat{x}'\frac{\partial\hat{y}}{\partial\hat{x}'}\right)+\frac{\partial\hat{y}}{\partial\hat{x}'}\frac{\partial\hat{y}}{\partial\hat{t}}}{\sqrt{1+\left(\frac{\partial\hat{y}}{\partial\hat{x}'}\right)^2}}\right]\\
&-\gamma\frac{\partial\hat{y}}{\partial\hat{x}'}\left[\frac{\frac{\mathrm{d}\psi}{\mathrm{d}\hat{t}}\left(\hat{x}'+\hat{y}\frac{\partial\hat{y}}{\partial\hat{x}'}\right)+\frac{\partial\hat{y}}{\partial\hat{t}}}{\sqrt{1+\left(\frac{\partial\hat{y}}{\partial\hat{x}'}\right)^2}}\right]\mathrm{d}\hat{x}',
\end{aligned} \tag{3.31}$$

and

$$\frac{\mathrm{d}\psi}{\mathrm{d}\hat{t}} = \frac{-\int_{\mathrm{Flagellum}_{\hat{x}}} \left[ \frac{\frac{\partial \hat{y}}{\partial \hat{x}'}\frac{\partial \hat{y}}{\partial \hat{t}}\left(\hat{x}'\frac{\partial \hat{y}}{\partial \hat{x}'}-\hat{y}\right)+\gamma\frac{\partial \hat{y}}{\partial \hat{t}}\left(\hat{y}\frac{\partial \hat{y}}{\partial \hat{x}'}+\hat{x}'\right)}{\sqrt{1+\left(\frac{\partial \hat{y}}{\partial \hat{x}'}\right)^2}} + \left(\hat{x}'\frac{\partial \hat{y}}{\partial \hat{x}'}-\hat{y}\right)\left(\int_0^{\hat{x}'} \frac{\frac{\partial \hat{y}}{\partial \hat{\tilde{x}}}\frac{\partial^2 \hat{y}}{\partial \hat{t}\partial \hat{\tilde{x}}}}{\sqrt{1+\left(\frac{\partial \hat{y}}{\partial \hat{\tilde{x}}}\right)^2}}\,\mathrm{d}\hat{\tilde{x}}\right)\right] \mathrm{d}\hat{x}'}{\int_{\mathrm{Flagellum}_{\hat{x}}} \frac{\left(\hat{x}'\frac{\partial \hat{y}}{\partial \hat{x}'}-\hat{y}\right)^2+\gamma\left(\hat{y}\frac{\partial \hat{y}}{\partial \hat{x}'}+\hat{x}'\right)^2}{\sqrt{1+\left(\frac{\partial \hat{y}}{\partial \hat{x}'}\right)^2}}\,\mathrm{d}\hat{x}'}. \tag{3.32}$$

The notation $\int_{\mathrm{Flagellum}_{\hat{x}}}$ in equations (3.31) and (3.32) denotes an integral in $\hat{x}'$ from $\hat{x}' = 0$ to $\hat{x}' = X(\hat{t})$, where $X(\hat{t})$ varies to conserve the arc-length of the symmetric (s) and hyperactive (h) waveforms in (3.30). However, as the symmetric waveform beats with a low amplitude, $X(\hat{t}) \approx 1.3$ for the symmetric waveform, given there are approximately 1.3 wavelengths down a symmetric flagellum in bothgolden-hamster and human sperm; see table (3.1). The hyperactive waveform has a larger amplitude, thus, $X(\hat{t})$ satisfies

$$\int_0^{X(\hat{t})} \sqrt{1+\left(\frac{\partial \hat{y}}{\partial \hat{x}'}^{h}(\hat{x}',\hat{t})\right)^2}\, d\hat{x}' = \tilde{L} \approx \int_0^{1.3} \sqrt{1+\left(\frac{\partial \hat{y}}{\partial \hat{x}'}^{s}(\hat{x}',0)\right)^2}\, d\hat{x}'. \tag{3.33}$$

Here, the total arc-length of the symmetric waveform at $\hat{t} = 0$ is used as defining the dimensionless flagellum length, $\tilde{L}$; due to the small amplitude of the symmetric waveforms, the effects on $X(\hat{t})$ of using other reference values of $\hat{t}$ are negligible.

### 3.3.6 Model Summary

By prescribing either symmetric or hyperactive waveforms given by (3.30), one can calculate the rate of change of the tethering angle, $\mathrm{d}\psi/\mathrm{d}t$ from (3.32) or (3.28) depending on whether the sperm cell is freely hinged, or clamped, at the tethering point. This expression is then inserted into (3.31) to calculate $\hat{F}^B_{\hat{x}}(\hat{t})$, the dimensionless force in the body-fixed $x$ direction. Following the previous argument of the balance of forces in a Stokes fluid, the (dimensionless) force acting on the tethering point is given by $-\hat{F}^B_{\hat{x}}(\hat{t})$. Thus, when $\hat{F}^B_{\hat{x}}(\hat{t}) > 0$, the sperm flagellum pushes the cell into its substrate, with the converse for $\hat{F}^B_{\hat{x}}(\hat{t}) < 0$. The results are presented in terms of dimensionless variables, where the parameter estimates and scalings used have been given in Section 3.3.5 and Table 3.1.

## 3.4 Experimental Data

This section describes the experimental methods used for the production of images illustrating human-sperm behaviour in a resected, epithelial tract, for qualitative comparison with the theoretical results. The experiments were conducted by T. Connolly

and J. Kirkman-Brown; see the statement of originality in Section 1.6.

Healthy sperm donors were recruited at the Birmingham Women's Hospital (HFEA Centre 0119), in accordance with the Human Embryology Authority Code of Practice and provided informed consent according to Local Ethical Approval (South Birmingham LREC# 2003/239). Human spermatozoa were obtained by masturbation and the semen allowed to liquify at 20 °C for 30 minutes. Sperm were then selected by a modified, direct swim-up technique into sEBSS (supplemented Earl's Balance Salt Solution). After a 1-hour incubation at 37 °C, 6% $CO_2$ and at an angle of 45 °, the top 0.5ml layer of each tube, containing the selected, motile cells, was collected and pooled. Sperm concentration was determined using a Neubauer counting chamber, in accordance with the World Health Organisation methods [1] and adjusted with sEBSS + 0.3% BSA (Bovine Serum Albumin) and 10mM HEPES (a buffer) to 0.5 million cells/ml. Sperm were then allowed to capacitate for at least 3 hours, at 37 °C and 6% $CO_2$ prior to imaging experiments.

All explant preparations of female, reproductive-tract cells were performed immediately after patient surgery, with tract tissue placed directly into HBSS (Hank's Balanced Salt Solution). Patients were selected on the basis of undergoing routine hysterectomy or bilateral salpingectomy and consented according to Local Ethical Approval (06/Q2601/51). Patients were excluded on the basis of any underlying tubal pathology. After transfer to the University of Birmingham laboratory, epithelium was isolated by dissecting small pieces of the epithelial surface under a stereomicroscope. Hanks balanced salt solution with Calcium and Magnesium (HBSS, Invitrogen) and supplemented, Earles Balanced Salt Solution (sEBSS, Biological Industries, Israel) were used. Both solutions had additional 100 $\mu$g/ml streptomycin, 100 units/ml penicillin (Gibco), 10mM HEPES and 10% FBS (Fetal Bovine Solution, Biosera).

The cell interactions were imaged in glass-bottomed chambers (Imaging Chamber #01, Cairn Research Ltd) on a Nikon TE2000 with Hoffman Modulation Contrast optics at 40x, with image acquisition on a QuantEM camera (Photometrics UK) controlled by an integrated, imaging system running Cairn Optomorph (Cairn Research Ltd).

## 3.5 Results

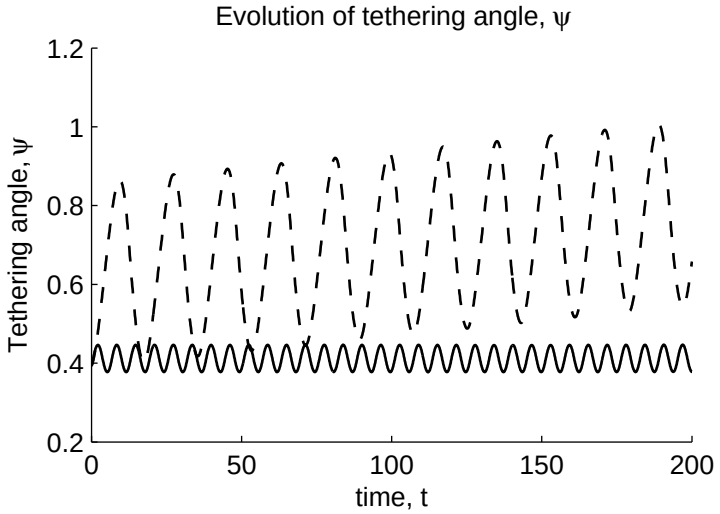


Figure 3.5: The evolution of the angle between the body-fixed frame and the inertial frame, $\psi(T)$, for a freely hinged sperm in terms of dimensionless time, $\omega t$, where $\omega$ is the symmetric, waveform frequency. The initial condition $\psi_0 = \pi/8$. The relative, hyperactivation, parameter values chosen for this figure are $\Delta = 4$, $K = 4/7$ and $\Omega = 0.35$ from golden-hamster sperm observations [72]. The results for symmetric and hyperactivated waveforms are given by continuous and dashed curves respectively. Note that, as expected, the symmetric waveforms do not cause a net rotation, however the hyperactive waveforms exhibit a net, linear, angular velocity which would rotate the flagellum about the tethering point until the whole flagellum is within microns from a surface or intersects the surface, by which point the model has become invalid.

Modelling predictions are presented for the cases of a sperm being freely hinged, or clamped, at the point of tethering in order to see the differences between the symmetric and hyperactive behaviour. In addition, further results illustrating the significance of the hyperactivation parameters are presented, together with images from observations of adhered, human-sperm cells exhibiting a tugging motion away from an epithelial substrate; the associated movie can be found in the supplementary material of the publication [29].

All forces are given in the body-fixed frame, i.e. the frame inclined at a tethering angle $\psi(t)$ from the inertial frame (figure 3.2), where the planar waveform $y(x,t)$ is prescribed along the body-fixed $x$ axis. Results for the forces are presented dimensionlessly with respect to the force scale $C_T\lambda^2\omega$, where $C_T$ is the tangential, resistance coefficient from (3.2) and $\lambda$ and $\omega$ are respectively the symmetric, flagellar wavelength and beat frequency used for non-dimensionalisation, as detailed in Section 3.3.5. In

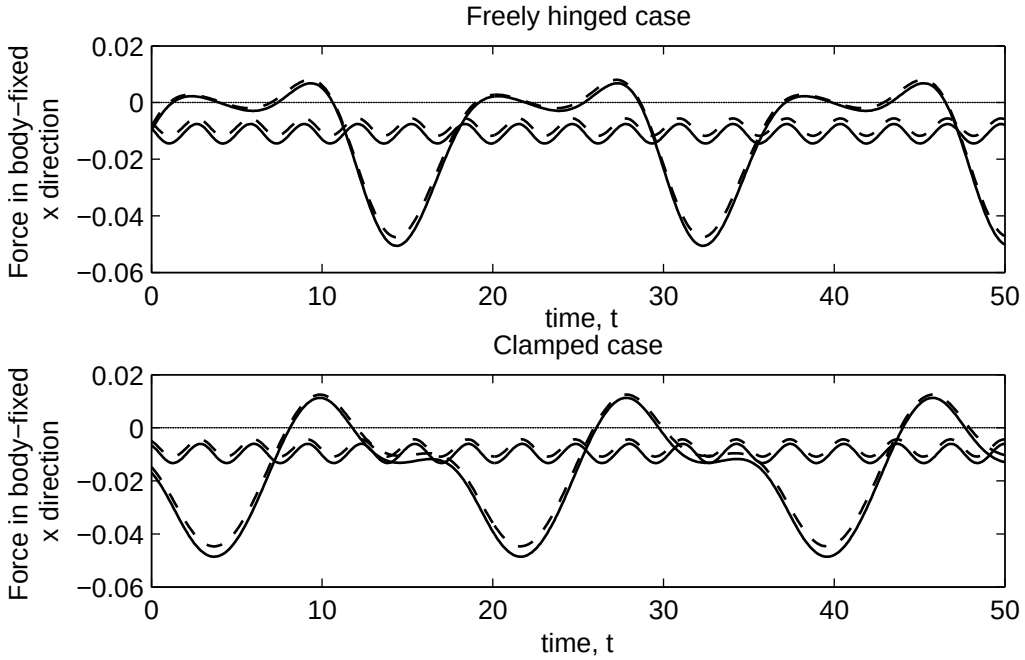


Figure 3.6: Plots of the dimensionless force along the body-fixed $x$ direction exerted on the tethering point for the parameters of table 3.1 and golden-hamster hyperactivation parameters: $\Delta = 4$, $K = 4/7$ and $\Omega = 0.35$ [72]. The vertical axes are in units of $C_T\lambda^2\omega$ where $C_T$ is the tangential, resistance coefficient, $\lambda$ is the symmetric flagellar wavelength and $\omega$ is the symmetric, waveform frequency used for non-dimensionalisation; the horizontal axes are in units of dimensionless time. The results for symmetric and hyperactivated waveforms are given by the continuous curves with the smaller and larger amplitudes respectively in each plot. They do not depend on the initial angle of the body-fixed frame to the inertial frame, $\psi_0$. Similar results which include the effect of a boundary at a height $10a$ from the flagellum, where $a$ is the flagellum radius, are given by the dashed curves. The freely hinged and clamped cases are shown in the upper and lower graphs respectively and, for reference, the horizontal line of zero force in the body-fixed $x$ direction is highlighted in both. The graphs predict that symmetric waveforms always push into the tethering point since the force in the body-fixed $x$ direction exerted on the tethering point is always negative, as expected. However, the force along the body-fixed $x$ direction can become positive for the hyperactive waveform, indicating a tugging motion on the tethering point, though on average the force still pushes into the tether. The effect of a nearby boundary does not appear to change these conclusions.

particular, note that $\lambda$ differs between human and hamster when re-dimensionalising; see table 3.1.

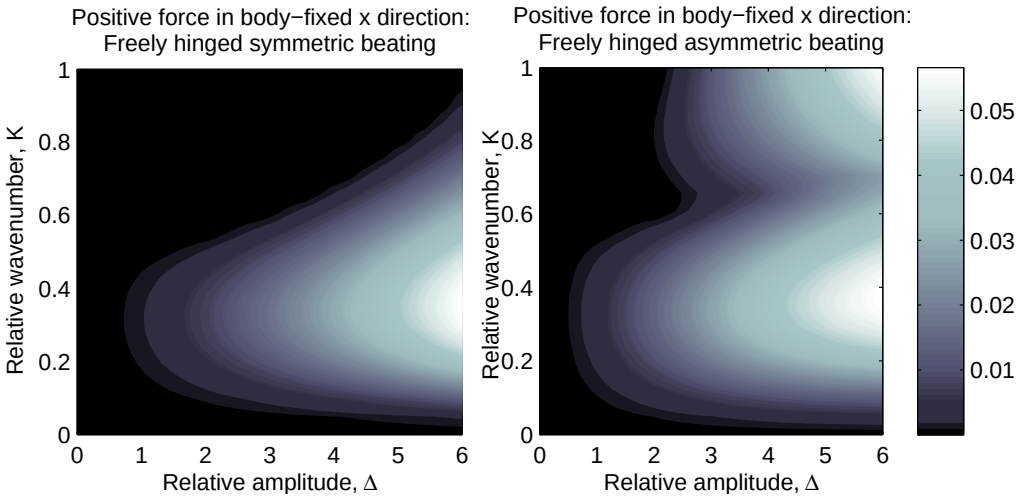


Figure 3.7: Dimensionless plots of the maximum positive (pulling) force in the body-fixed $x$ axis for freely hinged waveforms against the relative, hyperactivation parameters $\Delta$ and $K$, representing the changes in amplitude and wavenumber relative to the symmetric waveform given by (3.30). A value of zero corresponds to no tugging force being exerted by the flagellum. Prior to any effects of hyperactivation, $\Delta = K = 1$; changes in the relative frequency, $\Omega$, have a negligible effect and hence are not shown. *Left:* Tugging forces for freely hinged waveforms with beat symmetry are initiated and enhanced by decreasing $K$ and/or increasing $\Delta$. *Right:* Freely hinged waveforms with beat asymmetry require less extreme decreases in $K$ and increases in $\Delta$ to generate pulling motion. A complex, bimodal, dependence on the wavenumber can also be observed.

For a sperm freely hinged to a tethering point, with the relative, hyperactivation, parameter values $K$, $\Delta$ and $\Omega$ for golden-hamster sperm, figure 3.5 shows a net, linear, rotation rate about the point of tethering in the direction of the beat asymmetry for the hyperactivated sperm. The model additionally predicts that a freely hinged sperm rotates about the point of tethering until the flagellum is within a few flagella radii from a surface, at which point the model would break down.

Figure 3.6 shows that the force along the body-fixed $x$ direction, exerted on the tethering point, is always negative for the symmetric beat pattern in equation (3.30). Given the body-fixed $x$ axis points in a direction away from the tethering point, this indicates that the flagellum exerts a pushing force on the point of tethering, regardless of whether the tethering is freely hinged or clamped. For a sperm with a beat pattern

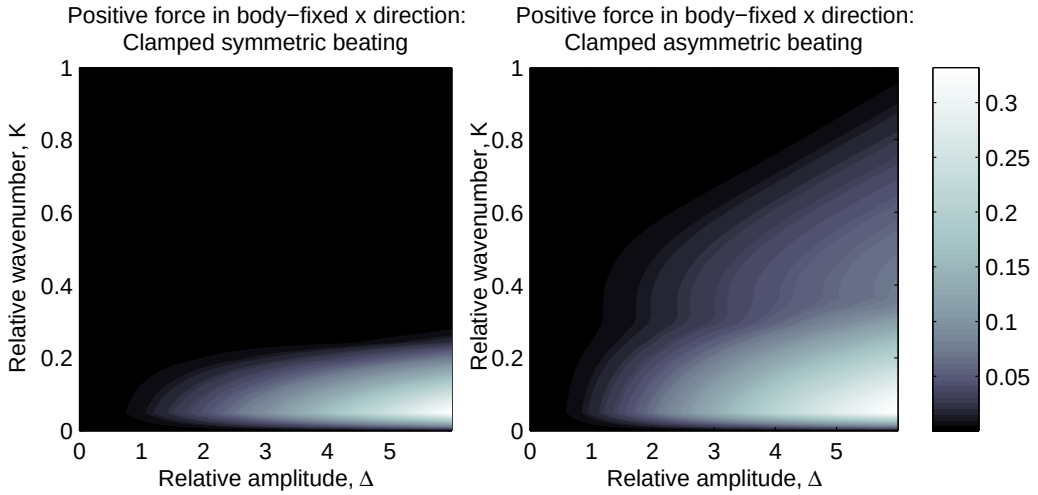


Figure 3.8: Dimensionless plots of the maximum positive (pulling) force in the body-fixed $x$ axis for clamped waveforms against the relative, hyperactivation parameters $\Delta$ and $K$, representing the changes in amplitude and wavenumber relative to the symmetric waveform given by (3.30). A value of zero corresponds to no tugging force being exerted by the flagellum. Prior to any effects of hyperactivation, $\Delta = K = 1$; changes in the relative frequency, $\Omega$, have a negligible effect and hence are not shown. *Left:* A pulling motion can only be generated by clamped waveforms with beat symmetry when the relative wavenumber is extensively reduced, below that observed for golden-hamster sperm. *Right:* For clamped waveforms with beat asymmetry, less extreme changes in the relative amplitude and especially the relative wavenumber are required to induce a pulling motion.

altered by the relative, hyperactivation parameters associated with golden-hamster sperm however, the force along the body-fixed $x$ direction can become positive, more so in the clamped case. Although, on average, the force still pushes into the tether, this demonstrates that cell tugging behaviour occurs for certain parts of the beat cycle, challenging intuitive reasoning that sperm are always pushed by their flagella, as seen when swimming. Furthermore, note that the maximum, dimensionless value of these tugging forces is about 0.01, which, on redimensionalising, corresponds to around 3 picoNewtons for a golden-hamster sperm. While the strengths of the bonds between the sperm head and the female reproductive tract are currently unknown, micropipette studies on symmetric sperm binding to the viscoelastic *zona pellucida* (outer layer of the egg) indicate that the bond strengths are on the order of 10 picoNewtons. These experimental results cannot be used to infer any conclusions in the current context, however they do highlight that the forces involved are on the picoNewton scale.

Additionally, the dashed lines in figure 3.6 highlight that the leading-order effect of including a planar boundary as near as ten flagella radii to the waveforms leave the qualitative conclusions unchanged. More extensive simulations (results not shown) also highlight that this insensitivity extends to the upper limit of validity of Katz *et. al*'s wall resistive force theory study [55], replacing $q$ in equation (3.2) with values of $h$ up to $L/2$, where $L$ is the flagellum length.

A parameter sweep presenting the maximum pulling forces generated upon hyperactivation, in particular by changes in the relative wavenumber, $K$, the relative amplitude, $\Delta$, and the asymmetry is given in figure 3.7 for a freely hinged sperm and figure 3.8 for a clamped sperm, using the dimensionless waveforms in equation (3.30). Where no pulling force was generated, i.e. the sperm was always being pushed further into the tethering point, the plot remains black. In each of the freely hinged and clamped cases, both the hyperactive-symmetric and hyperactive-asymmetric waveforms from (3.30) were investigated to highlight the effects of asymmetry. The symmetric waveform from equation (3.30) which has not undergone hyperactivation corresponds to the point $\Delta = K = 1$ in figure 3.7 and figure 3.8.

The effect of varying the relative frequency, $\Omega$, was also explored but no additional pulling behaviour away from the tethering point was ever generated and hence detailed results are not presented.

In the freely hinged case, figure 3.7, significant cell tugging is predicted for a symmetric waveform when the amplitude is sufficiently increased and wavenumber sufficiently decreased in unison. Upon including beat asymmetry, much less extreme changes are required to induce tugging and, in contrast to the amplitude dependence, a complex bimodal dependence on the wavenumber can be observed. In particular, for the golden-hamster, relative, hyperactivation parameters of $\Delta = 4$ and $K = 4/7$, tugging motion occurs for both symmetric and asymmetric waveforms.

For the clamped case, figure 3.8, a waveform exhibiting beat symmetry does not exhibit tugging on the tethering point unless the relative wavenumber is reduced to $K \approx 0.2$ or less, which is below the observed reductions in wavenumber for golden-hamster sperm. With asymmetry, the combined effect of a sufficient decrease in relative amplitude and increase in relative wavenumber again generates pulling forces which can be larger than those generated by a freely hinged sperm. In particular it is the combined action of both changes in the flagellum amplitude and wavenumber that

generates a substantive tugging force. Further, note that for the relative hyperactivation parameters of golden-hamster sperm, $\Delta = 4$ and $K = 0.35$, only asymmetric beating will induce the tugging motion, unlike the previous freely hinged case.

A video showing both freely hinged and clamped, hyperactive, human-sperm cells in a low viscosity medium was captured over 21 seconds. It shows that a sperm exhibiting an oscillatory, rocking motion with large-amplitude, asymmetric, flagellar beating is able to pull away from the tethering point, whereas the clamped sperm seems to be stuck, although slight oscillations back and forth into the point of tethering can be seen; see supplementary movie in the publication [29]. Snapshots are presented in figure 3.10, with the last diagram highlighting the head paths of both the rocking, hinged, sperm and the one which is essentially clamped.

## 3.6 Leading-Order Dynamics

Given the dimensionless waveforms in (3.30) depend on the constant $A$, where $A$ is the typical, symmetric-beat amplitude, $D$, divided by the symmetric-beat wavelength, $\lambda$, one expects $A$ to be small. If this is the case, leading-order expressions in $A$ can be obtained from equations (3.31), (3.32) and (3.33) and subsequently compared to the results in Section (3.5).

From equation (3.33) determining the upper $x$-limit of the integrals, $\hat{X}(\hat{t})$, the leading-order terms in $y$ give

$$X(t) = \Lambda = 1.3, \qquad \forall t, \tag{3.34}$$

so that the leading-order expression for the rate of change of the tethering angle, (3.32), takes the form

$$\frac{d\psi}{d\hat{t}} = -\frac{\int_0^\Lambda \frac{\partial \hat{y}}{\partial \hat{t}} \hat{x}' \, d\hat{x}'}{\int_0^\Lambda \hat{x}'^2 \, d\hat{x}'}. \tag{3.35}$$

Inserting (3.35) into the leading-order expression for the force in the body-fixed $x$ direction, (3.31), gives

$$\hat{F}^B_{\hat{x}}(\hat{t}) = \int_0^\Lambda \left[ \int_0^{x'} \frac{\partial \hat{y}}{\partial \bar{x}} \frac{\partial^2 \hat{y}}{\partial \bar{t} \partial t} \, d\bar{x} \right] - (\gamma - 1) \frac{\partial \hat{y}}{\partial \hat{t}} \frac{\partial \hat{y}}{\partial \hat{x}'} - \frac{d\psi}{d\hat{t}} \left\{ (\gamma - 1) \hat{x}' \frac{\partial \hat{y}}{\partial \hat{x}'} + \hat{y} \right\} d\hat{x}'. \tag{3.36}$$

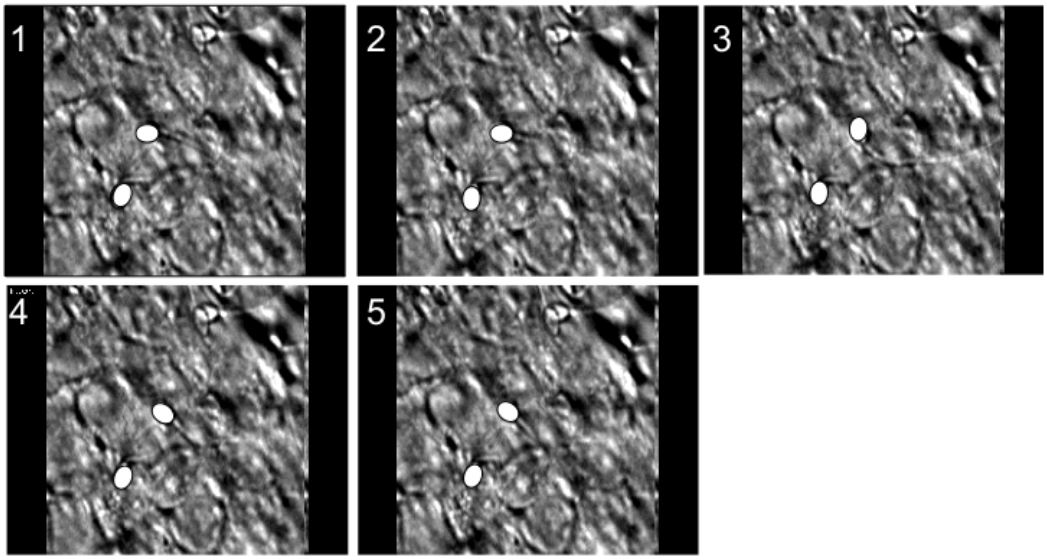


Figure 3.9: Snapshots every 5 seconds showing a hyperactivated, human sperm cell (the upper of the highlighted heads in the first frame) which can hinge about its apparent substrate tether, exhibiting large-amplitude, asymmetric, flagellar beating, and a hyperactivated, human sperm cell below it which appears to be clamped; see supplementary movie with the online publication [29].

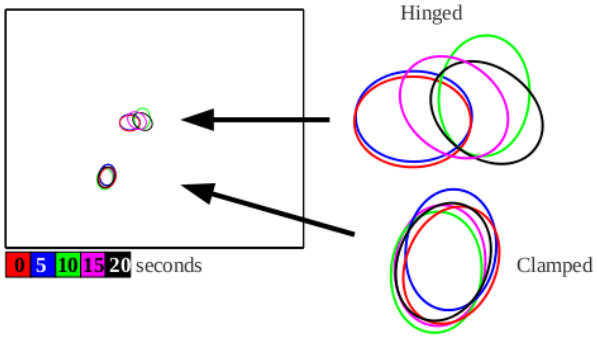


Figure 3.10: On the left, an overlay of all the head positions for the two sperm cells in figure (a), ordered chronologically every 5 seconds by colour. On the right, separate magnified views of these head positions. Over time, the hinged sperm with large-amplitude beating moves back from its initial tether, rocking as it does so in contrast to the other sperm.

The leading-order expressions are now analysed for a typical, dimensionless waveform given by

$$\hat{y}(\hat{x},\hat{t}) = A\hat{x}[\alpha + \sin(K\hat{x} - \Omega\hat{t})]. \tag{3.37}$$

Following the discussion after equation (3.7), the force acting on the tethering point due to the flagellum is given by $-\hat{F}^B_{\hat{x}}(\hat{t})$. By inserting the waveform from (3.37) into (3.35) and (3.36),

$$-\hat{F}^B_{\hat{x}} \sim -\frac{A^2\Omega}{12K^5\Lambda^3}\left[a_0 + a_2\cos(2\Omega\hat{t}) + b_2\sin(2\Omega\hat{t}) + \alpha\{a_1\cos(\Omega\hat{t}) + b_1\sin(\Omega\hat{t})\}\right], \tag{3.38}$$

where

$$\begin{aligned}
a_0 = \delta\Bigg[&2\{72 - 36\gamma + 9\gamma K^2\Lambda^2 - 9(\gamma-1)K^4\Lambda^4\} \\
&+18\{-8 + 4\gamma + (4-3\gamma)K^2\Lambda^2\}\cos K\Lambda + 72\{\gamma-2\}K\Lambda\sin K\Lambda\Bigg] \\
&+ 2(\gamma-1)K^6\Lambda^6, \\
a_1 = \delta\Bigg[&-36\gamma K^3\Lambda^3\cos K\Lambda + 18\gamma\{2 - K^2\Lambda^2\}K^2\Lambda^2\sin K\Lambda\Bigg] \\
&- 12\{\gamma-2\}K^3\Lambda^3 + 12(\gamma-2)K^3\Lambda^3\cos K\Lambda + 12(\gamma-2)K^4\Lambda^4\sin K\Lambda, \\
b_1 = \delta\Bigg[&36\gamma K^2\Lambda^2 - 18\gamma\{2 - K^2\Lambda^2\}K^2\Lambda^2\cos K\Lambda - 36\gamma K^3\Lambda^3\sin K\Lambda\Bigg] \\
&- 12\{\gamma-2\}K^4\Lambda^4\cos K\Lambda + 12(\gamma-2)K^3\Lambda^3\sin K\Lambda, \\
a_2 = \delta\Bigg[&36\{\gamma-2\} - 18\{-8 + 4\gamma + (4-3\gamma)K^2\Lambda^2\}\cos K\Lambda - 72\{\gamma-2\}K\Lambda\sin K\Lambda \\
&- \frac{3K^4\Lambda^4}{2} + 18\{-4 + 2\gamma + (8-5\gamma)K^2\Lambda^2 + (\gamma-1)K^4\Lambda^4\}\cos 2K\Lambda \\
&+3\left\{24(\gamma-2) + 6(4-3\gamma)K^2\Lambda^2 + \frac{(1-2K^2\Lambda^2)K^2\Lambda^2}{4}\right\}K\Lambda\sin 2K\Lambda\Bigg] \\
&+ 3(\gamma-1)K^5\Lambda^5\sin 2K\Lambda, \\
b_2 = \delta\Bigg[&72\{\gamma-2\}K\Lambda\cos K\Lambda - 18\{-8 + 4\gamma + (4-3\gamma)K^2\Lambda^2\}\sin K\Lambda \\
&- 3\{24(\gamma-2) + 6(4-3\gamma)K^2\Lambda^2\}K\Lambda\cos 2K\Lambda \\
&+18\{-4 + 2\gamma + (8-5\gamma)K^2\Lambda^2 + (\gamma-1)K^4\Lambda^4\}\sin 2K\Lambda\Bigg] \\
&\frac{3K^3\Lambda^3}{4} + \left\{3(\gamma-1)K^5\Lambda^5 - \frac{3(1-2K^2\Lambda^2)K^3\Lambda^3}{4}\right\}\cos 2K\Lambda,
\end{aligned} \tag{3.39}$$

and $\delta = 0$ gives the clamped case, whilst $\delta = 1$ gives the freely hinged case. Equation (3.38) shows the dimensionless force in the body $x$ direction scales quadratically with the amplitude-wavelength ratio, $A$, and linearly with the relative, frequency change, $\Omega$. The wave number scaling is not as obvious, but for large wave numbers,

$$-\hat{F}^B_{\hat{x}}|_{K \text{ large}} \sim -\frac{A^2\Omega\Lambda^2(\gamma - 3/2)}{4}\left[\sin(2K\Lambda - 2\Omega\hat{t}) + \frac{2K\Lambda}{3}\right], \tag{3.40}$$

whereas for $K \to 0$,

$$-\hat{F}^B_{\hat{x}}|_{K \to 0} \sim \frac{A^2\Omega\Lambda^2\gamma(1-\delta)}{4}\left[\sin(2\Omega\hat{t}) - 2\alpha\cos(\Omega\hat{t})\right]. \tag{3.41}$$

From these results at leading-order, a large wave number will tend to shift the dimensionless force in the body $x$-axis into the negative region, thus prohibiting the generation of positive forces in which the flagellum is pulling away from the point of tethering. This is observed regardless of whether the waveform is symmetric, asymmetric, clamped or freely hinged. As the wave number decreases, however, the force in the clamped case ($\delta = 0$) tends to equation (3.41) centred about the $x$-axis, hence will definitely exhibit positive (pulling) contributions, regardless of whether the waveform is symmetric or asymmetric. For the freely-hinged case ($\delta = 1$), however, $-\hat{F}^B_{\hat{x}}|_{K \to 0} = 0$, suggesting the full, nonlinear model in Section 3.3.6 is needed for further insight.

For the cases of human and golden-hamster sperm, where $\Lambda = 1.3$ indicates the number of wavelengths down the flagellum for a symmetric beat pattern from table 3.1, equation (3.40) suggests pulling motion can occur for non-hyperactive ($K = 1$) symmetric beating; this is in contrast to results of the full model in figure 3.6, illustrating how misleading the geometrically linear approximation is [39].

## 3.7 Discussion

Using RFT [42, 64], a model has been developed for a tethered sperm with prescribed, flagellar waveforms, examining how the latter affect the total force, and torque, exerted by a tethered flagellum on the point of tethering. Beat patterns have been constructed, representing symmetric and hyperactive beating, the latter being motivated by observations of the changes in golden-hamster sperm flagella on capacitation [72]. Two boundary conditions have been explored, in which the sperm is either freely hinged or clamped at the tethering point.

Although, on average, the force still pushes into the tether, hyperactive sperm do indeed appear to have the ability to generate pulling forces throughout certain parts of each beat cycle, acting away from the point of tethering in a Newtonian fluid, thus inducing a cell tugging behaviour. This in turn has the potential to facilitate sperm escape from a binding, counterintuitive to the notion that a flagellum always pushes the sperm cell. While the tugging forces for golden-hamster sperm are on a scale of picoNewtons, it should be noted that the strength of the binding to the female reproductive tract is unknown. Thus, it is not feasible to predict whether the magnitude of the pulling motion is, in isolation, sufficient to overcome binding thresholds or whether other biological mechanisms are also required.

Within this framework, the numerical studies demonstrate that mammalian sperm exhibiting typical symmetric beating do not induce any tugging motion, but the relative changes in waveform parameters associated with hyperactive, golden-hamster sperm are sufficient to induce tugging; the latter prediction is regardless of whether the sperm is clamped or freely hinged. Moreover, on performing parameter sweeps, large regions of parameter space with increased amplitudes and decreased wavenumbers, typifying the effects of hyperactivation are seen to induce a tugging behaviour. This in turn demonstrates the mechanical feasibility of the hypothesis that hyperactivation can contribute to bond breaking for a tethered sperm in a Newtonian medium. It also emphasises that regulating the wavenumber, amplitude and beat asymmetry can be exploited for the mechanical control of a flagellated cell's behaviour when tethered at a surface.

The results have also highlighted that the onset of the tugging motion, in general, depends on the nature of the binding. In particular much more extreme changes in waveform amplitude and wavenumber are required to induce tugging for clamped, beat patterns exhibiting beat symmetry; the reduction in wavenumber in particular is significantly outside the observed range in this scenario. Furthermore, the bimodal variation in the tugging force with changes in the wavenumber for the freely hinged, asymmetrically beating sperm emphasises that the presence or absence of tugging for a tethered flagellum is complex, requiring detailed physical models and simulation.

The model bases any pushing or pulling behaviour on the forces resolved in the body-fixed $x$ axis, along the axis of the flagellum waveform. There are, however, other forces to consider, such as the forces transverse to the tethering point (the body-fixed

$y$ direction); these shearing forces could also have the potential to detach the sperm head from the epithelial walls of the female reproductive tract. Transverse forces are readily calculated from the model using the second component of the body-force vector in equation (3.18). An inspection of these forces for human and golden-hamster sperm suggests they are two to three times larger than the perpendicular forces for clamped waveforms, and on the same scale as the perpendicular forces for freely-hinged waveforms. Similarly, any torques at the head-tail junction can be calculated for the clamped-sperm cases (though, by construction, these are zero for the freely hinged cases). Both of these effects would generate a torque on the sperm head (see figure 3.3), though further models for the sperm head and the nature of the acrosomal bindings are required in order to deduce the forces and torques on the tethering point. Also, while the inclusion of transverse forces and torques could support the model predictions, suggesting hyperactivation facilitates sperm release, there still remains the problem of the lack of available, experimental data on the binding forces and torques in the female reproductive tract. Thus, model predictions in the current context, using the force in the body-fixed $x$ direction, offer an initial insight into the situation. They are also sufficient to highlight qualitatively that a hyperactive waveform is capable of generating opposing forces, solely from mechanical considerations.

The geometrically linear terms in the integrands of equations (3.23) and (3.32) allow the derivation of exact expressions for the leading-order, body forces for small-amplitude waveforms. The results based on these leading-order approximations for golden-hamster sperm suggest pulling motions in all cases, unlike the full model, emphasising that geometric nonlinearities are important in understanding the influence of hyperactivation on tethered-sperm behaviour. They do, however, demonstrate that an increase in the wavenumber beyond the reduction seen in golden-hamster sperm ensures no pulling motion occurs, (3.40), thus suggesting that the decrease in wavenumber observed in hyperactivation is desirable for sperm escape.

Interestingly, the observed, relative reduction in beat frequency for golden-hamster sperm from symmetric to hyperactive beating appears not to contribute to the generation of these pulling forces away from the tether. Also, changes in viscosity for a given beat pattern do not alter whether or not a tugging force is present, as it appears only in the force and torque scales of the dimensionless model. Notably, large viscosities do change the nature of the waveform by reducing the absolute values of the amplitude and wavenumber for symmetric and hyperactivated, golden-hamster sperm [92];

however these observations relate to sperm immersed in a physiological, mucus substitute, the effects of which would require elasticity and shear-thinning to be included in the current model [*ibid*]. As such, definitive conclusions about whether hyperactivation assists the breaking of epithelial bonds in-vivo at the isthmic epithelium in the presence of mucus cannot be inferred from this study, as rheological fluids are present.

The experimental, imaging data for both a clamped and hinged, tethered, human sperm in a low viscosity medium is not inconsistent with the modelling predictions. The hinged sperm with large-amplitude, asymmetric beating moves backwards, away from the point of tethering via an oscillatory rocking motion. This explicitly demonstrates a tugging behaviour when exhibiting the characteristics required in the model, namely asymmetry and an increased, beat amplitude for freely hinged sperm. The clamped sperm can be seen to oscillate back and forth very slightly with the same mean position over the 21 second video (see supplementary movie with the online publication [29]), hinting at a cell tugging behaviour. Possible reasons for why the clamped sperm remains pinned, on average, whereas the hinging sperm moves backward are unclear; the clamped sperm may be mechanically defective or it may require larger forces to escape its particular tethering, for example.

The use of RFT [42, 64] for the present model has been justified from observation [35] and theoretically in Section 3.5, noting, for instance, that the flow fields induced by a mammalian sperm head have been shown to be insufficient to violate applying RFT to their flagella [54]. Thus, more accurate frameworks such as slender body theory in Chapter 4, or even direct, numerical simulations, are unlikely to alter the conclusions which are based on qualitative aspects of the net, flagellar forces. Once the sperm has broken its tether, however, the cell body undergoes complex reorientations in the presence of a surface which is a fraction of a body-length away, requiring more sophisticated treatments. In addition, the nature of the sperm-substrate binding has been considered only in two simple settings and does not consider any chemical or physical changes in the acrosomal head due to the capacitation process, which could potentially alter the nature of the binding. Complex configurations with multiple, cilia attachments to various parts of the sperm head are also possible [91], while rheological factors present further opportunities for generalistions.

Nonetheless and in summary, a theoretical model has been presented supporting the hypothesis that observed, waveform changes associated with hyperactivation in

mammalian sperm immersed in a Newtonian fluid can directly contribute to epithelial escape, acting to pull the sperm away from the substrate.

# Chapter 4

# Slender Body Theory with Generalisations to Different Body Shapes

## 4.1 Chapter Introduction

The third aspect studied is that of low Reynolds number, slender-body theory (SBT), a means of deriving the Stokes flow past a thin, slender body with a curvilinear centre-line. The theory distributes weighted combinations of Stokes flow singularities along the centre-line, exploiting the asymptotically small slenderness ratio, $\varepsilon$, defined as the maximum cross-sectional radius of the slender-body divided by the body length (or half-length). In this chapter, a new SBT is formulated, incorporating slender bodies whose cross-sectional radius can vary arbitrarily along the length of the body. In particular, any inaccuracies arising at the ends of the slender body are controlled.

The chapter first introduces slender bodies immersed in a Stokes fluid, with particular attention given to the SBT of Johnson [53]. In Johnson's work, the leading-order flow field is based on the singularity representation of the flow past a translating, prolate spheroid; see Section 1.3.2.2. The limitations of Johnson's model are discussed, noting the restricted class of permissible, slender-body shapes, before posing a new form of the leading-order velocity field based on the regularised singularities of Section 1.3.4 [25], allowing for more general, body shapes. The leading-order, no-slip boundary condition is subsequently enforced via a velocity field *ansatz*, with a requirement that no slip must be satisfied for all points around a circular, cross section, independent of any cross-sectional angle, $\phi$, say. This $\phi$-independence is thus enforced, to asymptotic accuracy, resulting in a relationship between the weightings of the regularised

singularities that must be satisfied.

The SBT developed here is also approximated by inspecting the leading-order terms, thus yielding RFT and fully determining the associated, resistance coefficients in terms of the constant, fluid viscosity, $\mu$, and the slenderness ratio, $\varepsilon$. Finally, the theory is summarised, ready for numerical implementation in Chapter 5, and the model is discussed, noting any limitations.

## 4.2 Slender-Body Theory (SBT)

### 4.2.1 The Slender Body

Consider a three-dimensional, long, thin, slender body at time $t$ specified by a centre-line, $\boldsymbol{\xi}(s,t)$, where $s \in [-L, L]$ is the arc-length along the centre-line. A transverse, cross-sectional radius at each point $s$ is given by $\eta(s,\phi)$, where $\phi$ is the cross-sectional angle. The slender body is assumed to have local axisymmetry, thus the cross section at any point $s$ along the centre-line will be circular; this requires the cross-sectional radius to be independent of $\phi$, written henceforth as $\eta(s)$.

As the body is slender, the maximum of $\eta(s)$, the cross-sectional radius, is assumed to be very small when compared with the half-length, $L$, of the centre-line. Thus a slenderness ratio, $\varepsilon$, can be defined as

$$\varepsilon := \frac{\max_{s\in[-L,L]}\{\eta(s)\}}{L} \ll 1. \tag{4.1}$$

### 4.2.2 The Governing Equations

Slender-body theory seeks to model the fluid flow around the slender body described in Section 4.2.1 with a prescribed centre-line, $\boldsymbol{\xi}(s,t)$, and cross-sectional radius, $\eta(s)$, immersed in a low Reynolds number, viscous fluid governed by Stokes' equations. As Stokes' equations are quasi-steady, the explicit $t$ dependence is once again dropped in the variable arguments without loss of generality; see the discussion following equation (1.8). The velocity field of the fluid, $\mathbf{u}(\mathbf{x})$, evaluated at a field point $\mathbf{x}$ in the fluid domain satisfies the dimensional, Stokes equations, (1.7) and (1.8). These

are re-written again for convenience:

$$\nabla \cdot \mathbf{u} = 0, \tag{4.2}$$

$$\mathbf{0} = -\nabla p + \mu \nabla^2 \mathbf{u}, \tag{4.3}$$

where $p(\mathbf{x})$ is the pressure field and $\mu$ is the constant, dynamic viscosity of the fluid. In order to link the geometry of the slender body to the fluid dynamics, the no-slip boundary condition on the surface of the slender body is imposed. In order to write this succinctly, further notation is first introduced.

The basis $\mathbf{e}_t(s)$, $\mathbf{e}_n(s)$ and $\mathbf{e}_b(s)$ denote unit vectors tangential, normal and binormal, respectively, to the curved centre-line of the slender body, $\boldsymbol{\xi}(s)$, at a point $s$ along the arc-length of the centre-line; see figure 4.1. The standard Frenet–Serret relations give that

$$\begin{aligned} \mathbf{e}_t(s) &= \frac{\partial \boldsymbol{\xi}}{\partial s}, \\ \frac{\partial \boldsymbol{e}_t}{\partial s} &= \kappa(s)\mathbf{e}_n(s), \\ \mathbf{e}_b(s) &= \mathbf{e}_t(s) \times \mathbf{e}_n(s), \end{aligned} \tag{4.4}$$

where $\kappa(s)$ is the curvature of the centre-line at $s$, given by

$$\kappa(s) := \left| \frac{\partial \boldsymbol{e}_t}{\partial s} \right|. \tag{4.5}$$

Recall that the radius of curvature is the reciprocal of the curvature given by the definition in (4.5). It is *a posteriori* assumed that the radius of curvature is much larger than the maximum of the cross-sectional radius, necessary for the asymptotic analysis in Section 4.3.2, noting that the cross-sectional radius is a small length scale.

A radial, unit vector embedded in a transverse cross section to the body centre-line at $s$ is defined in terms of a cross-sectional angle, $\phi$, by

$$\mathbf{e}_r(s, \phi) := \mathbf{e}_n(s) \cos\phi + \mathbf{e}_b(s) \sin\phi. \tag{4.6}$$

The slender body is taken to be inextensible and unshearable [5], so that material cross sections remain perpendicular to the centre-line tangent, $\mathbf{e}_t(s)$, at each point along the arc-length, $s$; see figure 4.1. Denoting the surface velocity as $\mathbf{U}(s, \phi)$, where $\phi$ is the cross-sectional angle from the centre-line to a point on the surface in (4.6), it decomposes into

$$\mathbf{U}(s, \phi) = \mathbf{V}(s) + \boldsymbol{\Omega}(s) \times \eta(s)\mathbf{e}_r(s, \phi), \tag{4.7}$$

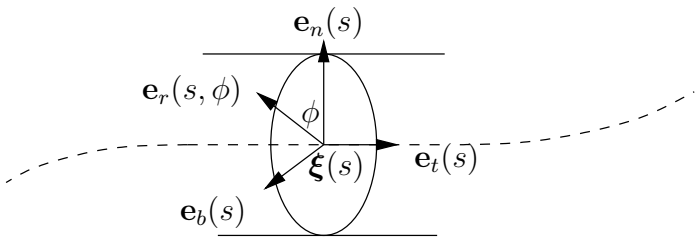


Figure 4.1: The tangential, normal and binormal unit vectors of a slender body at a point $s$ along the arc-length of the centre-line, given respectively by $\mathbf{e}_t(s)$, $\mathbf{e}_n(s)$ and $\mathbf{e}_b(s)$, where time dependence is implicit. The unit radial vector, $\mathbf{e}_r(s,\phi)$, depending on the cross-sectional angle, $\phi$, is also shown.

where $\mathbf{V}(s)$ and $\boldsymbol{\Omega}(s)$ are the translational and angular velocity components respectively; note that $\mathbf{V}(s)$ is independent of the cross-sectional angle, $\phi$. If one were to prescribe a time-dependent centre-line, then $\mathbf{V}(s) = \partial\boldsymbol{\xi}/\partial t$. For kinematic problems, $\mathbf{V}$ may be prescribed and is spatially constant for a rigid body.

Returning to the formulation of the no-slip boundary condition, the velocity field, when measured on the surface of the slender body, must exactly equal the surface velocity of the slender body. Hence, for a point on the surface, $\mathbf{X}(s,\phi)$, satisfying

$$\mathbf{X}(s,\phi) = \boldsymbol{\xi}(s) + \eta(s)\mathbf{e}_r(s,\phi), \tag{4.8}$$

the boundary condition is

$$\mathbf{u}(\mathbf{X}(s,\phi)) = \mathbf{U}(s,\phi). \tag{4.9}$$

### 4.2.3 Non-dimensionalisation

All lengths are non-dimensionalised by $L$, the half-length of the slender-body centre-line; thus, the cross-sectional radius, $\eta(s)$, is at most $O(\varepsilon)$, where $\varepsilon \ll 1$ from (4.1). Explicitly,

$$\eta(s) = \varepsilon\hat{\eta}(\hat{s}), \tag{4.10}$$

where $\hat{s} \in [-1,1]$ is the dimensionless arc-length; the hatted variables denote dimensionless, $O(1)$ quantities. The full surface velocity from (4.7) with the respective translational and rotational components are non-dimensionalised by a typical velocity scale, $U$, giving

$$\hat{\mathbf{U}}(\hat{s},\phi) = \hat{\mathbf{V}}(\hat{s}) + \varepsilon\hat{\boldsymbol{\Omega}}(\hat{s}) \times \hat{\eta}(\hat{s})\mathbf{e}_r(\hat{s},\phi). \tag{4.11}$$

The velocity field of the fluid, $\mathbf{u}(\mathbf{x})$, is non-dimensionalised by the same velocity scale $U$, while the pressure field, $p(\mathbf{x})$, is non-dimensionalised by $\mu U/L$. Dimensionless

variables are assumed henceforth and hatted notation is dropped.

### 4.2.4 The Leading-Order Problem

Upon neglecting $O(\varepsilon)$ terms to inspect the leading order problem, the dimensionless, surface velocity in (4.11) and hence the boundary condition, (4.9), only consist of the translational, velocity component, $\mathbf{V}(s)$, assuming the magnitude of the angular velocity, $|\boldsymbol{\Omega}|$, is sufficiently small; it transpires that the angular velocity is required to be $o(1)$ for the subsequent analysis. However, to avoid considerations of any local rotation, thus requiring higher-order, weighted singularities [21, 53], the SBT developed in this chapter assumes that the surface velocity is solely translational; extensions to include $\boldsymbol{\Omega} \sim O(1)$ are discussed in Chapter 6. Thus,

$$\mathbf{u}(\mathbf{X}(s,\phi)) \sim \mathbf{V}(s) \qquad \forall \phi \in [0, 2\pi), \tag{4.12}$$

where $\mathbf{X}(s,\phi)$ from (4.8) is written dimensionlessly as

$$\mathbf{X}(s,\phi) = \boldsymbol{\xi}(s) + \varepsilon\eta(s)\mathbf{e}_r(s,\phi). \tag{4.13}$$

The surface velocity of the slender body, at leading order, is thus equal to the velocity of the centre-line at each point, $s$.

### 4.2.5 Johnson's Approach

Johnson [53] poses an *ansatz* for the leading-order, velocity field based on the exact, singularity representation for the flow field around a rigid, translating, prolate spheroid by Chwang and Wu [22]; see Section 1.3.2.2. The singularities used are the Stokeslet, $\mathbf{S}(\mathbf{x},\mathbf{y})$ from (1.40), and the potential dipole, $\mathbf{D}(\mathbf{x},\mathbf{y})$ from (1.52), re-written here for convenience:

$$\mathbf{S}(\mathbf{x},\mathbf{y}) := \frac{\mathbf{I}}{|\mathbf{x}-\mathbf{y}|} + \frac{(\mathbf{x}-\mathbf{y})\otimes(\mathbf{x}-\mathbf{y})}{|\mathbf{x}-\mathbf{y}|^3}, \tag{4.14}$$

and

$$\mathbf{D}(\mathbf{x},\mathbf{y}) := -\frac{\mathbf{I}}{|\mathbf{x}-\mathbf{y}|^3} + \frac{3(\mathbf{x}-\mathbf{y})\otimes(\mathbf{x}-\mathbf{y})}{|\mathbf{x}-\mathbf{y}|^5}. \tag{4.15}$$

Johnson [53] also considers slender bodies with arbitrary, locally axisymmetric, cross-sectional radius functions that tend to prolate spheroids at the ends,

$$\eta^2(s) \to (1-s^2)(1+O(\varepsilon^2)), \qquad \text{for} \quad s \to \pm 1. \tag{4.16}$$

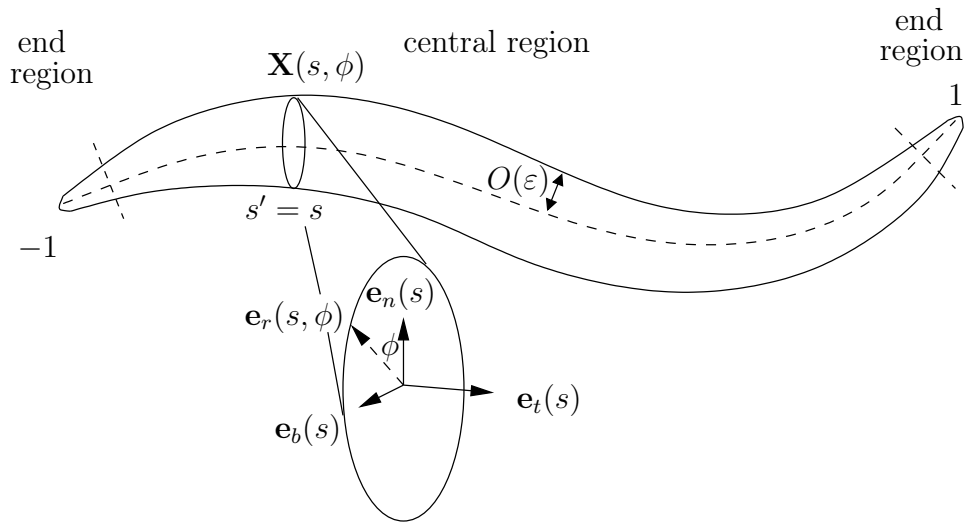


Figure 4.2: The dimensionless slender body with $O(\varepsilon)$ radius described in Johnson's SBT [53]. The centre-line has a dimensionless arc-length in the interval $[-1,1]$, where the body is split into three regions. The no-slip boundary condition is applied on the surface of the body, where $\mathbf{X}(s,\phi)$ denotes a point on the surface in the transverse cross section at $s$, dependent on the cross-sectional angle, $\phi$. Importantly, the no-slip boundary condition at leading order must be $\phi$-independence; it must not depend on where $\mathbf{X}(s,\phi)$ lies around the circular, cross section at $s$.

By ensuring the slender-body had prolate-spheroidal caps, previous inaccuracies relating to the singularities evaluated at the end-points of the slender body are rectified; see the literature review in Section 1.4. By splitting the centre-line into a central region and two end regions, asymptotically matching the solution accordingly, Johnson presents the leading-order flow field as

$$\mathbf{u}(\mathbf{x}) = \int_{-e}^{e} \mathbf{S}(\mathbf{x},\boldsymbol{\xi}(s'))\boldsymbol{\alpha}(s') + W(s')\mathbf{D}(\mathbf{x},\boldsymbol{\xi}(s'))\boldsymbol{\beta}(s')\,\mathrm{d}s', \tag{4.17}$$

where

$$e := \sqrt{1-\varepsilon^2} \tag{4.18}$$

denotes the effective eccentricity, and

$$W(s') = \begin{cases} \eta(s')^2, & \text{in the central region,} \\ (e^2 - s'^2), & \text{in the end regions.} \end{cases} \tag{4.19}$$

Here, $\boldsymbol{\alpha}(s')$ and $\boldsymbol{\beta}(s')$ are *a priori* unknown weightings for the distributions of singular Stokeslets and potential dipoles respectively, both varying with the integration variable, $s'$. For a straight, prolate ellipsoid, the effective eccentricity, $e$, is exactly the eccentricity of the prolate spheroid, with (dimensionless) foci at $\pm e$, thus the

limits of integration can be thought of as the effective foci of the slender body. In addition, the integration limits, $s' = \pm e$, do not include the singular end points, $\pm 1$, given $0 < e < 1$ from (4.18), ensuring the velocity flow-field *ansatz* (4.17) is regular, despite the use of singularities.

The factor $W(s')$ changes depending on the region. In the end regions, in which the body assumes the form of prolate-spheroidal caps, the weighting used is the same parabolic factor of the exact, singularity representation of the flow around a translating, prolate spheroid [22]; see Section 1.3.2.2. However, in the central region, the weighting varies with $\eta(s)$, thus accounting for the changes is the cross-sectional radius of the body.

Upon enforcing the $\phi$-independent, leading-order boundary condition from (4.12),

$$\mathbf{V}(s) = \int_{-e}^{e} \mathbf{S}(\mathbf{X}(s,\phi), \boldsymbol{\xi}(s'))\boldsymbol{\alpha}(s') + W(s')\mathbf{D}(\mathbf{X}(s,\phi), \boldsymbol{\xi}(s'))\boldsymbol{\beta}(s')\,\mathrm{d}s', \tag{4.20}$$

for all $\phi \in [0, 2\pi)$. Johnson notes that the resulting integral equation in (4.20) is $\phi$-independent only if

$$\boldsymbol{\beta}(s) = \frac{(1-e^2)}{2}\left(\frac{s}{1-s^2}\right)\frac{\eta(s)}{\eta'(s)}\,\boldsymbol{\alpha}(s), \tag{4.21}$$

albeit with a sign difference due to his definition of the potential dipole. This relationship between $\boldsymbol{\beta}(s)$ and $\boldsymbol{\alpha}(s)$ allows the integral equation to be written in terms of just one unknown, the Stokeslet strength, $\boldsymbol{\alpha}(s')$. By prescribing a translational, surface velocity, $\mathbf{V}(s)$, one can proceed to solve the integral equation, thus determining $\boldsymbol{\alpha}(s')$ at leading order. Once $\boldsymbol{\alpha}(s')$ is calculated, it is subsequently inserted back into (4.17) which determines the flow field everywhere in the fluid domain, $\mathbf{u}(\mathbf{x})$, satisfying the boundary condition to leading order.

However, there is an inherent constraint on the prescribed, cross-sectional radius function, $\eta(s)$, in Johnson's SBT [53]. As $\boldsymbol{\beta}(s')$ is integrated over $s' \in [-e, e]$ in the singularity representation of the velocity field, (4.17), the relationship (4.21) must not attain singular values. Given that $\eta(s) > 0$ for $s \in (-1, 1)$, $\eta'(s)$ must not have any zeros other than at $s = 0$, such that the limit of $s/\eta'(s)$ exists at $s = 0$. This restricts the range of permissible shapes allowed in the slender-body theory by Johnson [53]. An example of a permissible shape is the prolate ellipsoid, $\eta(s) = \sqrt{1-s^2}$. Here,

$$\boldsymbol{\beta}(s') = -(1-e^2)\boldsymbol{\alpha}(s')/2. \tag{4.22}$$

Some examples of non-permissible shapes, however, include a tapered flagellum, as ubiquitously observed for mammalian sperm [34], where the zero derivative is not at the centre, $s = 0$, or a wave-like shape which introduces more zero derivatives away from $s = 0$.

Thus, a new SBT based on the regularised singularities from Section 1.3.4 is designed to incorporate these more general shapes. The new SBT also avoids Johnson's procedure of splitting up the centre-line into three regions and varying the singularity weightings with $\eta(s)$ in the central region.

## 4.3 Regularised Singularity SBT

### 4.3.1 Initial Flow-Field *Ansatz*

Motivated by the leading-order, velocity field in (4.17) by Johnson [53], a new, leading-order, velocity-field *ansatz* is posed in terms of regularised Stokeslets and potential dipoles (see Section 1.3.4), as

$$\mathbf{u}(\mathbf{x}) = \int_{-e}^{e} \mathbf{S}^{\chi(s')}(\mathbf{x}, \boldsymbol{\xi}(s'))\boldsymbol{\alpha}(s') + (e^2 - s'^2)\mathbf{D}^{\chi(s')}(\mathbf{x}, \boldsymbol{\xi}(s'))\boldsymbol{\beta}(s')\,\mathrm{d}s', \tag{4.23}$$

where the dimensionless, effective eccentricity is defined as

$$e := \sqrt{1 - \varepsilon^2}. \tag{4.24}$$

The regularised singularities, (1.98) and (1.99), are re-written for convenience, albeit with the square of the regularisation parameter, $\delta^2$, denoted by a function, $\chi(s')$, so that

$$\mathbf{S}^{\chi(s')}(\mathbf{x}, \mathbf{y}) := \frac{(|\mathbf{x} - \mathbf{y}|^2 + 2\chi(s'))\mathbf{I}}{(\,|\mathbf{x} - \mathbf{y}|^2 + \chi(s')\,)^{3/2}} + \frac{(\mathbf{x} - \mathbf{y}) \otimes (\mathbf{x} - \mathbf{y})}{(\,|\mathbf{x} - \mathbf{y}|^2 + \chi(s')\,)^{3/2}}, \tag{4.25}$$

and

$$\mathbf{D}^{\chi(s')}(\mathbf{x}, \mathbf{y}) := -\frac{(|\mathbf{x} - \mathbf{y}|^2 - 2\chi(s'))\mathbf{I}}{(\,|\mathbf{x} - \mathbf{y}|^2 + \chi(s')\,)^{5/2}} + \frac{3(\mathbf{x} - \mathbf{y}) \otimes (\mathbf{x} - \mathbf{y})}{(\,|\mathbf{x} - \mathbf{y}|^2 + \chi(s')\,)^{5/2}}. \tag{4.26}$$

The regularisation parameter, $\chi(s')$, is *a posteriori* defined as

$$\chi(s) := \varepsilon^2[(1 - s^2) - \eta^2(s)], \tag{4.27}$$

so that the degree of regularisation of the forces varies as the cross-sectional radius varies; see figure 4.3. It differs from the regularisation constant, $\delta^2$, used by Cortez [25], in that it is now a function depending on the integration variable, $s'$. It is also

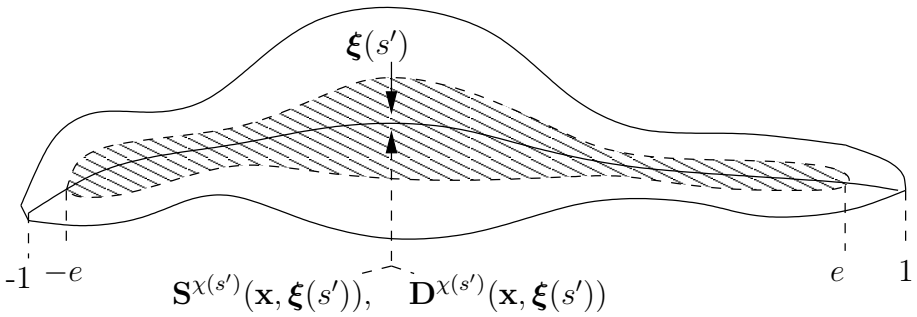


Figure 4.3: A slender body with a varying, cross section. The centre-line is distributed with regularised Stokeslets and regularised potential dipoles being integrated from $s' = -e$ to $s' = e$.

fully defined by (4.27) and can take negative values. The latter observation can be justified as follows.

From the definition in (4.27),

$$\chi(s') > -\varepsilon^2\eta^2(s'), \tag{4.28}$$

where $s'$ is the integration parameter, $s' \in [-e, e]$. Equality can never be obtained given $\eta^2(s')$ is only zero at $s' = \pm 1$, the end-points where the body is closed, yet $s'$ ranges from $-e$ to $e$, where $0 < e < 1$. From (4.23), the field point $\mathbf{x}$ must lie on, or outside the surface of the slender body, so that

$$|\mathbf{x} - \boldsymbol{\xi}(s')|^2 > \varepsilon^2\eta^2(s'), \tag{4.29}$$

given $\varepsilon\eta(s')$ is the radius of the slender body and $\boldsymbol{\xi}(s')$ is the centre-line. The bound in (4.29) can also never be attained, using the same argument as above. Both (4.28) and (4.29) give

$$|\mathbf{x} - \boldsymbol{\xi}(s')|^2 + \chi(s') > 0, \tag{4.30}$$

so that denominators in the definitions of the regularised singularities, (4.25) and (4.26), are never zero. Thus, $\chi(s') < 0$ is possible without the integrand in (4.23) becoming singular. Notably, for any points for which $\chi(s') = 0$, or for the specific case of $\chi(s') \equiv 0$, implying $\eta(s) = \sqrt{1 - s^2}$ from (4.27), the resulting, strict inequalities in (4.28), (4.29) and (4.30) ensure the integrand (4.23) remains non-singular.

As in Johnson's SBT [53], the slender body has prolate ellipsoidal caps so that the *ansatz* has the correct behaviour at the end-points, thus

$$\eta^2(s) \to 1 - s^2, \qquad s \to \pm 1. \tag{4.31}$$

Also, when $\eta(s)$ is prescribed, $\max_s[\eta^2(s)]$ should be $O(1)$ to ensure that $\chi(s)$ remains $O(\varepsilon^2)$ and the body is slender, necessary for the asymptotic analysis.

The leading-order boundary condition in (4.12) is enforced via the *ansatz*, (4.23), at a surface point (4.13), giving

$$\mathbf{V}(s) = \int_{-e}^{e} \mathbf{S}^{\chi(s')}(\mathbf{X}(s,\phi),\boldsymbol{\xi}(s'))\boldsymbol{\alpha}(s') + (e^2 - s'^2)\mathbf{D}^{\chi(s')}(\mathbf{X}(s,\phi),\boldsymbol{\xi}(s'))\boldsymbol{\beta}(s')\,\mathrm{d}s', \quad (4.32)$$

which must hold for all $\phi \in [0, 2\pi)$; it is this latter condition which determines the relationship between $\boldsymbol{\beta}(s')$ and $\boldsymbol{\alpha}(s')$, as was demonstrated by Johnson [53] in obtaining (4.21); it is thus necessary to ensure that the integral equation arising from the boundary condition, (4.32), has no $\phi$-dependence, determining the relationship between $\boldsymbol{\beta}(s')$ and $\boldsymbol{\alpha}(s')$.

Let

$$\mathbf{r}(s, s', \phi) := \mathbf{X}(s,\phi) - \boldsymbol{\xi}(s'), \quad (4.33)$$

be vector from the centre-line being integrated in (4.32), $\boldsymbol{\xi}(s')$, out to the point on the surface of the slender body, $\mathbf{X}(s,\phi)$, at which the boundary condition is evaluated; see figure 4.4. As the integration parameter runs along the arc-length of the centre-line, the vector $\boldsymbol{\xi}(s')$ moves with the integration variable whilst $\mathbf{X}(s,\phi)$ remains stationary. Recall from (4.13) that the point on the surface is given by

$$\mathbf{X}(s,\phi) = \boldsymbol{\xi}(s) + \varepsilon\eta(s)\mathbf{e}_r(s,\phi). \quad (4.34)$$

where, from (4.6),

$$\mathbf{e}_r(s,\phi) := \mathbf{e}_n(s)\cos\phi + \mathbf{e}_b(s)\sin\phi. \quad (4.35)$$

For Johnson's work outlined in Section 4.2.5, the initial *ansatz* for the flow field, (4.17), contained singular Stokeslets and potential dipoles, (4.14) and (4.15). These singularities are inversely proportional to powers of $|\mathbf{r}(s, s', \phi)|$. However, the new integrand in (4.32) is composed of distributions of regularised singularities, containing inverse powers of $r_\chi(s, s')$, say, where

$$r_\chi(s, s', \phi) := \sqrt{|\mathbf{r}(s, s', \phi)|^2 + \chi(s')} > 0. \quad (4.36)$$

This is due to the denominators in the definitions of the regularised Stokeslet and potential dipole, (4.25) and (4.26) possessing additional $\chi(s')$ contributions. Thus,

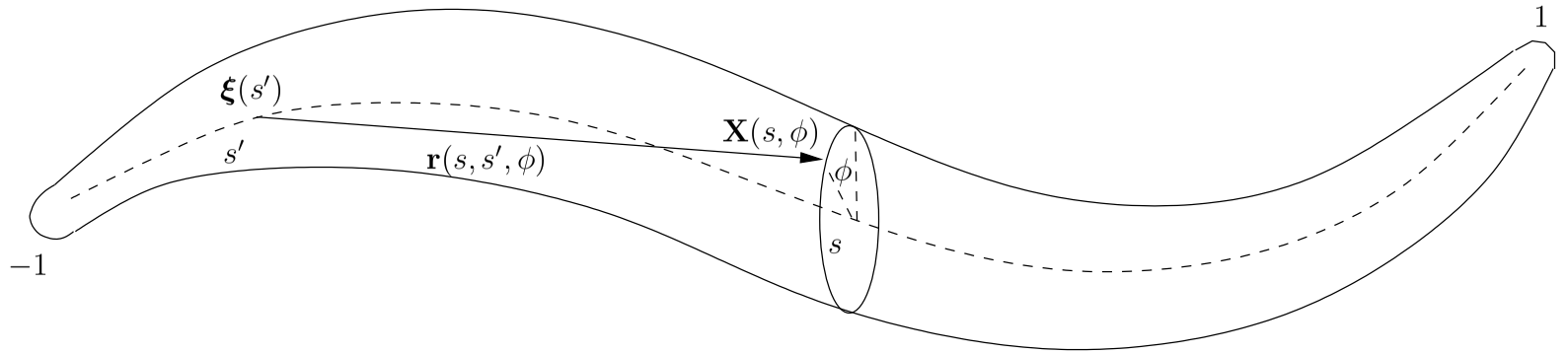


Figure 4.4: The vector $\mathbf{r}(s, s', \phi)$ from the centre-line being integrated at $s'$, $\boldsymbol{\xi}(s')$, to the point on the body surface at which the no-slip boundary condition is being enforced, $\mathbf{X}(s, \phi)$.

the scalar $r_\chi(s, s', \phi)$ represents the distance from the centre-line of the body to the point on the surface, albeit modified by the regularisation parameter, $\chi(s')$. As the integration variable, $s' \in [-e, e]$, runs along the arc-length of the centre-line, for each point $s \in [-1, 1]$ being evaluated in (4.32), the latter variable must be treated as a constant in the subsequent manipulations of the integral.

Using the notation from (4.33) and (4.36), the regularised singularities, (4.25) and (4.26), can be written as

$$\mathbf{S}^{\chi(s')}(\mathbf{X}(s,\phi), \boldsymbol{\xi}(s')) := \frac{\mathbf{I}}{r_\chi(s,s',\phi)} + \frac{\chi(s')\mathbf{I}}{r_\chi^3(s,s',\phi)} + \frac{\mathbf{r}(s,s',\phi) \otimes \mathbf{r}(s,s',\phi)}{r_\chi^3(s,s',\phi)}, \tag{4.37}$$

$$\mathbf{D}^{\chi(s')}(\mathbf{X}(s,\phi), \boldsymbol{\xi}(s')) := -\frac{\mathbf{I}}{r_\chi^3(s,s',\phi)} + \frac{3\chi(s')\mathbf{I}}{r_\chi^5(s,s',\phi)} + \frac{3\mathbf{r}(s,s',\phi) \otimes \mathbf{r}(s,s',\phi)}{r_\chi^5(s,s',\phi)}. \tag{4.38}$$

Combining (4.33), (4.34) and (4.36) gives the denominators of the singularities in (4.37) and (4.38), as powers of

$$r_\chi(s,s',\phi) = \sqrt{|\boldsymbol{\xi}(s) - \boldsymbol{\xi}(s') + \varepsilon\eta(s)\mathbf{e}_r(s,\phi)|^2 + \chi(s')} > 0, \tag{4.39}$$

where, from (4.27), the regularisation parameter is given by

$$\chi(s) := \varepsilon^2[(1-s^2) - \eta^2(s)]. \tag{4.40}$$

### 4.3.2 Enforcing the $\phi$-Independent Boundary Condition

When the integration variable, $s'$, is close to the point of evaluation of the boundary condition, $s$, equations (4.39) and (4.40) give that

$$r_\chi(s, s' \approx s, \phi) = \varepsilon\sqrt{1-s^2}. \tag{4.41}$$

For $s$ not to close to the end-points, this is $O(\varepsilon)$, but it cannot be equal to zero given $s'$ ranges from $-e$ to $e$. The maximum value $s'$ can take is $e$, so for $s$ located close to an end point, $s' \approx s = e$ say, the expression given by (4.41) is $O(\varepsilon^2)$, noting relation (4.24) between the effective eccentricity, $e$, and the slenderness ratio, $\varepsilon$. In both cases, this motivates a change of variables to inspect an inner region of the integral equation, (4.32), introducing

$$\sigma := \frac{s' - s}{\varepsilon}. \tag{4.42}$$

Rescaling the integral equation from the outer variable, $s'$, to the inner variable, $\sigma$, effectively zooms into the region of the integral near $s' \approx s$, allowing one to identify

easily any terms which depend on the cross-sectional angle, $\phi$. If the integral equation in (4.32) is to satisfy the leading-order boundary condition, (4.12), it must be the case that the inner solution is $\phi$-independent; this is now verified upon rescaling with (4.42) and taking the leading-order terms.

Thus (4.32) identically becomes, using the singularity definitions, (4.37) and (4.38),

$$\begin{aligned}\mathbf{V}(s) = \int_{-(e+s)/\varepsilon}^{(e-s)/\varepsilon} \Bigg[ \Bigg\{ & \frac{\mathbf{I}}{r_\chi(s, s+\varepsilon\sigma, \phi)} + \frac{\chi(s+\varepsilon\sigma)\mathbf{I}}{r_\chi^3(s, s+\varepsilon\sigma, \phi)} \\ & + \frac{\mathbf{r}(s, s+\varepsilon\sigma, \phi) \otimes \mathbf{r}(s, s+\varepsilon\sigma, \phi)}{r_\chi^3(s, s+\varepsilon\sigma, \phi)} \Bigg\} \boldsymbol{\alpha}(s+\varepsilon\sigma) \\ & + (e^2 - [s+\varepsilon\sigma]^2) \Bigg\{ - \frac{\mathbf{I}}{r_\chi^3(s, s+\varepsilon\sigma, \phi)} + \frac{3\chi(s+\varepsilon\sigma)\mathbf{I}}{r_\chi^5(s, s+\varepsilon\sigma, \phi)} \\ & + \frac{3\mathbf{r}(s, s+\varepsilon\sigma, \phi) \otimes \mathbf{r}(s, s+\varepsilon\sigma, \phi)}{r_\chi^5(s, s+\varepsilon\sigma, \phi)} \Bigg\} \boldsymbol{\beta}(s+\varepsilon\sigma) \Bigg] \varepsilon \mathrm{d}\sigma, \end{aligned} \tag{4.43}$$

where $r_\chi(s, s+\varepsilon\sigma, \phi)$ is given by equation (4.39). The temptation to expand the integrand variables in powers of $\varepsilon\sigma$ is hindered by the fact that, when $s'$ is an $O(1)$ distance from $s$, then $\sigma = (s'-s)/\varepsilon \sim O(1/\varepsilon)$. This highlights that $\varepsilon\sigma$ is not necessarily a small parameter for all $\sigma$. However, the integrand in (4.43) consists of inverse powers of $r_\chi(s, s', \phi)$, so that when the integration variable, $s'$, is an $O(1)$ distance from the point of evaluation, $s$, then $|\boldsymbol{\xi}(s) - \boldsymbol{\xi}(s')|$ increases (assuming the centre-line does not come close to self-intersection). This, in turn, causes $r_\chi(s, s', \phi)$ to increase, noting (4.39), and thus the magnitude of the terms in the integrand decrease. This suggests that, for cases when $\varepsilon\sigma$ may not be a small parameter in which to expand integrand variables, the decaying integrand itself in these regions away from $s' \approx s$ ensures that the contributions here are small.

To see this more rigorously, consider the first integral from equation (4.43), namely

$$\begin{aligned} I(s) &:= \int_{-(e+s)/\varepsilon}^{(e-s)/\varepsilon} \frac{\boldsymbol{\alpha}(s+\varepsilon\sigma)}{r_\chi(s, s+\varepsilon\sigma, \phi)} \varepsilon \mathrm{d}\sigma, \\ &= \int_{-(e+s)/\varepsilon}^{(e-s)/\varepsilon} \frac{\boldsymbol{\alpha}(s+\varepsilon\sigma)}{\sqrt{|\boldsymbol{\xi}(s) - \boldsymbol{\xi}(s+\varepsilon\sigma) + \varepsilon\eta(s)\mathbf{e}_r(s, \phi)|^2 + \chi(s+\varepsilon\sigma)}} \varepsilon \mathrm{d}\sigma, \end{aligned} \tag{4.44}$$

where the definition of $r_\chi(s, s+\varepsilon\sigma, \phi)$ from (4.39) has been used. In particular, $s$ is assumed to be in the central region of the centre-line, not too close to the end-points (although a similar analysis follows for $s$ taken close to the end-points). To ensure the terms in (4.44) can be expanded in powers of $\varepsilon\sigma$, the end regions of the integral,

for which $\sigma \sim O(1/\varepsilon)$, are removed using an arbitrary, fixed length, $\delta \sim O(1)$, where clearly $\delta \gg \varepsilon$. Thus,

$$I(s) = I_1(s) + I_2(s) + I_3(s), \tag{4.45}$$

where

$$I_1(s) := \int_{-(e+s)/\varepsilon}^{-[(e+s)/\varepsilon]+\delta} \frac{\boldsymbol{\alpha}(s+\varepsilon\sigma)}{\sqrt{|\boldsymbol{\xi}(s) - \boldsymbol{\xi}(s+\varepsilon\sigma) + \varepsilon\eta(s)\mathbf{e}_r(s,\phi)|^2 + \chi(s+\varepsilon\sigma)}}\,\varepsilon \mathrm{d}\sigma, \tag{4.46}$$

$$I_2(s) := \int_{-[(e+s)/\varepsilon]+\delta}^{[(e-s)/\varepsilon]-\delta} \frac{\boldsymbol{\alpha}(s+\varepsilon\sigma)}{\sqrt{|\boldsymbol{\xi}(s) - \boldsymbol{\xi}(s+\varepsilon\sigma) + \varepsilon\eta(s)\mathbf{e}_r(s,\phi)|^2 + \chi(s+\varepsilon\sigma)}}\,\varepsilon \mathrm{d}\sigma, \tag{4.47}$$

$$I_3(s) := \int_{[(e-s)/\varepsilon]-\delta}^{(e-s)/\varepsilon} \frac{\boldsymbol{\alpha}(s+\varepsilon\sigma)}{\sqrt{|\boldsymbol{\xi}(s) - \boldsymbol{\xi}(s+\varepsilon\sigma) + \varepsilon\eta(s)\mathbf{e}_r(s,\phi)|^2 + \chi(s+\varepsilon\sigma)}}\,\varepsilon \mathrm{d}\sigma. \tag{4.48}$$

For the central region, $I_2(s)$, variables can be expanded as-per-usual, so that

$$\boldsymbol{\xi}(s') \sim \boldsymbol{\xi}(s) + \varepsilon\sigma\mathbf{e}_t(s) + O(\varepsilon^2\sigma^2\kappa), \tag{4.49}$$

$$\chi(s') \sim \chi(s) + O(\varepsilon^3\sigma), \tag{4.50}$$

$$\boldsymbol{\alpha}(s') \sim \boldsymbol{\alpha}(s) + \varepsilon\sigma\frac{\partial\boldsymbol{\alpha}}{\partial s}(s) + O(\varepsilon^2\sigma^2), \tag{4.51}$$

In (4.49), the Frenet–Serret equations from (4.4) have been used, recalling that the curvature of the centre-line, $\kappa(s)$, is much smaller than $1/\varepsilon$, so that $\varepsilon\kappa \ll 1$. In (4.50), $\partial\chi(s)/\partial s \sim O(\varepsilon^2)$ has been enforced, noting that $\chi(s) \sim O(\varepsilon^2)$ from (4.40). Also from (4.40), this implies that the prescribed radius function, $\eta(s)$, must be such that $\eta(s)\eta'(s) \sim O(1)$ or less. In (4.51), it is assumed that $\partial^2\boldsymbol{\alpha}(s)/\partial^2 s$ is $O(1)$; this may be verified *a posteriori* upon obtaining an approximate RFT relationship for $\boldsymbol{\alpha}(s)$ in Section 4.3.3. In particular, $\partial\boldsymbol{\alpha}(s)/\partial s \propto \frac{\partial V}{\partial s}$ at leading order and, for static, translating bodies, $\frac{\partial V}{\partial s} = 0$, thus $\partial\boldsymbol{\alpha}(s)/\partial s \sim o(1)$. However, the analysis proceeds using $\partial\boldsymbol{\alpha}(s)/\partial s \sim O(1)$ as this is the only constraint required.

Hence, upon inserting the definition of the regularisation parameter, (4.40),

$$\begin{aligned}
I_2(s) &\sim \int_{-[(e+s)/\varepsilon]+\delta}^{[(e-s)/\varepsilon]-\delta} \frac{\boldsymbol{\alpha}(s)}{\sqrt{\sigma^2+1-s^2}}\,\mathrm{d}\sigma + \frac{\partial\boldsymbol{\alpha}}{\partial s}\int_{-[(e+s)/\varepsilon]+\delta}^{[(e-s)/\varepsilon]-\delta} \frac{\varepsilon\sigma}{\sqrt{\sigma^2+1-s^2}}\,\mathrm{d}\sigma + \text{h.o.t.} \\
&= \boldsymbol{\alpha}(s)\log\left[\frac{e-s-\varepsilon\delta+\sqrt{\varepsilon^2+(e-s-\varepsilon\delta)^2-\varepsilon^2s^2}}{-e-s+\varepsilon\delta+\sqrt{\varepsilon^2+(-e-s+\varepsilon\delta)^2-\varepsilon^2s^2}}\right], \\
&\qquad - 2s\frac{\partial\boldsymbol{\alpha}}{\partial s} + O\left(\varepsilon^2\delta^2\frac{\partial\boldsymbol{\alpha}}{\partial s}\right), \\
&\sim \boldsymbol{\alpha}(s)\left[2\log\left(\frac{2}{\varepsilon}\right) - \frac{\delta\varepsilon}{1-s} - \frac{\delta\varepsilon}{1+s}\right] - 2s\frac{\partial\boldsymbol{\alpha}}{\partial s} + O(\varepsilon^2),
\end{aligned} \tag{4.52}$$

recalling $e = \sqrt{1-\varepsilon^2}$ from (4.24) and $\partial\boldsymbol{\alpha}(s)/\partial s \sim O(1)$.

For the end region near $s' = e$, the integral, $I_3(s)$, is rewritten in terms of a translated variable, $u = (e-s)/\varepsilon - \sigma$, so that

$$I_3(s) = \int_0^{\delta} \frac{\boldsymbol{\alpha}(e-\varepsilon u)}{\sqrt{|\boldsymbol{\xi}(s) - \boldsymbol{\xi}(e-\varepsilon u) + \varepsilon\eta(s)\mathbf{e}_r(s,\phi)|^2 + \chi(e-\varepsilon u)}}\,\varepsilon \mathrm{d}u. \tag{4.53}$$

This is similarly expanded in terms of $\varepsilon u$, where $u$ ranges from 0 to $\delta$, and leading-order terms are retained, giving

$$I_3(s) \sim \int_0^{\delta} \frac{\boldsymbol{\alpha}(e)}{\sqrt{|\boldsymbol{\xi}(s) - \boldsymbol{\xi}(e) + \varepsilon u\mathbf{e}_t(e) + \varepsilon\eta(s)\mathbf{e}_r(s,\phi)|^2 + \chi(e)}}\,\varepsilon \mathrm{d}u \\ + O\left(\varepsilon^2\delta^2 \frac{\partial\boldsymbol{\alpha}}{\partial s}\right). \tag{4.54}$$

As $\eta^2(s) \to 1 - s^2$ for $s \to \pm 1$ from (4.31), then $\eta^2(e) \sim O(\varepsilon^4)$, implying $\chi(e) \sim \varepsilon^4$ from (4.40). Letting

$$\mathbf{B}(s,\phi) := \boldsymbol{\xi}(s) - \boldsymbol{\xi}(e) + \varepsilon\eta(s)\mathbf{e}_r(s,\phi), \tag{4.55}$$

equation (4.54) can be written as

$$\begin{aligned} I_3(s) &\sim \int_0^{\delta} \frac{\boldsymbol{\alpha}(e)}{|\mathbf{B}(s,\phi) + \varepsilon u\mathbf{e}_t(e)|}\,\varepsilon \mathrm{d}u + O(\varepsilon^2), \\ &\leq \int_0^{\delta} \frac{\boldsymbol{\alpha}(e)}{|\mathbf{B}(s,\phi)| - \varepsilon u}\,\varepsilon \mathrm{d}u + O(\varepsilon^2), \\ &\sim -\boldsymbol{\alpha}(e)\log\left[1 - \frac{\varepsilon\delta}{|\mathbf{B}(s,\phi)|}\right] + O(\varepsilon^2), \\ &\sim \frac{\varepsilon\delta\boldsymbol{\alpha}(e)}{1-s} + O(\varepsilon^2), \end{aligned} \tag{4.56}$$

using

$$\begin{aligned} |\mathbf{B}(s,\phi)| &\sim |\boldsymbol{\xi}(s) - \boldsymbol{\xi}(e)| + O(\varepsilon), \\ &\sim e - s + O(\varepsilon), \\ &\sim 1 - s + O(\varepsilon). \end{aligned} \tag{4.57}$$

In (4.57), it is assumed that the centre-line does not come close to self-intersection, hence $|\boldsymbol{\xi}(s) - \boldsymbol{\xi}(e)|$ is greater than $O(\varepsilon)$ and approximated by the arc-length between the two, centre-line points. Repeating the procedure at the end region near $-e$ gives

$$I_1(s) \sim \frac{\varepsilon\delta\boldsymbol{\alpha}(-e)}{1+s} + O(\varepsilon^2), \tag{4.58}$$

hence, adding (4.52), (4.56) and (4.58) gives

$$\begin{aligned} I(s) &\sim 2\boldsymbol{\alpha}(s)\log\left(\frac{2}{\varepsilon}\right) + \frac{\varepsilon\delta[\boldsymbol{\alpha}(-e)-\boldsymbol{\alpha}(s)]}{1+s} + \frac{\varepsilon\delta[\boldsymbol{\alpha}(e)-\boldsymbol{\alpha}(s)]}{1-s} - 2s\frac{\partial\boldsymbol{\alpha}}{\partial s} + O(\varepsilon^2), \\ &\sim 2\boldsymbol{\alpha}(s)\log\left(\frac{2}{\varepsilon}\right) - \frac{\varepsilon\delta\boldsymbol{\alpha}'(s)(e+s)}{1+s} + \frac{\varepsilon\delta\boldsymbol{\alpha}'(s)(e-s)}{1-s} - 2s\frac{\partial\boldsymbol{\alpha}}{\partial s} + o(\varepsilon), \\ &\sim 2\boldsymbol{\alpha}(s)\log\left(\frac{2}{\varepsilon}\right) - 2s\frac{\partial\boldsymbol{\alpha}}{\partial s} + o(\varepsilon), \end{aligned} \tag{4.59}$$

using $e \sim 1 + O(\varepsilon^2)$. As $\delta \sim O(1)$, equation (4.59) determines the integral up to $o(\varepsilon)$ corrections, with the $\delta$ terms cancelling each other out, as expected, given the original integral did not contain $\delta$. Had the integration range not been split, so that the terms inside the integral in (4.44) were expanded naively in powers of $\varepsilon\sigma$, despite $\sigma \sim O(1/\varepsilon)$ at the ends, then

$$\begin{aligned} I &\sim \int_{-(e+s)/\varepsilon}^{(e-s)/\varepsilon} \frac{\boldsymbol{\alpha}(s)}{\sqrt{\sigma^2+1-s^2}}\,\mathrm{d}\sigma + \frac{\partial\boldsymbol{\alpha}}{\partial s}\int_{-(e+s)/\varepsilon}^{(e-s)/\varepsilon} \frac{\sigma}{\sqrt{\sigma^2+1-s^2}}\,\mathrm{d}\sigma + \text{h.o.t.} \\ &\sim \boldsymbol{\alpha}(s)\log\left[\frac{1+e}{1-e}\right] - 2s\frac{\partial\boldsymbol{\alpha}}{\partial s} + o(\varepsilon), \\ &\sim 2\boldsymbol{\alpha}(s)\log\left(\frac{2}{\varepsilon}\right) - 2s\frac{\partial\boldsymbol{\alpha}}{\partial s} + o(\varepsilon). \end{aligned} \tag{4.60}$$

Thus, when compared to (4.59), the absolute error in taking the naive approximation is $o(\varepsilon)$; for the work in this chapter and the next, errors smaller than $O(\varepsilon)$ are deemed acceptable.

Following the previous example, all variables inside the integral equation, (4.43), are expanded in $\varepsilon\sigma$, retaining the leading-order terms. Thus, the expansions (4.49), (4.50) and (4.51), with an analogous expansion for $\boldsymbol{\beta}(s')$ following the latter, are inserted into (4.39) and (4.43), to give

$$\begin{aligned} \mathbf{V}(s) \approx \int_{-(e+s)/\varepsilon}^{(e-s)/\varepsilon} \Bigg[ &\left\{ \frac{\mathbf{I}}{\sqrt{\sigma^2+1-s^2}} + \frac{\chi(s)\mathbf{I}}{\varepsilon^2(\sigma^2+1-s^2)^{3/2}} \right. \\ &\left. + \frac{(\sigma\mathbf{e}_t(s)+\eta(s)\mathbf{e}_r(s,\phi)) \otimes (\sigma\mathbf{e}_t(s)+\eta(s)\mathbf{e}_r(s,\phi))}{(\sigma^2+1-s^2)^{3/2}} \right\} \boldsymbol{\alpha}(s) \\ &+ (e^2 - [s+\varepsilon\sigma]^2) \left\{ -\frac{\mathbf{I}}{(\sigma^2+1-s^2)^{3/2}} + \frac{3\chi(s)\mathbf{I}}{\varepsilon^2(\sigma^2+1-s^2)^{5/2}} \right. \\ &\left. + \frac{(\sigma\mathbf{e}_t(s)+\eta(s)\mathbf{e}_r(s,\phi)) \otimes (\sigma\mathbf{e}_t(s)+\eta(s)\mathbf{e}_r(s,\phi))}{(\sigma^2+1-s^2)^{5/2}} \right\} \frac{\boldsymbol{\beta}(s)}{\varepsilon^2} \Bigg]\,\mathrm{d}\sigma. \end{aligned} \tag{4.61}$$

The parabolic modulation, $(e^2-[s+\varepsilon\sigma]^2)$ in (4.61), has not been expanded in terms of $\varepsilon$, but instead has been left intact. This is to ensure the expanded terms respect both

their order and the boundary conditions on approaching $s' \to \pm e$. As an aside, note that this is equivalent to doing a two-variable expansion, in that $\boldsymbol{\beta}(s')$ is effectively treated as a slow variable while the parabolic modulation assumes the role of a fast variable; further details may be found on p74 *et seq.* of Johnson's thesis [52].

Note the following observations: the curvature has dropped out of the boundary condition in (4.61), thus indicating that the centre-line is approximately straight. Also, the body is assumed to have prolate-spheroidal caps and the definition of the regularisation parameter, (4.40), contains $1 - s^2$, the square of the radius for a prolate spheroid. These observations motivate the use of the no-slip boundary condition for the flow past a translating, straight, prolate spheroid.

From Section 1.3.2.2, the no-slip boundary condition, (1.74), can be written using the notation (and non-dimensionalisation) in this chapter, with the straight centre-line oriented in the $\mathbf{e}_t(s)$ direction. This gives, with superscript $P$ referring to the exact, singularity representation of the flow past a translating, prolate spheroid,

$$\mathbf{V}^P = \int_{-e}^{e} \left[ \mathbf{S}(\mathbf{X}(s,\phi), \boldsymbol{\xi}(s')) - \frac{(1-e^2)}{2e^2}(e^2 - s'^2)\mathbf{D}(\mathbf{X}(s,\phi), \boldsymbol{\xi}(s')) \right] \boldsymbol{\alpha}^P(s)\, \mathrm{d}s', \quad (4.62)$$

for all $\phi$, where $\mathbf{X}(s,\phi)$ is a point on the surface,

$$\mathbf{X} = \boldsymbol{\xi}(s) + \varepsilon\sqrt{1-s^2}\mathbf{e}_r(s,\phi), \quad (4.63)$$

and $\mathbf{e}_r(s,\phi)$ is the cross-sectional, radial, unit vector such that

$$\mathbf{e}_r = \mathbf{e}_n(s)\cos\phi + \mathbf{e}_b(s)\sin\phi. \quad (4.64)$$

Here, $\mathbf{S}(\mathbf{x},\mathbf{y})$ and $\mathbf{D}(\mathbf{x},\mathbf{y})$ are the singular Stokeslet and potential dipole singularities, (4.14) and (4.15) respectively. Rewriting (4.62) in inner variables, $\sigma = (s'-s)/\varepsilon$, noting that, due to the straight centre-line, $\boldsymbol{\xi}(s') = \boldsymbol{\xi}(s) + (s'-s)\mathbf{e}_t(s)$, gives

$$\begin{aligned}
\mathbf{V}^P = \int_{-(e+s)/\varepsilon}^{(e-s)/\varepsilon} \Bigg[ \Bigg\{ & \frac{\mathbf{I}}{\sqrt{\sigma^2+1-s^2}} \\
& + \frac{(\sigma\mathbf{e}_t(s) + \sqrt{1-s^2}\mathbf{e}_r(s,\phi)) \otimes (\sigma\mathbf{e}_t(s) + \sqrt{1-s^2}\mathbf{e}_r(s,\phi))}{(\sigma^2+1-s^2)^{3/2}} \Bigg\} \\
& - \frac{1}{2e^2}(e^2 - [s+\varepsilon\sigma]^2) \Bigg\{ -\frac{\mathbf{I}}{(\sigma^2+1-s^2)^{3/2}} \\
& + \frac{(\sigma\mathbf{e}_t(s) + \sqrt{1-s^2}\mathbf{e}_r(s,\phi)) \otimes (\sigma\mathbf{e}_t(s) + \sqrt{1-s^2}\mathbf{e}_r(s,\phi))}{(\sigma^2+1-s^2)^{5/2}} \Bigg\} \boldsymbol{\alpha}^P(s) \Bigg] \, \mathrm{d}\sigma.
\end{aligned} \quad (4.65)$$

This known, singularity representation for the flow past a prolate spheroid, in particular the $\phi$-independent boundary condition (4.65), motivates the following steps in relation to the SBT boundary condition in (4.61). The first step, highlighted by (4.62), is to let

$$\boldsymbol{\beta}(s) = -\frac{(1-e^2)}{2e^2}\boldsymbol{\alpha}(s) = -\frac{\varepsilon^2}{2e^2}\boldsymbol{\alpha}(s), \tag{4.66}$$

and check whether this leads to the same $\phi$-independence exhibited by the exact, prolate-spheroidal solution (4.65). The second step is to address the additional terms arising in the SBT boundary condition (4.61) due to the regularised singularities that do not appear in the exact representation for the prolate spheroid, (4.65). These extra terms are

$$\int_{-(e+s)/\varepsilon}^{(e-s)/\varepsilon} \left[ \frac{\chi(s)\boldsymbol{\alpha}(s)}{\varepsilon^2(\sigma^2+1-s^2)^{3/2}} + (e^2-[s+\varepsilon\sigma]^2)\frac{3\chi(s)\boldsymbol{\beta}(s)}{\varepsilon^2(\sigma^2+1-s^2)^{5/2}} \right] \mathrm{d}\sigma. \tag{4.67}$$

Using the relation between $\boldsymbol{\beta}(s)$ and $\boldsymbol{\alpha}(s)$ from (4.66), these terms become

$$\begin{aligned}
&\frac{\chi(s)\boldsymbol{\alpha}(s)}{\varepsilon^2}\int_{-(e+s)/\varepsilon}^{(e-s)/\varepsilon} \left[ \frac{1}{(\sigma^2+1-s^2)^{3/2}} - \frac{3}{2e^2}(e^2-[s+\varepsilon\sigma]^2)\frac{1}{(\sigma^2+1-s^2)^{5/2}} \right] \mathrm{d}\sigma, \\
&= \frac{\chi(s)\boldsymbol{\alpha}(s)}{\varepsilon^2}\left[ \frac{2e}{1-e^2s^2} - \left(\frac{3}{2e^2}\right)\left(\frac{4e^3}{3(1-e^2s^2)}\right) \right], \\
&= \mathbf{0}.
\end{aligned} \tag{4.68}$$

Hence, by direct integration, the extra terms in (4.68) integrate to zero, further reinforcing the choice of $\boldsymbol{\beta}(s)$ in terms of $\boldsymbol{\alpha}(s)$ from (4.66). The remaining terms in the SBT boundary condition (4.61) are collected and compared with the exact, prolate-spheroid solution in (4.65). The remaining terms are given by

$$\begin{aligned}
\mathbf{V}(s) \approx \int_{-(e+s)/\varepsilon}^{(e-s)/\varepsilon} \Bigg[ &\Bigg\{ \frac{\mathbf{I}}{\sqrt{\sigma^2+1-s^2}} \\
&+ \frac{(\sigma\mathbf{e}_t(s)+\eta(s)\mathbf{e}_r(s,\phi)) \otimes (\sigma\mathbf{e}_t(s)+\eta(s)\mathbf{e}_r(s,\phi))}{(\sigma^2+1-s^2)^{3/2}} \Bigg\} \\
&- \frac{1}{2e^2}(e^2-[s+\varepsilon\sigma]^2) \Bigg\{ -\frac{\mathbf{I}}{(\sigma^2+1-s^2)^{3/2}} \\
&+ \frac{(\sigma\mathbf{e}_t(s)+\eta(s)\mathbf{e}_r(s,\phi)) \otimes (\sigma\mathbf{e}_t(s)+\eta(s)\mathbf{e}_r(s,\phi))}{(\sigma^2+1-s^2)^{5/2}} \Bigg\} \boldsymbol{\alpha}(s) \Bigg] \mathrm{d}\sigma,
\end{aligned} \tag{4.69}$$

which is essentially identical to (4.65), where the only difference is that $\sqrt{1-s^2}$ is replaced by $\eta(s)$ in the numerators of the integrand. Knowing that (4.65) is $\phi$-independent, the last step is to now ensure that (4.69) is also $\phi$-independent, checking

whether the presence of $\eta(s)$ in place of $\sqrt{1-s^2}$ breaks the $\phi$-independence.

Inserting the radial, unit vector in terms of $\phi$ from (4.35) into the known solution for the prolate spheroid, (4.65), and writing $\boldsymbol{\alpha}(s)$ in tangential, normal and binormal components, gives

$$\begin{aligned}
\mathbf{V}^P = \int_{-(e+s)/\varepsilon}^{(e-s)/\varepsilon} \Bigg\{ & \frac{\alpha_t \mathbf{e}_t + \alpha_n \mathbf{e}_n + \alpha_b \mathbf{e}_b}{\left(\sigma^2 + 1 - s^2\right)^{1/2}} \\
& + \frac{\alpha_t \sigma^2 + \alpha_n \sqrt{1-s^2}\sigma\cos\phi - \alpha_b \sqrt{1-s^2}\sigma\sin\phi}{\left(\sigma^2 + 1 - s^2\right)^{3/2}} \mathbf{e}_t \\
& + \frac{\alpha_t \sqrt{1-s^2}\sigma\cos\phi + \alpha_n (1-s^2)\left[\frac{\cos 2\phi + 1}{2}\right] - \alpha_b (1-s^2)\left[\frac{\sin 2\phi}{2}\right]}{\left(\sigma^2 + 1 - s^2\right)^{3/2}} \mathbf{e}_n \\
& + \frac{-\alpha_t \sqrt{1-s^2}\sigma\sin\phi - \alpha_n (1-s^2)\left[\frac{\sin 2\phi}{2}\right] + \alpha_b (1-s^2)\left[\frac{1-\cos 2\phi}{2}\right]}{\left(\sigma^2 + 1 - s^2\right)^{3/2}} \mathbf{e}_b \Bigg\} \\
- \frac{1}{2e^2}\left(e^2 - [s+\varepsilon\sigma]^2\right) \Bigg\{ & - \frac{\alpha_t \mathbf{e}_t + \alpha_n \mathbf{e}_n + \alpha_b \mathbf{e}_b}{\left(\sigma^2 + 1 - s^2\right)^{3/2}} \\
& + \frac{3\left(\alpha_t \sigma^2 + \alpha_n \sqrt{1-s^2}\sigma\cos\phi - \alpha_b \sqrt{1-s^2}\sigma\sin\phi\right)}{\left(\sigma^2 + 1 - s^2\right)^{5/2}} \mathbf{e}_t \\
& + \frac{3\left(\alpha_t \sqrt{1-s^2}\sigma\cos\phi + \alpha_n (1-s^2)\left[\frac{\cos 2\phi + 1}{2}\right] - \alpha_b (1-s^2)\left[\frac{\sin 2\phi}{2}\right]\right)}{\left(\sigma^2 + 1 - s^2\right)^{5/2}} \mathbf{e}_n \\
& + \frac{3\left(-\alpha_t \sqrt{1-s^2}\sigma\sin\phi - \alpha_n (1-s^2)\left[\frac{\sin 2\phi}{2}\right] + \alpha_b (1-s^2)\left[\frac{1-\cos 2\phi}{2}\right]\right)}{\left(\sigma^2 + 1 - s^2\right)^{5/2}} \mathbf{e}_b \Bigg\} \, \mathrm{d}\sigma.
\end{aligned} \tag{4.70}$$

It is now clear where the $\phi$ dependence explicitly lies. The linearly independent $\phi$ terms, $\sin\phi$, $\cos\phi$, $\sin(2\phi)$ and $\cos(2\phi)$, are collected up, knowing that their coefficients must all be zero as the expression is $\phi$-independent, being the exact solution for the flow around a prolate spheroid. These coefficients are combinations of integrals that evaluate to zero, useful for simplifying the SBT boundary condition, (4.69). Hence, from (4.70), it must be true that

$$\begin{aligned}
\mathbf{0} = & (\alpha_n \mathbf{e}_t + \alpha_t \mathbf{e}_n)\sqrt{1-s^2} J_1 \cos\phi - (\alpha_b \mathbf{e}_t + \alpha_t \mathbf{e}_b)\sqrt{1-s^2} J_1 \sin\phi \\
& + (\alpha_n \mathbf{e}_n - \alpha_b \mathbf{e}_b)\left(\frac{1-s^2}{2}\right) J_2 \cos(2\phi) - (\alpha_b \mathbf{e}_n + \alpha_n \mathbf{e}_b)\left(\frac{1-s^2}{2}\right) J_2 \sin(2\phi),
\end{aligned} \tag{4.71}$$

for all $\phi \in [0, 2\pi)$, so that

$$J_1 = J_2 = 0, \tag{4.72}$$

where

$$J_1 := \int_{-(e+s)/\varepsilon}^{(e-s)/\varepsilon} \left[ \frac{\sigma}{(\sigma^2+1-s^2)^{3/2}} - \frac{3}{2e^2}(e^2-[s+\varepsilon\sigma]^2)\frac{\sigma}{(\sigma^2+1-s^2)^{5/2}} \right] \mathrm{d}\sigma, \quad (4.73)$$

$$J_2 := \int_{-(e+s)/\varepsilon}^{(e-s)/\varepsilon} \left[ \frac{1}{(\sigma^2+1-s^2)^{3/2}} - \frac{3}{2e^2}(e^2-[s+\varepsilon\sigma]^2)\frac{1}{(\sigma^2+1-s^2)^{5/2}} \right] \mathrm{d}\sigma. \quad (4.74)$$

These results can now be used to investigate the boundary condition, (4.69), which is written in a similar way as

$$\begin{aligned}
\mathbf{V}(s) \approx \int_{-(e+s)/\varepsilon}^{(e-s)/\varepsilon} & \left\{ \frac{\alpha_t\mathbf{e}_t + \alpha_n\mathbf{e}_n + \alpha_b\mathbf{e}_b}{(\sigma^2+1-s^2)^{1/2}} + \frac{\alpha_t\sigma^2}{(\sigma^2+1-s^2)^{3/2}}\mathbf{e}_t \right. \\
& \left. + \frac{\frac{1}{2}\alpha_n\eta^2(s)}{(\sigma^2+1-s^2)^{3/2}}\mathbf{e}_n + \frac{\frac{1}{2}\alpha_b\eta^2(s)}{(\sigma^2+1-s^2)^{3/2}}\mathbf{e}_b \right\} \\
& - \frac{1}{2e^2}(e^2-[s+\varepsilon\sigma]^2) \left\{ -\frac{\alpha_t\mathbf{e}_t + \alpha_n\mathbf{e}_n + \alpha_b\mathbf{e}_b}{(\sigma^2+1-s^2)^{3/2}} + \frac{3\alpha_t\sigma^2}{(\sigma^2+1-s^2)^{5/2}}\mathbf{e}_t \right. \\
& \left. + \frac{\frac{3}{2}\alpha_n\eta^2(s)}{(\sigma^2+1-s^2)^{5/2}}\mathbf{e}_n + \frac{\frac{3}{2}\alpha_b\eta^2(s)}{(\sigma^2+1-s^2)^{5/2}}\mathbf{e}_b \right\} d\sigma \\
& + (\alpha_n\mathbf{e}_t + \alpha_t\mathbf{e}_n)\eta(s)J_1\cos\phi - (\alpha_b\mathbf{e}_t + \alpha_t\mathbf{e}_b)\eta(s)J_1\sin\phi \\
& + (\alpha_n\mathbf{e}_n - \alpha_b\mathbf{e}_b)\left(\frac{\eta^2(s)}{2}\right)J_2\cos(2\phi) - (\alpha_b\mathbf{e}_n + \alpha_n\mathbf{e}_b)\left(\frac{\eta^2(s)}{2}\right)J_2\sin(2\phi).
\end{aligned} \quad (4.75)$$

Knowing $J_1 = J_2 = 0$ from (4.72), (4.75) is clearly $\phi$-independent, which confirms that the relation between $\boldsymbol{\alpha}(s)$ and $\boldsymbol{\beta}(s)$ in (4.66) does indeed ensure the boundary condition holds for all $\phi \in [0, 2\pi)$.

### 4.3.3 Deriving RFT

Continuing with the manipulation in (4.75) leads to

$$\mathbf{V}(s) \approx \frac{1}{C_T}\alpha_t(s)\mathbf{e}_t(s) + \frac{1}{C_N}\alpha_n(s)\mathbf{e}_n(s) + \frac{1}{C_B}\alpha_b(s)\mathbf{e}_b(s), \quad (4.76)$$

where

$$\begin{aligned}
\frac{1}{C_T} := \int_{-(e+s)/\varepsilon}^{(e-s)/\varepsilon} & \left[ \left\{ \frac{1}{(\sigma^2+1-s^2)^{1/2}} + \frac{\sigma^2}{(\sigma^2+1-s^2)^{3/2}} \right\} \right. \\
& \left. - \frac{1}{2e^2}(e^2-[s+\varepsilon\sigma]^2) \left\{ -\frac{1}{(\sigma^2+1-s^2)^{3/2}} + \frac{3\sigma^2}{(\sigma^2+1-s^2)^{5/2}} \right\} \right] \mathrm{d}\sigma,
\end{aligned} \quad (4.77)$$

and

$$\frac{1}{C_N} = \frac{1}{C_B} := \int_{-(e+s)/\varepsilon}^{(e-s)/\varepsilon} \left[ \left\{ \frac{1}{\left(\sigma^2+1-s^2\right)^{1/2}} + \frac{\eta^2(s)}{2\left(\sigma^2+1-s^2\right)^{3/2}} \right\} \right.$$
$$\left. -\frac{1}{2e^2}(e^2-[s+\varepsilon\sigma]^2) \left\{ -\frac{1}{\left(\sigma^2+1-s^2\right)^{3/2}} + \frac{3\eta^2(s)}{2\left(\sigma^2+1-s^2\right)^{5/2}} \right\} \right] \mathrm{d}\sigma. \quad (4.78)$$

These integrals can be evaluated exactly, giving

$$\frac{1}{C_T} = \frac{-2e + (1+e^2)\log\left(\frac{1+e}{1-e}\right)}{e^2}, \quad (4.79)$$

and

$$\frac{1}{C_N} = \frac{2e + (3e^2-1)\log\left(\frac{1+e}{1-e}\right)}{2e^2}. \quad (4.80)$$

The coefficients, (4.79) and (4.80), do not depend on $\eta^2(s)$, but are exactly those found in the prolate-spheroid solution, (1.75).

The force exerted on any surface enclosing a Stokeslet of strength $\boldsymbol{\alpha}$ is given by $8\pi\mu\boldsymbol{\alpha}$ from (1.47), while the analogous force due to the potential dipoles is zero, (1.61). These results can be used to derive an approximation to SBT, namely RFT.

In order to satisfy the boundary conditions at a point $s$, the Stokeslet and potential-dipole distributions, $\boldsymbol{\alpha}(s')$ and $\boldsymbol{\beta}(s')$, were taken to be their leading-order contributions at $s$, $\boldsymbol{\alpha}(s)$ and $\boldsymbol{\beta}(s)$. If this approximation is made along the whole centre-line of the slender body, then the force exerted on the body at $s$ due to the singularities is given by

$$\mathbf{f}(s) = 8\pi\mu\boldsymbol{\alpha}(s). \quad (4.81)$$

Thus, inverting (4.76) and taking leading-order expressions from (4.79) and (4.80) gives resistive-force theory in the form

$$\mathbf{f}(s) \approx \left(\frac{2\pi\mu}{\log\left(\frac{2}{\varepsilon}\right)-\frac{1}{2}}\right) V_t(s)\mathbf{e}_t(s) + \left(\frac{4\pi\mu}{\log\left(\frac{2}{\varepsilon}\right)+\frac{1}{2}}\right) V_n(s)\mathbf{e}_n(s)$$
$$+ \left(\frac{4\pi\mu}{\log\left(\frac{2}{\varepsilon}\right)+\frac{1}{2}}\right) V_b(s)\mathbf{e}_b(s). \quad (4.82)$$

Due to the absence of $\eta(s)$, this form is identical to that of Johnson, [53], if one were to use the inner solution developed in his work.

### 4.3.4 Theory Summary

The SBT developed in this chapter describes the flow around a thin, slender body with a dimensionless, circular, cross-sectional radius, $\varepsilon\eta(s)$ non-dimensionalised with the half-length of the body centre-line, $L$. The radius function varies with the arc-length, $s$, along a prescribed, curvilinear centre-line, $\boldsymbol{\xi}(s)$. The slenderness ratio, $\varepsilon$, is given by

$$\varepsilon := \frac{\max_{s\in[-L,L]}\{\eta(s)\}}{L} \ll 1. \tag{4.83}$$

The flow field describing the flow of a low Reynolds number, viscous fluid around the slender body is given by

$$\mathbf{u}(\mathbf{x}) = \int_{-e}^{e}\left[\mathbf{S}^{\chi(s')}(\mathbf{x},\boldsymbol{\xi}(s')) - \frac{(1-e^2)}{2e^2}(e^2-s'^2)\mathbf{D}^{\chi(s')}(\mathbf{x},\boldsymbol{\xi}(s'))\right]\boldsymbol{\alpha}(s')\,\mathrm{d}s', \tag{4.84}$$

where

$$e := \sqrt{1-\varepsilon^2}, \tag{4.85}$$

is the effective eccentricity and

$$\mathbf{S}^{\chi(s')}(\mathbf{x},\mathbf{y}) := \frac{(|\mathbf{x}-\mathbf{y}|^2+2\chi(s'))\mathbf{I}}{(\,|\mathbf{x}-\mathbf{y}|^2+\chi(s')\,)^{3/2}} + \frac{(\mathbf{x}-\mathbf{y})\otimes(\mathbf{x}-\mathbf{y})}{(\,|\mathbf{x}-\mathbf{y}|+\chi(s')\,)^{3/2}}, \tag{4.86}$$

and

$$\mathbf{D}^{\chi(s')}(\mathbf{x},\mathbf{y}) := -\frac{(|\mathbf{x}-\mathbf{y}|^2-2\chi(s'))\mathbf{I}}{(\,|\mathbf{x}-\mathbf{y}|^2+\chi(s')\,)^{5/2}} + \frac{3(\mathbf{x}-\mathbf{y})\otimes(\mathbf{x}-\mathbf{y})}{(\,|\mathbf{x}-\mathbf{y}|+\chi(s')\,)^{5/2}}. \tag{4.87}$$

The regularisation parameter, $\chi(s')$, is defined as

$$\chi(s) := \varepsilon^2[(1-s^2)-\eta^2(s)], \tag{4.88}$$

The theory satisfies, to leading-order in the slenderness parameter, the no-slip boundary condition,

$$\mathbf{u}(\mathbf{X}(s,\phi)) = \mathbf{V}(s), \tag{4.89}$$

for all $\phi\in[0,2\pi)$ and for a point on the surface, $\mathbf{X}(s,\phi)$, given by

$$\mathbf{X}(s,\phi) = \boldsymbol{\xi}(s) + \varepsilon\eta(s)\mathbf{e}_r(s,\phi), \tag{4.90}$$

where

$$\mathbf{e}_r(s,\phi) := \mathbf{e}_n(s)\cos\phi + \mathbf{e}_b(s)\sin\phi. \tag{4.91}$$

The translational surface velocity, $\mathbf{V}(s)$, is prescribed, as is the static centre-line of the slender body. Note that the theory can be developed with an angular velocity,

$\boldsymbol{\Omega} \sim O(1)$, introducing an additional, $O(\varepsilon)$ term in the boundary condition, (4.89). However, the initial *ansatz* for the flow field in (4.84) must be modified to include higher-order, weighted singularities based on exact solutions for rotating and translating prolate spheroids, [21, 53]. The weightings can then be chosen to ensure the *ansatz* is independent of $\phi$ when satisfying the no-slip boundary condition, as also described in Section 6.2 regarding further extensions to the work in this thesis.

## 4.4 Discussion

A slender-body theory (SBT) has been developed which extends the range of permissible shapes to those with circular cross sections and a varying cross-sectional radius along the body, $\eta(s)$, for which $\mathrm{d}\eta/\mathrm{d}s$ can be zero at any $s$; this builds upon the work of Johnson [53] in which $\mathrm{d}\eta/\mathrm{d}s = 0$ at $s = 0$ only, thus the revised theory allows bodies of more general, slender shapes to be modelled, such as tapering or wave-like structures. This has applications in modelling biological microswimmers where, for example, the mammalian sperm tapers due to outer-dense fibres, [34].

In Johnson's SBT [53], the boundary condition is satisfied to algebraic leading order by posing a velocity-field *ansatz* in terms of an integral of weighted, singular Stokeslets and potential dipoles. By taking the leading-order terms in the boundary condition, the surface velocity is effectively translational and thus does not depend on any cross-sectional angle, $\phi$, within the slender body itself; it is this $\phi$-independence which must be enforced when seeking to satisfy the leading-order, boundary condition with a velocity-field *ansatz*. In doing so, a relationship between the weighting of the potential dipole and the Stokeslet distributions emerges. For Johnson's work, it is this relationship that places the restriction on $\eta(s)$, namely that $\mathrm{d}\eta/\mathrm{d}s = 0$ at $s = 0$ and only at $s = 0$.

In addition to the restriction, the weighting between the potential dipole and the Stokeslet used in Johnson's SBT [53], given by equation (4.19), varies depending on whether the integration parameter, $s'$, lies within the end regions or the central region of the centre-line. In the end regions, where the slender body takes the form of prolate-spheroidal caps, the weighting is analogous to that used in the exact, singularity representation for the flow past a translating, prolate spheroid, [22], as expected. In the central region, however, the weighting depends on $\eta(s)$. Thus, the variations in the cross-sectional radius along the centre-line are accounted for by adjusting the

potential-dipole weighting in the central region accordingly.

In the current context, however, a velocity field has been posed in terms of regularised Stokeslets and potential dipoles, without the need to split the centre-line into end regions and a central region. Also, the weighting between the regularised singularities does not vary with $\eta(s)$. Instead, it is the regularisation parameter itself which varies with $\eta(s)$, accounting for the changes in the cross-sectional radius along the centre-line. This simplifies the analysis, in that asymptotic matching between three, different regions is not required. It also avoids placing restrictions on the zeros of $\eta'(s)$.

RFT has been derived from the SBT in this chapter by taking the leading-order, logarithmic terms from the inner solution. It states that the force exerted by the slender body at a point $s$ along the centre-line in a direction tangential, normal or binormal to the centre-line, is proportional to the velocity of the centre-line at that point, in the same direction. The constants of proportionality are seen to be larger for the normal and binormal components, highlighting how a larger force is generated when the motion of the slender body is in these directions, as opposed to a tangential motion. The RFT does not depend on the cross-sectional radius, $\eta(s)$, but effectively assumes the slender body is approximated by a straight, prolate spheroid at $s$.

While the range of permissible shapes has been greatly improved, there still exist model limitations. The slender body being considered must have prolate-ellipsoidal ends, thus shapes with spikes or angular tips are not permissible in this model. The centre-lines of the shapes must have a radius of curvature which is much greater than the maximum, cross-sectional radius of the slender body, ensuring $\varepsilon\kappa \ll 1$. This restricts configurations for which there are sharp bends, although it does not restrict the centre-line to small-amplitude waves. Another condition on the body centre-line is that it does not come close to self-intersection.

The variations in the cross-sectional radius, $\eta(s)$, influence the near-field flow around the slender body, though the effects are subleading in the far-field given $\eta$ and the regularisation parameter $\chi$ are $O(\varepsilon)$ and $O(\varepsilon^2)$ quantities respectively. There are many examples of when variations in the near-field, due to the slender-body shape, are important in determining the correct behaviour of the fluid and the body. In biology, the near-field feeding currents generated by certain flagellated cells in order to capture local food sources would be affected by the variations in the shape and size

of flagella [45]. The dynamical effect of blebbing in fish-sperm flagella [3], whereby portions of the flagellum bulge out due to fluid intake, is of interest. This change in flagellum shape can now be incorporated to study whether it contributes to reduced motility, in addition to the fluid-intake effects which bleb the flagellum (intracellular hypotonicity). Also, studies of bacteria motility [49] highlight that large changes in the orientation of the body occur in the near-field of other boundaries, or bacteria, in the fluid; thus, including effects due to the geometry of the bacteria would offer further insight into these near-field dynamics. In industry, the sedimentation of non-spherical, slender particles can now be modelled using SBT, for example rigid fibres [20], useful for processes in which particulate separation is of interest. The particle geometry would affect the forces, torques and subsequent settling behaviour of the particle.

The next chapter implements the SBT derived here, highlighting the simple, numerical implementation of the theory, along with the ability to calculate flow fields around more generalised, slender-body shapes.

# Chapter 5

# Numerical Implementation of Slender Body Theory

## 5.1 Chapter Introduction

This chapter leads on from Chapter 4, implementing numerically the SBT developed for slender bodies with varying, cross-sectional radii. Slender bodies are chosen which are permissible in the new theory of Chapter 4, but were not previously permissible in existing theory [53]. Such slender bodies include those with a wave-like and a tapering shape, both of which are defined at the beginning of the chapter. Different, curvilinear centre-lines are also presented, before a full discretisation of the model is conducted.

In particular, the no-slip boundary condition is discretised, giving a matrix system of equations, allowing the weighting of the singularities to be determined as a function of arc-length. This weighting is subsequently inserted back into the singularity representation of the flow field, determining the flow at any point in the fluid domain.

## 5.2 Prescribing Body Geometries

### 5.2.1 Geometric Constraints

Consider again the flow field given in Chapter 4 by

$$\mathbf{u}(\mathbf{x}) = \int_{-e}^{e} \left[ \mathbf{S}^{\chi(s')}(\mathbf{x}, \boldsymbol{\xi}(s')) - \frac{(1-e^2)}{2e^2}(e^2 - s'^2)\mathbf{D}^{\chi(s')}(\mathbf{x}, \boldsymbol{\xi}(s')) \right] \boldsymbol{\alpha}(s')\, \mathrm{d}s', \qquad (5.1)$$

where the effective eccentricity is

$$e := \sqrt{1-\varepsilon^2}, \tag{5.2}$$

with

$$\mathbf{S}^{\chi(s')}(\mathbf{x},\mathbf{y}) := \frac{(|\mathbf{x}-\mathbf{y}|^2+2\chi(s'))\mathbf{I}}{(\,|\mathbf{x}-\mathbf{y}|^2+\chi(s')\,)^{3/2}} + \frac{(\mathbf{x}-\mathbf{y})\otimes(\mathbf{x}-\mathbf{y})}{(\,|\mathbf{x}-\mathbf{y}|+\chi(s')\,)^{3/2}}, \tag{5.3}$$

and

$$\mathbf{D}^{\chi(s')}(\mathbf{x},\mathbf{y}) := -\frac{(|\mathbf{x}-\mathbf{y}|^2-2\chi(s'))\mathbf{I}}{(\,|\mathbf{x}-\mathbf{y}|^2+\chi(s')\,)^{5/2}} + \frac{3(\mathbf{x}-\mathbf{y})\otimes(\mathbf{x}-\mathbf{y})}{(\,|\mathbf{x}-\mathbf{y}|+\chi(s')\,)^{5/2}}. \tag{5.4}$$

Recall that the regularisation parameter, $\chi(s')$, is defined as

$$\chi(s) := \varepsilon^2[(1-s^2)-\eta^2(s)], \tag{5.5}$$

and, from the justifications presented in equation (4.30), this choice of $\chi(s')$ ensures the denominators of any singularity terms in the integrand of (5.1) can never be zero.

The prescribed variables in the model, (5.1)–(5.5) are the cross-sectional radius, $\eta(s)$, and the curvilinear centre-line, $\boldsymbol{\xi}(s)$. In the asymptotic analysis of Chapter 4, emerging constraints for these prescribed variables include:

$$\eta^2(s) \to (1-s^2), \qquad \text{as} \quad s \to \pm 1, \tag{5.6}$$

from (4.31), and

$$\max_s \left[\eta^2(s)\right] \sim O(1) \sim \eta(s)\eta'(s), \tag{5.7}$$

from the discussions after equations (4.31) and (4.50) respectively. From equation (4.49), the curvilinear centre-line must be such that $\varepsilon\kappa(s) \ll 1$, where $\kappa(s)$ is its curvature. The centre-line also must not come close to self-intersection, as discussed following equations (4.43) and (4.57).

### 5.2.2 Cross-Sectional Radii

The prescribed, cross-sectional, radius functions, $\eta(s)$, are those taking the form of a wave-like surface and of a taper. Both of these bodies were not permissible in Johnson's SBT [53] as the former has more than one turning point, while the latter has one turning point which is not in the centre of the shape.

The wave-like surface is prescribed using a cosine wave, taking the form

$$\eta^2(s) = (1 - s^2)\left(1 + 0.4\cos\left(\frac{7\pi s}{2}\right)\right). \tag{5.8}$$

The scaling of $7\pi/2$ ensures that there are 3 maxima in the radius function along the centre-line, creating three wave-like peaks. The factor of 0.4 ensures that the slender-body radius does not become zero at any point other than the ends, though beaded shapes, where the body has a zero radius at certain points along the centre-line, are still permissible in this SBT. The added constant of 1 ensures the shape in (5.8) satisfies the constraint in (5.6) at the end-points.

The tapered shape is constructed based on the graph of

$$h_1(s) = \frac{s}{1 + s^2}, \qquad \text{for} \quad s \geq 0. \tag{5.9}$$

To avoid one end at infinity, the graph is translated downwards by a small, positive constant, $\delta > 0$, such that

$$h_2(s) = \frac{s}{1 + s^2} - \delta, \qquad \text{for} \quad s \geq 0, \tag{5.10}$$

which intersects the $s$-axis at $s = (1 \pm k)/2\delta$, where $k := \sqrt{1 - 4\delta^2}$. To ensure $k$ is real, $\delta$ is chosen to be less than 0.5. Thus, translating and rescaling the $s$ variable to pin these intersections at $s = \pm 1$ gives

$$h_3(s) = \frac{(ks + 1)/2\delta}{1 + (ks + 1)^2/4\delta^2} - \delta, \qquad \text{for} \quad s \geq 0, \tag{5.11}$$

so that $h_3(\pm 1) = 0$. The function is then stretched by a scale factor, $b$, in the $y$ direction to form a more pronounced peak, before being translated up by 1 to ensure the function decays to $\pm 1$ at the ends, thus giving

$$\eta^2(s) = (1 - s^2)\left(1 + b\left[\frac{(ks + 1)/2\delta}{1 + (ks + 1)^2/4\delta^2} - \delta\right]\right). \tag{5.12}$$

Both $b \sim O(1)$ and $\delta < 0.5$ are to be prescribed, noting $k := \sqrt{1 - 4\delta^2}$; the values chosen for the upcoming simulations are $b = 8$ and $\delta = 0.05$ to ensure that $\eta(s)\eta'(s) \sim O(1)$ from (5.7) and $\delta < 0.5$ for real values of $k$.

The two shapes given by equations (5.8) and (5.12) are illustrated in the first row of figure 5.1.

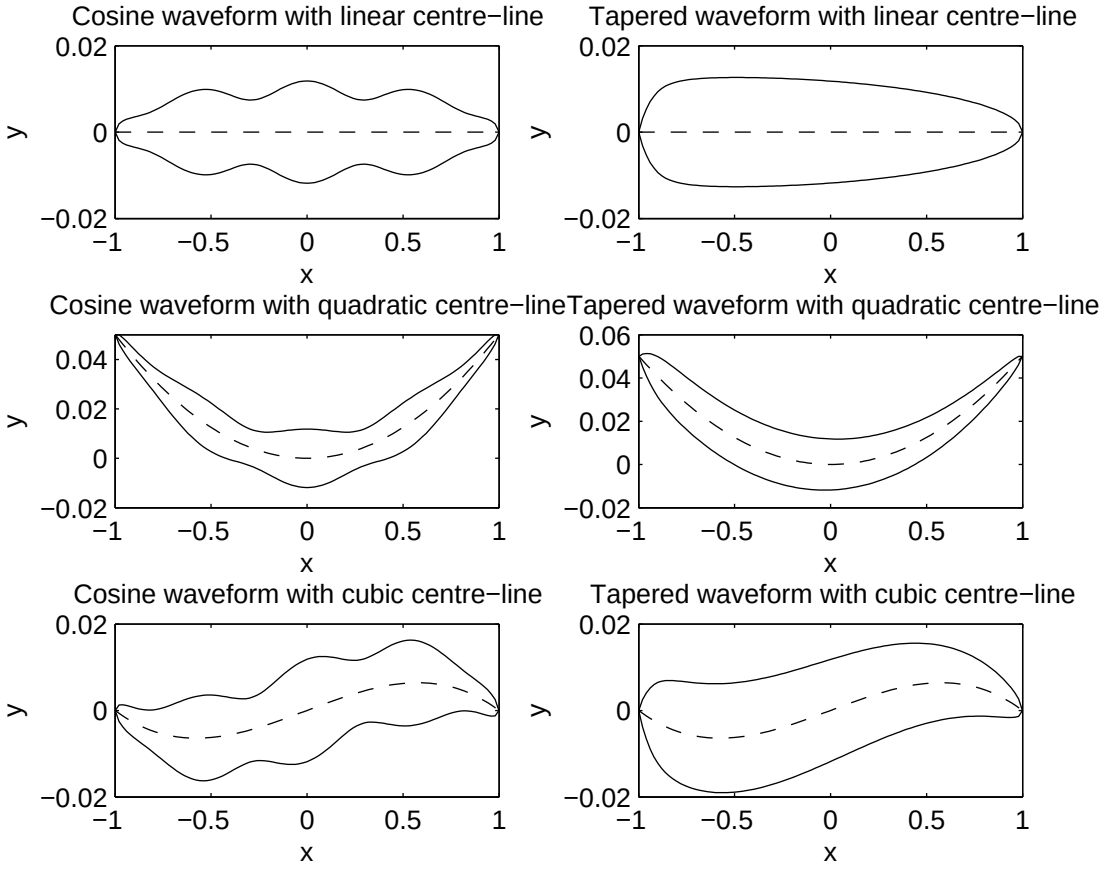


Figure 5.1: The different geometric configurations of the slender bodies considered in the numerical simulations. The body shapes are given by continuous lines while the centre-line is given by a dashed line. In the left-hand column, the slender body has a wave-like cosine shape defined by equation (5.8). In the right-hand column, the slender body follows a tapered form as described by equation (5.12). The first, second and third rows illustrate the two shapes extending from linear, quadratic and cubic centre-lines respectively, given by equations (5.18)–(5.20). Note that the aspect ratios of these plots are not unity so that the bodies are indeed slender.

### 5.2.3 Body Centre-Lines

The curvilinear centre-lines of the slender bodies are prescribed as either a linear function, a quadratic function or a cubic function of arc-length, $s$. The centre-lines considered here are two-dimensional, so that, for a Cartesian frame of reference, the centre-lines follow curves in the $(x, y)$ plane. Consequently, the binormal unit vector is trivially $\mathbf{e}_b(s) = \mathbf{e}_z$. Thus the position vector of a point on the centre-line has no component in this direction, and can be written in terms of the unit vectors in the tangential and normal directions, $\mathbf{e}_t(s)$ and $\mathbf{e}_n(s)$ respectively.

In a Cartesian frame,

$$\boldsymbol{\xi}(s) = \begin{pmatrix} x(s) \\ y(s) \\ 0 \end{pmatrix}. \tag{5.13}$$

As arc-length is conserved,

$$1 = \left(\frac{\mathrm{d}x}{\mathrm{d}s}\right)^2 + \left(\frac{\mathrm{d}y}{\mathrm{d}s}\right)^2, \tag{5.14}$$

so that

$$x(s) = \int_{-1}^{s} \sqrt{1 - \left(\frac{\mathrm{d}y(\bar{s})}{\mathrm{d}\bar{s}}\right)^2}\, \mathrm{d}\bar{s}. \tag{5.15}$$

The unit tangential and normal components, $\mathbf{e}_t(s)$ and $\mathbf{e}_n(s)$, are given by

$$\mathbf{e}_t(s) = \begin{pmatrix} \frac{\mathrm{d}x}{\mathrm{d}s} \\ \frac{\mathrm{d}y}{\mathrm{d}s} \\ 0 \end{pmatrix}, \tag{5.16}$$

and

$$\mathbf{e}_n(s) = \begin{pmatrix} -\frac{\mathrm{d}y}{\mathrm{d}s} \\ \frac{\mathrm{d}x}{\mathrm{d}s} \\ 0 \end{pmatrix}, \tag{5.17}$$

respectively.

The linear, quadratic and cubic centre-lines are prescribed, respectively, as

$$y_1(s) = 0, \tag{5.18}$$

$$y_2(s) = cs^2/2, \tag{5.19}$$

$$y_3(s) = cs(1 - s^2)/6, \tag{5.20}$$

where $c > 0$ is chosen so as to ensure the curvature, $\kappa(s)$, satisfies $\varepsilon\kappa(s) \ll 1$. The curvature, from (4.5), is given by

$$\begin{aligned}\kappa(s) &= \sqrt{\frac{\mathrm{d}^2x}{\mathrm{d}s^2} + \frac{\mathrm{d}^2y}{\mathrm{d}s^2}}, \\ &= \frac{\left|\frac{\mathrm{d}^2y}{\mathrm{d}s^2}\right|}{\sqrt{1 - \left(\frac{\mathrm{d}y}{\mathrm{d}s}\right)^2}},\end{aligned} \tag{5.21}$$

using (5.14). Thus, for the centre-lines given by (5.18)–(5.20),

$$\kappa_1(s) = 0, \tag{5.22}$$

$$\kappa_2(s) = \frac{c}{\sqrt{1 - c^2s^2}}, \tag{5.23}$$

$$\kappa_3(s) = \frac{c|s|}{\sqrt{1 - c^2(1 - 3s^2)^2/36}}. \tag{5.24}$$

Given $s \in [-1, 1]$, (5.23) implies that $c < 1$, while (5.24) implies $c < 3$, thus $c$ is chosen to satisfy $0 < c < 1$. In particular, to ensure $\kappa_i$ for $i \in \{1, 2, 3\}$ does not become larger than $O(1/\varepsilon)$ at the ends, $c$ is chosen to be much smaller than unity; the upcoming simulations use $c = 0.1$.

The cosine and tapered slender bodies, given by equations (5.8) and (5.12) respectively, are illustrated in figure 5.1 extending from the three different centre-lines given by equations (5.18)–(5.20).

## 5.3 Discretising the Boundary Condition

### 5.3.1 The Boundary Condition

The velocity representation in (5.1) must satisfy, to leading-order in the slenderness parameter, the no-slip boundary condition,

$$\mathbf{u}(\mathbf{X}(s, \phi)) = \mathbf{V}(s), \tag{5.25}$$

for all $\phi \in [0, 2\pi)$ and for a point on the surface, $\mathbf{X}(s, \phi)$, given by

$$\mathbf{X}(s, \phi) = \boldsymbol{\xi}(s) + \varepsilon\eta(s)\mathbf{e}_r(s, \phi), \tag{5.26}$$

where

$$\mathbf{e}_r(s, \phi) := \mathbf{e}_n(s)\cos\phi + \mathbf{e}_b(s)\sin\phi. \tag{5.27}$$

The translational surface velocity, $\mathbf{V}(s)$, is a prescribed function, given the centre-lines considered here are rigid and translating. Note that the theory can also be developed with an angular velocity, $\boldsymbol{\Omega} \sim O(1)$, present in the boundary condition; see the end of Section 4.3.4 and Chapter 6.

Applying the boundary condition in (5.25) to (5.1) gives the integral equation,

$$\mathbf{V}(s) = \int_{-e}^{e} \Big[ \mathbf{S}^{\chi(s')}(\boldsymbol{\xi}(s) + \varepsilon\eta(s)\mathbf{e}_r(s,\phi), \boldsymbol{\xi}(s')) \\ -\frac{(1-e^2)}{2e^2}(e^2 - s'^2)\mathbf{D}^{\chi(s')}(\boldsymbol{\xi}(s) + \varepsilon\eta(s)\mathbf{e}_r(s,\phi), \boldsymbol{\xi}(s')) \Big] \boldsymbol{\alpha}(s')\,\mathrm{d}s', \tag{5.28}$$

which is satisfied, at leading order, for all $\phi \in [0, 2\pi)$. The singularities are given by (5.3) and (5.4), depending on the difference between their two arguments. This difference is denoted

$$\mathbf{r}(s, s', \phi) := \boldsymbol{\xi}(s) + \varepsilon\eta(s)\mathbf{e}_r(s,\phi) - \boldsymbol{\xi}(s'), \tag{5.29}$$

following the notation from (4.33). Using expressions for the centre-line, (5.13), the unit, normal vector, (5.17), and the unit, radial vector, (5.27), the expression in (5.29) is written as

$$\mathbf{r}(s, s', \phi) = \begin{pmatrix} y(s) - y(s') \\ x(s) - x(s') \\ 0 \end{pmatrix} + \varepsilon\eta(s)\cos\phi \begin{pmatrix} -\frac{\mathrm{d}y}{\mathrm{d}s} \\ \frac{\mathrm{d}x}{\mathrm{d}s} \\ 0 \end{pmatrix} + \varepsilon\eta(s)\sin\phi \begin{pmatrix} 0 \\ 0 \\ 1 \end{pmatrix}, \tag{5.30}$$

where, from (5.15),

$$x(s) = \int_{-1}^{s} \sqrt{1 - \left(\frac{\mathrm{d}y(\bar{s})}{\mathrm{d}\bar{s}}\right)^2}\,\mathrm{d}\bar{s}. \tag{5.31}$$

The integral equation in (5.28) is thus re-written as

$$\mathbf{V}(s) = \int_{-e}^{e} \left[ \mathbf{S}^{\chi(s')}(\mathbf{r}(s, s', \phi)) - \frac{(1-e^2)}{2e^2}(e^2 - s'^2)\mathbf{D}^{\chi(s')}(\mathbf{r}(s, s', \phi)) \right] \boldsymbol{\alpha}(s')\,\mathrm{d}s', \tag{5.32}$$

where, from (4.37) and (4.38),

$$\mathbf{S}^{\chi(s')}(\mathbf{r}(s, s', \phi)) := \frac{\mathbf{I}}{r_\chi(s, s', \phi)} + \frac{\chi(s')\mathbf{I}}{r_\chi^3(s, s', \phi)} + \frac{\mathbf{r}(s, s', \phi) \otimes \mathbf{r}(s, s', \phi)}{r_\chi^3(s, s', \phi)}, \tag{5.33}$$

$$\mathbf{D}^{\chi(s')}(\mathbf{r}(s, s', \phi)) := -\frac{\mathbf{I}}{r_\chi^3(s, s', \phi)} + \frac{3\chi(s')\mathbf{I}}{r_\chi^5(s, s', \phi)} + \frac{3\mathbf{r}(s, s', \phi) \otimes \mathbf{r}(s, s', \phi)}{r_\chi^5(s, s', \phi)}. \tag{5.34}$$

Note that

$$r_\chi(s, s', \phi) := \sqrt{|\mathbf{r}(s, s', \phi)|^2 + \chi(s')} > 0. \tag{5.35}$$

### 5.3.2 Centre-Line Discretisation

In order to solve the integral equation (5.32) for $\boldsymbol{\alpha}(s)$, the integration variable along the arc-length of the centre-line, $s' \in [-e, e]$, is discretised into $N$ elements of equal arc-length. The discretisation follows a similar procedure to that used by Smith *et. al.* [83] when modelling slender cilia, though an extension is applied to the current context in that, on each of the $N$ centre-line elements, the singularity weighting, $\boldsymbol{\alpha}(s')$, is assumed to be a linear function:

$$\boldsymbol{\alpha}(s') = \boldsymbol{\alpha}_0 + s'\boldsymbol{\alpha}_{01}. \tag{5.36}$$

Hence, (5.32) becomes

$$\begin{aligned}\mathbf{V}(s) = \sum_{j=1}^{j=N} \int_{-e+(j-1)/N}^{e+j/N} \Big[ &\mathbf{S}^{\chi(s')}(\mathbf{r}(s, s', \phi)) \\ &-\frac{(1-e^2)}{2e^2}(e^2 - s'^2)\mathbf{D}^{\chi(s')}(\mathbf{r}(s, s', \phi))\Big] \{\boldsymbol{\alpha}_{0j} + \boldsymbol{\alpha}_{1j}s'\}\, \mathrm{d}s',\end{aligned} \tag{5.37}$$

which introduces $3 \times 2N$ unknowns, namely the 3 components of each vector $\boldsymbol{\alpha}_{0j}$ and $\boldsymbol{\alpha}_{1j}$, for $j = 1 : N$.

The arc-length, $s \in [-1, 1]$, at which the boundary condition is evaluated, is discretised into $2N$ points, so that, for $i = 1 : 2N$,

$$s_i := -1 + (i - 1/2)/N. \tag{5.38}$$

Hence, the system of discretised equations is given by

$$\begin{aligned}\mathbf{V}(-1 + (i-1/2)/N) = \sum_{j=1}^{j=N} \int_{-e+(j-1)/N}^{e+j/N} \Big[ &\mathbf{S}^{\chi(s')}(\mathbf{r}(-1 + (i-1/2)/N, s', \phi)) \\ -\frac{(1-e^2)}{2e^2}(e^2 - s'^2)&\mathbf{D}^{\chi(s')}(\mathbf{r}(-1 + (i-1/2)/N, s', \phi))\Big] \{\boldsymbol{\alpha}_{0j} + \boldsymbol{\alpha}_{1j}s'\}\, \mathrm{d}s',\end{aligned} \tag{5.39}$$

for $i = 1 : 2N$. Equation (5.39) can be written more clearly as

$$\mathbf{V}_i = \sum_{j=1}^{j=N} G_{ij}\boldsymbol{\alpha}_{0j} + H_{ij}\boldsymbol{\alpha}_{1j}, \tag{5.40}$$

where

$$\mathbf{V}_i := \mathbf{V}(-1 + (i - 1/2)/N), \tag{5.41}$$

with

$$G_{ij} := \int_{-e+(j-1)/N}^{e+j/N} \Big[ \mathbf{S}^{\chi(s')}(\mathbf{r}(-1+(i-1/2)/N, s', \phi)) \\ -\frac{(1-e^2)}{2e^2}(e^2 - s'^2)\mathbf{D}^{\chi(s')}(\mathbf{r}(-1+(i-1/2)/N, s', \phi)) \Big] \, \mathrm{d}s', \tag{5.42}$$

and

$$H_{ij} := \int_{-e+(j-1)/N}^{e+j/N} s' \Big[ \mathbf{S}^{\chi(s')}(\mathbf{r}(-1+(i-1/2)/N, s', \phi)) \\ -\frac{(1-e^2)}{2e^2}(e^2 - s'^2)\mathbf{D}^{\chi(s')}(\mathbf{r}(-1+(i-1/2)/N, s', \phi)) \Big] \, \mathrm{d}s'. \tag{5.43}$$

In the subsequent results, the integrals from (5.42) and (5.43) are evaluated using a composite Simpson's rule with $M$ intervals, where $M$ is an even integer. For a general function, $g(s)$, the rule is given by

$$\int_a^b g(s')\, ds' = \frac{H}{3}\left[ g(s_0) + 2\sum_{m=1}^{m=M/2-1} g(s_{2m}) + 4\sum_{m=1}^{m=M/2} g(s_{2m-1}) + g(s_M) \right], \tag{5.44}$$

where $s_0 = a$, $s_M = b$, $s_m = a + mH$ and $H = (b-a)/M$.

To solve the system in (5.40) numerically, the translational velocity, $\mathbf{V}(s)$, must be prescribed. For the following simulations, a constant velocity is used:

$$\mathbf{V}(s) = \begin{pmatrix} 1 \\ 0 \\ 0 \end{pmatrix}, \tag{5.45}$$

for all $s \in [-1, 1]$.

Note that the integrals in (5.42) and (5.43), although not singular, have sharp peaks near $s' \approx s$, as discussed following equation (4.41) in Chapter 4.

### 5.3.3 Convergence of the Numerical Scheme

In order to test the convergence of the numerical scheme outlined above, a known solution of the integral equation is required. From Section 1.3.2.2, the (dimensionless) solution of the integral equation for the flow past a translating prolate spheroid for which

$$\eta(s) = \sqrt{1 - s^2}, \tag{5.46}$$

is given by

$$\boldsymbol{\alpha}^{prolate} = \mathbf{C}\mathbf{U}, \tag{5.47}$$

where

$$\mathbf{C} := \begin{pmatrix} \frac{e^2}{-2e+(1+e^2)\log\left(\frac{1+e}{1-e}\right)} & 0 & 0 \\ 0 & \frac{2e^2}{2e+(3e^2-1)\log\left(\frac{1+e}{1-e}\right)} & 0 \\ 0 & 0 & \frac{2e^2}{2e+(3e^2-1)\log\left(\frac{1+e}{1-e}\right)} \end{pmatrix}, \tag{5.48}$$

noting the eccentricity is given by $e = \sqrt{1-\varepsilon^2}$.

The numerical solution for the prolate spheroid is denoted $\boldsymbol{\alpha}^{num}(s, \phi; N, M)$; $N$ is the number of elements used to discretise the centre-line, where, on each element, $\boldsymbol{\alpha}^{num}$ assumes a linear function and $M$ is the number of intervals on that element used by the composite Simpson's rule to integrate the kernel.

For convergence, the error between the exact and numerical solutions for the prolate spheroid is required to decrease as either $N$ or $M$ increases. For a given $N$ and $M$, this error is denoted

$$\mathcal{E}(s, \phi) = |\boldsymbol{\alpha}^{num}(s, \phi) - \boldsymbol{\alpha}^{prolate}|. \tag{5.49}$$

Based on the leading-order, asymptotic analysis following equation (4.44), the errors along the arc-length, $s$, are expected to be algebraic in the slenderness ratio, $\varepsilon$, unlike the logarithmic accuracy of RFT derived in Section 4.3.3. Also, by construction in Chapter 4, the errors due to variations in the cross-sectional angle, $\phi$, must be $O(\varepsilon)$ or less.

## 5.4 Determining the Flow Field Numerically

### 5.4.1 Discretising the Fluid Domain

Once $\boldsymbol{\alpha}(s)$ has been determined numerically as a piecewise-linear function for values of $s$ along the centre-line, it is subsequently inserted back into the singularity

representation of the flow field, (5.1), giving

$$\mathbf{u}(\mathbf{x}) = \sum_{j=1}^{j=N} \int_{-e+(j-1)/N}^{e+j/N} \Big[ \mathbf{S}^{\chi(s')}(\mathbf{x}, \boldsymbol{\xi}(s')) - \frac{(1-e^2)}{2e^2}(e^2 - s'^2)\mathbf{D}^{\chi(s')}(\mathbf{x}, \boldsymbol{\xi}(s')) \Big] \{\boldsymbol{\alpha}_{0j} + \boldsymbol{\alpha}_{1j} s'\} \, \mathrm{d}s'. \tag{5.50}$$

The prescribed centre-lines, as given by (5.13), are two-dimensional and the cross-sectional angle of the surface point in the boundary condition is taken to be $\phi = 0$ (though azimuthal variations are considered later in Section 5.5.3 as part of the error analysis). Thus, the fluid domain of interest is the two-dimensional plane in which the centre-line lies, the plane effectively bisecting the slender body. The binormal vector, $\mathbf{e}_b$, is taken (without loss of generality) to be normal to this plane; thus, all binormal contributions to the flow field in this plane are zero.

In (5.50), the position vector, $\mathbf{x}$, is discretised, for $i, k \in \{1, 2, \ldots M, M+1\}$, as

$$\begin{aligned} \mathbf{x}_{ik} &= \begin{pmatrix} x_i \\ y_k \end{pmatrix}, \\ &= \begin{pmatrix} -D + \frac{2D(i-1)}{M} \\ -H + \frac{2H(k-1)}{M} \end{pmatrix}, \end{aligned} \tag{5.51}$$

where $D$ and $H$ are the respective half-lengths of the rectangular domain in the $(x, y)$ plane.

There is, however, a simplification in that the flow field, (5.50), does not need evaluating for any points $\mathbf{x}_{ik}$ within the slender-body, given this space is occupied by the body itself. Thus, for these points, $\mathbf{x}_{ik}$, the simulations set

$$\mathbf{u}(\mathbf{x}_{ik}) = \mathbf{0}. \tag{5.52}$$

Inserting (5.51) into (5.50) gives the numerical flow field in a rectangular domain around the slender body.

## 5.5 Numerical Results

### 5.5.1 Flow Fields

Examples of the velocity flow fields past slender bodies with the varying, cross sections described in Section 5.2.2, and the curvilinear centre-lines from Section 5.2.3

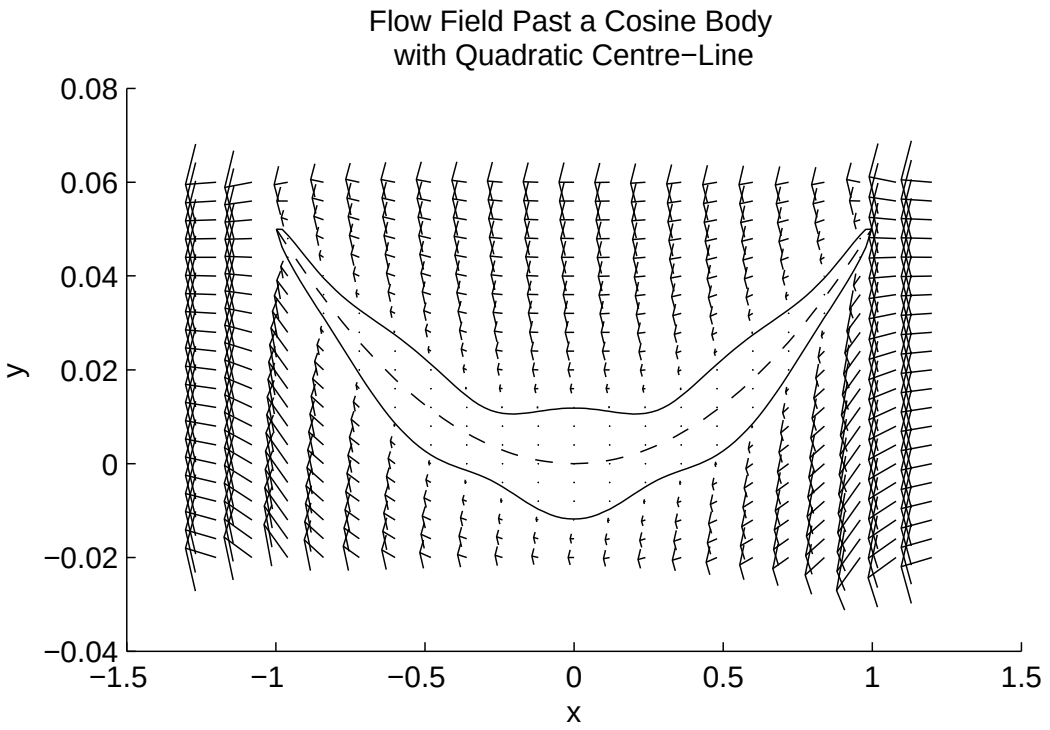


Figure 5.2: The flow field generated by a translating, wave-like (cosine), slender body with its cross-sectional radius given by equation (5.8) and a quadratic centre-line given by (5.19). The plot is fixed in the frame of reference translating with the body at a velocity $(1, 0, 0)^T$, thus arrows depict the incoming fluid with velocity $(-1, 0, 0)^T$, satisfying the no-slip boundary condition on the body surface. Note the different scales for the dimensionless horizontal and vertical axes.

are presented.

The first example is that of the wave-like (cosine) radius function from equation (5.8) extending from a centre-line that is quadratic in arc-length, as specified in equation (5.19); see figure 5.2. The results are shown in a frame moving with the body at a translational velocity $\mathbf{V} = (1, 0, 0)^T$, so that the ambient fluid moves with a constant velocity $(-1, 0, 0)^T$. The no-slip boundary condition is enforced; thus, in the moving frame, the velocity tends to zero on the surface of the body.

The second example is that of the tapered, slender body with a cross-sectional radius specified by equation (5.12) with a centre-line that is cubic in arc-length, (5.20); see figure 5.3. Again, the results are shown in a frame moving with the body.

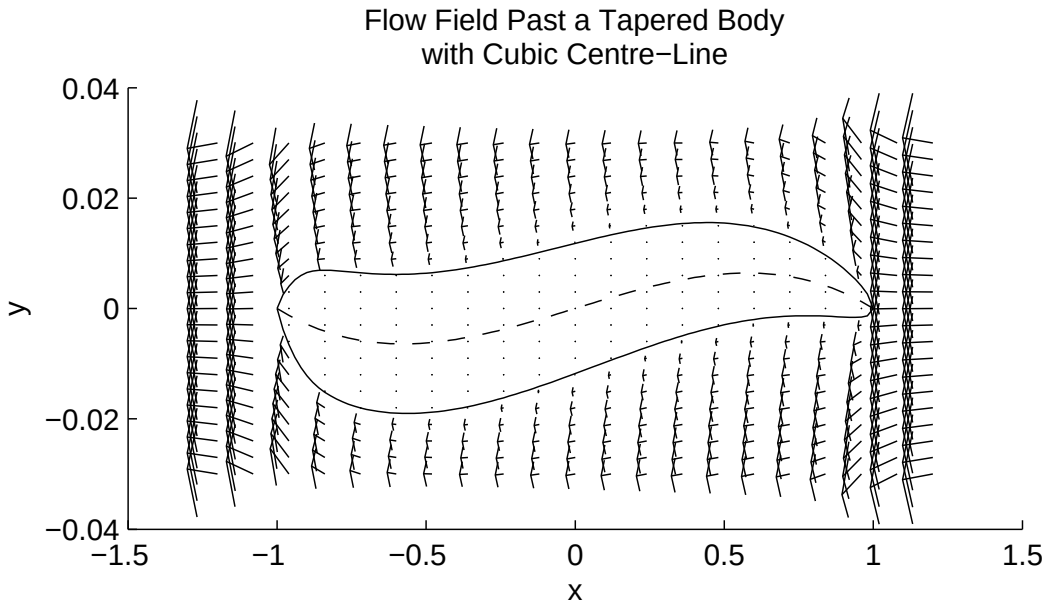


Figure 5.3: The flow field generated by a translating, tapered, slender body with its cross-sectional radius given by equation (5.12) and a cubic centre-line given by (5.20). The plot is fixed in the frame of reference translating with the body at a velocity $(1, 0, 0)^T$, thus arrows depict the incoming fluid with velocity $(-1, 0, 0)^T$, satisfying the no-slip boundary condition on the body surface. Note the different scales for the dimensionless horizontal and vertical axes.

### 5.5.2 Convergence Results

The numerical scheme to determine the solution to the integral equation, $\boldsymbol{\alpha}$, arising from the no-slip boundary condition around the slender-body surface has been tested using the known solution for a prolate spheroid; see equations (5.47) and (5.48). The error, defined by equation (5.49), is given by the modulus of the difference between the numerical and the exact solutions, and has been investigated for different step sizes in the discretisation procedure. Given the centre-line is split into $N$ elements between $\pm e$, each of which contain $M$ intervals for the use of the composite Simpson's rule, the step size, $h$, is given by

$$h = \frac{2e}{NM}, \tag{5.53}$$

where $e = \sqrt{1 - \varepsilon^2}$ is the eccentricity of the prolate spheroid.

Figure 5.4 shows curves of both the mean error along the centre-line and the error at the end points, the latter being of interest given the analysis of Chapter 4 suggests that the largest source of error is at the end points of the slender body. The errors are

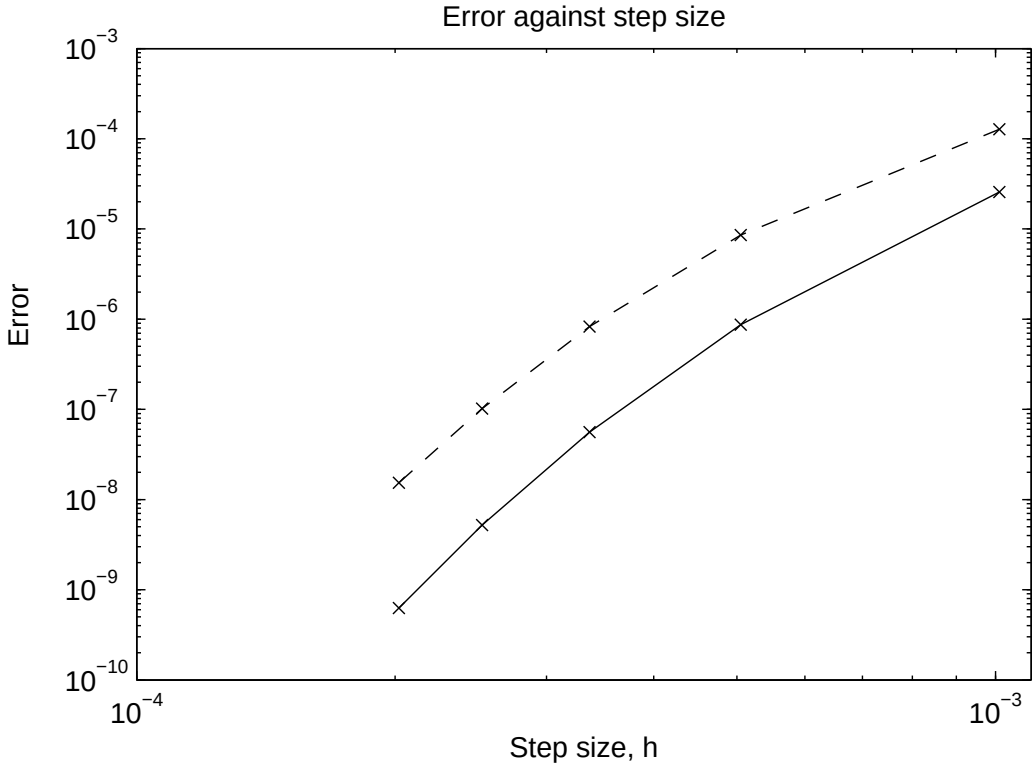


Figure 5.4: Graphs of the mean error (solid curve), $\bar{\mathcal{E}}(\phi)$ defined by taking the mean of equation (5.49) over the arc-length of the centre-line, and the end error (dashed curve), $\mathcal{E}(0, \phi)$, for the flow around a prolate spheroid; see Section 5.3.3. The number of elements along the centre-line, $N$, varies from $N = 10$ to $N = 50$ in increments of 10 whilst keeping constant the number of intervals, $M = 200$, for the Simpson's rule on each element. The step size, $h$, is given by $h = 2e/(NM)$, where $e = \sqrt{1 - \varepsilon^2}$. The simulations use a slenderness ratio of $\epsilon = 0.01$ and a fixed cross-sectional angle of $\phi = 0$; variations of $\phi$ are given later in figure 5.6 and shown to be negligible. The translational surface velocity of the prolate spheroid is $\mathbf{V}(s) = (1, 0, 0)^T$ for all $s$.

plotted for values of $N = 10$ to $N = 50$, increasing in increments of 10; the number of intervals used for the composite Simpson's rule is held constant at $M = 200$. The errors are plotted against the step sizes, $h$ from (5.53), indicating that an increase in the number of elements $N$, upon which the solution of the integral equation assumes a linear function, implies a reduction in both mean error and end errors. The translational surface velocity used in the boundary condition is $\mathbf{V}(s) = (1, 0, 0)^T$ for all $s$, with a slenderness ratio of $\varepsilon = 0.01$ and $\phi = 0$. As expected, the end errors are indeed greater than the mean of the error along the arc-length of the centre-line.

Figure 5.5 again shows a plot of the mean error along the centre-line and at the end points, but this time with the number of elements held constant, $N = 15$, while the

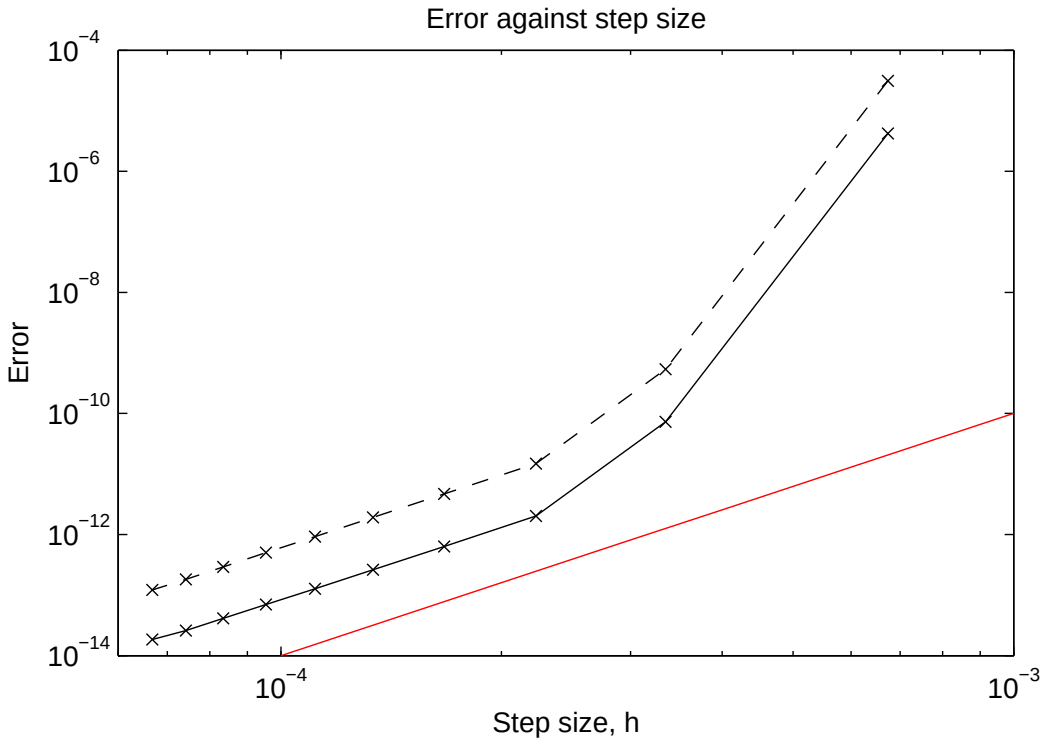


Figure 5.5: Graphs of the mean error (solid curve), $\bar{\mathcal{E}}(\phi)$ defined by taking the mean of equation (5.49) over the arc-length of the centre-line, and the end error (dashed curve), $\mathcal{E}(0,\phi)$, for the flow around a prolate spheroid; see Section 5.3.3. The number of elements along the centre-line, $N$, is held constant whilst the number of intervals, $M$, for the Simpson's rule on each element varies from $M = 200$ to 2000 in increments of 200. The step size, $h$, is given by $h = 2e/(NM)$, where $e = \sqrt{1-\varepsilon^2}$. For reference, a red line has been added to the log-log plot with a gradient of 4; the error curves tend to this gradient in the small $h$ limit, highlighting that the error is $O(h^4)$, as expected when using the Simpson's rule. The simulations use a slenderness ratio of $\epsilon = 0.01$, and a fixed cross-sectional angle of $\phi = 0$; variations of $\phi$ are given later in figure 5.6 and shown to be negligible. The translational surface velocity of the prolate spheroid is $\mathbf{V}(s) = (1,0,0)^T$ for all $s$.

number of intervals used for the composite Simpson's rule increases from $M = 200$ to $M = 2000$ in increments of 200. The horizontal axis displays the step sizes, $h$, from equation (5.53). The results show that an increase in the refinement of the Simpson's rule gives a reduction in both the mean error and the end errors. Furthermore, in the small $h$ limit these errors scale with $h^4$, deducible from the (red) reference line on the log-log with gradient 4; this agrees with the well-known $h^4$ error dependence of the Simpson's rule. Again, the translational surface velocity used in the boundary condition is $\mathbf{V}(s) = (1,0,0)^T$ for all $s$, with a slenderness ratio of $\varepsilon = 0.01$ and $\phi = 0$.

Together, both figures 5.4 and 5.5 highlight that, upon refinement of the numerical

scheme, the numerical solution for the prolate spheroid converges to the exact solution.

### 5.5.3 Error Around a Cross Section

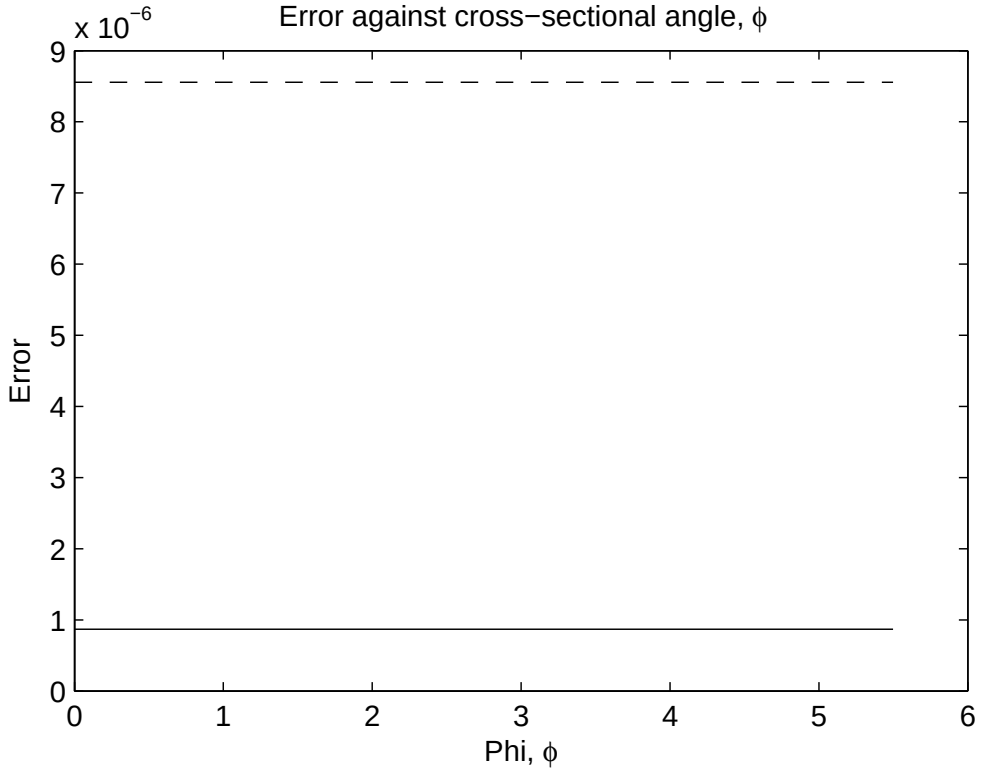


Figure 5.6: Graphs of the mean error (solid curve), $\bar{\mathcal{E}}(\phi)$ defined by taking the mean of equation (5.49) over the arc-length of the centre-line, and the end error (dashed curve), $\mathcal{E}(0,\phi)$, for the flow around a prolate spheroid; see Section 5.3.3. The number of elements along the centre-line is $N = 15$ and the number of intervals for the Simpson's rule on each element is $M = 200$. The simulations use a slenderness ratio of $\epsilon = 0.01$, evaluating the integral at different cross-sectional angles, $\phi = 2\pi q/8$ where $q = 0, 1, ..., 7$. The translational surface velocity of the prolate spheroid is $\mathbf{V}(s) = (1, 0, 0)^T$ for all $s$.

Figure 5.6 displays both the mean error along the arc-length of the centre-line and the end error against the cross-sectional angle, $\phi$, at which the no-slip boundary condition is evaluated. By construction in Chapter 4, the errors must be at least $O(\varepsilon)$, given that the boundary condition was forced to be $\phi$-independent at leading order in the slenderness ratio, $\varepsilon$. The values of $\phi$ plotted range from $\phi = 0$ to $\phi = 7\pi/4$, increasing in increments of $\pi/4$. The translational surface velocity of the prolate spheroid is $\mathbf{V}(s) = (1, 0, 0)^T$ for all $s$, $N = 15$, $M = 200$ and the slenderness ratio is $\varepsilon = 0.01$.

The curves show that variations in the mean and end errors as $\phi$ varies are negligible.

### 5.5.4 Error Along Arc-Length

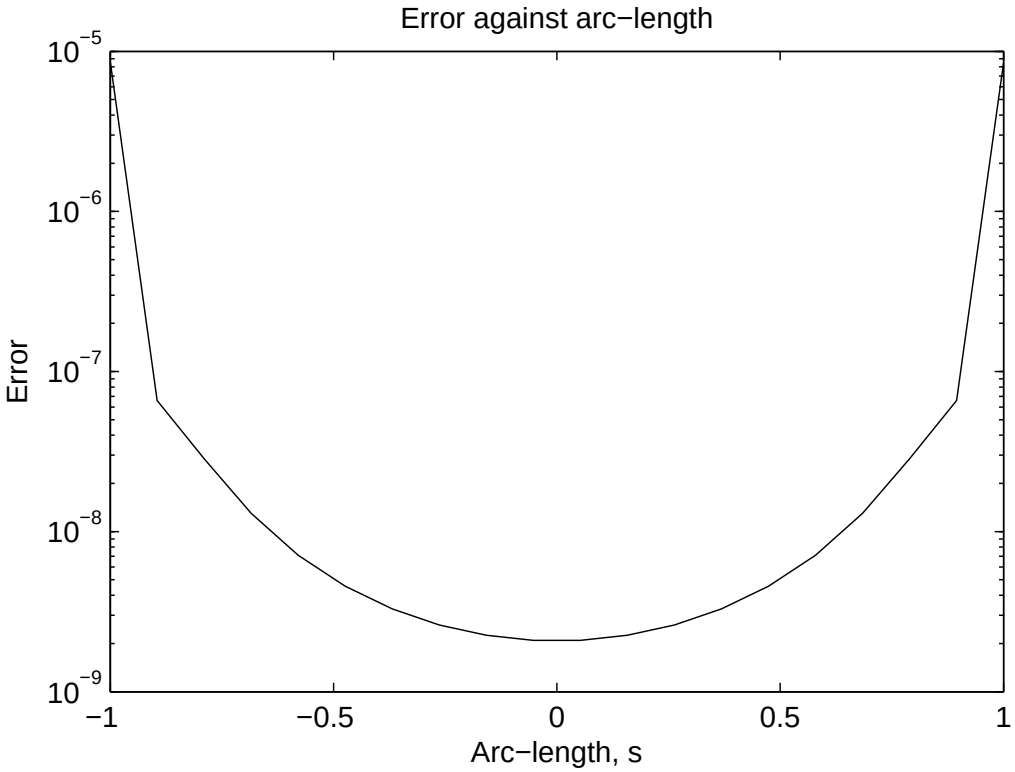


Figure 5.7: A graph of the error, $\mathcal{E}(s,0)$ defined by equation (5.49), for the flow around a prolate spheroid; see Section 5.3.3. The number of elements along the centre-line is $N = 15$ and the number of intervals for the Simpson's rule on each element is $M = 200$. The simulations use a slenderness ratio of $\epsilon = 0.01$, evaluating the integral at $\phi = 0$. The translational surface velocity of the prolate spheroid is $\mathbf{V}(s) = (1, 0, 0)^T$ for all $s$.

The error in equation (5.49) has also been investigated along the arc-length, $s$, of the centre-line of the prolate spheroid. Figure 5.7 plots the error against the arc-length of the centre-line, $s$, where $\varepsilon = 0.01$, $N = 15$, $M = 200$ and $\phi = 0$. As expected from the analysis of Chapter 4, the errors are largest at the ends of the flagellum.

## 5.6 Discussion

The SBT developed in Chapter 4 has been implemented numerically in order to deduce the flow field around a slender body with a varying, cross-sectional radius. In

particular, two bodies, previously not permissible in existing theories, have been analysed, one with a wave-like surface and the other with a tapering body. In addition, three, curvilinear centre-lines have been applied to the respective bodies, taking the form of linear, quadratic and cubic functions in arc-length, $s$. Results have been obtained which confirm that the errors are small.

The flow fields produced by the SBT, figures 5.2 and 5.3, do indeed appear to satisfy the no-slip boundary condition on the surface of the slender body.

An error analysis comparing the numerical solution of the arising integral equation to an exact solution for the flow around a prolate spheroid has been conducted. For the simulation parameters presented, the error converges as the discretisation procedure is refined. This is true when increasing either the number of centre-line elements, $N$, upon which the solution of the integral equation assumes a linear function, and the number of intervals, $M$, used within each element for the composite Simpson's rule on the integral kernel; results are shown in figures 5.4 and 5.5. The graphs also highlight that the end errors are greater than the mean error along the whole centre-line, as expected following the analysis of Chapter 4. Given the slenderness ratio used was $\varepsilon = 0.01$, the values of $N$ and $M$ investigated give rise to numerical errors at least as small as $O(\varepsilon^2)$; thus, for the flow-field simulations and $\phi$ and $s$ error analyses, both using $N = 15$ and $M = 200$, any numerical errors would not interfere with investigations of the asymptotic error at $O(\varepsilon)$.

The error around a cross section and the error along the arc-length have also been investigated for $\varepsilon = 0.01$, both of which suggest asymptotic errors arising due to $\phi$ and $s$ variations respectively are again much smaller than $O(\varepsilon)$. For the case of $\phi$ variations around the cross section, the error is negligible, confirming the validity of setting $\phi = 0$ in other error-analysis simulations. The simulations in this chapter suggest that the flow fields generated using the SBT around bodies with slenderness ratios of $\varepsilon = 0.01$ are accurate up to $O(\varepsilon^2)$ errors. This slenderness ratio is common for biological flagella, for example those of human and golden-hamster sperm, where table 3.1 in Chapter 3 gives $\varepsilon \sim O\left(10^{-2}\right)$; smaller slenderness ratios lie outside the parameter regime of interest for most, if not all, biological microswimmers.

While the limitations of the applicability of the model are discussed in Section 4.4, the limitations of the numerical scheme have been highlighted in figures 5.4 and 5.5,

illustrating that a better refinement using higher values of $N$ and $M$ will ensure that numerical errors do no mask any investigations of asymptotic errors.

# Chapter 6

# Overall Conclusions and Possible Extensions

## 6.1 Conclusions

### 6.1.1 Overview

The thesis has focused on three different aspects of microswimming in a low Reynolds number environment, each of which employs, or uses theories derived from, singularity methods of Stokes flow. The situations modelled include the effects of viscoelasticity on the idealised, three-sphere swimmer, the potential for sperm-cell release from a binding due to a hyperactive beat, and the development of a slender-body theory for more general body shapes. The conclusions of each study are subsequently summarised, before possible directions of future work are considered in each.

### 6.1.2 The Three-Sphere Microswimmer in a Viscoelastic Fluid

The three-sphere swimmer [70] has been investigated in both a Newtonian fluid and a nonlinear, viscoelastic medium, the latter following an Oldroyd-B constitutive law, though this law can be generalised to include other nonlinear models for the fluid rheology. The internal forces acting on the three spheres, induced by the motion of the connecting rods due to, say, motors within the spheres themselves, are prescribed; this is termed the *mobility* problem, differing from the *kinematic* problem in which the rod displacements are prescribed directly. The *kinematic* problem, in the existing literature [36], is not recommended for the analysis of a swimmer in a viscoelastic fluid as feedback effects between the forces and displacements could be neglected.

The internal forces prescribed are periodic, differing by a phase difference to ensure a net, swimmer displacement is achieved by breaking reciprocal motion in a Newtonian fluid. Modelling assumptions include that the Deborah number of the viscoelastic fluid is $O(1)$ and the mean, sphere separation is much greater than the sphere radii. The rod oscillations, induced by the internal forces, are assumed to be smaller than the sphere radii, given the pragmatic constraint of a motor device fitting within the spheres. The net displacement of the swimmer in one beat cycle has been calculated in both a Newtonian and a viscoelastic environment.

In the Newtonian fluid, the calculated, net displacement of the swimmer is in agreement with existing models of the three-sphere swimmer. The flow field generated, however, differs from those in the literature, in that the interaction flows between the three spheres are accounted for. For a formal, asymptotic analysis, the inclusion of these terms is necessary, though they do not contribute to the final, time-averaged displacement in one beat cycle. Thus, the negligibility of sphere-interaction terms, a common assumption in existing work, has been verified *a posteriori*.

In the viscoelastic fluid, the net displacement of the swimmer over one beat cycle is predicted to be greater than that in a Newtonian fluid, at least for prescribed, sinusoidal, internal forces. The efficiency of the swimmer also increases when immersed in a viscoelastic environment. These findings are in agreement with undulating, sheet swimmers [96] in which, for prescribed, internal forces, the swimming speed increases in a viscoelastic fluid compared with a Newtonian medium. The increase observed in the work by Teran *et. al.* [96] suggest the optimal swimming speed was a result of a resonance between the undulation frequency and the fluid at optimality, associated with regions of highly stressed fluid at the distal end of the swimmer. No resonance, however, is observed in the model of Chapter 2, though this is not solely due to the use of small-amplitude assumptions, given systems with small-amplitude assumptions and prescribed forces regularly lead to resonances (such as in the case of a simple harmonic oscillator). Thus, while the conclusions of net displacement qualitatively agree, the influence of viscoelasticity appears to be different between the two studies.

The results are in contrast to other work on simple swimmers in viscoelastic environments, such as the work of Fu *et. al.* [36] in which nonlinear, viscoelastic effects decrease the swimmer speeds for infinite, undulating cylinders. Thus, the study in Chapter 2 reinforces that the responses of inertialess swimmers to non-Newtonian

rheologies is complex, depending on the specific, swimmer geometry.

The model also highlights the differences between the *kinematic problem*, in which the relative, shape-changing parameters are prescribed, and the *mobility* problem, where the forces are given. For the *kinematic* problem, in the case of linear viscoelasticity, it is evident from the leading-order relation

$$\mathbf{w}_0^{(\alpha)} := \mathbf{u}_0^{(\alpha)}, \quad q_0^{(\alpha)} := \mathcal{L}[p_0^{(\alpha)}], \quad \boldsymbol{\tau}_{w_0}^{(\alpha)} = \left(\nabla \mathbf{w}_0^{(\alpha)}\right)^T + \nabla \mathbf{w}_0^{(\alpha)} := \mathcal{L}[\boldsymbol{\tau}_0^{(\alpha)}]. \tag{6.1}$$

in equation (2.81) of Chapter 2 that displacements are unaffected by linear viscoelasticity as the velocity field is unchanged. In contrast, the force balances are altered by the appearance of the temporal operator $\mathcal{L}$ in the pressure and stresses. Hence the common observation that linear viscoelasticity is insufficient to observe even leading-order rheological effects [59] is only immediately relevant for the *kinematic* problem. This is much more commonly studied, but not necessarily easier to implement in an engineering context and inappropriate for biological flagella, where microswimmers rely on molecular-motor regulation rather than regulation in the context of cell-level displacements. This study nonetheless emphasises the need for the explicit consideration of asymptotically higher orders for a consistent asymptotic expansion in determining net displacements; thus one might, once more, generally conclude that viscoelastic microswimming can only be understood with the consideration of nonlinear constitutive relations. However, this study shows that linear viscoelasticity is sufficient, though the fact the nonlinear terms in the viscoelastic constitutive equation play no role in the net displacement (for either the *kinematic* or *mobility* problems) can only be deduced *a posteriori*; the assumption of linear viscoelasticity cannot be made from the outset.

More generally, our observations highlight that there is no high-level understanding of rheological effects on microswimming at the present time; the effects are highly context-dependent, though the study of idealised swimmers offers the opportunity to explore, and characterise, rheological microswimming. This can explore, for example, when linear viscoelasticity is sufficient to study leading-order, viscoelastic effects.

### 6.1.3 Hyperactivated, Tethered-Sperm Motility

A model has been developed which considers a sperm cell tethered to the walls of the female reproductive tract, examining the forces generated by the sperm flagel-

lum given a prescribed beat pattern propagating down the flagellum. The two beat patterns prescribed, based on experimental observations, are *symmetric* beating with low amplitude, symmetric waveforms and *hyperactive* beating, with large-amplitude waveforms exhibiting lower wavenumbers and frequencies than the former, possessing either waveform symmetry or asymmetry. The forces generated by the two waveforms, in particular those which push or pull the sperm cell into or away from the wall, have been calculated using resistive-force theory (RFT). Explicit attention has also been paid to potential sources of error in using RFT, confirming that they are subleading. Two different boundary conditions at the tethering point have been applied, one in which the sperm head is freely hinged and another in which the cell is clamped.

The model predicts that hyperactive sperm have the ability to mechanically generate forces that act to pull the sperm cell away from the wall binding, counterintuitive to the notion that a flagellum always pushes the sperm cell. While this has been hypothesised in the biological literature based on observations, the model here demonstrates the mechanical consistency of this hypothesis based on the physics of microswimming.

For the specific case of golden-hamster sperm, the model predicts that the observed, symmetric waveform does not induce any tugging behaviour; thus, as expected, the sperm cell does not appear to have the ability to escape. However, for golden-hamster sperm exhibiting hyperactive beating, in which the amplitude increases by three or four times that of the symmetric beat, while the wavenumber and frequency decrease respectively to 4/7 and 0.35 of their symmetric counterparts [72], tugging forces are indeed generated, suggesting a mechanical contribution to sperm escape. Subsequent parameter studies also suggest that small changes to these values, 4/7 and 0.35, can still induce pulling forces.

Upon generalising the model to consider hyperactive sperm from other species, parameter sweeps have been conducted, analysing the relative changes in amplitude, wavenumber, symmetry and beat frequency of the hyperactive waveform compared to the symmetric waveform. Whilst changes in the beat frequency were not predicted to contribute to any tugging forces generated, large regions of parameter space with regards to the remaining, relative parameters indicate that tugging forces can arise, even for symmetrically beating flagella. This emphasises that the the regulation of the wavenumber, amplitude and beat asymmetry can be exploited for the mechanical

control of the cell behaviour when tethered to a surface.

The nature of the binding at the tethering point has also been investigated via the clamped and freely hinged boundary conditions. In particular, the results indicate that, for the clamped scenario, much larger changes in these relative parameters are required to generate pulling forces when compared to freely hinged cells. These requirements, for symmetric waveforms, include larger increases in amplitude and decreases in wavenumber, the latter being significantly outside the observed range in this biological scenario.

The presence of tugging forces, for certain regions of parameter space, appears to be complex. For example, upon varying the wavenumber, there exist bimodal variations in the generated forces predicted by asymmetric, freely hinged flagella. In addition, leading-order simplifications of the model do not capture the dynamics of the full, nonlinear model, demonstrating that geometric nonlinearity is important in understanding the behaviour of a hyperactivated sperm cell.

The results of the model have also been compared to experimental imaging data for a human sperm cell in a low-viscosity medium with motions indicative of a clamped and freely hinged binding to the underlying substrate (excised, female reproductive tract). The experimental data highlights that, for a clamped sperm cell, the hyperactive beat pattern propagating along the flagellum does not result in sperm escape. However, for the freely hinged sperm, the large-amplitude, asymmetric beating appears to move the cell backwards, in an oscillatory manner, away from the point of tethering. Cautious interpretation is required due to the lack of statistical significance. Nonetheless, the model agrees with the experimental data here, in that large-amplitude, asymmetric waves for freely hinged sperm are predicted to mechanically generate tugging forces.

### 6.1.4 Slender-Body Theory with Generalisations to Different Body Shapes

The flow past a slender body with a curvilinear centre-line and circular cross sections that can vary arbitrarily in radius along the body has been investigated and developed into a slender-body theory (SBT). The SBT builds upon the previous work of Johnson [53] in which the flow field around the slender body is represented by an integral of weighted Stokeslets and potential dipoles, distributed along the centre-line

of the body. The theory in Chapter 4, however, re-derives a slender-body, flow-field representation based on regularised singularities [25], where the regularisation parameter is a fully determined function.

For a cross-sectional radius function given by $\eta(s)$ along the arc-length, $s$, of the slender-body centre-line, describing the shape of the slender body, existing SBTs in the literature are restricted to geometries for which $\mathrm{d}\eta/\mathrm{d}s = 0$ at the centre of the body only. However, the SBT developed here allows $\mathrm{d}\eta/\mathrm{d}s = 0$ for any number of points along the arc-length of the centre-line. Thus, the flow fields around tapered shapes, ribbed / wave-like bodies and beaded shapes can now all be calculated.

Regularised singularities are used, whereby the regularisation parameter varies accordingly with the cross-sectional radius, so as to account for the variations in geometry along the centre-line of the body. This treatment of the regularisation parameter as a function, with a fully determined definition, is novel. By exploiting the regularisation parameter in this way, the theory does not require singularity weightings that differ in their expressions between the end regions and central region of the body, as in existing work [53], thus simplifying the numerical implementation of the SBT.

RFT has also been derived from the SBT in Chapter 4 by taking the leading-order, logarithmic terms. The RFT does not depend on the cross-sectional radius, $\eta(s)$; instead, it is asymptotically consistent, at the level of RFT, to approximate the slender body by a straight, prolate spheroid at $s$. This reinforces the need for a full SBT when seeking to include the effects of a varying, cross-sectional radius along a slender body.

The SBT has been implemented numerically for shapes taking a prescribed, tapered or wave-like form, with curvilinear centre-lines that are linear, quadratic or cubic in arc-length. An error analysis for the prolate spheroid has been conducted, exploring differences between the numerical solution of the integral equation, arising in the no-slip boundary condition, and the exact solution. The analysis confirms that the errors in the theory are subleading, with the largest being those at the ends of the body. These end errors, for the simulations conducted, are at most $O(\varepsilon^2)$, where $\varepsilon$ is the slenderness ratio of the body. The variations with cross-sectional angle, $\phi$, are negligible and the numerical scheme is shown to converge upon refinement.

## 6.2 Further Work

There are many opportunities for further work based on the models developed in the thesis, either by extending the individual models themselves or by combining different aspects of the three.

For the three-sphere swimmer, it emerges *a posteriori* that linear viscoelasticity is sufficient to deduce the leading-order dynamics in the *mobility* problem. The extent to which this may generalise is unclear and merits further investigation in order to understand when simple, fully linear methods might be exploited in some setting to understand inertialess swimming in rheological media.

A possible, analytical extension based on the three-sphere model itself includes the addition of unsteady terms within the governing, Stokes equations. The effects of these unsteady terms have yet to be explored on the three-sphere swimmer, though methods based on unsteady singularities could offer further insight into the potential dynamics of unsteady swimming.

The singularity methods used in Chapter 2 present the groundwork for investigating other types of swimmer models in a viscoelastic environment following the Olydroyd-B constitutive relation. Such swimmers include the 'push-me-pull-you' models [6] based on connected, spherical bladders changing their volumes and those which move in two-dimensions. The effects of nearby surfaces in viscoelastic environments can also be investigated for these swimmers.

A further, exciting opportunity is the generalisation of tracer studies to consider how viscoelasticity alters the flow fields and the movement of tracers around swimmers. Finally, the fact simple analytics emerges from these studies suggests that many body effects can be considered in viscoelastic media, for instance the extent to which nearby swimmers synchronise in the *mobility* problem, where relative displacements are dynamic, and more generally population models which rely on analytical details such as the far fields generated by swimmers.

The work on hyperactive sperm cells can be extended experimentally, in that the typical strengths of the bindings between the sperm head and the epithelial, wall cells of the female reproductive tract could be quantified. In particular, the possibility of

perturbing sperm using optical traps [48] promises much more extensive, mechanical data. For instance, given the tugging forces for golden-hamster sperm are on a scale of picoNewtons, it would then be feasible to predict whether the magnitude of the pulling motion is, in isolation, sufficient to overcome binding thresholds or whether other biological mechanisms are also required.

The fluid-mechanical framework used to study sperm motility in Chapter 3 suggests that viscosity does not have an effect on the pulling forces generated, given viscosity is non-dimensionalised out of the system. Experimentally, however, changes in viscosity, in particular for larger values, does change the nature of the flagellum waveform by reducing the absolute values of the amplitude and wavenumber for symmetric and hyperactivated, golden-hamster sperm [92]. These observations could be modelled by considering the *mobility* problem, assuming a suitable model for the internal forces generated along the flagellum [18, 66, 74] and incorporating any elastic properties of the flagellum. Further extensions to the framework include the presence of a physiological, mucus substitute, whereby elastic and shear-thinning properties of the fluid are considered. This would further strengthen conclusions supporting the hypothesis that hyperactivation assists the breaking of epithelial bonds in-vivo, or alternatively could predict that no tugging motion is observed.

Other effects which can be included in the current, tethered-sperm model relate to the two, simplified, boundary conditions used at the tethering point. More biologically realistic, chemical or physical changes in the acrosomal head due to capacitation could be modelled here. The tethered-sperm model also does not describe the cell body after it has broken away from the tethering point, in which it would undergo complex reorientations in the presence of nearby surfaces. Though RFT was justified for the tethered situation, a model for the release of a sperm would require more sophisticated treatments.

The SBT developed in this thesis has numerous applications which can now be studied. Biologically, the effects of tapering along a sperm flagellum due to outer, dense fibres [34] can be modelled, as well as the effect of wave-like ridges seen in the flagellated protozoa *Astasia Longa* [81]. The theory can also be implemented numerically for a wider range of parameters, including the prescription of a time-varying centreline with corresponding, surface velocity.

Regarding the asymptotic analysis underlying the slender-body theory, the no-slip boundary condition could be enforced at higher orders in $\varepsilon$, the slenderness ratio. This would follow a similar analysis to Johnson [53], though with the incorporation of regularised singularities. A particularly important example of this is to consider a surface velocity with an angular component, $\boldsymbol{\Omega} \sim O(1)$, which introduces additional, $O(\varepsilon)$ terms in the no-slip boundary condition. An initial *ansatz* for the flow field can be motivated by exact solutions for rotating, prolate spheroids [21, 53], which would induce higher-order, weighted singularities in the expansions. More generally, the slender-body theory presented here does not require asymptotic matching across three, different regions of the body centre-line, making these potential extensions more tractable than in Johnson's presentations [53]. A core, numerical extension would be incorporating the force balances required to simulate the net displacement of a swimmer. Finally, the framework could also be developed to investigate the effects of a nearby wall via half-space singularities [16], the absence of neutral buoyancy and the effects of a net, gravitational force on the slender body, high curvature centre-lines, or bodies without prolate-spheroidal caps.

Ideas within the three topics explored in the thesis could also be linked together. The SBT developed in Chapter 3 could be used to model the flow field around a beaded swimmer, for example following the shape of the three-sphere model, determining the net, swimmer velocity. Other existing, or newly created, swimmers can be incorporated, given the developed SBT only requires the prescription of a cross-sectional radius and a body centre-line. The SBT may also be generalised to a swimmer, such as a mammalian sperm, with a tapered flagellum, to investigate the effects of tapering on sperm escape for the tethered-sperm model. Finally, the ability to study non-trivial geometries within a highly efficient numerical scheme offers the prospect of geometrical optimisation of microswimmers. To date, this has only been studied with boundary element methods (Keaveny *et. al.* [56]).

# Appendix A

# Solving the $\mathbf{v}_1$ Equations

The Appendix relates to Chapter 3: "The Three-Sphere Microswimmer in a Viscoelastic Fluid". The problem concerns the flow field, $\mathbf{v}_1^{(\alpha)}$, outside a unit sphere satisfying the forced, Stokes problem:

$$\begin{aligned} -\nabla s_1^{(\alpha)} + \nabla^2 \mathbf{v}_1^{(\alpha)} &= \nabla \cdot \boldsymbol{\eta}^{(\alpha)}, \\ \nabla \cdot \mathbf{v}_1^{(\alpha)} &= 0, \\ \mathbf{v}_1^{(\alpha)} &= \mathbf{0} \qquad \text{on } |\mathbf{x}| = 1, \end{aligned} \tag{A.1}$$

for some pressure function $s_1^{(\alpha)}$. The forcing term depends on

$$\begin{aligned} \boldsymbol{\eta}^{(\alpha)} := \left(1 + \Gamma \frac{\partial}{\partial t}\right)^{-1} \Big\{ & \mathbf{u}_0^{(\alpha)} \cdot \nabla [\Lambda \boldsymbol{\tau}_0^{(\alpha)} - \Gamma \boldsymbol{\mathcal{E}}_0^{(\alpha)}] \\ & - \{ (\nabla \mathbf{u}_0^{(\alpha)})^T \cdot [\Lambda \boldsymbol{\tau}_0^{(\alpha)} - \Gamma \boldsymbol{\mathcal{E}}_0^{(\alpha)}] \\ & + [\Lambda \boldsymbol{\tau}_0^{(\alpha)} - \Gamma \boldsymbol{\mathcal{E}}_0^{(\alpha)}] \cdot \nabla \mathbf{u}_0^{(\alpha)} \} \\ & - \mathbf{U}_0^{(\alpha)} \cdot \nabla [\Lambda \boldsymbol{\tau}_0^{(\alpha)} - \Gamma \boldsymbol{\mathcal{E}}_0^{(\alpha)}] \Big\}. \end{aligned} \tag{A.2}$$

Equation (A.2) is a known function, given $\boldsymbol{\tau}_0^{(\alpha)}$ and $\boldsymbol{\mathcal{E}}_0^{(\alpha)}$ are defined in (2.79) in terms of the lead-order flow field, $\mathbf{u}_0^{(\alpha)}$, given by:

$$\begin{aligned} \mathbf{u}_0^{(\alpha)}(\mathbf{x}) \sim -\mathbf{U}_0^{(\alpha)} + \sum_{\gamma=1}^{3} \mathbf{G}(\mathbf{x}, \mathbf{x}^{(\gamma)}) \left[ \mathbf{U}_0^{(\gamma)} - \sum_{\nu \neq \gamma} \left\{ \delta \mathbf{K}^{(\gamma,\nu)} \mathbf{U}_0^{(\nu)} \right\} \right] \\ + \delta^2 \hat{\mathbf{u}}^{(\alpha)}|_{\epsilon=0} + O(\delta^3), \end{aligned} \tag{A.3}$$

from (2.81) and (2.82). The notation is defined in Chapter 3, Section 2.3.3. For reference later, $\mathbf{G}(\mathbf{x}, \mathbf{y})$ is the singularity combination of a Stokeslet, $\mathbf{S}(\mathbf{x}, \mathbf{y})$, and potential dipole, $\mathbf{D}(\mathbf{x}, \mathbf{y})$, taking the form

$$\mathbf{G}(\mathbf{x}, \mathbf{x}^{(\alpha)}) := \frac{3}{4} \mathbf{S}(\mathbf{x}, \mathbf{x}^{(\alpha)}) - \frac{1}{4} \mathbf{D}(\mathbf{x}, \mathbf{x}^{(\alpha)}). \tag{A.4}$$

In particular, it is required to show that $\mathbf{v}_1^{(\alpha)}$ satisfies the following condition on the surface of the unit sphere:

$$\mathbf{v}_1^{(\alpha)} = \mathbf{0} \qquad \text{on} \quad |\mathbf{x}| = 1, \qquad \beta = \alpha, \tag{A.5}$$

and the following condition on the surfaces of the two, other unit spheres, located at $O(1/\delta)$ distances away:

$$\mathbf{v}_1^{(\alpha)} \sim \delta^2 \mathbf{A}^{(\alpha)} \qquad \text{on} \quad |\mathbf{x} - \mathbf{x}^{(\beta)}| = 1, \quad \beta \neq \alpha. \tag{A.6}$$

Note that the two other spheres are both fictitious boundaries, given they are not part of the domain in the $\mathbf{v}_1^{(\alpha)}$ problem, (A.1).

When solving the $\mathbf{v}_1^{(\alpha)}$ equations, only the leading-order contributions of the forcing term, $\nabla \cdot \boldsymbol{\eta}^{(\alpha)}$, are considered in (A.1) as these are sufficient to deduce the boundary conditions (A.5) and (A.6). In fact, (A.5), which states that the flow around the unit sphere is zero, is automatically satisfied by the boundary condition in the $\mathbf{v}_1^{(\alpha)}$ problem (A.1). Thus, attention is given to the flow, $\mathbf{v}_1^{(\alpha)}$, due to the other spheres. To obtain the leading-order contributions to $\nabla \cdot \boldsymbol{\eta}^{(\alpha)}$, note that the leading-order expression for $\mathbf{u}_0^{(\alpha)}(\mathbf{x})$ from (A.3) is

$$\mathbf{u}_0^{(\alpha)}(\mathbf{x}) \sim -\mathbf{U}_0^{(\alpha)} + \mathbf{G}(\mathbf{x}, \mathbf{0})\mathbf{U}_0^{(\alpha)} + O(\delta). \tag{A.7}$$

This gives the leading order expression for $\boldsymbol{\eta}^{(\alpha)}$ as

$$\begin{aligned} \boldsymbol{\eta}^{(\alpha)} \approx \left(1 + \Gamma\frac{\partial}{\partial t}\right)^{-1} \Big[ & \mathbf{G}(\mathbf{x}, \mathbf{0})\mathbf{U}_0^{(\alpha)} \cdot \nabla[\Lambda\boldsymbol{\tau}_0^{(\alpha)} - \Gamma\boldsymbol{\mathcal{E}}_0^{(\alpha)}] \\ & -\{(\nabla\mathbf{G}(\mathbf{x}, \mathbf{0})\mathbf{U}_0^{(\alpha)})^T \cdot [\Lambda\boldsymbol{\tau}_0^{(\alpha)} - \Gamma\boldsymbol{\mathcal{E}}_0^{(\alpha)}] \\ & +[\Lambda\boldsymbol{\tau}_0^{(\alpha)} - \Gamma\boldsymbol{\mathcal{E}}_0^{(\alpha)}] \cdot \nabla\mathbf{G}(\mathbf{x}, \mathbf{0})\mathbf{U}_0^{(\alpha)}\} \\ & -2\mathbf{U}_0^{(\alpha)} \cdot \nabla[\Lambda\boldsymbol{\tau}_0^{(\alpha)} - \Gamma\boldsymbol{\mathcal{E}}_0^{(\alpha)}]\Big], \end{aligned} \tag{A.8}$$

where, from equations (2.79) and (A.7),

$$\begin{aligned} \mathcal{L}[\boldsymbol{\tau}_0^{(\alpha)}] &= \boldsymbol{\mathcal{E}}_0^{(\alpha)}, \\ &\approx (\nabla\mathbf{G}(\mathbf{x}, \mathbf{0})\mathbf{U}_0^{(\alpha)})^T + \nabla\mathbf{G}(\mathbf{x}, \mathbf{0})\mathbf{U}_0^{(\alpha)}, \end{aligned} \tag{A.9}$$

recalling from (2.80) the definition of $\mathcal{L}$:

$$\mathcal{L} := \left(1 + \Gamma\frac{\partial}{\partial t}\right)^{-1} \left(1 + \Lambda\frac{\partial}{\partial t}\right). \tag{A.10}$$

As detailed in Chapter 3, a periodic solution is sought in which initial, transient behaviour has decayed, entailing the inverse operator in the definition of $\mathcal{L}$ in (A.10) is uniquely defined.

By taking the divergence of $\boldsymbol{\eta}^{(\alpha)}$ in (A.8),

$$\nabla \cdot \boldsymbol{\eta}^{(\alpha)} \approx \mathbf{C} + \nabla P, \tag{A.11}$$

where

$$\begin{aligned}\mathbf{C} := \left(1 + \Gamma\frac{\partial}{\partial t}\right)^{-1} \nabla \cdot \Big[&\mathbf{G}(\mathbf{x}, \mathbf{0})\mathbf{U}_0^{(\alpha)} \cdot \nabla[\Lambda\boldsymbol{\tau}_0^{(\alpha)} - \Gamma\boldsymbol{\mathcal{E}}_0^{(\alpha)}] \\ &-\{(\nabla\mathbf{G}(\mathbf{x}, \mathbf{0})\mathbf{U}_0^{(\alpha)})^T \cdot [\Lambda\boldsymbol{\tau}_0^{(\alpha)} - \Gamma\boldsymbol{\mathcal{E}}_0^{(\alpha)}] \\ &+[\Lambda\boldsymbol{\tau}_0^{(\alpha)} - \Gamma\boldsymbol{\mathcal{E}}_0^{(\alpha)}] \cdot \nabla\mathbf{G}(\mathbf{x}, \mathbf{0})\mathbf{U}_0^{(\alpha)}\}\Big],\end{aligned} \tag{A.12}$$

and

$$P := -2\left(1 + \Gamma\frac{\partial}{\partial t}\right)^{-1} \left[\mathbf{U}_0^{(\alpha)} \cdot [\Lambda\nabla \cdot \boldsymbol{\tau}_0^{(\alpha)} - \Gamma\nabla \cdot \boldsymbol{\mathcal{E}}_0^{(\alpha)}]\right]. \tag{A.13}$$

The last term in (A.11) has extracted the gradient operator, $\nabla$, given $\mathbf{U}_0^{(\alpha)}$ is spatially constant; the subsequent, divergence operator has commuted with the gradient operator, forming $P$ in (A.13).

Equation (A.12) is rewritten in tensor notation (index summation assumed) where $r = |\mathbf{x}|$, $r_i = x_i$ and $\mathbf{U}_0^{(\alpha)}$ has components $U_i^{(\alpha)}$, so that

$$C_i = C_{ijk}\left(1 + \Gamma\frac{\partial}{\partial t}\right)^{-1} [U_j^{(\alpha)}(\Lambda\mathcal{L}^{-1} - \Gamma)[U^{(\alpha)}]_k]. \tag{A.14}$$

The operator $(\Lambda\mathcal{L}^{-1} - \Gamma)$ is due to $(\Lambda\boldsymbol{\tau}_0^{(\alpha)} - \Gamma\boldsymbol{\mathcal{E}}_0^{(\alpha)})$ terms in (A.12) using the relation from (A.9) to write both $\boldsymbol{\tau}_0^{(\alpha)}$ and $\boldsymbol{\mathcal{E}}_0^{(\alpha)}$ in terms of $\mathbf{U}_0^{(\alpha)}$.

The $r_3$ direction is taken along the axis of the swimmer, $\mathbf{e}_z$, so that $r_3 = z$ and $U_i^{(\alpha)} = U^{(\alpha)}\delta_{i3}$. As $\mathbf{G}(\mathbf{x}, \mathbf{y})$ in (A.4) is a weighted Stokeslet plus a weighted, potential dipole, it is a function solely of radial components. Upon re-dimensionalisation to a sphere of radius $a$ (see Section 1.3.2.1), powers of $a/r$ in the tensor $\mathbf{G}(\mathbf{x}, \mathbf{y})$ are identified by looking at the forms of the Stokeslet and potential dipole. Hence, the form of equation (A.12) can be deduced by multiplying, and differentiating, powers

of $a/r$ accordingly. Returning to dimensionless variables, the form of $C_{ijk}$ in equation (A.14) is hence known, becoming

$$C_i = \bar{C}_i \left(1 + \Gamma \frac{\partial}{\partial t}\right)^{-1} U^{(\alpha)}(\Lambda \mathcal{L}^{-1} - \Gamma)[U^{(\alpha)}], \tag{A.15}$$

where $\bar{C}_i$ is given in terms of obtainable constants $A_{mn}$, whose values are not required for this calculation, by

$$\begin{aligned}\bar{C}_i = &\left(\frac{A_{11}}{r^2} + \frac{A_{12}}{r^4} + \frac{A_{13}}{r^6}\right)\frac{r_i z^2}{r^6} + \left(\frac{A_{21}}{r^2} + \frac{A_{22}}{r^4} + \frac{A_{23}}{r^6}\right)\frac{r_i}{r^4} \\ &+ \left(\frac{A_{31}}{r^2} + \frac{A_{32}}{r^4} + \frac{A_{33}}{r^6}\right)\frac{\delta_{i3} z}{r^4}.\end{aligned} \tag{A.16}$$

Next, note the relation

$$\frac{\partial^2}{\partial z^2}\left(\frac{r_i}{r^m}\right) = -\frac{2m\delta_{i3} z}{r^{m+2}} - \frac{m r_i}{r^{m+2}} + \frac{m(m+2) r_i z^2}{r^{m+4}}, \tag{A.17}$$

for integers $m$, which rearranges to give

$$\begin{aligned}\frac{r_i z^2}{r^{m+4}} &= \frac{1}{m(m+2)}\left[\frac{\partial^2}{\partial z^2}\left(\frac{r_i}{r^m}\right) + \frac{m r_i}{r^{m+2}}\right] + \frac{2\delta_{i3} z}{(m+2) r^{m+2}}, \\ &= -\frac{\partial}{\partial r_i}\left(\frac{1}{m(m+2)}\left[\frac{\partial^2}{\partial z^2}\left(\frac{1}{(m-2) r^{m-2}}\right) + \frac{1}{r^m}\right]\right) + \frac{2\delta_{i3} z}{(m+2) r^{m+2}}.\end{aligned} \tag{A.18}$$

Thus, all the $A_{1j}$ terms in (A.16) of the form $r_i z^2/r^k$ can be expressed as a gradient of a radial function plus a $\delta_{i3} z/r^k$ term, the latter being the same form as the $A_{3j}$ terms. The $A_{2j}$ terms in (A.16) of the form $r_i/r^k$ can be immediately expressed as a gradient of radial function using the identity

$$\frac{r_i}{r^{m+2}} = -\frac{\partial}{\partial r_i}\left(\frac{1}{m r^m}\right). \tag{A.19}$$

Hence $\bar{C}_i$ in (A.16) takes the form

$$\bar{C}_i = \frac{\partial \psi}{\partial r_i} + \left[\frac{(A_{31} + A_{11}/3)}{r^2} + \frac{(A_{32} + A_{12}/4)}{r^4} + \frac{(A_{33} + A_{13}/5)}{r^6}\right]\frac{\delta_{i3} z}{r^4}, \tag{A.20}$$

where $\psi$ includes all the radial functions within any gradients; these functions are not required explicitly. Substituting (A.20) into (A.11) and (A.15) gives

$$\frac{\partial \eta_{ij}}{\partial r_j}^{(\alpha)} = \left[\sum_{m=1}^{3} \frac{\zeta_m^{(\alpha)}}{r^{2m}}\right]\frac{\delta_{i3} z}{r^4} + \frac{\partial \bar{\psi}}{\partial r_i}, \tag{A.21}$$

where $\bar{\psi} = \psi + P$ and

$$\zeta_m^\alpha := (A_{3m} + \frac{A_{1m}}{2+m}) \left(1 + \Gamma \frac{\partial}{\partial t}\right)^{-1} U^{(\alpha)} (\Lambda \mathcal{L}^{-1} - \Gamma)[U^{(\alpha)}]. \tag{A.22}$$

The $\mathbf{v}_1^{(\alpha)}$ problem, (A.1), is thus

$$\begin{aligned} -\nabla \bar{s}_1^{(\alpha)} + \nabla^2 \mathbf{v}_1^{(\alpha)} &= \left[\sum_{m=1}^{3} \frac{\zeta_m^\alpha}{r^{2m}}\right] \frac{z\mathbf{e}_z}{r^4}, \\ \nabla \cdot \mathbf{v}_1^{(\alpha)} &= 0, \\ \mathbf{v}_1^{(\alpha)} &= \mathbf{0} \qquad \text{on } r = 1, \end{aligned} \tag{A.23}$$

where $\bar{s}_1^{(\alpha)} = s_1^{(\alpha)} + \bar{\psi}$ is the modified pressure term, absorbing any gradients of radial functions.

To proceed, the problem is split into a particular integral, denoted by superscript $p$, satisfying

$$\begin{aligned} -\nabla s^p + \nabla^2 \mathbf{v}^p &= \left[\sum_{m=1}^{3} \frac{\zeta_m^\alpha}{r^{2m}}\right] \frac{z\mathbf{e}_z}{r^4}, \\ \nabla \cdot \mathbf{v}^p &= 0, \end{aligned} \tag{A.24}$$

and a complementary function, denoted by superscript $c$, satisfying

$$\begin{aligned} -\nabla s^c + \nabla^2 \mathbf{v}^c &= \mathbf{0}, \\ \nabla \cdot \mathbf{v}^c &= 0, \\ \mathbf{v}^c &= -\mathbf{v}^p \qquad \text{on } r = 1, \end{aligned} \tag{A.25}$$

where $\mathbf{v}_1^{(\alpha)} = \mathbf{v}^c + \mathbf{v}^p$ and $\bar{s}_1^{(\alpha)} = s^p + s^c$. From the particular-integral equations, (A.24), one can deduce a form $s^p$ and hence $\mathbf{v}^p$. To do so, note

$$\nabla^2 \nu_{(m)} = \frac{1}{r^m}, \qquad \nu_{(m)} = \frac{1}{(m-2)(m-3)r^{m-2}} \qquad m > 3, \tag{A.26}$$

$$\nabla^2 \chi_{i(m)} = \frac{r_i}{r^m}, \qquad \chi_{i(m)} = \frac{r_i}{(m-2)(m-5)r^{m-2}} \qquad m > 5, \tag{A.27}$$

where the latter is the vector Laplacian operator. Thus

$$\begin{aligned} -\nabla s^p + \nabla^2 \mathbf{v}^p &= \left[\sum_{m=1}^{3} \frac{\zeta_m^\alpha}{r^{2m}}\right] \frac{z\mathbf{e}_z}{r^4}, \\ &= \sum_{m=1}^{3} \frac{\zeta_m^\alpha}{(2m+2)} \frac{\partial}{\partial z} \left[\frac{1}{r^{2m+2}}\right] \mathbf{e}_z, \\ &= \sum_{m=1}^{3} \frac{\zeta_m^\alpha}{(2m+2)} \frac{\partial}{\partial z} \left[\nabla^2 \nu_{2m+2}\right] \mathbf{e}_z, \end{aligned} \tag{A.28}$$

Taking the divergence, recalling $\nabla \cdot \mathbf{v}^p = 0$, gives

$$\nabla^2 s^p = \sum_{m=1}^{3} \frac{\zeta_m^\alpha}{(2m+2)} \frac{\partial^2}{\partial z^2} \left[\nabla^2 \nu_{2m+2}\right], \tag{A.29}$$

hence a solution is

$$s^p = \sum_{m=1}^{3} \frac{\zeta_m^\alpha}{(2m+2)} \frac{\partial^2}{\partial z^2} \left[\frac{1}{2m(2m-1)r^{2m}}\right]. \tag{A.30}$$

Continuing,

$$\begin{aligned} \nabla s^p &= -\sum_{m=1}^{3} \frac{\zeta_m^\alpha}{(2m+2)} \frac{\partial^2}{\partial z^2} \left[\frac{r_i}{(2m-1)r^{2m+2}}\right], \\ &= -\sum_{m=1}^{3} \frac{\zeta_m^\alpha}{(2m+2)(2m-1)} \frac{\partial^2}{\partial z^2} \left[\nabla^2 \chi_{i(2m+2)}\right]. \end{aligned} \tag{A.31}$$

Substituting this back into (A.28) gives

$$\nabla^2 v_i^p = \sum_{m=1}^{3} \frac{\zeta_m^\alpha}{(2m+2)} \left\{ \frac{\partial}{\partial z} \left[\nabla^2 \nu_{2m+2}\right] \delta_{i3} - \frac{1}{(2m-1)} \frac{\partial^2}{\partial z^2} \left[\nabla^2 \chi_{i(2m+2)}\right] \right\}, \tag{A.32}$$

so that a solution for the particular integral is

$$\begin{aligned} v_i^p &= \sum_{m=1}^{3} \frac{\zeta_m^\alpha}{(2m+2)} \left\{ \frac{\partial}{\partial z} \left[\nu_{2m+2}\right] \delta_{i3} - \frac{1}{(2m-1)} \frac{\partial^2}{\partial z^2} \left[\chi_{i(2m+2)}\right] \right\}, \\ &= \sum_{m=1}^{3} \frac{\zeta_m^\alpha}{(2m+2)} \left\{ \frac{\partial}{\partial z} \left[\frac{1}{2m(2m-1)r^{2m}}\right] \delta_{i3} \right. \\ &\qquad \left. - \frac{1}{(2m-1)} \frac{\partial^2}{\partial z^2} \left[\frac{r_i}{2m(2m-3)r^{2m}}\right] \right\}. \end{aligned} \tag{A.33}$$

Evaluating the $z$-derivatives,

$$\begin{aligned} v_i^p = \sum_{m=1}^{3} \frac{\zeta_m^\alpha}{(2m+2)} &\left\{ \frac{-z}{(2m-1)r^{2m+2}} \delta_{i3} \right. \\ &\left. - \frac{1}{(2m-1)(2m-3)} \left[\frac{2\delta_{i3} z}{r^{2m+2}} + \frac{r_i}{r^{2m+2}} - \frac{(2m+2) r_i z^2}{r^{2m+4}}\right] \right\}, \end{aligned} \tag{A.34}$$

which, on $r = 1$, $z = \cos\theta$ in standard spherical polar coordinates, becomes

$$\begin{aligned} \mathbf{v}^p|_{r=1} = \sum_{m=1}^{3} \frac{\zeta_m^\alpha}{(2m+2)} &\left\{ \frac{-\cos\theta \mathbf{e}_z}{(2m-1)} \right. \\ &\left. - \frac{[2\cos\theta \mathbf{e}_z + \mathbf{e}_r - (2m+2)\mathbf{e}_r \cos^2\theta]}{(2m-1)(2m-3)} \right\}. \end{aligned} \tag{A.35}$$

This can be written, noting $\cos\theta\mathbf{e}_z = \cos^2\theta\mathbf{e}_r - \sin\theta\cos\theta\mathbf{e}_\theta$ in spherical coordinates, as

$$\mathbf{v}^p|_{r=1} = \sum_{m=1}^{3} \frac{[(3\cos^2\theta - 1)\mathbf{e}_r + (2m-1)\sin\theta\cos\theta\mathbf{e}_\theta]\zeta_m^\alpha}{(2m+2)(2m-1)(2m-3)}. \tag{A.36}$$

The complementary problem,

$$\begin{aligned} -\nabla s^c + \nabla^2\mathbf{v}^c &= \mathbf{0}, \\ \nabla\cdot\mathbf{v}^c &= 0, \\ \mathbf{v}^c &= -\mathbf{v}^p \qquad \text{on } r = 1, \end{aligned} \tag{A.37}$$

thus has a known, boundary condition, which in turn motivates the form of $\mathbf{v}^c$. Thus the complementary function is a linear combination of

$$\begin{aligned} \mathbf{v}_1^c &= \frac{\cos^2\theta\mathbf{e}_r}{r^2}, \\ \mathbf{v}_2^c &= \frac{\mathbf{e}_r}{r^2}, \\ \mathbf{v}_3^c &= \frac{(3\cos^2\theta - 1)\mathbf{e}_r}{r^4} + \frac{2\cos\theta\sin\theta\mathbf{e}_\theta}{3r^4}, \end{aligned} \tag{A.38}$$

all of which satisfy the Stokes' equations. It is now clear that the dominant contribution to $\mathbf{v}_1^{(\alpha)}$, as $r$ increases away from sphere $\alpha$, comes from the complementary function, $O(1/r^2)$. In particular, on another sphere the first term is $O(\delta^2)$ and

$$\begin{aligned} \cos\theta &\sim 1 + O(\epsilon\delta), \\ 1/r &\sim \delta + O(\epsilon\delta^2), \\ \mathbf{e}_r &\sim \mathbf{e}_z + O(\epsilon\delta), \end{aligned} \tag{A.39}$$

so

$$\mathbf{v}_1^{(\alpha)} \sim \delta^2\mathbf{A}^{(\beta)} \qquad \text{on} \quad |\mathbf{x} - \mathbf{x}^{(\beta)}| = 1, \quad \beta \in \{1,2,3\}, \tag{A.40}$$

for constant vectors $\mathbf{A}^{(\beta)}$, where $\mathbf{A}^{(\alpha)} = \mathbf{0}$, and $\mathbf{A}^{(\beta)}$ is of $O(1)$ magnitude.

# Bibliography


[1] World Health Organisation. WHO Laboratory Manual for the Examination of Human Semen and Sperm-Cervical Mucus Interactions, 4th Edition, Cambridge University Press, 1999.

[2] J. Ainley, S. Durkin, R. Embid, P. Boindala, and R. Cortez. The method of images for regularized stokeslets. *Journal of Computational Physics*, **227**(9):4600–4616, 2008.

[3] S. M. H. Alavi, A. Hatef, M. Pšeničkа, V. Kašpar, S. Boryshpolets, B. Dzyuba, J. Cosson, V. Bondarenko, M. Rodina, D. Gela, et al. Sperm biology and control of reproduction in sturgeon:(ii) sperm morphology, acrosome reaction, motility and cryopreservation. *Reviews in Fish Biology and Fisheries*, **22**(4):861–886, 2012.

[4] G. P. Alexander, C. M. Pooley, and J. M. Yeomans. Hydrodynamics of linked sphere model swimmers. *Journal of Physics: Condensed Matter*, **21**(20):204108, 2009.

[5] S. Antman. *Nonlinear problems of elasticity*, **107**. Springer, 2005.

[6] J. E. Avron, O. Kenneth, and D. H. Oaknin. Push-me-pull-you: an efficient micro-swimmer. *New Journal of Physics*, **7**(1):234, 2005.

[7] J. M. Baltz, P. O. Williams, and R. A. Cone. Dense fibers protect mammalian sperm against damage. *Biology of Reproduction*, **43**(3):485, 1990.

[8] G. Batchelor. *An Introduction to Fluid Dynamics*. Cambridge University Press, 1967.

[9] G. K. Batchelor. Slender-body theory for particles of arbitrary cross-section in Stokes flow. *Journal of Fluid Mechanics*, **44**(03):419–440, 1970.

[10] L. E. Becker, S. A. Koehler, and H. A. Stone. On self-propulsion of micro-machines at low Reynolds number: Purcell's three-link swimmer. *Journal of Fluid Mechanics*, **490**:15–35, 2003.

[11] B. Behkam and M. Sitti. Modeling and testing of a biomimetic flagellar propulsion method for microscale biomedical swimming robots. In *Proceedings of*, pages 37–42, 2005.

[12] R. B. Bird, R. C. Armstrong, and O. Hassager. *Fluid Mechanics, Vol. 1 of Dynamics of Polymeric Liquids*. Wiley, New York, 1977.

[13] R. B. Bird and J. M. Wiest. Constitutive equations for polymeric liquids. *Annual review of Fluid Mechanics*, **27**(1):169–193, 1995.

[14] J. R. Blake. A note on the image system for a stokeslet in a no-slip boundary. *Proc. Camb. Phil. Soc.*, **70**, 1971.

[15] J. R. Blake. Singularities of viscous flow. *Journal of Engineering Mathematics*, **8**(2), 1974.

[16] J. R. Blake and A. T. Chwang. Fundamental singularities of viscous flow. *Journal of Engineering Mathematics*, **8**(1), 1974.

[17] J. D. Bleil and P. M. Wassarman. Structure and function of the zona pellucida. *Developmental Biology*, **76**:185–202, 1980.

[18] C. J. Brokaw. Control of flagellar bending: a new agenda based on dynein diversity. *Cell motility and the cytoskeleton*, **28**(3):199–204, 1994.

[19] C.J. Brokaw. Calcium sensors in sea urchin sperm flagella. *Cell Motility and the Cytoskeleton*, **18**:123–130, 1991.

[20] J. E. Butler and E. S. G. Shaqfeh. Dynamic simulations of the inhomogeneous sedimentation of rigid fibres. *Journal of Fluid Mechanics*, **468**(1):205–237, 2002.

[21] A. T. Chwang and T. Y. Wu. Hydromechanics of low-reynolds-number flow. part 1. rotation of axisymmetric prolate bodies. *Journal of Fluid Mechanics*, **63**(3):607–622, 1974.

[22] A. T. Chwang and T. Y. Wu. Hydromechanics of low-reynolds-number flow. part 2. singularity method for stokes flows. *Journal of Fluid Mechanics*, **67**:787–815, 1974.

[23] R. Cortez. The method of regularized Stokeslets. *SIAM Journal on Scientific Computing*, **23**(4):1204–1225, 2001.

[24] R. Cortez, L. Fauci, N. Cowen, and R. Dillon. Simulation of swimming organisms: coupling internal mechanics with external fluid dynamics. *Computing in Science & Engineering*, **6**(3):38–45, 2004.

[25] R. Cortez, L. Fauci, and A. Medovikov. The method of regularized Stokeslets in three dimensions: Analysis, validation, and application to helical swimming. *Physics of Fluids*, **17**, 2005.

[26] R. Cortez and M. Nicholas. Slender body theory for Stokes flows with regularized forces. *Communications in Applied Mathematics and Computational Science*, **7**:33–62, 2012.

[27] R. G. Cox. The motion of long slender bodies in a viscous fluid. *Journal of Fluid Mechanics*, **44**:791–810, 1970.

[28] J. M. Cummins and P. F. Woodall. On mammalian sperm dimensions. *J. Reprod. Fert.*, **75**:153–175, 1985.

[29] M. P. Curtis, J. C. Kirkman-Brown, T. J. Connolly, and E. A. Gaffney. Modelling a tethered mammalian sperm cell undergoing hyperactivation. *Journal of Theoretical Biology*, **309**:1–10, 2012.

[30] R. P. Demott and S. S. Suarez. Hyperactivated sperm progress in the mouse oviduct. *Biology of Reproduction*, **46**:779–785, 1992.

[31] R. H. Dillon, L. J. Fauci, C. Omoto, and X. Yang. Fluid dynamic models of flagellar and ciliary beating. *Annals of the New York Academy of Sciences*, **1101**(1):494–505, 2007.

[32] D. J. Earl, C. M. Pooley, J. F. Ryder, I. Bredberg, and J. M. Yeomans. Modeling microscopic swimmers at low reynolds number. *The Journal of Chemical Physics*, **126**(6):064703, 2007.

[33] G. J. Elfring, O. S. Pak, and E. Lauga. Two-dimensional flagellar synchronization in viscoelastic fluids. *Journal of Fluid Mechanics*, **646**:505, 2010.

[34] D. W. Fawcett. A comparative view of sperm ultrastructure. *Biology of Reproduction Supplement*, **2**:90–127, 1970.

[35] B. M. Friedrich, I. H. Riedel-Kruse, J. Howard, and F. Julicher. High-precision tracking of sperm swimming fine structure provides strong test of resistive force theory. *J. Exp. Biol.*, pages 1226–1234, 2010.

[36] H. C. Fu, T. R. Powers, and C. W. Wolgemuth. Theory of swimming filaments in viscoelastic media. *Physical Review Letters*, **99**(25):258101, 2007.

[37] H. C. Fu, C. W. Wolgemuth, and T. R. Powers. Swimming speeds of filaments in nonlinearly viscoelastic fluids. *Phys. Fluids*, **21**:033102, 2009.

[38] G. R. Fulford, D. F. Katz, and R. L. Powell. Swimming of spermatozoa in a linear viscoelastic fluid. *Biorheology*, **35**:296–309, 1998.

[39] H. Gadêlha, E. A. Gaffney, D. J. Smith, and J. C. Kirkman-Brown. Nonlinear instability in flagellar dynamics: a novel modulation mechanism in sperm migration? *Journal of The Royal Society Interface*, **7**(53):1689–1697, 2010.

[40] E. A. Gaffney, H. Gadêlha, D. J. Smith, J. R. Blake, and J. C. Kirkman-Brown. Mammalian sperm motility: observation and theory. *Annual Review of Fluid Mechanics*, **43**:501–528, 2011.

[41] R. Golestanian and A. Ajdari. Analytic results for the three-sphere swimmer at low reynolds number. *Phys. Rev. E*, **77**(3):036308, 2008.

[42] J. Gray and G. J. Hancock. The propulsion of sea-urchin spermatozoa. *J. Exp. Biol.*, **32**:802–814, 1955.

[43] G. J. Hancock. The self-propulsion of microscopic organisms through liquids. *Proc. R. Soc. B*, **217**:96–121, 1953.

[44] J. Happel and H. Brenner. *Low Reynolds number hydrodynamics*. Kluwer Academic Publishers, 1983.

[45] J. J. L. Higdon. The generation of feeding currents by flagellar motions. *Journal of Fluid Mechanics*, **94**(02):305–330, 1979.

[46] J. J. L. Higdon. A hydrodynamic analysis of flagellar propulsion. *Journal of Fluid Mechanics*, **90**:685–711, 1979.

[47] H. C. Ho and S. S. Suarez. Hyperactivation of mammalian spermatozoa: function and regulation. *Reproduction*, **122**(4):519–526, Oct 2001.

[48] N. Hyun, C. Chandsawangbhuwana, Q. Zhu, L. Shi, C. Yang-Wong, and M. W. Berns. Effects of viscosity on sperm motility studied with optical tweezers. *Journal of Biomedical Optics*, **17**(2):025005–1, 2012.

[49] T. Ishikawa, G. Sekiya, Y. Imai, and T. Yamaguchi. Hydrodynamic interactions between two swimming bacteria. *Biophysical journal*, **93**(6):2217–2225, 2007.

[50] T. L. Jahn and J. J. Votta. Locomotion of protozoa. *Annual Reviews*, 1972.

[51] D. F. James. Boger fluids. *Annual Reviews of Fluid Mechanics*, **41**:129–142, 2009.

[52] R. Johnson. *Slender Body Theory for Stokes flow and flagellar hydrodynamics*. PhD thesis, California Institute of Technology, May 1977.

[53] R. Johnson. An improved slender body theory for Stokes flow. *Journal of Fluid Mechanics*, **99**:411–431, 1980.

[54] R. E. Johnson and C. J. Brokaw. Flagellar hydrodynamics: A comparison between resistive force theory and slender body theory. *Biophysical Journal*, **25**:113–127, 1979.

[55] D. F. Katz, J. R. Blake, and S. L. Paveri-Fontana. On the movement of slender bodies near plane boundaries at low reynolds number. *Journal of Fluid Mechanics*, **72**(3):529–540, 1975.

[56] E. E. Keaveny and M. J. Shelley. Applying a second-kind boundary integral equation for surface tractions in Stokes flow. *Journal of Computational Physics*, **230**(5):2141–2159, 2011.

[57] J. B. Keller and S. I. Rubinow. Slender body theory for slow viscous flow. *Journal of Fluid Mechanics*, **75**:705–714, 1976.

[58] S. Kim and S. J. Karrila. *Microhydrodynamics*. Butterworth-Heinemann New York, 1991.

[59] E. Lauga. Propulsion in a viscoelastic fluid. *Physics of Fluids*, **19**:083–104, 2007.

[60] E. Lauga. Life at high deborah number. *EPL (Europhysics Letters)*, **86**:64001, 2009.

[61] E. Lauga and T. Powers. The hydrodynamics of swimming microorganisms. *Rep. Prog. Phys*, **72**, 2009.

[62] M. Leoni, J. Kotar, B. Bassetti, P. Cicuta, and M. C. Lagomarsino. A basic swimmer at low reynolds number. *Soft Matter*, **5**(2):472–476, 2009.

[63] M. J. Lighthill. On the squirming motion of nearly spherical deformable bodies through liquids at very small reynolds numbers. *Communications on Pure and Applied Mathematics*, **5**(2):109–118, 1952.

[64] M. J. Lighthill. Flagellar hydrodynamics. *SIAM Review*, **18**(2), 1976.

[65] M. J. Lighthill. Reinterpreting the basic theorem of flagellar hydrodynamics. *Journal of Eng. Math.*, **30**:25–34, 1996.

[66] C. B. Lindemann. Testing the geometric clutch hypothesis. *Biology of the Cell*, **96**(9):681–690, 2004.

[67] N. Liron and S. Mochon. The discrete-cilia approach to propulsion of ciliated micro-organisms. *Journal of Fluid Mechanics*, **75**:593–607, 1976.

[68] K. E. Machin. Wave propagation along flagella. *J. exp. Biol*, **35**(4):796–806, 1958.

[69] T. D. Montenegro-Johnson, A. A. Smith, D. J. Smith, D. Loghin, and J. R. Blake. Modelling the fluid mechanics of cilia and flagella in reproduction and development. *The European Physical Journal E: Soft Matter and Biological Physics*, **35**(10):1–17, 2012.

[70] A. Najafi and R. Golestanian. A simplest swimmer at low reynolds number: Three linked spheres. *Phys. Rev. E*, **69**(6):629–629, 2004.

[71] H. Ockendon and J. R. Ockendon. *Viscous flow*, **13**. Cambridge University Press, 1995.

[72] J. Ohmuro and S. Ishijima. Hyperactivation mode conversion. *Molecular Reproduction and Development*, **73**:1412–1421, 2006.

[73] J. G. Oldroyd. On the formulation of rheological equations of state. *Proceedings of the Royal Society of London. Series A. Mathematical and Physical Sciences*, **200**(1063):523–541, 1950.

[74] S. D. Olson, L. J. Fauci, and S. S. Suarez. Mathematical modeling of calcium signaling during sperm hyperactivation. *Molecular Human Reproduction*, **17**(8, SI):500–510, Aug 2011.

[75] S. D. Olson, S. S. Suarez, and L. J. Fauci. Coupling biochemistry and hydrodynamics captures hyperactivated sperm motility in a simple flagellar model. *Journal of Theoretical Biology*, **280**(1):203–216, 2011.

[76] N. Phan-Thien, T. Tran-Cong, and M. Ramia. A boundary-element analysis of flagellar propulsion. *Journal of Fluid Mechanics*, **35**:295–309, 1998.

[77] H. Pleiner, M. Liu, and H. R. Brand. Nonlinear fluid dynamics description of non-newtonian fluids. *Rheologica Acta*, **43**(5):502–508, 2004.

[78] C. M. Pooley, G. P. Alexander, and J. M. Yeomans. Hydrodynamic interaction between two swimmers at low reynolds number. *Physical Review Letters*, **99**(22):228–103, 2007.

[79] C. Pozrikidis. *Boundary integral and singularity methods for linearized viscous flow*. Cambridge University Press, 1992.

[80] E. M. Purcell. Life at low reynolds number. *Am. J. Phys*, **45**(1):3–11, 1977.

[81] D. L. Ringo. Electron microscopy of *Astasia Longa*. *Journal of Eukaryotic Microbiology*, **10**(2):167–173, 1963.

[82] H. Shum, E. A. Gaffney, and D. J. Smith. Modelling bacterial behaviour close to a no-slip plane boundary: the influence of bacterial geometry. *Proc. Roy. Soc. A*, 2010.

[83] D. J. Smith, E. A. Gaffney, and J. R. Blake. Discrete cilia modelling with singularity distributions: application to the embryonic node and the airway surface liquid. *Bulletin of Mathematical Biology*, **69**(5):1477–1510, 2007.

[84] D. J. Smith, E. A. Gaffney, and J. R. Blake. Mathematical modelling of cilia-driven transport of biological fluids. *Proc. R. Soc. A*, **465**:2417–2439, 2009.

[85] D. J. Smith, E. A. Gaffney, J. R. Blake, and J. C. Kirkman-Brown. Human sperm accumulation near surfaces: a simulation study. *Journal of Fluid Mechanics*, **621**(1):289–320, 2009.

[86] D. J. Smith, E. A. Gaffney, H. Gadêlha, N. Kapur, and J. C. Kirkman-Brown. Bend propagation in the flagella of migrating human sperm and its modulation by viscosity. *Cell Motility and the Cytoskeleton*, **66**:220–236, 2009.

[87] D. J. Smith, A. A. Smith, and J. R. Blake. Mathematical embryology: the fluid mechanics of nodal cilia. *Journal of Engineering Mathematics*, **70**(1):255–279, 2011.

[88] C. R. Stauss, T. J. Votta, and S. S. Suarez. Sperm motility hyperactivation facilitates penetration of the hamster zona pellucida. *Biology of Reproduction*, **53**(6):1280–1285, 1995.

[89] G. G. Stokes. On the effect of the internal friction of fluids on the motion of pendulums. 1851.

[90] S. S. Suarez. Hyperactivated motility in sperm. *Journal of Andrology*, **17**(4):331, 1996.

[91] S. S. Suarez. Interactions of spermatozoa with the female reproductive tract. *Reproduction, fertility and development*, **19**:103–110, 2007.

[92] S. S. Suarez, D. F. Katz, D. H. Owen, J. B. Andrew, and R. L. Powell. Evidence for the function of hyperactivated motility in sperm. *Biology of Reproduction*, **44**:375–381, 1991.

[93] P. Y. Tam, D. F. Katz, and S. A. Berger. Non-linear viscoelastic properties of cervical mucus. *Biorheology*, **17**(5-6):465, 1980.

[94] G. I. Taylor. Analysis of the swimming of microscopic organisms. *Proc. R. Soc. Lond. Ser. A*, **209**:447–461, 1951.

[95] G. I. Taylor. The action of waving cylindrical tails in propelling microscopic organisms. *Proc. R. Soc. Lond. Ser. A*, **211**:225–239, 1952.

[96] J. Teran, L. Fauci, and M. Shelley. Viscoelastic fluid response can increase the speed and efficiency of a free swimmer. *Physical Review Letters*, **104**(3):38101, 2010.

[97] J. Teran and L. Fauci M. Shelley. Peristaltic pumping and irreversibility of a stokesian viscoelastic fluid. *Physics of Fluids*, **20**:073101, 2008.

[98] J. P. K. Tillett. Axial and transverse stokes flow past slender axisymmetric bodies. *Journal of Fluid Mechanics*, **44**:401–417, 1970.

[99] E. Topfer-Petersen, A. Wagner, J. Friedrich, A. Petrunkina, M. Ekhlasi-Hundrieser, D. Waberski, and W. Drommer. Function of the mammalian oviductal sperm reservoir. *J. of Exp. Zoology*, (292):210–215, 2002.

[100] E. O. Tuck. Some methods for flows past blunt slender bodies. *Journal of Fluid Mechanics*, **18**:619–635, 1964.

[101] T. Ullah. *Modeling a two-link rigid swimmer scalloping in linear viscoelastic fluid*. PhD thesis, Massachusetts Institute of Technology, 2007.

[102] G. G. Vernon and D. M. Woolley. Microtubule displacements at the tips of living flagella. *Cell Motility and the Cytoskeleton*, **52**:151–160, 2002.

[103] H. A. von Oberbeck. Ueber stationäre flüssigkeitsbewegungen mit berüsichtigung der inner reibung. *J. für die reine und angewandte Mathematik*, pages 62–80, 1876.

[104] H. Winet, G. S. Bernstein, and J. Head. Observations on the response of human spermatozoa to gravity, boundaries and fluid shear. *Reproduction*, **70**:511–523, 1984.

[105] R. Zargar and A. Najafiand M. Miri. Three-sphere low-reynolds-number swimmer near a wall. *Physical Review E*, **80**(2):026308, 2009.